Quantum simulation of many-body dynamics

by

Kushal Seetharam

B.S.E, Duke University (2014)
S.M., Massachusetts Institute of Technology (2019)

Submitted to the Department of Electrical Engineering and Computer Science
in partial fulfillment of the requirements for the degree of

Doctor of Philosophy

at the

MASSACHUSETTS INSTITUTE OF TECHNOLOGY

September 2022

Author .....
Department of Electrical Engineering and Computer Science
August 26, 2022

Certified by .....
Eugene Demler
Professor of Physics, ETH Zürich
Thesis Supervisor

Accepted by .....
Leslie A. Kolodziejski
Professor of Electrical Engineering and Computer Science
Chair, Department Committee on Graduate Students

Quantum simulation of many-body dynamics

by

Kushal Seetharam

Submitted to the Department of Electrical Engineering and Computer Science
on August 26, 2022, in partial fulfillment of the
requirements for the degree of
Doctor of Philosophy

Abstract

Quantum computers and simulators have the potential to improve our understanding of physics, material science, chemistry, and biology by providing a window into the dynamics of quantum many-body systems that appear in these fields. In addition to growing our knowledge of fundamental science, an increased understanding of these systems could lead to technological innovations in energy, industrial processes, and medicine. There are several different quantum hardware platforms and simulation modalities, however, which can be used to perform quantum simulations of many-body dynamics. This thesis seeks to uncover guidelines to a seemingly simply question: how do we answer useful questions using quantum simulators? Answering this involves learning what are good questions to ask quantum simulators, which questions should be asked to which platforms, and how we should ask each question (digital, analog, or hybrid simulation). We develop intuition for these guidelines by exploring three quantum simulation contexts: Bose-Fermi mixtures, dissipative spin chains, and nuclear magnetic resonance (NMR) spectroscopy experiments.

Thesis Supervisor: Eugene Demler
Title: Professor of Physics, ETH Zürich

Acknowledgments

My PhD has been a transformative experience. I am grateful to my parents for their love and uncoditional support, my brother for encouraging me to study physics and pointing me to salient references along the way, and my friends for keeping me honest and providing a wall that I could talk at.

I would like to thank my advisor, Eugene Demler, for opening the door for me to become a theorist, even though I did not have the most typical training and background. Eugene has always encouraged his students to work on a diversity of topics, and I have learned an appreciable amount physics from him. Perhaps more importantly, I have learned to ask good questions, never be hesitant to dive into something new, and that getting the calculation right is only half the job. The other half is to have a good story to tell.

I owe a large debt to Yulia Shchadilova, Jamir Marino, and Dries Sels, who were postdoctoral fellows from whom I learned how to effectively do research as well as how to operate in the academic community. Thank you for the endless discussions that have helped me grow both scientifically and personally. I would like to thank Mikhail Zvonarev for countless discussions about physics, the psychology of academics, and, in particular, how to write academic papers with clarity and integrity. Having a story to tell is only valuable if you are able to communicate it effectively.

Lastly, I am grateful to my committee members Will Oliver and Isaac Chuang, for broadening my horizons. From Will, I have gained an appreciation for how hard it is to develop and scale quantum technology, while the quantum information class I took with Ike forms the basis for how I interpret the field today.

My salutations to the many others I have learned from on this journey.

Contents

List of Figures

Part I

Introduction

The information revolution of the late 20th century was built on the first generation of quantum technology, with the semiconductor transistors underlying modern computers, lasers used in optical communication, and nuclear magnetic resonance (NMR) used in drug development and medical MRI machines intrinsically reliant on quantum effects. Due to improvements in semiconductor fabrication and the experimental control of lasers, we are now poised to enter a new chapter of the Information Age: one built on the next generation of quantum technology. These devices will controllably manifest properties such as quantum coherence and entanglement which can be exploited for applications in computing, sensing, and communication. In addition to catalyzing discovery in various scientific disciplines, this technology will complement classical information systems and enable improvements in medicine, material science, industrial processes, and cryptography. Making this 'quantum leap', however, requires a fundamentally interdisciplinary effort. Physics, computer science, electrical engineering, and material science are required to develop high fidelity controllable quantum devices, while many of the early applications of these devices are in chemistry, biology, and artificial intelligence. As quantum technology is still in its adolescence, achieving a practical advantage will likely require co-design of the quantum device or algorithm and its intended application, thus necessitating even closer collaboration between different fields.

Quantum computers and simulators, in particular, have received a lot of attention in both academia and industry due to their potential to catalyze progress in physics and material science, chemistry and drug development, as well as optimization and machine learning [124, 290, 24]. For example, a sufficiently powerful quantum computer may allow us to reverse engineer how bacteria do nitrogen-fixation and produce ammonium cheaply [295]. The current industrial process is an inefficient alternative which is responsible for 5% of the world's natural gas production, representing about 2% of the world's energy use, with this has serious environmental and economical consequences [341]. Quantum computers would also allow us insight into the electronic structure of materials such as perovskites, organic polymers, and high-temperature superconductors, which in turn, may enable technological advances that greatly in-

crease the viability of clean energy sources like solar, wind, and fusion.

In the above mentioned applications, quantum computers are often believed to have a formal advantage compared to classical computers: there exist quantum algorithms addresing critical bottlenecks of the application that are exponentially faster than known classical algorithms. This advantage, however, relies on delicate quantum properties such as coherence and entanglement which are washed out by noise resulting from interactions between the qubits and their environment. Theoretically, it is known that a noiseless quantum computer can be built out of a much larger noisy quantum system using error correction protocols. Even optimistic estimates, however, place such a noiseless fault-tolerant quantum computer (FTQC) at least 10-20 years away.

It is an open question whether the noisy intermediate scale quantum (NISQ) computers and analog quantum simulators available in the near-term can offer a formal exponential advantage, or even a practical speed-up compared to classical algorithms for any real application in science or industry. A common opinion in the quantum community is that the first useful task a NISQ computer may perform is the simulation of quantum dynamics [68, 290, 24, 80]. For example, digital quantum simulation, accomplished by discretizing the dynamics into several gates, is a flexible approach with controllable error that can improve our understanding of spin systems [203, 309], quantum chemistry [175, 274], biochemistry [328], and high energy physics [148, 243]. The strength of digital quantum simulation is that any Hamiltonian describing the dynamics of the system can be implemented, including Hamiltonians with complicated and long-range interactions that are necessary for quantitatively accurate descriptions of high-temperature superconductors, quantum chemistry, and optimization problems [80]. This approach also can simulate quantum dynamics with an arbitrary low error for a polynomial cost in computation time. The downside, however, is that general purpose digital quantum simulation requires fault-tolerant quantum computers, which come with an enormous hardware and runtime overhead.

Analog quantum simulation, accomplished by engineering the native dynamics of a quantum system to mimic a target system of interest, has also shown promise in

the study of quantum many-body systems in condensed matter physics, quantum chemistry, and high energy physics contexts [124]. Systems of ultracold atoms, for example, may be used to simulate models of high temperature superconductivity [38], the electronic structure of molecules [10], and lattice gauge theories [19] in addition to topics of fundamental interest such as quantum magnetism and topological phases of matter [135, 311]. Trapped ion systems have proven useful in simulating the dynamics and equilibrium properties of various models of quantum magnetism [36, 260], superconductivity [331], and vibronic modes of molecules, [335]. Superconducting circuits have been explored in the study of both equilibrium and dynamical properties of a range of quantum many-body systems, including Bose-Hubbard physics [157], models of quantum magnetism [151], disordered systems [305], and dynamical lattice gauge theories [235].

The benefit of analog quantum simulation is a direct, resource-efficient simulation of quantum systems that can be performed in the relatively near-term. The downsides are that analog simulators can only realize a limited set of models that can be natively realized and programmed, and even computations of these models are limited by control, calibration, and decoherence errors in the hardware [80]. While it is therefore unclear whether analog simulators can perform a practically useful computation that is intractable on classical computers, there is some hope that such a practical quantum advantage may be achievable for qualitative physics questions of fundamental interest. Specificaly, ultracold atoms in optical lattices may be able to capture the dynamics of the Fermi-Hubbard model better than the best classical algorithms, thereby granting qualitative insight into the behavior of high-temperature superconductors. The argument for such an advantage arises from using Hamiltonian verification procedures to quantify the control and calibration errors in the analog quantum simulator and then using Lieb-Robinson bounds relying on the local nature of interactions in the Hamiltonian to bound the propagation of these errors [116]. Developing other applications where analog quantum simulators may be useful requires an understanding of (1) how to engineer the dynamics of different platforms to realize a wider array of models, and (2) how correlations spread in both closed and

open quantum systems with different interaction profiles in order to bound errors in these platforms.

Each quantum hardware platform has its advantages and disadvantages, with certain simulation contexts being a more natural fit on specific platforms [80]. Ultracold atoms in harmonic potentials or optical lattices are well-suited for simulating systems of bosons and fermions that comprise solid-state systems. Gases of ultracold atoms in harmonic potentials are well-suited for examining interacting Bose gases, interacting Fermi gases, and Bose-Fermi mixtures as examined in Part II of the thesis. When optical lattice potentials are used to trap the atoms, they naturally realize Hubbard models for bosons and fermions, which are paradigmatic models describing the physics of many strongly correlated quantum systems including high-temperature superconductors [38]. While atomic platforms can already reach large numbers of particles and therefore simulate thermodynamically large many-body systems, they have no local control and can only perform analog simulation of a limited set of locally-interacting models that are naturally realized in the system. When the atoms are coupled to an optical cavity, this tunability can be partially alleviated and they can realize interesting magnetic spin models with different interaction profiles, as examined in Part III of the thesis. Ultracold atoms trapped in optical tweezers and excited to Rydberg states fully resolves the tunability issues and allows for both digital and analog quantum simulation of a range of spin models, with the added benefit of easily admitting complicated interaction geometries. However, zero-point motion of the atoms and the necessity of increasingly powerful lasers to scale the platform have currently limited systems to a few hunderd atoms.

Trapped ion and superconducting quantum simulators are explored in Part IV of the thesis. Trapped ions are suited for both digital and analog quantum simulation of a range of magnetic spin models. They benefit from natural implementations of long-range interactions leading to the ability to realize a diverse array of interaction graphs [86, 233]. However, heating of motional modes of the ion chain limits the systems to about 50 ions in a chain, with complicated architectures required to scale to larger systems [80, 124]. Superconducting systems are well-suited to both digital

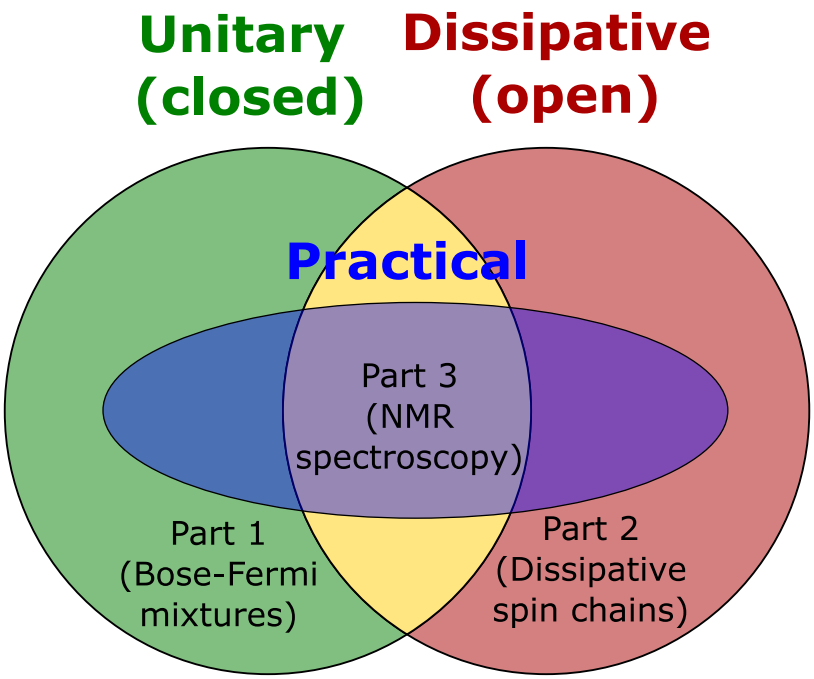

Figure 1: Different contexts of quantum simulation of quantum many-body dynamics.

and analog simulation of interacting systems of spins and bosons. They are limited to local interactions, but can be fabricated to realize different interaction geometries. These systems have fast dynamical time scales compared to atoms and ions (MHz vs kHz), but correspondingly shorter coherence times. Superconducting devices also benefit from fast local control and readout, but require consistent calibration.

In order to make progress in answering practically useful questions using quantum simulators, we must improve our understanding of which platforms suit different application contexts, and when a digital, analog, or hybrid simulation approach is appropriate. In this thesis, we explore three contexts of quantum simulation of many-body dynamics through which we can shed light on these questions (see Fig. 1). In Part II, we investigate the unitary dynamics of closed systems of Bose-Fermi mixtures using ultracold atom quantum simulators. In Part III, we study the dissipative dynamics of open spin chains using cavity-QED quantum simulators comprised of cold atoms trapped inside an optical cavity. In Part IV, we examine a quantum simulation application of practical utility: NMR spectroscopy. The dynamics of NMR

systems can be modeled as purely unitary, purely dissipative, or a combination of both depending on the experimental protocol. We explore the suitability of trapped ion and superconducting quantum simulators, as well as digital, analog, and hybrid simulation approaches for different NMR contexts. In Part V, we synthesize key lessons learned and open questions that emerge from the connections between topics explored in Parts II-IV. The material in this thesis corresponds to the work in Refs. [319, 320, 321, 322, 323, 324, 325, 326].

Part II

Dynamics of closed systems: Bose-Fermi mixtures

Chapter 1

Introduction

Every observed subatomic particle in nature is either a boson or a fermion. Bosons typically correspond to force carriers, such as photons associated with electromagnetism, while fermions typically carry mass and correspond to matter. In many-body systems, the emergent degrees of freedom can be bosonic, fermionic, or in special cases anyonic. Most quantum many-body systems that appear in both physics and chemistry can thus be described as mixtures of bosons and fermions. A canonical example is given by semiconductors and other solid-state systems, where many important properties such as transport are determined by the interaction between electrons (fermions) and phonons (bosons).

Quantum degenerate gases of bosons and fermions have emerged as a leading quantum simulation platform to study several such quantum many-body systems as they provide a highly controllable setting to investigate different prototypical models [39]. Bose gases have been used to study Bose-Einstein condensation (BEC) and superfluidity [37], the Mott insulator to superfluid transition [134], Luttinger liquids [180], quantum Hall physics [45], localization physics [301, 31], and quantum magnetism [168]. Fermi gases have been used to investigate pairing in conventional BCS superconductors [38], the BEC-BCS crossover [385], high temperature superconductivity [38], the equation of state in extreme systems like neutron starts [265], and itinerant ferromagnetism [170].

Given the success of exploring purely bosonic and fermionic many-body systems

using degenerate Bose and Fermi gases, it is natural to consider degenerate Bose-Fermi mixtures and the simulation applications they open up. Such platforms would enable investigation of electron-phonon and strongly correlated electron systems in condensed matter physics [226, 184], the electronic structure of molecules in quantum chemistry [10, 11], and lattice gauge theories in high-energy physics [73], which also relate to the low-energy behavior of some condensed matter systems with normal and/or topological order [19]. Ultracold quantum gases forming Bose-Fermi mixtures are well isolated from their environment and are widely tunable to different limits of the system [39], thus providing a promising analog quantum simulation platform to examine the unitary dynamics of various closed quantum many-body systems.

In the limit that either the Bose or Fermi quantum gas is much more dilute than the other, we can describe the system in terms of an impurity particle from the minority gas interacting with a bath formed by the majority gas. Such impurity systems are closely linked to a concept that has proved essential to understanding Bose-Fermi mixtures, and quantum many-body systems more generally: the quasiparticle. The original manifestations of this concept was the polaron. A polaron is an impurity that has been dressed by a cloud of excitations of the surrounding bath which, in equilibrium, results in a renormalization of its mass, energy, and other properties. A toy analogy can be made to a ball rolling around a rubber sheet; the ball creates a deformation in the sheet that moves along with the ball and modifies its motion. The ball represents the impurity and the deformation in the sheet represents the cloud of particles in the many-body bath that dresses the impurity. Depending on whether the excitations dressing the impurity are bosonic or fermionic, we call the resulting quasiparticle a Bose polaron or a Fermi polaron.

Landau introduced the original manifestation of the polaron in 1933 when he examined an electron getting trapped by a crystal lattice [199]. The codification of an electron trapped by a crystal lattice as a phonon-dressed quasiparticle called a polaron was done by Pekar in 1946 and then further developed in a joint paper between Pekar and Landau in 1948 [282, 198]. While the initial treatment of the polaron was in the strong-coupling regime, it was soon extended to the weak coupling

regime by Fröhlich [119]. Since these original investigations, it has been discovered that polaronic physics is relevant to a variety of modern fields including superconductivity [4, 91, 141, 184], organic transistors [161], and biophysics [287]. Polarons also serve as an archetype upon which we can build an understanding of other types of quantum impurity problems [317]. As polarons are a paradigmatic quasiparticle, investigating their ground state properties, their far-from-equilibrium dynamics, and any connection between the two may help elucidate the non-equilibrium behavior of quasiparticles which characterize other quantum many-body systems [339]. Therefore, studying the mobile impurity limit of a Bose-Fermi mixture is a promising avenue to gain insight into the dynamics of closed quantum many-body systems more broadly.

Understanding the dynamics of a mobile impurity in an interacting quantum many-body medium is still challenging, however, due to the necessity of including entanglement between the impurity and excited states of the environment in a wide range of energy scales. Recently, ensembles of ultracold atoms have emerged as a versatile analog quantum simulation platform that is well suited to enabling investigation of polaronic physics. Control of host atom species allows specification of fermionic or bosonic statistics and effective spin degrees of freedom. Additionally, tunability of the interaction strength between the impurity and host atom through Feshbach resonances and powerful measurement techniques including radio frequency (RF) spectroscopy, Ramsey interferometery, absorption imaging, and time-of-flight imaging enable a detailed study of these systems.

This toolbox has been instrumental in several fundamental experimental studies of polaronic physics. In a one-dimensional quantum gas, for example, polaronic renormalization of the impurity mass has been studied in Ref. [61]. Additionally, a mobile impurity pulled through a one-dimensional quantum gas by gravity was shown to exhibit Bloch oscillations on top of a finite drift velocity in the absence of a periodic lattice [251]. In a three-dimensional Bose gas cooled into a Bose-Einstein Condensate (BEC), the radio-frequency (RF) spectrum [158, 172, 377] and Loschmidt echo [339] of the polaron quasiparticle formed by the impurity and BEC has been probed as a function of interaction strength, but experiments have yet to examine quantities that

are sensitive to the finite momentum of the impurity.

The ability to perform analog quantum simulations of polaronic systems in ultracold atoms has motivated a bevy of theoretical studies as well. The first theoretical studies of Bose polarons in a cold atoms context were done using the Fröhlich model, suitable for weak impurity-bath coupling [246, 78, 350, 60, 363], and later extended to beyond Fröhlich terms that allow investigation of the strong-coupling regime [293, 72, 280, 333, 174, 136]. Much of this initial theoretical work focused on characterizing the quasiparticle nature of the equilibrium polaron through quantities like the energy [293, 332, 334] and effective mass [333, 137, 139]. Further study was done to understand the non-equilibrium dynamics of polarons [48, 312, 83, 138, 182, 83, 334, 142, 204, 97, 43, 267, 65, 98] and examine experimentally relevant protocols including harmonically trapped and oscillating BECs [61, 140, 254, 253, 256]. Much recent work has been focused on extending the previous results to the case of finite temperature [217, 143, 103, 114] and multiple impurities [360, 255, 263].

A wide variety of theoretical methods have been used in these works. Variational approaches have been used to predict RF spectra, average values of different observables, spatial density profiles, and even systems with multiple impurities [334, 360, 97, 333, 332]. T-matrix approximations have also been used to study the RF spectra while confirming the importance of beyond-Fröhlich terms in the Hamiltonian at strong interactions [293]. Renormalization group methods have been used to examine trajectories and the effect of quantum fluctuations on top of the mean-field solution [139, 140, 137, 142]. Markovian master equations have been used to study thermalization dynamics and polaron formation [204, 267], while finite temperature effects have also been studied with diagrammatic techniques for strong coupling [143] and perturbation theory for weak coupling [217]. Non-perturbative methods have also been used to examine impurity dynamics in harmonically trapped 1D BECs [254, 253] and the subsonic-supersonic dynamics of weakly interacting impurities [43]. Quantum Monte Carlo computations have also been used to study the energy and other properties of the Bose polaron [280, 281]. Efforts to study the strong coupling regime by moving beyond Bogoliubov theory have also been made [98].

In this part of the thesis, we explore how analog quantum simulations performed in ultracold atoms can shed light on a gap in the literature on Bose polarons: the dynamics of a fast mobile impurity in a weakly-interacting BEC. The novel behavior we uncover using the theoretical treatment described in Chap. 2 gives insight into how friction manifests in quantum many-body systems, Chap. 3, and has implications for experimental protocols seeking to measure basic quasiparticle properties such as the polaron's effective mass, Chap. 4. We discuss how these effects can be observed in ultracold atom platforms, thus giving an example of how analog quantum simulations can elucidate the dynamics of closed quantum many-body systems.

Chapter 2

Bose Polaron Model

In this chapter we develop a theoretical model describing a finite momentum impurity interacting with a surrounding BEC and derive equations of motion for the dynamics of the system. Specifically, we consider an impurity atom immersed into a weakly interacting BEC of ultracold atoms near the inter-species Feshbach resonance, which can be used to tune the impurity-boson interaction. In the first section, we lay out the treatment for a homogeneous system without trapping potentials or external forces. In the second section, we show how the local density approximation can be used to extend the formalism for realistic trapping potentials and external forces. The formalism developed in these sections enables study of the dynamics investigated in Chap. 3 and Chap. 4 respectively.

2.1 System

We consider a system contained in a three-dimensional box, $d = 3$, of length L in each dimension, with periodic boundary conditions.

2.1.1 Hamiltonian

The microscopic Hamiltonian of entire system,

$$\hat{H} = \hat{H}_0 + \hat{H}_{\mathrm{IB}} \tag{2.1}$$

consists of two parts:

$$\hat{H}_0 = \sum_{\mathbf{k}} \varepsilon^I_{\mathbf{k}} \hat{d}^\dagger_{\mathbf{k}} \hat{d}_{\mathbf{k}} + \sum_{\mathbf{k}} \varepsilon^B_{\mathbf{k}} \hat{a}^\dagger_{\mathbf{k}} \hat{a}_{\mathbf{k}} + \frac{1}{L^d} \frac{g_{\mathrm{BB}}}{2} \sum_{\mathbf{k},\mathbf{k}',\mathbf{q}} \hat{a}^\dagger_{\mathbf{k}+\mathbf{q}} \hat{a}^\dagger_{\mathbf{k}'-\mathbf{q}} \hat{a}_{\mathbf{k}'} \hat{a}_{\mathbf{k}} \tag{2.2}$$

represents free impurities in an interacting Bose gas, and

$$\hat{H}_{\mathrm{IB}} = \frac{1}{L^d} g_{\mathrm{IB}} \sum_{\mathbf{k},\mathbf{k}',\mathbf{q}} \hat{d}^\dagger_{\mathbf{k}'+\mathbf{q}} \hat{d}_{\mathbf{k}+\mathbf{q}} \hat{a}^\dagger_{\mathbf{k}} \hat{a}_{\mathbf{k}'} \tag{2.3}$$

represents the interaction between the impurities and the Bose gas. The boson creation (annihilation) operator in the momentum space is $\hat{a}^\dagger_{\mathbf{k}}$ ($\hat{a}_{\mathbf{k}}$); the same for the impurity is $\hat{d}^\dagger_{\mathbf{k}}$ ($\hat{d}_{\mathbf{k}}$). The boson, $\varepsilon^B_{\mathbf{k}}$, and impurity, $\varepsilon^I_{\mathbf{k}}$, kinetic energies, are

$$\varepsilon^B_{\mathbf{k}} = \frac{\mathbf{k}^2}{2m_B}, \qquad \varepsilon^I_{\mathbf{k}} = \frac{\mathbf{k}^2}{2m_I}. \tag{2.4}$$

Here, m_B (m_I) stands for the boson (impurity) mass. The microscopic Hamiltonian, as defined by Eq. (2.1) contains an arbitrary number of the impurity particles. For our work, however, we are interested in the states containing only one impurity.

The Hamiltonian (2.2) can be transformed in according to the standard Bogoliubov theory [285]; using the linear transformation

$$\hat{a}_{\mathbf{k}} = u_{\mathbf{k}} \hat{b}_{\mathbf{k}} - v_{\mathbf{k}} \hat{b}^\dagger_{-\mathbf{k}}, \qquad \mathbf{k} \neq 0 \tag{2.5}$$

with the coefficients $u_{\mathbf{k}}, v_{-\mathbf{k}} = \sqrt{\frac{\varepsilon^B_{\mathbf{k}} + g_{\mathrm{BB}} n_0}{2\omega_{\mathbf{k}}} \pm \frac{1}{2}}$ we get

$$\hat{H}_0 = \sum_{\mathbf{k}} \varepsilon^I_{\mathbf{k}} \hat{d}^\dagger_{\mathbf{k}} \hat{d}_{\mathbf{k}} + \sum_{\mathbf{k}} \omega_{\mathbf{k}} \hat{b}^\dagger_{\mathbf{k}} \hat{b}_{\mathbf{k}} \tag{2.6}$$

for the terms in Eq. (2.2) relative to the FMGS energy of the condensate. The operators $\hat{b}^\dagger_{\mathbf{k}}$ ($\hat{b}_{\mathbf{k}}$) create (annihilate) Bogoliubov quasiparticles with momentum $\mathbf{k}$ and dispersion

$$\omega_{\mathbf{k}} = \sqrt{\varepsilon^B_{\mathbf{k}} (\varepsilon^B_{\mathbf{k}} + 2 g_{\mathrm{BB}} n_0)}. \tag{2.7}$$

Here, $n_0 = N/L^d$ is the gas density (we let it be equal to the condensate density

for the observables discussed in the paper), and N is the number of bosons. The dispersion (2.7) yields the sound velocity

$$c = \sqrt{\frac{g_{\rm BB} n_0}{m_B}}. \tag{2.8}$$

It also sets the healing length

$$\xi = (2 m_B g_{\rm BB} n_0)^{-1/2} \tag{2.9}$$

at which the transition between the particle and phonon regimes of the BEC excitations occurs. The s-wave scattering length, $a_{\rm BB} \geq 0$, sets the value of the coupling strength $g_{\rm BB}$ in Eq. (2.2):

$$g_{\rm BB} = \frac{4\pi a_{\rm BB}}{m_B}. \tag{2.10}$$

The Hamiltonian (2.3) represents the impurity-boson interaction potential in a way that is uniform in momentum space and, therefore, requires a regularization to be physically meaningful. We implement the regularization procedure commonly used in the existing literature [293, 332, 334]: we impose a sharp ultraviolet (UV) cutoff Λ onto the the momentum space of the problem. The interaction parameter $g_{\rm IB}$ and the impurity-boson scattering length $a_{\rm IB}$ are connected through the Lippmann-Schwinger equation

$$g_{\rm IB}^{-1} = \frac{\mu}{2\pi} a_{\rm IB}^{-1} - \frac{1}{L^d} \sum_{\mathbf{k}}^{\Lambda} \frac{2\mu}{\mathbf{k}^2}. \tag{2.11}$$

Here,

$$\mu = \frac{m_I m_B}{m_I + m_B} \tag{2.12}$$

is the reduced mass of the two-body impurity-boson system. We stress that the second term in Eq. (2.11) renormalizes $g_{\rm IB}$, thus giving a meaning to the interaction term (2.3) in the $\Lambda \to \infty$ limit. The observables from our paper are evaluated for Λ large enough to be viewed as if we took the $\Lambda \to \infty$ limit.

2.1.2 Lee-Low-Pines transformation

Now we take our model defined in the laboratory reference frame and write it in the mobile impurity reference frame. These reference frames are connected with the Lee-Low-Pines transformation,

$$\hat{\mathcal{S}} = e^{i\hat{\mathbf{R}}_{\mathrm{imp}}\hat{\mathbf{P}}_{\mathrm{ph}}}, \tag{2.13}$$

named after the original work [207]. Here, $\hat{\mathbf{R}}_{\mathrm{imp}}$ is the position operator of the impurity. Any operator $\hat{\mathcal{O}}$ defined in the laboratory frame takes the form

$$\hat{\mathcal{O}}_{\mathrm{LLP}} = \hat{\mathcal{S}}\hat{\mathcal{O}}\hat{\mathcal{S}}^{\dagger} \tag{2.14}$$

in the mobile impurity reference frame. Note that we constrain our system to the case of a single impurity.

The total momentum of the system

$$\hat{\mathbf{P}} = \hat{\mathbf{P}}_{\mathrm{imp}} + \hat{\mathbf{P}}_{\mathrm{ph}} \tag{2.15}$$

is conserved. In the above expression, the impurity momentum $\hat{\mathbf{P}}_{\mathrm{imp}}$ and total phonon momentum $\hat{\mathbf{P}}_{\mathrm{ph}}$ are given as

$$\hat{\mathbf{P}}_{\mathrm{imp}} = \sum_{\mathbf{k}} \mathbf{k}\hat{d}^{\dagger}_{\mathbf{k}}\hat{d}_{\mathbf{k}} \tag{2.16}$$

$$\hat{\mathbf{P}}_{\mathrm{ph}} = \sum_{\mathbf{k}} \mathbf{k}\hat{b}^{\dagger}_{\mathbf{k}}\hat{b}_{\mathbf{k}}. \tag{2.17}$$

The final Hamiltonian $\hat{H}_{\mathrm{LLP}}$ after the transformation reads:

$$\hat{H}_{\mathrm{LLP}} \equiv \hat{\mathcal{S}}\hat{H}\hat{\mathcal{S}}^{\dagger} = \hat{H}_{0,\mathrm{LLP}} + \hat{H}_{\mathrm{IB,LLP}} \tag{2.18}$$

where

$$\hat{H}_{0,\mathrm{LLP}} = \sum_{\mathbf{k}} \omega_{\mathbf{k}}\hat{b}^{\dagger}_{\mathbf{k}}\hat{b}_{\mathbf{k}} + \frac{1}{2m_I}\left(\hat{\mathbf{P}}_{\mathrm{imp}} - \sum_{\mathbf{k}} \mathbf{k}\hat{b}^{\dagger}_{\mathbf{k}}\hat{b}_{\mathbf{k}}\right)^2 \tag{2.19}$$

and

$$\hat{H}_{\mathrm{IB,LLP}} = g_{\mathrm{IB}} n_0 + g_{\mathrm{IB}} \sqrt{n_0} \frac{1}{\sqrt{L^d}} \sum_{\mathbf{k}\neq 0} W_{\mathbf{k}} \left(\hat{b}_{\mathbf{k}} + \hat{b}^{\dagger}_{-\mathbf{k}} \right) + g_{\mathrm{IB}} \frac{1}{L^d} \sum_{\mathbf{k}\neq 0, \mathbf{k}'\neq 0} V^{(1)}_{\mathbf{k},\mathbf{k}'} \hat{b}^{\dagger}_{\mathbf{k}} \hat{b}_{\mathbf{k}'} + \frac{1}{2} g_{\mathrm{IB}} \frac{1}{L^d} \sum_{\mathbf{k}\neq 0, \mathbf{k}'\neq 0} V^{(2)}_{\mathbf{k},\mathbf{k}'} \left(\hat{b}_{-\mathbf{k}} \hat{b}_{\mathbf{k}'} + \hat{b}^{\dagger}_{\mathbf{k}} \hat{b}^{\dagger}_{-\mathbf{k}'} \right) \quad (2.20)$$

Here, the interaction vertices satisfy the relations

$$W_{\mathbf{k}} = \sqrt{\frac{\varepsilon_{\mathbf{k}}}{\omega_{\mathbf{k}}}} \quad (2.21)$$

$$V^{(1)}_{\mathbf{k}\mathbf{k}'} \pm V^{(2)}_{\mathbf{k}\mathbf{k}'} = (W_{\mathbf{k}} W_{\mathbf{k}'})^{\pm 1} \quad (2.22)$$

Note that the lab frame impurity momentum operator $\hat{\mathbf{P}}_{\mathrm{imp}}$ that appears in Eq. (2.19) commutes with the Hamiltonian $\hat{H}_{\mathrm{LLP}}$ in the Lee-Low-Pines frame. We recognize it as the total momentum $\hat{\mathbf{P}}$ that commutes with the lab frame Hamiltonian $\hat{H}$ given in Eq. (2.1). Therefore, we can replace $\hat{\mathbf{P}}_{\mathrm{imp}}$ with the quantum number $\mathbf{P}$; dynamics under this model will decouple into sectors indexed by $\mathbf{P}$. As the system is spherically symmetric, there is no preferred orientation of $\mathbf{P}$ and hence physical quantities will only depend on the magnitude

$$P = |\mathbf{P}| \,. \quad (2.23)$$

The first term in Eq. (2.19) describes a weakly interacting BEC where excitations are Bogoliubov phonons with dispersion $\omega_{\mathbf{k}}$. Enacting the Lee-Low-Pines transformation allows us to eliminate impurity degrees of freedom in the Hamiltonian at the cost of introducing an additional interaction term between phonons that show up in second term of Eq. (2.19). The effective interaction strength $\frac{1}{2m_I}$ of this term is set by the impurity mass and vanishes for heavy impurities as the co-moving frame of the impurity and the original lab frame coincide.

After the Lee-Low-Pines transformation, the part of the original Hamiltonian representing the impurity-boson interaction turns into Eq. (2.20) which contains terms describing impurity-mediated interactions between the bosons. The linearized part of Eq. (2.20) constitutes the Fröhlich model which is suitable for describing weakly

interacting polaronic systems. The term linear in phonon operators describes the impurity exciting phonons directly out of the condensate. If the impurity interacts strongly with the bosonic bath, it can also mediate scattering between phonon excitations; this is the physics included in the quadratic terms in Eq. (2.20) and these terms are required for the study of strongly interacting polaronic systems beyond the Fröhlich model [332, 317].

2.1.3 Equations of motion

We derive equations of motion for the system for the system state by approximating the true wavefunction with a single variational wavefunction and then time-evolving this variational state according the the Hamiltonian (2.18). Formally, we use Dirac's time-dependent variational principle to derive equations of motion for the coefficients defining the variational state [167]. The finite momentum ground state (FMGS) is found by evolving the variational state in imaginary time while quench dynamics can be studied by evolving the state in real time. Our trial wavefunctions are coherent states of the form

$$|\Psi_{\rm coh}(t)\rangle = e^{\sum_{\mathbf{k}} \beta_{\mathbf{k}}(t)\hat{b}^\dagger_{\mathbf{k}} - \text{H.c.}} |0\rangle \tag{2.24}$$

as used in the literature (e.g. [332, 334, 360]). Note that H.c. means Hermitian conjugate. Here, $\beta_{\mathbf{k}}(t)$ are the coherent state amplitudes and $|0\rangle$ denotes the vacuum of Bogoliubov phonons (which is the FMGS of the BEC) in the co-moving frame of the impurity. We use want to derive equations of motion for the coherent state amplitudes corresponding to time-evolution in the Lee-Low-Pines frame

$$|\Psi_{\rm coh}(t)\rangle = e^{-i\hat{H}_{\rm LLP}t} |0\rangle \,. \tag{2.25}$$

To derive the equations of motion, we first construct the classical action $\mathcal{S} = \int \mathcal{L}(t)dt$ where

$$\mathcal{L}(t) = \langle \Psi_{\rm coh}(t)| \, i\partial_t - \hat{H}_{\rm LLP} \, |\Psi_{\rm coh}(t)\rangle \tag{2.26}$$

is a classical Lagrangian calculated by projecting the true many-body wavefunction onto the submanifold of Hilbert space spanned by our chosen class of trial wavefunctions. The least action principle then gives the standard Euler-Lagrange equations of motion

$$\frac{d}{dt}\frac{\partial \mathcal{L}}{\partial \dot{\beta}_{\mathbf{k}}} - \frac{\partial \mathcal{L}}{\partial \beta_{\mathbf{k}}} = 0 \tag{2.27}$$

which describe the dynamics of the variational parameters $\beta_{\mathbf{k}}(t)$ and $\phi(t)$. The explicit expressions for these equations of motion are

$$i\dot{\beta}_{\mathbf{k}} = g_{\mathrm{IB}}\sqrt{n_0}W_{\mathbf{k}} + \Omega_{\mathbf{k}}\beta_{\mathbf{k}} + g_{\mathrm{IB}}\left(W_{\mathbf{k}}\chi_{\beta}^{+} + W_{\mathbf{k}}^{-1}\chi_{\beta}^{-}\right) \tag{2.28}$$

where we have defined

$$\chi_{\beta}^{\pm} = \frac{1}{2}\sum_{\mathbf{k}'} W_{\mathbf{k}'}^{\pm 1}\left(\beta_{\mathbf{k}'} \pm \beta_{\mathbf{k}'}^{*}\right) \tag{2.29}$$

$$\Omega_{\mathbf{k}} = \omega_{\mathbf{k}} + \frac{\mathbf{k}^2}{2m_I} - \frac{1}{m_I}\mathbf{k}\left(\mathbf{P} - \mathbf{P}_{\mathrm{ph}}\right) \tag{2.30}$$

and $\mathbf{P}_{\mathrm{ph}} = \sum_{\mathbf{k}'} \mathbf{k}' \left|\beta_{\mathbf{k}'}\right|^2$ follows from Eq. (2.17) and Eq. (2.24). Similarly, we can relate the interaction parameter g_{BB} to the boson-boson scattering length a_{BB} by solving the two-body boson-boson scattering problem. As the boson-boson interaction is weak, we can use the Born approximation rather than the full Lippman-Schwinger equation to get $g_{\mathrm{BB}} = \frac{4\pi}{m_B}a_{\mathrm{BB}}$.

At this point, we are ready to study the FMGS or quench dynamics of the system by evolving the equations of motion in imaginary time or real time respectively. The FMGS can alternatively be studied by calculating the analytical saddle point solution to Eq. (2.28) as done in Sec. 2.1.4 below. However, this approach does not allow us to study the Cherenkov regime as the saddle point solution assumes that the variational parameters $\beta_{\mathbf{k}}$ are real; for large enough total momentum, this is not true. Nonetheless, the saddle point solution is still useful to predict the effective mass of slow polarons.

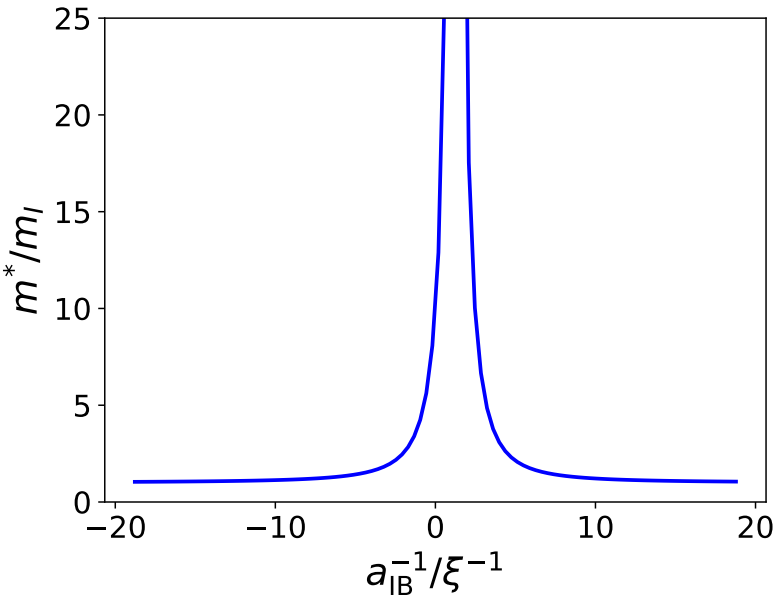

Figure 2: The dependence of the mass enhancement m^*/m_I given by the equation (2.36) on the inter-species scattering length a_{IB}^{-1} for $P = 0.1[m_I c]$.

2.1.4 Saddle Point Solution

Here, we derive the saddle point solution of the equations of motions (2.28). We set the left hand side of the first equation to zero and obtain the following equation which defines the saddle point

$$g_{\mathrm{IB}}\sqrt{n_0}W_{\mathbf{k}} + \Omega_{\mathbf{k}}\left[\beta\right]\beta_{\mathbf{k}} + g_{\mathrm{IB}}W_{\mathbf{k}}\sum_{\mathbf{k}'} W_{\mathbf{k}'}\beta_{\mathbf{k}'} = 0 \tag{2.31}$$

The equation for the imaginary part of the variational parameter always has a trivial solution $\mathrm{Im}\beta_{\mathbf{k}} = 0$. Further we imply that in the stationary state $\beta_{\mathbf{k}}$ is real.

To solve the equation for the real part of $\beta_{\mathbf{k}}$ we rewrite the equation (2.31) such that we obtain a closed equation for $\chi = \sum_{\mathbf{k}} W_{\mathbf{k}}\beta_{\mathbf{k}}$ and solve this equation to get an analytical expression for the coherent state amplitudes $\beta_{\mathbf{k}}$ (2.31):

$$\beta_{\mathbf{k}} = -\frac{W_{\mathbf{k}}}{\Omega_{\mathbf{k}}\left[\beta_{\mathbf{k}}\right]}\frac{2\pi\sqrt{n_0}}{\mu_{red}\left(a_{\mathrm{IB}}^{-1} - a_*^{-1}\left[\beta\right]\right)} \tag{2.32}$$

We introduce the shift of the Feshbach resonance $\frac{\mu_{red}}{2\pi} a_*^{-1}[\beta] \equiv \sum_k^{\Lambda} \left(\frac{2\mu_{red}}{k^2} - \frac{W_k^2}{\Omega_{\mathbf{k}}[\beta_{\mathbf{k}}]} \right)$. Note that this is just a formal solution, where $a_*^{-1}[\beta]$ and $\Omega_{\mathbf{k}}[\beta]$ are functionals of $\beta_{\mathbf{k}}$.

We substitute the solution for $\beta_{\mathbf{k}}$ to the functionals $\mathbf{P}_{\rm ph}[\beta]$ and $a_*^{-1}[\beta]$ and obtain two closed integral equations which fully describe the stationary state of the system in the long-time limit

$$\begin{aligned} \mathbf{P}_{\rm ph} =& \frac{4\pi^2 n_0}{\mu_{red}^2 \left(a_{\rm IB}^{-1} - a_*^{-1}\right)^2} \\ & \times \sum_{\mathbf{k}} \frac{\mathbf{k} W_{\mathbf{k}}^2}{\left(\omega_{\mathbf{k}} + \frac{\mathbf{k}^2}{2m_I} - \frac{\mathbf{k}}{m_I}(\mathbf{P} - \mathbf{P}_{\rm ph})\right)^2} \end{aligned} \tag{2.33}$$

$$a_*^{-1} = \sum_{\mathbf{k}} \left(\frac{4\pi}{|\mathbf{k}|^2} - \frac{2\pi \mu_{\rm red}^{-1} W_{\mathbf{k}}^2}{\omega_{\mathbf{k}} + \frac{\mathbf{k}^2}{2m_I} - \frac{\mathbf{k}}{m_I}(\mathbf{P} - \mathbf{P}_{\rm ph})} \right) \tag{2.34}$$

We solve these equations numerically for any given total momentum of the system $\mathbf{P}$ and given interaction $a_{\rm IB}^{-1}$.

The energy of the system simplifies in the case of fully real $\beta_{\mathbf{k}}$ to

$$E_{\rm pol} = \frac{1}{2m_I}\left(\mathbf{P}^2 - \mathbf{P}_{\rm ph}^2[\beta]\right) + \frac{2\pi}{\mu_{\rm red}} \frac{n_0}{a_{\rm IB}^{-1} - a_*^{-1}}. \tag{2.35}$$

The energy of the stationary state is divergent at $a_{\rm IB}^{-1} = a_*^{-1}$. Note, that even for the finite momentum $\mathbf{P}$, the energy of the system is a UV-convergent quantity. This directly follows from the equation (2.35) where all entries including a_*^{-1} and $\mathbf{P}_{\rm ph}$ are fully UV-convergent.

We calculate the effective mass by using the quasi-classical correspondence principle. In the stationary state the velocity carried by the the impurity, $\mathbf{P}_I/m_I$, should coincide with the velocity of the polaron, $\mathbf{P}/m^*$ where m^* is the effective mass of the polaron. Recalling that the momentum of the polaron carried by the impurity is the difference between the total momentum of the system and the momentum carried by the bosons so $\mathbf{P}_I = \mathbf{P} - \mathbf{P}_{\rm ph}$, we obtain the following expression for the effective mass

of the polaron

$$\frac{m_I}{m^*} = 1 - \frac{|\mathbf{P}_{\rm ph}|}{|\mathbf{P}|}. \tag{2.36}$$

The dependence of the polaron mass is shown in Fig. 2 across the Feshbach resonance. In contrast with the Fröhlich model where mean-field solution gives linear dependence of the effective polaron mass as a function of the interaction, accounting for the the two boson scattering terms in the Hamiltonian (Eq. (2.20)) provides a non-linear dependence of the effective polaron mass as a function of the interacting strength $a_{\rm IB}^{-1}$. The effective mass diverges as the shifted Feshbach resonance is approached $a_{\rm IB}^{-1} \to a_*^{-1} \pm 0$. The effective mass is infinite exactly at the resonance point.

2.1.5 Observables

The trial wavefunction $|\Psi_{\rm coh}(t)\rangle$ is characterized by the coherent state amplitudes $\beta_{\mathbf{k}}$; the square $|\beta_{\mathbf{k}}|^2$ of these amplitudes can be used to calculate a number of physical quantities that we can use to understand the system. The structure of the trial wavefunction captures the essential physics of the polaron system over a range of interaction strengths as it allows a large occupation of phonon modes, $\hat{b}_{\mathbf{k}}$, with the number of these excitations increasing for strong interactions [332, 334]. Entanglement between the impurity and host atoms is captured as these phonon excitations are defined in the Lee-Low-Pines frame. However, the wavefunction Eq. (2.24) does not explicitly account for correlations between different excitations, which are only implicitly accounted for when the dynamics of the true many-body wavefunction is projected onto the variational manifold. At strong interactions, these correlations become relevant as the number of excitations becomes sizable; this fact may account for the numerical discrepency in the critical momenta between the FMGS and dynamical protocols as see in Fig. 3 in the next chapter. Promoting the trial wavefunction Eq. (2.24) to a full Gaussian state [337], amounting to including terms quadratic in $\hat{b}_{\mathbf{k}}$ in the exponential, may resolve this quantitative discrepency. We leave such an extension to future work as the coherent state wavefunction is sufficient to gain deep insight into various observables of interest in the system.

Recalling that $\mathbf{P}$ is the total conserved momentum of the system, two such quantities that are relevant to both the FMGS and quench dynamics are

$$N_{\mathrm{ph}}(t) = \sum_{\mathbf{k}} |\beta_{\mathbf{k}}|^2 \tag{2.37}$$

and

$$\mathbf{P}_{\mathrm{ph}} = \sum_{\mathbf{k}} \mathbf{k} \, |\beta_{\mathbf{k}}|^2 \tag{2.38}$$

where expectations are taken over $|\Psi_{\mathrm{coh}}(t)\rangle$. These quantities are the average total phonon number and the average total phonon momentum. There are also two distribution functions that are useful to understand the system:

$$\begin{aligned} n_{\mathrm{ph}}(\mathbf{k}) &= \frac{1}{N_{\mathrm{ph}}} \left\langle \hat{b}_{\mathbf{k}}^{\dagger} \hat{b}_{\mathbf{k}} \right\rangle \\ &= \frac{1}{N_{\mathrm{ph}}} |\beta_{\mathbf{k}}|^2 \end{aligned} \tag{2.39}$$

and

$$\begin{aligned} n_{\mathrm{imp}}(\mathbf{p}) &= \left\langle \delta \left(\hat{\mathbf{P}}_{\mathrm{imp}} - \mathbf{p} \right) \right\rangle \\ &= e^{-N_{\mathrm{ph}}(t)} \delta \left(\mathbf{P} - \mathbf{p} \right) + \tilde{n}_{\mathrm{imp}}(\mathbf{p}) \end{aligned} \tag{2.40}$$

where

$$\tilde{n}_{\mathrm{imp}}(\mathbf{p}) = \frac{e^{-N_{\mathrm{ph}}(t)}}{(2\pi)^3} \sum_{\mathbf{r}} e^{-i(\mathbf{P}-\mathbf{p})\mathbf{r}} \left(e^{\sum_{\mathbf{k}} |\beta_{\mathbf{k}}|^2 e^{i\mathbf{k}\mathbf{r}}} - 1 \right). \tag{2.41}$$

The first function, Eq. (2.39), describes how individual phonon occupation is distributed over momentum space on average. The second function, Eq. (2.40), describes the impurity's momentum distribution and contains two terms. The first term is a delta function at $\mathbf{p} = \mathbf{P}$ corresponding to a coherent part of the distribution while the second term, Eq. (2.41), represents the incoherent part of the distribution. The expression in Eq. (2.40) can be derived as follows. The distribution of total phonon

momentum is:

$$n_{\mathrm{ph,tot}}(\mathbf{p}) = \langle \Psi_{\mathrm{coh}} | \, \delta\left(\hat{\mathbf{P}}_{\mathrm{ph}} - \mathbf{p}\right) | \Psi_{\mathrm{coh}} \rangle \tag{2.42}$$

$$= \langle \psi | \frac{1}{(2\pi)^3} \sum_{\mathbf{r}} e^{i\mathbf{r}\left(\hat{\mathbf{P}}_{\mathrm{ph}} - \mathbf{p}\right)} | \psi \rangle \tag{2.43}$$

$$= \frac{1}{(2\pi)^3} \sum_{\mathbf{r}} e^{-i\mathbf{p}\cdot\mathbf{r}} e^{\sum_{\mathbf{k}} |\beta_{\mathbf{k}}|^2 \left(e^{i\mathbf{k}\cdot\mathbf{r}} - 1\right)} \tag{2.44}$$

$$= \frac{1}{(2\pi)^3} \sum_{\mathbf{r}} e^{-i\mathbf{p}\cdot\mathbf{r}} e^{-N_{\mathrm{ph}} + \sum_{\mathbf{k}} |\beta_{\mathbf{k}}|^2 e^{i\mathbf{k}\cdot\mathbf{r}}} \tag{2.45}$$

We can manipulate the expression into a more illuminating form as follows:

$$n_{\mathrm{ph,tot}} = \frac{1}{(2\pi)^3} \sum_{\mathbf{r}} e^{-i\mathbf{p}\cdot\mathbf{r}} e^{-N_{\mathrm{ph}} + \sum_{\mathbf{k}} |\beta_{\mathbf{k}}|^2 e^{i\mathbf{k}\cdot\mathbf{r}}} \tag{2.46}$$

$$= \frac{e^{-N_{\mathrm{ph}}}}{(2\pi)^3} \sum_{\mathbf{r}} e^{-i\mathbf{p}\cdot\mathbf{r}} \left[e^{\sum_{\mathbf{k}} |\beta_{\mathbf{k}}|^2 e^{i\mathbf{k}\cdot\mathbf{r}}} - 1 + 1 \right] \tag{2.47}$$

$$= e^{-N_{\mathrm{ph}}} \frac{1}{(2\pi)^3} \sum_{\mathbf{r}} e^{-i\mathbf{p}\cdot\mathbf{r}} \tag{2.48}$$

$$+ \frac{e^{-N_{\mathrm{ph}}}}{(2\pi)^3} \sum_{\mathbf{r}} e^{-i\mathbf{p}\cdot\mathbf{r}} \left[e^{\sum_{\mathbf{k}} |\beta_{\mathbf{k}}|^2 e^{i\mathbf{k}\cdot\mathbf{r}}} - 1 \right] \tag{2.49}$$

$$= e^{-N_{\mathrm{ph}}} \delta(\mathbf{p}) + \tilde{n}(\mathbf{p}) \tag{2.50}$$

where the weight of the first term $e^{-N_{\mathrm{ph}}}$ corresponds to how connected the system is to the free impurity and the second term

$$\tilde{n}(\mathbf{p}) \equiv \frac{e^{-N_{\mathrm{ph}}}}{(2\pi)^3} \sum_{\mathbf{r}} e^{-i\mathbf{p}\cdot\mathbf{r}} \left[e^{\sum_{\mathbf{k}} |\beta_{\mathbf{k}}|^2 e^{i\mathbf{k}\cdot\mathbf{r}}} - 1 \right] \tag{2.51}$$

corresponds to particle momenta distributed over an incoherent background. Now we want to derive the impurity's momentum distribution. Using $\hat{\mathbf{P}} = \hat{\mathbf{P}}_{\mathrm{ph}} + \hat{\mathbf{P}}_{\mathrm{imp}}$, we

have

$$n_{\text{imp}}(\mathbf{p}) = \langle\psi|\delta\left(\hat{\mathbf{P}}_{\text{imp}} - \mathbf{p}\right)|\psi\rangle \tag{2.52}$$

$$= \langle\psi|\delta\left(\hat{\mathbf{P}} - \hat{\mathbf{P}}_{\text{ph}} - \mathbf{p}\right)|\psi\rangle \tag{2.53}$$

$$= \langle\psi|\delta\left(\mathbf{P} - \hat{\mathbf{P}}_{\text{ph}} - \mathbf{p}\right)|\psi\rangle \tag{2.54}$$

$$= \langle\psi|\delta\left(\hat{\mathbf{P}}_{\text{ph}} - [\mathbf{P} - \mathbf{p}]\right)|\psi\rangle \tag{2.55}$$

$$= n_{\text{ph,tot}}(\mathbf{P} - \mathbf{p}). \tag{2.56}$$

In the third line we have replaced $\hat{\mathbf{P}} \to \mathbf{P}$ as the total momentum $\hat{\mathbf{P}}$ is fixed for a specific $|\psi\rangle$; the Lee-Low-Pines frame block-diagonalizes by total momentum. We realize that the impurity's momentum distribution $n_{\text{I}}(\mathbf{p})$ is given by the phonon momentum distribution $n_{\text{ph,tot}}(\mathbf{p})$ with the domain of the phonon momentum function mapped from $\mathbf{p} \to \mathbf{P} - \mathbf{p}$. We can salso use this result to traightforwardly compute the distribution for impurity momenta with magnitude $p \equiv |\mathbf{p}|$ as

$$n_{\text{imp}}(p) = \sum_{\mathbf{p}'} \delta\left(|\mathbf{p}'| - p\right) n_{\text{imp}}(\mathbf{p}') \tag{2.57}$$

which corresponds to examining spherical shells of the full three-dimensional distribution $n_{\text{imp}}(\mathbf{p})$.

When examining the FMGS specifically, we are also interested in examining the energy and quasiparticle residue which are given in Eq. (2.58) and Eq. (2.59) below:

$$E = \left\langle \hat{H}_{\text{LLP}} \right\rangle = \frac{1}{2m_I}\left(\mathbf{P}^2 - \mathbf{P}_{\text{ph}}^2\right) + \sum_{\mathbf{k}} \Omega_{\mathbf{k}} |\beta_{\mathbf{k}}|^2 + g_{\text{IB}}\left(\chi_\beta^+ + \sqrt{n_0}\right)^2 - g_{\text{IB}}\left(\chi_\beta^-\right)^2 \tag{2.58}$$

$$Z = |\langle 0|\Psi_{\text{coh}}^{\text{gs}}\rangle|^2 = e^{-N_{\text{ph}}}. \tag{2.59}$$

where the average is taken over the FMGS trial wavefunction $|\Psi_{\text{coh}}^{\text{gs}}\rangle$ and $|0\rangle$ is the state corresponding to a non-interacting impurity immersed in a BEC. The quasiparticle residue characterizes how much bare impurity character is leftover in the interacting FMGS; it can therefore be used to probe the breakdown of the quasiparticle picture.

A natural generalization of the FMGS quasiparticle residue to the case of quench dynamics is the Loschmidt echo

$$S(t) = \langle 0|e^{i\hat{H}_{\rm free}t}e^{-i\hat{H}_{\rm LLP}t}|0\rangle \tag{2.60}$$

where

$$\hat{H}_{\rm free} = \sum_{\mathbf{k}} \omega_{\mathbf{k}} \hat{b}^{\dagger}_{\mathbf{k}} \hat{b}_{\mathbf{k}} + \frac{\hat{\mathbf{P}}^2}{2m_I} \tag{2.61}$$

is the Hamiltonian for the free impurity immersed in a BEC. Utilizing Eq. (2.25), we have

$$S(t) = e^{i\left[\frac{\mathbf{P}^2}{2m_I}t\right]}e^{-\frac{1}{2}N_{\rm ph}(t)}. \tag{2.62}$$

The Loschmidt echo therefore represents the overlap between the state during time evolution and the original bare impurity. The Fourier transform of the echo can also be used to compute the RF absorption spectrum [332].

The FMGS quasiparticle residue Z is connected to the Loschmidt echo at infinite time

$$|S\left(t_{\infty}\right)| \equiv \lim_{t\to\infty} |S(t)| = Z. \tag{2.63}$$

after an initial quench from a noninteracting state $|0\rangle$. We can derive this result as follows. Consider a quench from the FMGS $|0\rangle$ of the non-interacting state (associated with energy $E_{\downarrow}$) to an interacting state with dynamics determined by Hamiltonian $\hat{H}_{\uparrow}$. Let $\left\{|n_{\uparrow}\rangle\,; E^n_{\uparrow}\right\}$ be the eigenstates and energies of $\hat{H}_{\uparrow}$. The quasiparticle residue is defined as $Z \equiv |\langle 0|0_{\uparrow}\rangle|^2$ and the Loschmidt echo of a state $|\psi\left(t\right)\rangle$ after the quench

is defined as $S(t) \equiv e^{iE_\downarrow t} \langle 0|\psi(t)\rangle$. Inserting the identity $\hat{I} = \sum_n |n\rangle \langle n|$, we have

$$
\begin{aligned}
S(t) &= e^{iE_\downarrow t} \langle 0|\psi(t)\rangle && (2.64)\\
&= e^{iE_\downarrow t} \langle 0|e^{-i\hat{H}_\uparrow t}|0\rangle && (2.65)\\
&= e^{iE_\downarrow t} \sum_n e^{-iE_\uparrow^n t} |\langle 0|n_\uparrow\rangle|^2 && (2.66)\\
&= e^{-i\left(E_\uparrow^0 - E_\downarrow\right)t} Z \left(1 + \frac{1}{Z}\sum_{n>0} e^{i\left(E_\uparrow^0 - E_\uparrow^n\right)t} |\langle 0|n_\uparrow\rangle|^2\right) && (2.67)\\
&= e^{-i\omega_{\uparrow\downarrow}^0 t} Z \left(1 + \frac{1}{Z}\sum_{n>0} e^{i\omega_n t} |\langle 0|n_\uparrow\rangle|^2\right) && (2.68)
\end{aligned}
$$

where we have defined $\omega_{\uparrow\downarrow}^0 \equiv E_\uparrow^0 - E_\downarrow$ and $\omega_n \equiv E_\uparrow^0 - E_\uparrow^n$. We then have

$$
\begin{aligned}
|S(t)| = Z &\left(1 + \frac{1}{Z}\sum_{n>0} e^{i\omega_n t} |\langle 0|n_\uparrow\rangle|^2\right) && (2.69)\\
&\times \left(1 + \frac{1}{Z}\sum_{n>0} e^{-i\omega_n t} |\langle 0|n_\uparrow\rangle|^2\right)
\end{aligned}
$$

We know that $\omega_n < 0$ is a monotonic function of n and we can index the summation and eigenstates $|n_\uparrow\rangle$ with it.

$$
\begin{aligned}
|S(t)| = Z &\left(1 + \frac{1}{Z}\sum_{\omega_n<0} e^{i\omega_n t} f(\omega_n)\right) && (2.70)\\
&\times \left(1 + \frac{1}{Z}\sum_{\omega_n<0} e^{-i\omega_n t} f(\omega_n)\right)
\end{aligned}
$$

where $f(\omega_n) \equiv |\langle 0|\omega_n\rangle|^2$. By the Riemann-Lebesgue lemma, we have

$$
\lim_{t\to\infty} \left|\sum_{\omega_n<0} e^{i\omega_n t} f(\omega_n)\right| \to 0 \qquad (2.71)
$$

which immediately yields

$$
\lim_{t\to\infty} |S(t)| = Z \qquad (2.72)
$$

and we see that the Loschmidt echo must asymptote to the quasiparticle residue at

infinite time for all system conditions (initial momentum and interaction strengths).

2.2 Local Density Approximation

In Sec. 2.1, we described the Hamiltonian used to model a single finite-momentum impurity immersed in a BEC, the variational method and choice of coherent state ansatz used to derive dynamical equations, as well as observables and distribution functions that we use to characterize the system. Here, we extend the treatment to external potentials (such as harmonic traps) and forces via the local density approximation (LDA). Such potentials are relevant to many experimental set-ups as well as the protocols proposed in Ch. 4 to probe basic polaronic properties such as effective mass.

2.2.1 External Potentials and Forces

Consider applying an external potential $V_I(\mathbf{r})$ (with associated force $\mathbf{F}_I(\mathbf{r}) \equiv -\nabla V_I(\mathbf{r})$) on the impurity. This potential is represented by adding the term $\hat{V}_I = \sum_{\mathbf{r}} V_I(\mathbf{r})\,\hat{\psi}^\dagger(\mathbf{r})\,\hat{\psi}(\mathbf{r})$ to the initial microscopic Hamiltonian Eq. (2.1). The LDA assumes that the length scale the force $\mathbf{F}_I(\mathbf{r})$ varies over is large compared to the length scale of the polaron wavepacket and so we can consider $\mathbf{F}_I(\mathbf{r})$ as spatially homogeneous ($\mathbf{F}_I(\mathbf{r}) \to \mathbf{F}_I$). In this case, it can be shown that the effect of the external potential is to send $\mathbf{P} \to \mathbf{P}(t) = \mathbf{P} + t\mathbf{F}_I \equiv \mathbf{P}_0 + t\mathbf{F}_I$ in the Hamiltonian Eq. (2.18). The total system momentum now changes with time as $\mathbf{P}(t) = \mathbf{P}_0 + \int_0^t d\tau \mathbf{F}_I(\tau)$, but the initial momentum $\mathbf{P}_0$ is conserved in the sense that states with different initial momentum $\mathbf{P}_0$ do not mix during time-evolution.

Relying on the LDA assumption that the length scale the force $\mathbf{F}_I(\mathbf{r})$ varies over is large compared to the length scale of the polaron wavepacket, we can reintroduce the position dependance of the force through the expected value of the impurity's position $\mathbf{R}_I \equiv \langle \mathbf{R}_I \rangle$. This means we can substitute $\mathbf{F}_I \to \mathbf{F}_I(\langle \mathbf{R}_I \rangle) \equiv -\nabla V_I(\mathbf{r})|_{\mathbf{r}=\mathbf{R}_I}$ and now include position-dependent potentials that result in position-dependent forces. The expected value of the impurity's position itself depends on time as $\frac{d}{dt}\mathbf{R}_I(t) =$

$\frac{1}{m_I}\left\langle \hat{\mathbf{P}}_I \right\rangle = \frac{1}{m_I}\left(\mathbf{P}(t) - \left\langle \hat{\mathbf{P}}_{\text{ph}} \right\rangle\right) = \frac{1}{m_I}\left(\mathbf{P}(t) - \mathbf{P}_{\text{ph}}(t)\right)$.

Finally, recognizing that multiple external potentials/forces acting on the impurity can be taken into account by letting $\mathbf{F}_I \to \sum_\alpha \mathbf{F}_{I,\alpha}$ where α labels the force, our equations of motion are:

$$i\dot{\beta}_{\mathbf{k}} = \left(\omega_{\mathbf{k}} + \frac{|\mathbf{k}|^2}{2m_I} - \frac{1}{m_I}\mathbf{k}\cdot\left(\mathbf{P} - \mathbf{P}_{\text{ph}}[\beta]\right)\right)\beta_{\mathbf{k}} \tag{2.73}$$
$$+ g_{\text{IB}}\sqrt{n_0}W_{\mathbf{k}} + g_{\text{IB}}\left(W_{\mathbf{k}}\chi_\beta^+ + W_{\mathbf{k}}^{-1}\chi_\beta^-\right)$$
$$\dot{\phi} = g_{\text{IB}}n_0 + g_{\text{IB}}\sqrt{n_0}\chi_\beta^+ + \frac{1}{2m_I}\left(\mathbf{P}^2 - \mathbf{P}_{\text{ph}}^2[\beta]\right) \tag{2.74}$$
$$\dot{\mathbf{P}} = \sum_\alpha \mathbf{F}_{I,\alpha} \tag{2.75}$$
$$\dot{\mathbf{R}}_I = \frac{1}{m_I}\left(\mathbf{P} - \mathbf{P}_{\text{ph}}[\beta]\right) \tag{2.76}$$

It is important to note that the LDA assumption about length scales of the external potential versus the polaron wavepacket breaks down when the external potential changes sharply in space; this usually happens at the edges of the potential (e.g. edges of a harmonic potenital or potential imposed by an inhomogeneous BEC). We assume that the validity of the LDA in the middle of most relevant potentials ('volume' effect) dominates regions of invalidity at the edges of these potentials ('surface' effect). Additionally, other parts of the derivation (Bogoliubov approximation, etc.) start breaking down at the edges as well so there are multiple problems if surface effects become relevant.

2.2.2 Inhomogeneous BEC

While making the Bogoliubov approximation in the derivation of the Hamiltonian, we assumed that the condensate density $n_0 = \frac{1}{L^d}\left\langle \hat{a}_0^\dagger \hat{a}_0 \right\rangle$ was independent of position and time meaning that the BEC is homogeneous. If we want to consider experimentally realistic situations in which the BEC is confined by a trap, we need to take into account a spatially inhomogeneous BEC density. We again invoke the LDA assumption that the BEC density varies on a length scale that is large compared to

the polaron wavepacket; we can then take it as constant throughout the derivation of the Hamiltonian and equations of motion while reintroducing dependence on the average impurity position at the end. Consider the position-dependent density to be represented by $n_0(\mathbf{R})$. We reintroduce this position-dependence in the equations of motion to finally get:

$$\begin{aligned} i\dot{\beta}_{\mathbf{k}} &= g_{\mathrm{IB}}\sqrt{n_0(\mathbf{R}_I)}W_{\mathbf{k}} \\ &+ \left(\omega_{\mathbf{k}}\left[n_0(\mathbf{R}_I)\right] + \frac{|\mathbf{k}|^2}{2m_I} - \frac{1}{m_I}\mathbf{k}\cdot\left(\mathbf{P} - \mathbf{P}_{\mathrm{ph}}\left[\beta\right]\right)\right)\beta_{\mathbf{k}} \\ &+ g_{\mathrm{IB}}\left(W_{\mathbf{k}}\left[n_0(\mathbf{R}_I)\right]\chi_\beta^+ + W_{\mathbf{k}}^{-1}\left[n_0(\mathbf{R}_I)\right]\chi_\beta^-\right) \end{aligned} \tag{2.77}$$

$$\dot{\phi} = g_{\mathrm{IB}}n_0(\mathbf{R}_I) + g_\Lambda\sqrt{n_0(\mathbf{R}_I)}\chi_\beta^+ + \frac{1}{2m_I}\left(\mathbf{P}^2 - \mathbf{P}_{\mathrm{ph}}^2\left[\beta\right]\right) \tag{2.78}$$

$$\dot{\mathbf{P}} = \sum_\alpha \mathbf{F}_{I,\alpha} \tag{2.79}$$

$$\dot{\mathbf{R}}_I = \frac{1}{m_I}\left(\mathbf{P} - \mathbf{P}_{\mathrm{ph}}\left[\beta\right]\right) \tag{2.80}$$

where $W_{\mathbf{k}}\left[n_0(\mathbf{R})\right] = \left(\frac{\varepsilon_{\mathbf{k}}^B}{\omega_{\mathbf{k}}[n_0(\mathbf{R})]}\right)^{\frac{1}{2}}$, $\omega_{\mathbf{k}}\left[n_0(\mathbf{R})\right] = \sqrt{\varepsilon_{\mathbf{k}}^B\left(\varepsilon_{\mathbf{k}}^B + 2g_{\mathrm{BB}}n_0(\mathbf{R})\right)}$, and $\varepsilon_{\mathbf{k}}^B = \frac{|\mathbf{k}|^2}{2m_B}$. When implementing an inhomogeneous BEC in our simulations, we use a Thomas-Fermi profile for $n_0(\mathbf{R})$ assuming a harmonic trap with parameters typical of experimental set-ups (see Appendix **??**).

2.2.3 Impurity Potentials and Forces Included in Simulation

Impurity's trapping potential

Let us fix the direction of the external force ($\mathbf{F} = F\mathbf{e}_x$) and assume the impurity/polaron is initially at rest ($\mathbf{P} = 0$). For a harmonic confining potential with frequency ω in the direction of motion (direction of the applied force), we have a potential $V_I(x_I) = \frac{1}{2}m_I\omega_I^2x_I^2$. This gives a force $F_I(x_I) = -m_I\omega_I^2x_I$ where x_I is the average position of the impurity in the direction of the confining potential.

Polaron energy potential

Consider an impurity (not subject to any additional potentials or forces) in a spatially homogeneous BEC that happens to be in the polaron ground state $|\psi_{pol}[\mathbf{P}]\rangle$ with associated energy $E_{pol}[\mathbf{P}]$. Here $\mathbf{P}$ is the total system momentum which is a conserved quantity. Using our treatment of the system, we can give an expression for the polaron ground state energy (see Eq. (2.35)):

$$E_{pol}(\mathbf{P}) = \frac{1}{2m_I}\left(\mathbf{P}^2 - \mathbf{P}_{\text{ph}}^2[\beta]\right) + \frac{2\pi n_0}{\mu_{red}\left(a_{\text{IB}}^{-1} - a_*^{-1}(\mathbf{P})\right)} \tag{2.81}$$

where the resonance shift is given as:

$$a_*^{-1}(\mathbf{P}) = \frac{2\pi}{\mu_{red}}\sum_{\mathbf{k}}\left(\frac{2\mu_{red}}{|\mathbf{k}|^2} - \frac{W_{\mathbf{k}}^2}{\omega_{\mathbf{k}} + \frac{\mathbf{k}^2}{2m_I} - \frac{\mathbf{k}}{m_I}\cdot(\mathbf{P} - \mathbf{P}_{\text{ph}})}\right) \tag{2.82}$$

If we also include a spatially inhomogeneous BEC density $n_0(\mathbf{R})$, the ground state energy has position dependance both through the total momentum and the BEC density. In accordance to the LDA, we have:

$$E_{pol}[\mathbf{P}(t,\mathbf{R}(t)), n_0(\mathbf{R}(t))] = \frac{1}{2m_I}\left(\mathbf{P}^2 - \mathbf{P}_{\text{ph}}^2[\beta]\right) + \frac{2\pi n_0(\mathbf{R})}{\mu_{red}\left(a_{\text{IB}}^{-1} - a_*^{-1}[\mathbf{P}, n_0(\mathbf{R})]\right)} \tag{2.83}$$

$$a_*^{-1}[\mathbf{P}(t,\mathbf{R}(t)), n_0(\mathbf{R}(t))] = \frac{2\pi}{\mu_{red}}\sum_{\mathbf{k}}\left(\frac{2\mu_{red}}{|\mathbf{k}|^2} - \frac{W_{\mathbf{k}}^2[n_0(\mathbf{R})]}{\omega_{\mathbf{k}}[n_0(\mathbf{R})] + \frac{\mathbf{k}^2}{2m_I} - \frac{\mathbf{k}}{m_I}\cdot(\mathbf{P} - \mathbf{P}_{\text{ph}})}\right) \tag{2.84}$$

where we have made the position dependence explicit. We will assume that the polaron adiabatically follows its ground state. The phase $e^{-i\int_0^t E_{pol}[\mathbf{P}(\tau,\mathbf{R}_I(\tau)),n_0(\mathbf{R}_I(\tau))]d\tau}$ it picks up during time-evolutions looks like a time-dependent gauge transformation which can be equated to an additional external potential. In the context of the LDA, this amounts to including a force $\mathbf{F}_{pol} = -\bar{\nabla}E_{pol}$ as one of the $\mathbf{F}_\alpha$ in the equation of motion for the total momentum $\dot{\mathbf{P}} = \sum_\alpha \mathbf{F}_\alpha$. We read off the density-dependent

effective potential as

$$V_{pol}\left(\mathbf{R}\right) \equiv E_{pol}\left(\mathbf{R}\right) = \frac{2\pi n_0\left(\mathbf{R}\right)}{\mu_{red}\left(a_{\mathrm{IB}}^{-1} - a_*^{-1}\left[n_0\left(\mathbf{R}\right)\right]\right)} \tag{2.85}$$

$$a_*^{-1}\left[\mathbf{R}\right] = \frac{2\pi}{\mu_{red}} \sum_{\mathbf{k}} \left(\frac{2\mu_{red}}{\left|\mathbf{k}\right|^2} - \frac{W_{\mathbf{k}}^2\left[n_0\left(\mathbf{R}\right)\right]}{\omega_{\mathbf{k}}\left[n_0\left(\mathbf{R}\right)\right] + \frac{\mathbf{k}^2}{2m_I}} \right). \tag{2.86}$$

This potential results in the force $\mathbf{F}_{pol}\left(\mathbf{R}_I\right) = -\bar{\nabla} V_{pol}\left(\mathbf{R}\right)|_{\mathbf{R}=\mathbf{R}_I(t)}$ acting on the polaron (which we can take as being centered around the position of the impurity). In the BEC frame, this force changes the total system momentum $\mathbf{P} \to \mathbf{P} + \int_0^t d\tau \mathbf{F}_{pol}\left(\mathbf{R}_I(\tau)\right)$ (which is the polaron momentum) rather than directly affecting the impurity momentum $\mathbf{P}_I$ as the impurity trapping potential does. We can include both types of forces in the same expression for $\dot{\mathbf{P}}$ in the equations of motion, however; after the Lee-Low-Pines transformation, potentials that affect the total system momentum and those affecting the impurity momentum both appear in the Hamiltonian in the same way.

2.2.4 Oscillating BEC

In some cases of interest, the BEC may itself be undergoing dynamics such as oscillations. When deriving the Hamiltonian and equations of motion, we implicitly made the assumption that we were in the co-moving frame of the BEC. One can see this as we chose the $\mathbf{k} = 0$ mode of Bose atoms to form the condensate ($\hat{a}_{\mathbf{k}=0}^\dagger \propto \sqrt{n_0} \equiv \sqrt{n_{\mathbf{k}=0}}$). If the BEC was moving (e.g. with momentum $\mathbf{q}$) and we were working in the lab frame, then the $\mathbf{k} = \mathbf{q}$ modes would form the condensate (as it is the zero momentum modes in the Bose gas's frame of reference that forms the BEC). If we want to consider a BEC that is accelerating with respect to the lab frame, we still work in the co-moving frame of the BEC to keep our derivation intact; the cost, however, is to include ficticious forces on the impurity arising from this non-inertial frame.

Let the (inertial) lab frame be labeled by L and the (non-inertial) comoving frame of the BEC be labeled by B which has an origin $\mathbf{r}_{\mathrm{L,B}}\left(t\right)$ relative to L . If the BEC is oscillating in one direction with its position given by $\mathbf{r}_{BEC}\left(t\right) = \left(x_{BEC}\left(t\right) =\right.$

$aR_{TF,x}\cos(\omega_B t), 0, 0)$, then we only get the ficticious force associated with linear motion and the impurity in the comoving BEC frame feels a force

$$\begin{aligned}\mathbf{F}_{\mathrm{B}} &= \mathbf{F}_{\mathrm{L}} - m_I \frac{d^2\mathbf{r}_{BEC}}{dt^2} \\ &= \mathbf{F}_{\mathrm{L}} + m_I a R_{TF,x}\omega_B^2 \cos(\omega_B t)\,\mathbf{e}_x\end{aligned} \tag{2.87}$$

where $\mathbf{F}_L$ correspond to other forces it would feel if the BEC was stationary and $\mathbf{e}_x$ is the basis vector in the x-direction. The equations of motion calculated previously stay the same, but we must now include the ficticious force $\mathbf{F}_f = m_I a R_{TF}\omega^2 \cos(\omega t)\,\mathbf{e}_x$ as one of the forces $\mathbf{F}_{I,\alpha}$ in the equation for $\dot{\mathbf{P}}$. The quantities $\mathbf{R}_I$, $\mathbf{P}$, $\mathbf{P}_{ph}[\beta] = \sum_{\mathbf{k}} \mathbf{k}\,|\beta_{\mathbf{k}}|^2$, and $\mathbf{P}_I = \mathbf{P} - \mathbf{P}_{ph}[\beta]$ are all calculated in the non-inertial comoving frame of the BEC. The BEC density $n_0(\mathbf{R}_I)$ and forces that depend on it are also calculated as usual using $n_0(\mathbf{R})|_{\mathbf{R}=\mathbf{R}_I(t)}$ where $\mathbf{R}_I(t)$ is the position of the impurity in the comoving BEC frame as just mentioned. After making these calculations in the BEC frame, we can examine the position of the impurity in the lab frame $\tilde{\mathbf{R}}_I$ through the transformation $\tilde{\mathbf{R}}_I(t) = \mathbf{R}_I(t) + \mathbf{r}_{BEC}(t) = \mathbf{R}_I(t) + (aR_{TF,x}\cos(\omega_B t), 0, 0)$.

Chapter 3

Quantum Cherenkov transition of finite momentum Bose polarons

Armed with the formalism in Sec. 2.1, we investigate the motion of a finite mass impurity injected into a three-dimensional quantum Bose fluid as it starts shedding Bogoliubov excitations. Theoretical work has previously been done on fast impurities immersed in a BEC, including BECs flowing supersonically across an infinite-mass defect [59], supersonic impurities in a 1D quantum liquid [248], and a semiclassical treatment of weakly-interacting supersonic impurities in a 3D BEC [83]. The variational approach in Sec. 2.1 allows us to go beyond the semiclassical treatment and allow study of a finite mass impurity across a wide range of interaction strengths. Previous works using variational states primarily studied the system at zero momentum or finite momentum with an effective repulsive interaction between the impurity and the BEC [334, 97, 360]. Here, we focus on the case of an effective attractive interaction between the impurity and the BEC.

We uncover a transition in the dynamics as the impurity's velocity crosses a critical value which depends on the strength of the interaction between the impurity and bosons as well as the impurity's recoil energy. We find that in injection experiments, the two regimes differ not only in the character of the impurity velocity abatement, but also exhibit qualitative differences in the Loschmidt echo, density ripples excited in the BEC, and momentum distribution of scattered bosonic particles. The transition is

a manifestation of a dynamical quantum Cherenkov effect, and should be experimentally observable with ultracold atoms using Ramsey interferometry, RF spectroscopy, absorption imaging, and time-of-flight imaging. This quantum Cherenkov effect can be thought of as a velocity-dependent frictional force on the impurity that is modified by entanglement between the impurity and host atoms.

The nontrivial dependence of frictional forces on the velocity of moving objects is common to many classical systems, from sliding friction between solid bodies to drag forces in hydrodynamics. Electrodynamics provides an even more striking example, where a charged particle moving through a medium dissipates energy through light emission only if its velocity is above the speed of light in the medium, a phenomenon known as Cherenkov effect [40]. A similar effect in quantum mechanical systems can be found when a particle travels through a superfluid. When the impurity particle is moving at a constant velocity, as is the case when it is so heavy that its recoil can be neglected, the Landau criterion states that the particle will only dissipate energy by generating excitations in the medium if it is traveling above the speed of sound of the superfluid. Therefore, for an infinite mass object, the speed of sound of the superfluid BEC sets a kinematic scale according to the Landau criterion, with a conical wavefront of Bogoliubov excitations emitted as the relative motion of the system exceeds this velocity [17, 59, 109, 126, 127]. An impurity with finite mass, however, should exhibit dynamics that is far more complex. Specifically, it would recoil due to interactions with the surrounding quantum gas, yielding novel physics beyond the kinematic picture. Quantum fluctuations become highly relevant to the dynamics of even slowly moving impurities with finite mass [142].

In this chapter, we examine (i) the lowest energy state of the system at finite momentum, which we refer to as the finite momentum ground state (FMGS), and (ii) the stationary state following temporal evolution of the impurity in an initial plane-wave state after interactions with the gas are quenched on. In both scenarios, we find that the impurity-gas interaction determines a critical system momentum, $\mathbf{P}_{\text{crit}}$, upon which the system exhibits a transition between two qualitatively different regimes. We observe that $\mathbf{P}_{\text{crit}}$ coincides for the FMGS and dynamical quench transitions. At

small and intermediate interaction strengths, $\mathbf{P}_{\text{crit}}$ is set by the effective mass of the polaron. The recoil energy scale vanishes in the infinite impurity mass limit, where we recover the Landau criterion with $P_{\text{crit}} = |\mathbf{P}_{\text{crit}}|$ equivalent to the impurity mass times the BEC's speed of sound.

Below $\mathbf{P}_{\text{crit}}$, the polaron state overlaps with the free impurity and the impurity travels at an average velocity slower than the BEC's speed of sound, with this velocity depending on the momentum of the system. Above $\mathbf{P}_{\text{crit}}$, the polaron state is orthogonal to the free impurity and the impurity travels at the speed of sound with the rest of the system's momentum carried by long wavelength Bogoliubov excitations. The finite momentum quantum transition we observe draws parallels to the classical Cherenkov effect, in that the impurity injected into a medium above a medium-dependent critical velocity saturates to a finite universal speed at late times while generating a cone of excitations in the medium.

This chapter is organized as follows. We start by giving a summary of results in Sec. 3.1. In Sec. 3.2, we study the Cherenkov transition in the FMGS using imaginary time dynamics of the equations of motion. In Sec. 3.3, we examine manifestations of the transition in real-time dynamics. We close with a discussion in Sec. 3.4. The material in this chapter corresponds to the work in Refs. [326] and [325].

3.1 Summary of Results

While we primarily show results for the case case of impurities and bosons having equal mass, the transition we uncover and corresponding phenomenology holds for a wide range of mass ratios (see Sec. 3.3.5).

(I) *FMGS Transition.* If we pick an interaction strength and calculate the FMGS energy as a function of total momentum $\mathbf{P}$, we find that this relation is initially quadratic and then discontinuously becomes linear. We posit that the energy-momentum relation of a finite momentum impurity immersed in a weakly interacting BEC has

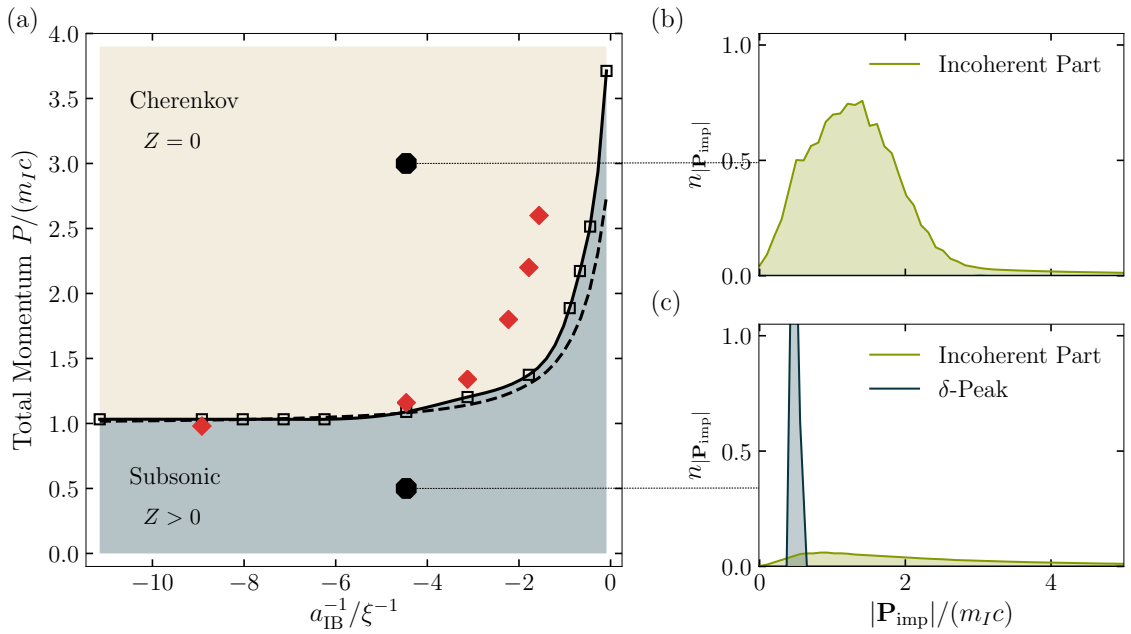

Figure 3: Quantum Cherenkov transition of a finite momentum impurity interacting with a weakly-interacting 3D BEC. (a) Phase diagram. The black solid line marks the numerically extracted critical momentum from the discontinuity in the second derivative of the FMGS energy. The black dashed line marks the predicted transition value m^*c. The critical momentum describing the transition between subsonic and Cherenkov regimes increases with interaction strength and is related to polaronic mass enhancement. The red diamonds represent the numerically extracted transition points in the long time limit of the quench dynamics. Panels (b) and (c) illustrate the impurity's momentum magnitude distribution in each regime. Note that we have introduced Gaussian broadening of the δ-peak in the distributions by hand; in reality we get a δ-peak at $|\mathbf{P}_{\mathrm{imp}}| = P$ with a weight Z. The mass ratio is $m_I/m_B = 1$ and we use a momentum space UV cutoff $\Lambda = 9.27[\xi^{-1}]$ where ξ is the healing length of the BEC.

the form

$$E(\mathbf{P}) = \begin{cases} \frac{\mathbf{P}^2}{2m^*}, & \text{if } |\mathbf{P}| \leq |\mathbf{P}_{\mathrm{crit}}| \\ c\mathbf{P}, & \text{if } |\mathbf{P}| > |\mathbf{P}_{\mathrm{crit}}| \end{cases} \tag{3.1}$$

where

$$|\mathbf{P}_{\mathrm{crit}}| = m^* c. \tag{3.2}$$

Note that m^* is the effective mass of the polaron which depends on the strength of

the interaction between impurity and Bose atoms while c is the speed of sound in the BEC which depends on the strength of the interaction between Bose atoms. We see that on the polaron side of this transition ($|\mathbf{P}| < |\mathbf{P}_{\text{crit}}|$), the FMGS energy is quadratic with total momentum, with the polaron's effective mass m^* being defined as the curvature of the energy around $|\mathbf{P}| = 0$. On the Cherenkov side of this transition ($|\mathbf{P}| > |\mathbf{P}_{\text{crit}}|$), the energy depends linearly on total momentum. The slope of the linear spectrum gives us the 'polaron velocity', which is the semiclassical velocity that a polaron FMGS needs to reach in order to enter the Cherenkov regime. We find this velocity equals the average velocity of the impurity as it must, and both are equal to the speed of sound c regardless of interaction strength. Momentum in this regime is shed into Bogoliubov excitations of the BEC.

By examining the full distribution function for individual phonons and the impurity's momentum (describing quantum fluctuations around the mean), we see evidence of quasiparticle breakdown at the transition, indicated by a vanishing quasiparticle residue. The phonons present in this regime have very low momentum and there is a dramatic increase in the number of phonons at the transition; the system redistributes momentum into these phonons in order to fix the impurity's average velocity to the BEC speed of sound. It is the large number of phonons in the Cherenkov regime that makes the quasiparticle residue vanish.

We identify the coherent part of the impurity's momentum distribution, represented by a delta function peak at the value of the total system momentum. The weight contained in this part corresponds to the quasiparticle residue in Eq. (2.59). The shape of the remaining incoherent part of the distribution is illustrated in Fig. 3. These features of the impurity's momentum distribution can be directly probed in time-of-flight measurements.

We find that the quasiparticle residue sharply drops to zero at the critical momentum, which we take as a signature of quasiparticle breakdown in the supersonic regime. We also see the incoherent part of the distribution become sharply peaked at the critical momentum before broadening out again. This can be understood by the reasoning given in [267] that at the critical momentum, the impurity travels at

the same speed as the phonon excitations and therefore the phonons cannot dissipate momentum away. Another way to think about this effect is that the available phase space to excite phonons vanishes as the impurity approaches the speed of sound [43].

We establish that the FMGS as a function of total momentum has a transition at a critical momentum set by the effective mass of the polaron in the subsonic regime (see Fig. 3). The transition occurs when the polaron velocity reaches the speed of sound.

(II) *Dynamical Transition.* We can also run the equations of motion in real time for various subsonic and supersonic momenta and examine the behavior of the system. The Cherenkov transition of the FMGS manifests in the dynamical behavior of various observables here. The Loschmidt Echo (dynamical equivalent of the quasiparticle residue) remains finite in the subsonic regime but has a power law decay to zero at long times in the Cherenkov regime for weak and intermediate interactions. This behavior is due to a logarithmic increase of total emitted phonon number at long times in the supersonic regime. Nielsen et al. and Boyanovsky et al. also predict this behavior in the Cherenkov regime [267, 43], but find an exponential decay instead of a power law; we attribute this difference to their use of the Markov approximation.

The dynamical transition is also evident in the behavior of the average impurity velocity. Initially supersonic impurities have an average impurity velocity which exhibit a power-law decay towards m^*c at long times, though convergence is slow; this is related to the divergence in the damping rate described in [267, 43] as the impurity approaches the critical momentum and cannot dissipate momentum through the phonon excitations. We therefore see that the Loschmidt echo and average impurity velocity both exhibit power-law decays in the supersonic regime with the onset of this behavior depending on interaction strength through a polaronic mass renormalization effect.

Similar to the classical Cherenkov effect, we also see the transition manifest in the density of the host liquid. For sufficiently fast impurities, we find a shock wave and wake in the density of the host liquid, with this modulation traveling along with the impurity. In comparison to previously studied shock waves in superfluids generated

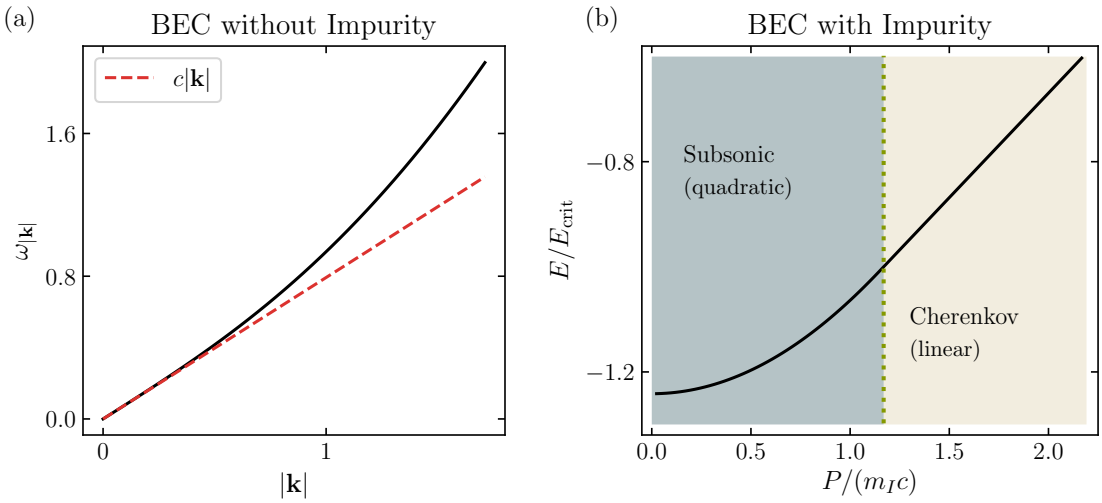

Figure 4: (a) The spectrum of Bogoliubov excitations ('phonons') in the BEC; the low energy spectrum is linear with such phonons traveling at the BEC speed of sound c. At larger momenta, the phonon dispersion becomes quadratic. (b) FMGS energy of the interacting impurity-BEC system. We find that the spectrum is initially quadratic (subsonic regime) and then discontinuously becomes linear (Cherenkov regime) at a criticial momentum (green dotted line), after which momentum is shed into Bogoliubov excitations. The FMGS energy-momentum relation therefore behaves in an opposite manner to the phonon dispersion which is first linear and then continuously becomes quadratic. For panel (b), the FMGS energy is computed for $a_{\rm IB}^{-1} = -4.46/\xi$ and a mass ratio of $m_I/m_B = 1$. We use a momentum space UV cutoff $\Lambda = 9.27/\xi$.

by constant velocity heavy obstacles [59] or density defects [101, 152, 368], the dynamics of the density cone we observe is modified by the entanglement between the impurity and host atoms; this entanglement is included in the theoretical treatment of the system via the Lee-Low-Pines transformation [207] and results in additional interaction between Bogoliubov excitations (see Chap. 2 for details). We therefore call this density modulation a polaron shock wave.

3.2 FMGS Transition

Here, we perform evolution of the system in imaginary time τ by running Eq. (2.28) with $t \to \tau = -it$ in order to numerically determine the FMGS. We examine characteristics of the FMGS of the system as we vary the total system momentum $\mathbf{P}$. We

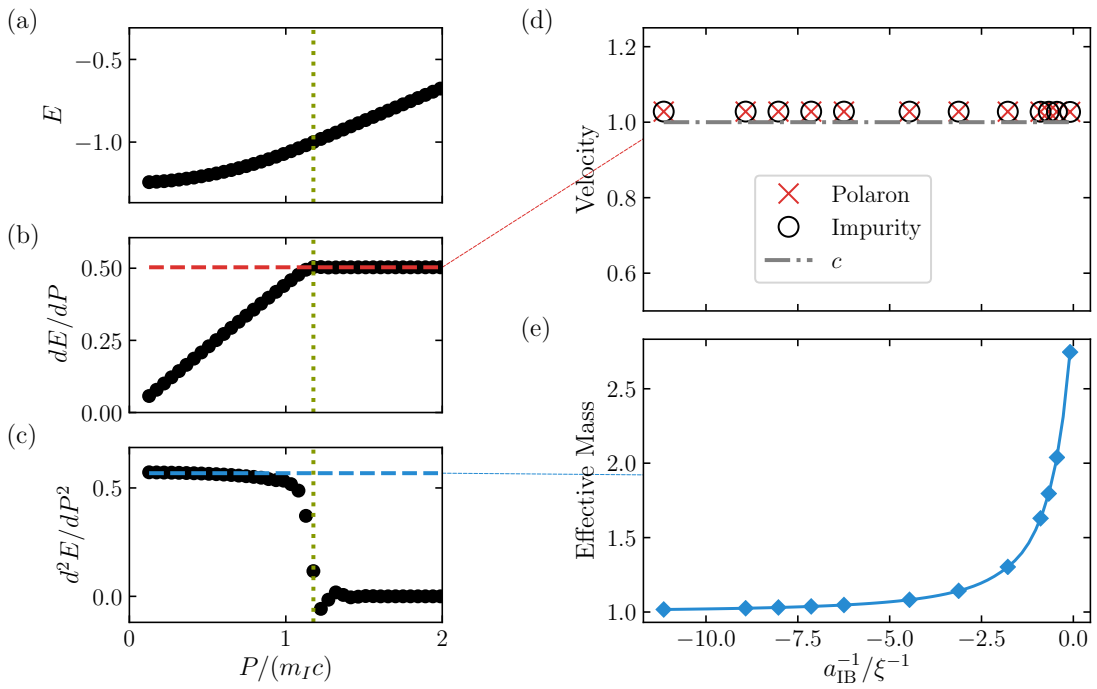

Figure 5: FMGS energy of an impurity immersed in a weakly interacting BEC. (a) The FMGS energy is initially quadratic (subsonic regime) and then becomes linear (Cherenkov regime) above a critical momentum where the critical momentum is indicated by the vertical green dotted line. The energy is plotted in units of $|E_{\mathrm{crit}}|$ which is the value of energy at critical momentum. Panels (b) and (c) show the first and second derivatives of the energy respectively; they confirm the functional form of the system's energy-momentum relation hypothesized in Eq. (3.1). These two curves are also normalized by $|E_{\mathrm{crit}}|$. Note that panels (a), (b), and (c) correspond to an interaction strength $a_{\mathrm{IB}}^{-1} = 4.46/\xi$. (d) Polaron group velocity and average velocity of the impurity in the Cherenkov regime (in units of c). The polaron velocity is given by the red 'x's; each 'x' corresponds to the constant plateu illustrated by the dashed red line in panel (b) which is computed for a specific interaction strength. The average impurity velocity is computed independently and confirmed to equal the polaron velocity as the Hellmann-Feyman theorem indicates. We see that the polaron velocity equals the BEC's speed of sound regardless of interaction strength, thus confirming half of the energy-momentum relation we hypothesis in Eq. (3.1). (e) Effective mass of polaron in units of m_I. Each point corresponds to the average value near P 0 illustrated by the dashed blue line in panel (c) which is computed for a specific interaction strength. The effective mass increases with interaction strength, but the group velocity does not. The mass ratio is $m_I/m_B = 1$ and we use a sharp UV cutoff $\Lambda = 9.27[\xi^{-1}]$.

find that the FMGS energy initially has a with quadratic dependence on $\mathbf{P}$ for small momenta and then undergoes a discontinuous transition to linear dependence on $\mathbf{P}$.

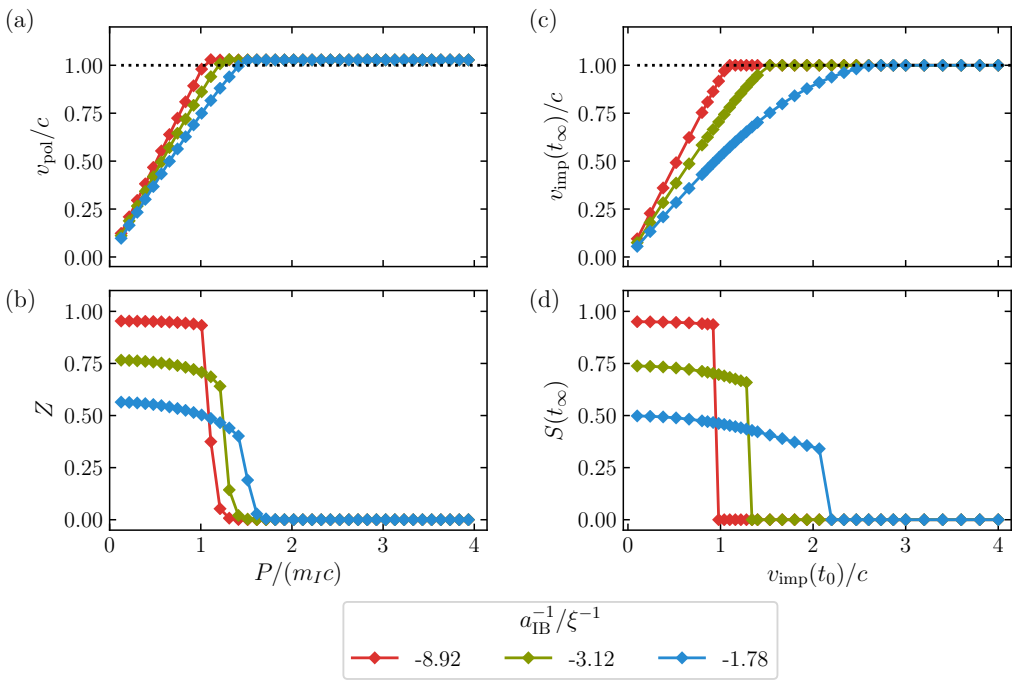

Figure 6: FMGS and dynamical observables that witness the quantum Cherenkov transition. The initial impurity velocity, $v_{\rm imp}(t_0)$, corresponds to the total momentum of the system, P, which is conserved. (a) FMGS polaron group velocity. (b) FMGS quasiparticle residue. (c) Long time limit of the average impurity velocity. (d) Long time limit of the Loschmidt echo. The impurity-boson mass ratio is $m_I/m_B = 1$.

The critical momentum increases for larger impurity-boson interaction strengths. In Fig. 3, we plot the phase diagram. Note that the system is spherically symmetric so physical quantities will only depend on the magnitude of the total momentum P, Eq. (2.23).

We posit that system's FMGS energy-momentum relation follows Eq. (3.1) with the critical momentum of the transition being given by Eq. (3.2). Examining the FMGS energy and its derivatives gives evidence for this hypothesis. In Fig. 5 (a)-(c), we confirm that for a fixed interaction strength, the energy is clearly quadratic at low momenta and then becomes linear. The system therefore behaves as a massive quasiparticle with effective mass $m^* = \nabla^2_{\mathbf{P}} E$ before the critical momentum $\mathbf{P}_{\rm crit}$. We call this regime the subsonic regime. Fig 5 (e) shows the effective mass for different interaction strengths; we see that it increases for stronger interactions which is the

expected mass-renormalized effect.

We call the linear energy-momentum regime the Cherenkov regime. In Fig. 5 (d), we plot the polaron's group velocity, defined as

$$\mathbf{v}_{\mathrm{pol}}\left(\mathbf{P}\right) = \nabla_{\tilde{\mathbf{P}}} E\Big|_{\tilde{\mathbf{P}}=\mathbf{P}} \tag{3.3}$$

and find that it is equal to the BEC's sound speed (2.8) regardless of interaction strength. The Hellmann-Feynman theorem tells us that the average impurity velocity defined as

$$\mathbf{v}_{\mathrm{imp}}\left(\mathbf{P}\right) = \frac{\langle \hat{\mathbf{P}}_{\mathrm{imp}} \rangle}{m_I} \tag{3.4}$$

must be equal to the polaron's group velocity $\mathbf{v}_{\mathrm{pol}}$ which we also confirm in the figure. The simulation-derived polaron velocity and average impurity velocity are within 2% of the BEC's sound speed. These velocities transition from an interaction-dependent subsonic value to the speed of sound when P_{crit} is crossed, as illustrated in Fig. 6(a). The low energy phonons that dress the impurity in the Cherenkov regime by definition have a group velocity c. We therefore have a physical picture in this regime of the impurity moving on average at the speed of sound along with low-energy phonons traveling at the same speed. The fact that the group velocity of the low-energy part of the phonon dispersion equals the group velocity of the high-energy part of the total system is not obvious a priori.

Next, we examine the critical momentum at which the transition occurs. In Fig. 3(a), we see that the transition happens at larger momentum for stronger interaction strengths. Note that the transition line in the figure is computed from the discontinuity in the second derivative of the energy. We also plot the predicted transition line given by Eq. (3.2) and see that it reasonably matches the true transition. Thus, we conclude that the transition occurs when the polaron's group velocity reaches the BEC's sound speed; the amount of momentum needed for this to occur increases for stronger interactions due to the polaronic mass-renormalization of the impurity.

We gain further insight into the transition by examining the impurity's momentum magnitude distribution, Eq. 2.57. The three-dimensional momentum distribu-

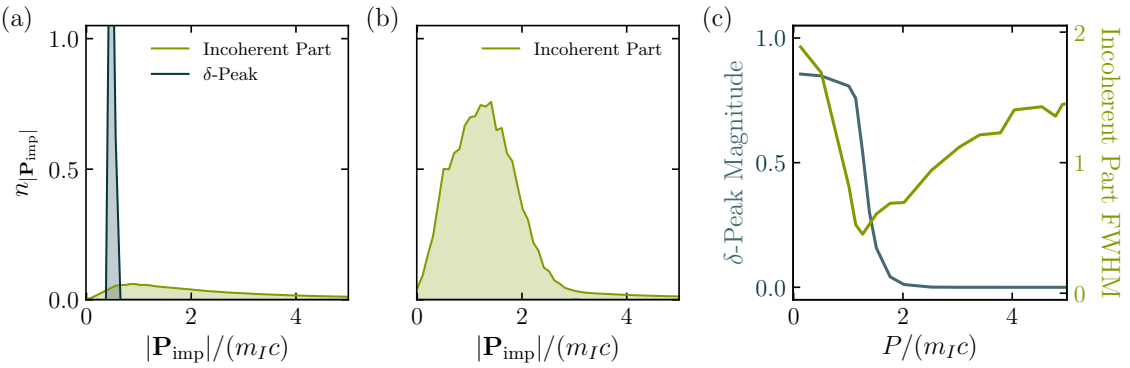

Figure 7: Distribution of impurity's momentum magnitude in FMGS. (a) Subsonic regime ($P = 0.5 m_I c$). (b) Cherenkov regime ($P = 3.0 m_I c$). Note that we have introduced Gaussian broadening of the δ-peak in the distributions by hand; in reality we get a δ-peak at $|\mathbf{P}_{\rm imp}| = P$ with a magnitude corresponding to the quasiparticle residue Z. (c) Magnitude of δ-peak, Z, and full width at half maximum (FWHM) of incoherent part of the distribution for different values of total system momentum P. The impurity-boson scattering length is $a_{\rm IB}^{-1} = -4.46/\xi^{-1}$ and the impurity-boson mass ratio is $m_I/m_B = 1$.

tion, Eq. (2.40), is comprised of a δ-peak with magnitude given by the quasiparticle residue, Z, and an incoherent part, $\tilde{n}_{\rm imp}(\mathbf{p})$. The momentum magnitude distribution, Eq. (2.57), is therefore also comprised of a δ-peak with magnitude Z and an incoherent part. In Fig. 7(a) and (b), we illustrate examples of $n_{\rm imp}(p)$ in the subsonic and Cherenkov regimes respectively. In Fig. 7(c), we plot the magnitude of the δ-peak and full width at half maximum of the incoherent part of the distribution as a function of total system momentum. We see that the magnitude of the δ-peak, given by the quasiparticle residue, is finite at low momenta corresponding to the subsonic regime, and then sharply decays to zero upon crossing the Cherenkov transition. We can understand the behavior of the quasiparticle residue as the system producing an 'infinite' number of low energy phonons in the Cherenkov regime and therefore having a vanishing overlap with the bare non-interacting impurity. At the transition point, the width of the incoherent part of the distribution becomes much narrower. As stated in [267], the system almost acts like a momentum eigenstate of a non-interacting impurity at the transition as phonons cannot dissipate momentum away from the impurity; the available phase space of excitations vanishes as the impurity approaches the speed of sound [43]. This feature of the momentum magnitude distribution can

be used to diagnose the FMGS transition in experiments via time of flight imaging.

In summary, the FMGS of the system exists either in a subsonic regime where the system truly behaves as a dressed quasiparticle with an effective mass, a quadratic energy-momentum relation, and non-zero quasiparticle residue or in a Cherenkov regime characterized by the impurity traveling at the speed of sound along with a large number of low energy phonons and a vanishing quasiparticle residue (quasiparticle breakdown). The critical momentum at which the transition occurs depends on the interaction strength and corresponds to the polaronic mass renormalization of how much momentum needs to be input into the system to get the impurity to travel at the speed of sound.

It is important to note that while the quasiparticle residue goes strictly to zero in the Cherenkov regime regardless of interaction strength, this effect becomes difficult to detect in practice at strong interactions where sufficiently large numbers of phonons are excited. Even in the subsonic regime where the residue is always finite, the large number of phonons makes this finite residue increasingly small. Therefore, at sufficiently strong interactions, the quasiparticle residue by itself cannot be used to distinguish between the subsonic regime and the Cherenkov regime.

3.3 Dynamical Transition

We take a non-interacting impurity propagating through a BEC in its FMGS and instantly switch on (quench) the impurity-BEC interaction at time $t_0 = 0$. We then evolve the system by running Eq. (2.28) in real time. Recall that the total momentum $\mathbf{P}$ of the system is conserved and this momentum initially resides on the non-interacting impurity; the initial velocity of the impurity is

$$\mathbf{v}_{\text{imp}}(t_0) = \frac{\mathbf{P}}{m_I}. \tag{3.5}$$

Hereafter, the initial impurity velocity and the total system momentum are used interchangeably depending on the context of the discussion.

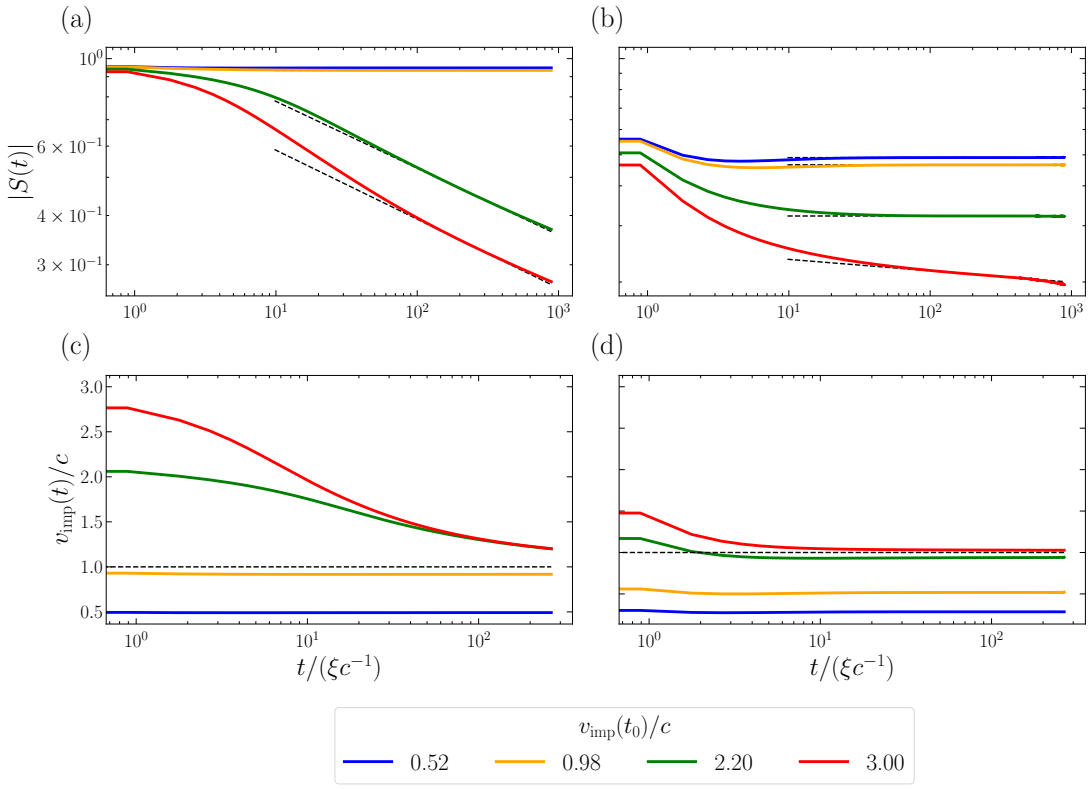

Figure 8: (a) Loschmidt echo at relatively weak interaction ($a_{\rm IB}^{-1} = -8.92/\xi$). Curves from the subsonic regime saturate to a finite value at long times. Curves in the Cherenkov regime decay to zero as a power-law at long times. (b) Loschmidt echo at strong interaction ($a_{\rm IB}^{-1} = -1.78/\xi$). Curves for sufficiently fast impurities also exhibit power-law decay. (c) Average speed of the impurity at relatively weak interaction ($a_{\rm IB}^{-1} = -8.92/\xi$). Curves from the subsonic regime saturate to different subsonic values at long times. Curves in the Cherenkov regime all approach the speed of sound at long times. (d) Average speed of the impurity at strong interaction ($a_{\rm IB}^{-1} = -1.78/\xi$). Curves approach the speed of sound for sufficiently fast impurities velocity. The mass ratio is $m_I/m_B = 1$ and we use a sharp UV cutoff $\Lambda = 13.91/\xi$.

The finite momentum transition of Sec. 3.2 also manifests in the dynamics of the system after the impurity is quenched from a non-interacting state to an interacting state. We find a qualitative change in the long-time value of the Loschmidt echo, Eq. (2.60), and of the average impurity velocity as $\mathbf{P}$ crosses a critical value $\mathbf{P}_{\rm crit}^{\rm dyn}$. We then discuss how $\mathbf{P}_{\rm crit}^{\rm dyn}$ is related to $\mathbf{P}_{\rm crit}$ for the FMGS transition studied in section 3.2.

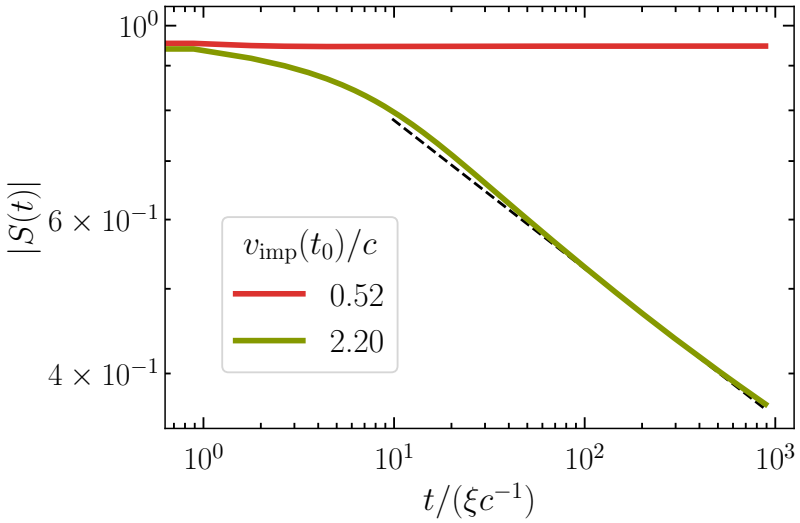

Figure 9: Loschmidt echo dynamics. The black dotted line is a visual guideline for the power-law decay of the Loschmidt echo in the Cherenkov regime. The impurity-boson scattering length is $a_{\mathrm{IB}}^{-1} = -8.92/\xi^{-1}$ and the impurity-boson mass ratio is $m_I/m_B = 1$.

3.3.1 Loschmidt Echo

The orthogonality catastrophe defined by the vanishing Z in Sec. 3.2 gives a natural motivation to examine the Loschmidt echo, Eq. (2.60), which characterizes the dynamical transition and can be experimentally measured using Ramsey interferometry on the impurity atom [183, 63]. We can express the Loschmidt echo as $S(t) = e^{i\frac{P^2}{2m_I}t}\langle 0|\Psi(t)\rangle$ where $|\Psi(t)\rangle$ is the wavefunction of the interacting system at time t.

Figures 8(a) and (b) illustrate its characteristic behavior for different initial impurity velocities, $\mathbf{v}_{\mathrm{imp}}(t_0)$, at weak and strong interactions, respectively. We see that $|S(t)|$ saturates to a non-zero value at long times for small momenta and undergoes a power-law decay to zero as we cross some critical momentum $\mathbf{P}_{\mathrm{crit}}^{\mathrm{dyn}}$. This power-law decay in the dynamical overlap corresponds to a logarithmic growth in the phonon number in the supersonic regime: per Eq. (2.62), we see that

$$N_{\mathrm{ph}}(t) \sim \begin{cases} \text{constant}, & \text{if } |\mathbf{P}| \leq \left|\mathbf{P}_{\mathrm{crit}}^{\mathrm{dyn}}\right| \\ \log t, & \text{if } |\mathbf{P}| > \left|\mathbf{P}_{\mathrm{crit}}^{\mathrm{dyn}}\right| \end{cases} \tag{3.6}$$

in the $t \to \infty$ limit. Physically, it is the divergence of $N_{\rm ph}$ which causes the decay of the Loschmidt echo. The increase in phonon number in the supersonic regime is the essence of the Cherenkov radiation phenomenon. Its divergence with time is, however, not obvious *a priori*. We expect that the coherent state variational ansatz employed in our work captures the leading terms in the behavior of $N_{\rm ph}$, as given by Eq. (3.6). Therefore, going beyond our ansatz, for example, by taking into account squeezing correlations between phonon modes [337], may only introduce subleading corrections to Eq. (3.6).

The power-law decay of the Loschmidt echo in the Cherenkov regime is illustrated clearly Fig. 9. The power-law behavior is reminiscent of the dynamical response in systems featuring orthogonality catastrophe, discussed for example in Ref. [183]. This form of the decay also confirms that the time evolution of the system is non-Markovian, as the use of the Markov approximation leads to an exponential decay of $S(t)$ and does not capture the dependence of $P_{\rm crit}$ on the impurity-gas coupling strength [204, 267, 43].

To find the value of the critical momentum $\left|\mathbf{P}_{\rm crit}^{\rm dyn}\right|$, we fit the long-time tail of $|S(t)|$ with a power-law,

$$|S(t)| = \text{const} \times t^{-\gamma}, \qquad t \to \infty. \tag{3.7}$$

We do the fit over the time range $80 \leq t/\xi c^{-1} \leq 90$ for all values of interactions available from our numerical simulation. Then, $\left|\mathbf{P}_{\rm crit}^{\rm dyn}\right|$ is identified as the momentum upon which the exponents become nonzero. We see that the critical momentum always corresponds to an initial velocity of the impurity, Eq. (3.5), that is above the speed of sound,

$$|\mathbf{v}_{\rm imp,crit}(t_0)| = \frac{\left|\mathbf{P}_{\rm crit}^{\rm dyn}\right|}{m_I} \geq c. \tag{3.8}$$

The equality is only reached in the limit of vanishing impurity-boson interaction, and the value of $|\mathbf{v}_{\rm imp,crit}(t_0)|$ increases with the strength of the interaction.

Finally, we extrapolate our data for $|S(t)|$ to find the value of $|S(t_\infty)|$, Eq. (2.63),

for various initial impurity velocities by making use of the fitting formula (3.7). When the exponent γ is zero, $|S(t)|$ saturates to a finite value. When γ is nonzero, $|S(t)|$ decays to zero. We illustrate this behavior in Fig. 6(d). We see that $|S(t_\infty)|$ has a discontinuous drop to zero between adjacent data points as the initial impurity velocity crosses the value (3.8).

The discontinuous behavior of $|S(t_\infty)|$ in the vicinity of $|\mathbf{P}_{\rm crit}^{\rm dyn}|$ identifies a dynamical transition. At the same time, $|S(t_\infty)|$ is determined by the FMGS quasiparticle residue Z, Eq. (2.63). We find in section 3.2 that this residue has a discontinuity at $|\mathbf{P}_{\rm crit}|$ and therefore signals the subsonic-Cherenkov FMGS transition. A comparison between $|\mathbf{P}_{\rm crit}^{\rm dyn}|$ and $|\mathbf{P}_{\rm crit}|$ is given in Fig. 3(a), where we plot critical points of the dynamical transition on top of the FMGS phase diagram. We see that the qualitative behavior of the critical line is the same for this dynamical transition compared to the FMGS, but quantitatively there is disagreement at stronger interactions. Per Eq. (2.63), however, we expect quantitative agreement of the transition line:

$$|\mathbf{P}_{\rm crit}^{\rm dyn}| = |\mathbf{P}_{\rm crit}| \,. \tag{3.9}$$

The fact that our numerical data does not exactly fulfil Eq. (3.9) at strong interactions may be due in part to different UV cutoffs being used for FMGS simulations versus quench dynamics; a smaller cutoff was used in the former to ensure that the imaginary time dynamics saturated within the limitations of available computational resources. Another contribution to the quantitative discrepancy may arise from limitations of the coherent state ansatz; higher order correlations between phonon modes are not explicitly captured and these correlations could become more relevant at stronger interactions. Using a full Gaussian state ansatz which includes squeezing on top of the coherent state could improve the agreement between the critical lines as discussed in Sec. 2.1.5.

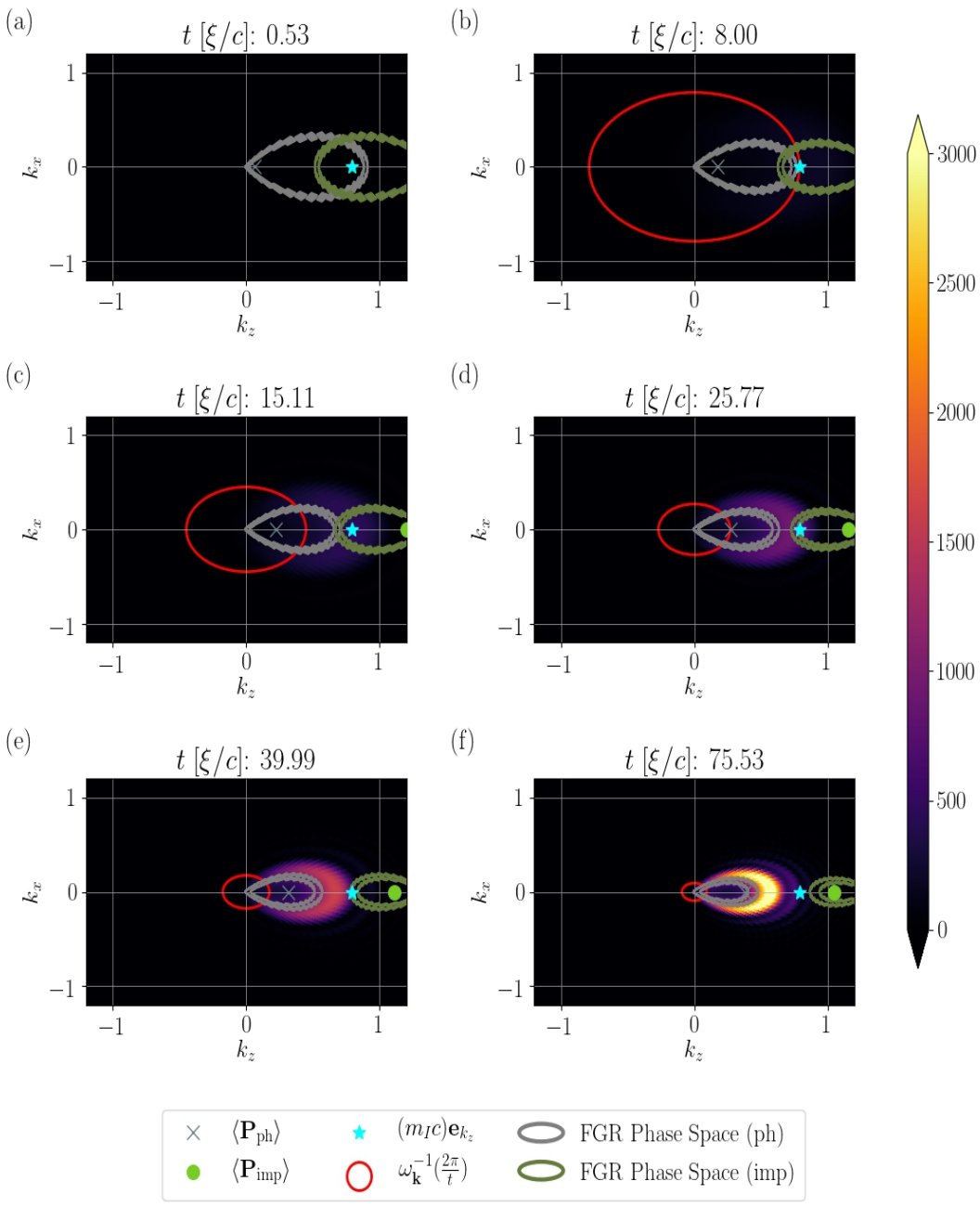

Figure 10: Mean phonon number distribution $n_{\rm ph}(\mathbf{k})$ at different times for a weakly interacting ($a_{\rm IB}^{-1} = -8.92/\xi$) and initially supersonic impurity ($v_{\rm imp}(t_0)/c = 1.8$). (a) Immediately after the quench we do not build up excitations as enough time hasn't passed. (b) & (c) We do not build excitations until enough time has passed to excite phonons in the phase space allowed by Fermi's golden rule (FGR). (d) - (f) We build up excitations exactly around this FGR phase space (which contracts over time as the impurity gets slower). The mass ratio is $m_I/m_B = 1$ and we use a sharp UV cutoff $\Lambda = 13.91/\xi$.

3.3.2 Comparison of Dynamics with Fermi's Golden Rule

As a check of our methods, we examine whether our variational wavefunction agrees with expectations from Fermi's golden rule physics at weak interactions. In Fig. 10, we plot the mean phonon number distribution $n_{\mathrm{ph,ind}}(\mathbf{k})$ at different times for a weakly interacting supersonic impurity; this check gives insight into the power-law decays that were discussed. The green dot (initially off-screen to the right at short times) is the average impurity momentum with the gray 'x' being the average total phonon momentum. The gray lobe in the plots corresponds to the phase space shell of phonons that can be excited according to Fermi's golden rule (FGR) if we limit ourselves to the Fröhlich model. The green lobe corresponds to the accessible momentum shell that the impurity would scatter to after such an emission. The blue star gives a reference for the speed of sound; the impurity stays supersonic so its average impurity momentum is always larger than this. The region inside the blue circle corresponds to the part of phase space where phonons have energy corresponding to the linear part of their Bogoliubov spectrum ("linear excitations"). The region outside the red circle corresponds to the phonon excitations that are accessible to the system at a given time based on the timescale set by their energy. Longer wavelength phonons (closer to $|\mathbf{k}| = 0$) become accessible at later times.

We see that we excite phonons around the FGR phase space lobe but only after enough time has passed to access those phonons; in the plots this corresponds to the portion of the gray lobe that is outside the red circle. As time elapses, the impurity slows down towards the speed of sound and the FGR phase space lobe therefore contracts; we thus see phonons excitations build up in the entire area swept out by the FGR lobe.

3.3.3 Average Impurity Velocity

Motivated by the fact that the impurity velocity acts as a signature of the FMGS transition, we also examine the dynamical impurity velocity

$$\mathbf{v}_{\mathrm{imp}}(t) = \frac{\langle \hat{\mathbf{P}}_{\mathrm{imp}}(t) \rangle}{m_I}. \tag{3.10}$$

in an effort to further understand the dynamical transition. Recall that the FMGS transition is characterized independently by a discontinuity in the quasiparticle residue and a discontinuity in the second derivative of the energy. Naturally, the average FMGS impurity velocity, Eq. (3.4), has a cusp at a point where the second derivative of the energy is discontinuous. This cusp can equivalently be used as a signature of the transition. The FMGS transition and dynamical transition are connected through the equivalence of the quasiparticle residue Z and the asymptotic behavior of the Loschmidt echo $|S(t_\infty)|$, Eq. (2.63). It is therefore natural to check whether there is a link between the FMGS impurity velocity and the asymptotic value

$$\mathbf{v}_{\mathrm{imp}}(t_\infty) \equiv \lim_{t\to\infty} \mathbf{v}_{\mathrm{imp}}(t) \tag{3.11}$$

of the average impurity velocity $\mathbf{v}_{\mathrm{imp}}(t)$ after a quench. Unlike Eq. (2.63), we do not have an analytic formula connecting $\mathbf{v}_{\mathrm{imp}}(t_\infty)$ and the FMGS impurity velocity, Eq. (3.4). Our numerical analysis suggests that

$$\mathbf{v}_{\mathrm{imp}}(t_\infty) = \begin{cases} \text{constant} < c, & \text{if } |\mathbf{P}| \leq \left|\mathbf{P}_{\mathrm{crit}}^{\mathrm{dyn}}\right| \\ c, & \text{if } |\mathbf{P}| > \left|\mathbf{P}_{\mathrm{crit}}^{\mathrm{dyn}}\right| \end{cases} \tag{3.12}$$

which indicates that the asymptotic average impurity velocity witnesses the dynamical transition, just as the ground state impurity velocity witnesses the FMGS transition.

Our numerical analysis allowing the extrapolation of $\mathbf{v}_{\mathrm{imp}}(t_\infty)$ is similar to the analysis of the Loschmidt echo in Sec. 3.3(a). Figures 8(c) and (d) illustrate the characteristic behavior of $\mathbf{v}_{\mathrm{imp}}(t)$ for different initial impurity velocities, $\mathbf{v}_{\mathrm{imp}}(t_0)$, at

weak and strong interactions, respectively. We see that the average impurity velocity decays to a subsonic value for smaller initial velocities, and decays towards the speed of sound for larger initial velocities. To find the asymptotic value of the impurity velocity, $\mathbf{v}_{\rm imp}(t_\infty)$, we separately consider the case where the velocity, $\mathbf{v}_{\rm imp}(t)$ with a power-law, has saturated to a value below c in the simulated time window, and the case where it has not. In the former case, we take $\mathbf{v}_{\rm imp}(t_\infty)$ to be the average of the last few values of $\mathbf{v}_{\rm imp}(t)$. In the latter case, we fit the long-time tail of $\mathbf{v}_{\rm imp}(t)$ with a power-law,

$$\mathbf{v}_{\rm imp}(t) = c \times t^{-\gamma}, \qquad t \to \infty. \tag{3.13}$$

We do the fit over the time range $80 \leq t/(\xi c^{-1}) \leq 90$ for all values of interactions available from our numerical simulation.

The extrapolated values $\mathbf{v}_{\rm imp}(t_\infty)$ for various initial impurity velocities are shown in Fig. 6(c). We find that the final impurity velocity is monotonic; it increases with initial impurity velocity until some critical $|\mathbf{v}_{\rm imp,crit}(t_0)|$ after which it saturates to c. For weak interactions, this critical initial velocity is seen to be the same as the critical transition point of the Loschmidt echo. For stronger interactions, however, there is a discrepancy in the critical initial velocities. We expect this discrepancy is due to the numerical difficulty of extrapolating $\mathbf{v}_{\rm imp}(t_\infty)$.

3.3.4 Host liquid density distribution

The density of atoms of the host liquid, $n_a(\mathbf{r}, t)$, shows qualitative differences on the two sides of the dynamical transition. In the subsonic phase, the impurity generates a rounded wave in the host gas density which propagates outwards faster than the impurity's motion. In the Cherenkov phase, the impurity generates a shock wave and wake in the host liquid density, with this modulation traveling along with the impurity even at late times. We illustrate the typical Cherenkov and subsonic patterns in Fig. 11(b) and (c) respectively, where we plot the integrated density, $n_a(x, z, t) = \int dy\, n_a(\mathbf{r}, t)$, at a specific time $t = 40\,\xi/c$ in the frame of the impurity propagating in the z-direction.

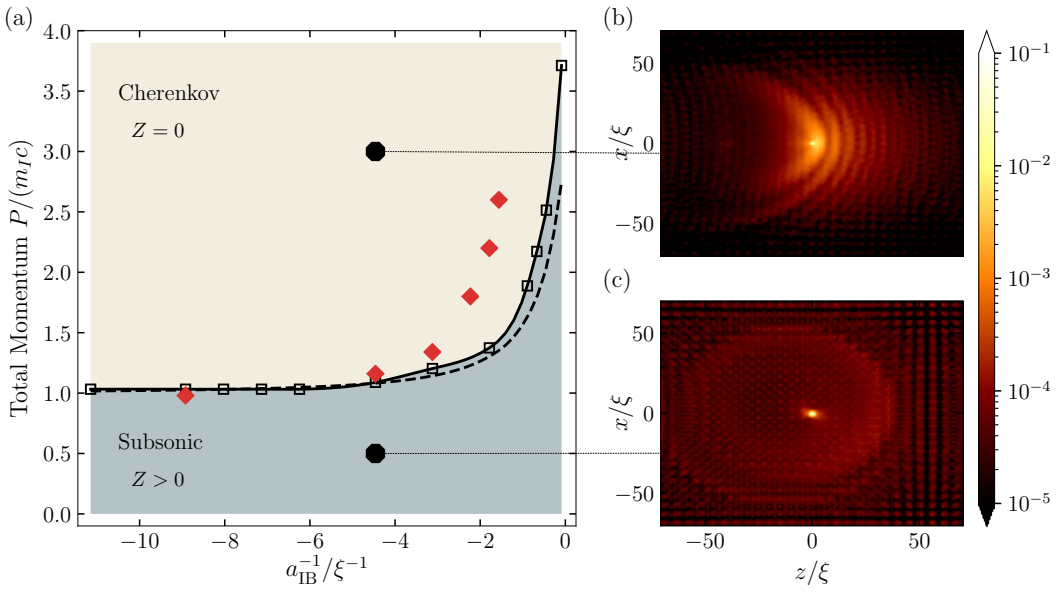

Figure 11: Quantum Cherenkov transition of a mobile impurity interacting with a 3D BEC. (a) Phase diagram depicting subsonic and Cherenkov regimes. The black squares mark the critical total system momentum, $P_{\rm crit}$, numerically extracted from the discontinuity in the second derivative of the FMGS energy. The black solid line is an interpolated guideline for the transition. The black dashed line depicts m^*c, where m^* is the polaron's mass, and c the BEC's speed of sound. For weak and intermediate interactions, the dashed and solid lines coincide. The red diamonds show the numerically extracted transition points for the long time limit of the dynamical protocol. Panels (b) and (c) illustrate the real-space density distribution of atoms in the host liquid in each regime. The distributions are plotted at time $t = 40\,\xi/c$ in the frame of the impurity propagating in the z-direction. The impurity-boson mass ratio is $m_I/m_B = 1$.

We can also integrate the real space density distribution of the host liquid plotted in Fig. 11(b) and (c) across the direction perpendicular to the impurity's motion. Specifically, in Fig. 12, we plot $n_a\left(z,t\right) = \int dx\,dy\,n_a\left(\mathbf{r},t\right)$ at a specific time $t = 40\,\xi/c$ in the frame of the impurity propagating in the z-direction. Panels (a) and (b) in Fig. 12 are typical patterns of the density in the subsonic and Cherenkov regimes respectively. We see a peak at the origin in both panels corresponding to the position of the impurity. In Fig. 12(b), representing the density in the Cherenkov regime, we see a shock wave followed by the first oscillation of the wake. The shock wave appears at approximately one healing length in front of the impurity ($z = \xi$). Both integrated densities, $n_a\left(x,z,t\right)$, depicted in Fig. 11, and $n_a\left(z,t\right) = \int dx\,n_a\left(x,z,t\right)$, depicted in

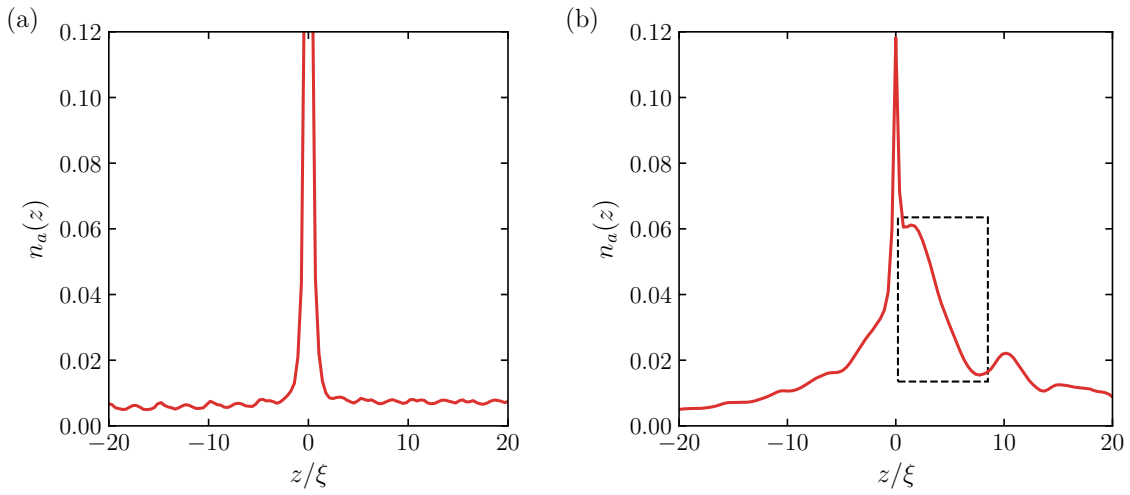

Figure 12: Integrated host liquid density distribution in direction of impurity propagation. (a) Subsonic regime ($P = 0.5 m_I c$). (b) Cherenkov regime ($P = 3.0 m_I c$). The dashed black rectangle highlights the shock wave in front of the impurity. The distributions are plotted at time $t = 40\,\xi/c$ in the frame of the impurity. The impurity-boson scattering length is $a_{\mathrm{IB}}^{-1} = -4.46/\xi^{-1}$ and the impurity-boson mass ratio is $m_I/m_B = 1$.

Fig. 12, are directly visible in experiments via absorption imaging.

In the Supplementary Videos of Ref. [326], we show the time-evolution of $n_a\left(x, z, t\right)$ for different interaction strengths and initial momenta. For interactions weak enough that an initially supersonic impurity decays towards c slowly, we observe the generation of a shock wave whose cone angle gradually becomes shallower as the impurity slows down. This dynamically changing cone angle, resulting from a changing Mach number $v_{\mathrm{imp}}\left(t\right)/c$, occurs due to finite recoil in the system which is not present in the classical limit of an infinitely heavy impurity. For strong interactions, the average velocity of an impurity in the Cherenkov regime quickly decays to c as it gets entangled with the host liquid. The impurity maintains a shallow shock wave and wake as it travels with constant average velocity c through the host liquid. Initially supersonic impurities that are in the subsonic regime, however, stop generating a shock wave and wake as time progresses. The existence of a persistent shock wave at late times therefore depends on how much velocity an initially supersonic impurity loses as it gets entangled with the host liquid. This dependence of the observed Cherenkov effect on the velocity of the entangled impurity highlights the quantum nature of the

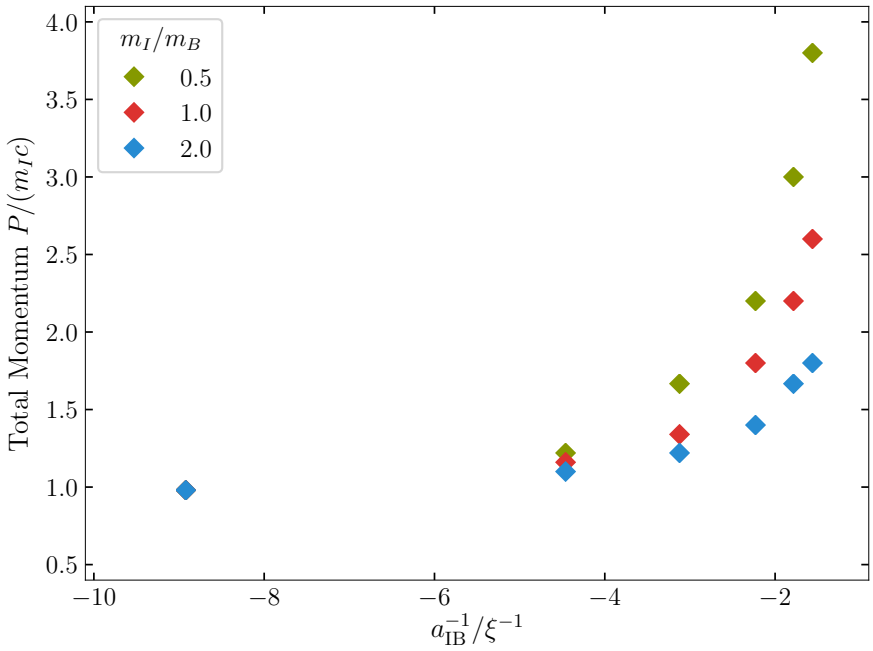

Figure 13: Dynamical quantum Cherenkov transition for different impurity-boson mass ratios.

transition arising from the impurity's finite mass and ensuing recoil.

If we make the boson-boson interaction in the host liquid weaker, the speed of sound decreases. In the limiting case of a non-interacting Bose gas, the system exhibits an orthogonality catastrophe where the FMGS quasiparticle residue will vanish for any choice of system parameters, a prediction that is consistent with Ref. [144].

3.3.5 Phase transition at different mass ratios

While we have focused on the case of equal impurity and boson masses so far, the dynamical transition exists for a range of mass ratios. In Fig. 13, we show the dynamical transition points P_{crit}, depicted by the red diamonds in Fig. 3(a), for various impurity-boson mass ratios. We see that for a fixed interaction strength, heavier impurities have a smaller critical momentum closer to $m_I c$; interactions must be stronger to appreciably renormalize the mass of heavy impurities. In the limit of an infinitely heavy impurity and finite interaction strength, the interactions have a negligible effect and the transition occurs at the point of the classical Cherenkov

transition, $P_{\text{crit}} \to m_I c$.

3.4 Discussion

We find a quantum Cherenkov transition that exists for all impurity-boson mass ratios and interaction strengths. In the limit of infinite m_I, we recover the kinematic Landau criterion for an macroscopic classical obstacle propagating through a superfluid. Finite m_I introduces the impurity's recoil energy as a relevant scale, thus making the quantum nature of the impurity important to the physics of the transition. For weak and intermediate interactions, the transition can be described in terms of mass renormalization by applying the Landau criterion to a polaron quasiparticle with effective mass m^*. For stronger interactions, however, we find that this description is no longer sufficient as P_{crit} is larger than $m^* c$, and the momentum dependence of the FMGS energy, Eq. (3.1), can no longer be captured by just m^*. In contrast to the classical Cherenkov effect, a mobile quantum impurity injected into a quantum liquid expresses whether it is in the Cherenkov regime only at late times.

The existence of a finite momentum transition in other impurity systems, and whether the FMGS and dynamical manifestations of such a transition occur at the same point, can provide insight into how dynamical behavior can be classified. For example, the finite momentum behavior of an impurity interacting repulsively with a one-dimensional Fermi gas has been examined [248, 181, 122]. There, a FMGS transition exists as momentum is increased, while a dynamical quench protocol similar to the one in our work exhibits a crossover. Specifically, in the one-dimensional gas studied in Ref. [122], the behavior of the post-quench long time limit of the average impurity velocity, $v_{\text{imp}}(t_\infty)$, is a smooth and non-monotonous function of the initial velocity $v_{\text{imp}}(t_0)$; it never reaches the speed of sound in the gas. Furthermore, $v_{\text{imp}}(t_\infty) \to 0$ as $v_{\text{imp}}(t_0) \to \infty$. This behavior may be associated with the prevailing role of a few initial central collisions between the impurity and host particles in the one-dimensional gas; such collisions take away virtually all momentum from the impurity. In contrast, for the three-dimensional gas studied in our work, small-angle

collisions play an important role, thus ensuring that the impurity may have $v_{\mathrm{imp}}(t_\infty)$ remain far from zero for any arbitrarily high initial impurity velocity as shown in Fig. 6(c). Two-dimensional gases may have collisions in-between these two cases, and therefore we have no *a priori* conclusions about the behaviour of $v_{\mathrm{imp}}(t_\infty)$ for large initial velocities in these systems.

Experimentally, the transition we observe can be detected through time-of-flight imaging of a dilute impurity gas immersed in a BEC. We have established that the width of the impurity's momentum distribution acts a signature of the transition in the FMGS. Alternatively, Ramsey interferometry or RF spectroscopy, as detailed in Ref. [63], can be used to detect the dynamical transition as the onset of a power-law decay in the Loschmidt echo signifies the critical point. Absorption imaging of the density distribution of host atoms would directly reveal the polaron shock wave and wake of sufficiently fast impurities. We assume a homogeneous BEC in the vicinity of the impurity, which can be realized using a sufficiently large box trap. The dynamical quantum Cherenkov transition we uncover provides a route to experimentally pinpoint the characteristic dynamical properties of impurities immersed in quantum liquids, which would grant insight into the far-from-equilibrium behavior of quantum many-body systems.

Chapter 4

Experimental probes of finite momentum Bose polarons

Early experimental work on Bose polarons focused on gaining coherent control of impurities immersed in cold Bose gases [316, 344, 310, 120]. Later experiments studying polarons in three dimensional BECs have primarily characterized the polaron energy and probed quasiparticle breakdown due to finite temperature effects using RF spectroscopy [172, 158, 377]. For Bose polarons in one dimension, impurity trajectories have been examined to give an indirect signature of the effective mass [61]. However, no direct measurements of a Bose polaron's effective mass have yet been made in 1D and no experimental investigations of the effective mass have been made at all in 3D BECs. Theoretical predictions for the polaron's effective mass show large quantitative and qualitative discrepencies; for example, they disagree on whether the effective mass diverges at strong impurity-boson interactions or whether it stays finite [293, 137, 72]. Experimentally probing the quasiparticle nature of the impurity-bath system through effective mass measurements as well as exploring when this quasiparticle picture breaks down is therefore a fruitful line of inquiry. In this chapter, we discuss experimental protocols that can be used to study polaronic mass renormalization.

We leverage the formalism in Sec. 2.2 to describe the dynamics of experimentally viable setups involving slowly varying traps and other external forces. In Sec. 4.1, we

discuss a dynamical protocol to measure the effective mass of a Bose polaron in a homogeneous BEC. In Sec. 4.2, we discuss a protocol involving dipole oscillations of the BEC and the resulting dynamics of the impurity both for the case of a homogeneous BEC and an inhomogeneous BEC resulting from a harmonically trapped Bose gas. We find that the dynamical transition discussed in Chap. 3 manifests in both these protocols as well. Specifically, We find that the protocol in Sec. 4.1 runs into errors introduced by supersonic impurities, while the protocol in Sec. 4.2 exhibits locking of the impurity onto the motion of the BEC due to Cherenkov physics. This latter protocol, however, shows a more robust signature of mass renormalization for attractive impurity-boson interactions as well as evidence of quasiparticle breakdown for repulsive impurity-boson interactions. Examination of the physics of fast impurities therefore gives insight into the design of experimental protocols intended to study quasiparticles in impurity-bath systems. For example, if seeking to use a protocol like the one in Sec. 4.1 to measure the effective mass of a polaron, the initial impurity velocities and magnitude of the external force should be limited so that the impurity doesn't end up supersonic. Additionally, protocols similar to Sec. 4.2 are often used to study hydrodynamics and collective modes of Bose-Fermi mixtures, but we see that in the limit of dilute impurities it is predominantly sensitive to Cherenkov physics. The material in this chapter corresponds to the work in Ref. [323].

4.1 Effective Mass Protocol

Here, we discuss a protocol involving the application of a constant external force to the impurity in order to measure the effective mass of a polaron. The protocol is as follows (Fig. 14). We initialize the system in a polaron ground state. Then we impart a known amount of momentum $\Delta\mathbf{P} = \int_0^{\Delta t} d\tau \mathbf{F}(\tau)$ to the impurity using an external force $\mathbf{F}(t)$. The application of this force will change the impurity's velocity by $\Delta\mathbf{v}$. The ratio $m^* = |\Delta\mathbf{P}| \,/\, |\Delta\mathbf{v}|$ of the momentum imparted to the system and the impurity's change in velocity therefore represents the inertia in the polaron state and can therefore be interpreted as the effective mass of the polaron. Specifically, we

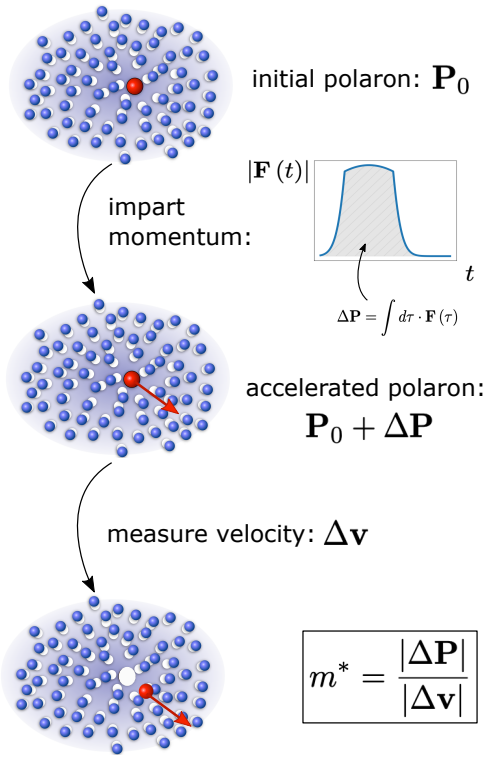

Figure 14: Protocol to measure effective mass. (a) First we apply an external force on the impurity for a fixed amount of time and calculate the total momentum imparted to the system. (b) We then calculate the change in velocity of the impurity after the final velocity has saturated. (c) Taking the ratio of momentum imparted to the system and the impurity velocity difference gives us the effective mass.

apply a constant external force of fixed magnitude F for a time Δt which imparts a momentum $\Delta P = F\Delta t$ to the system. We then measure the change in the impurity's speed Δv (in the direction of the external force) and compute the effective mass as $m^* = F\Delta t/\Delta v$. We assume a homogeneous BEC in this protocol to more clearly showcase certain physics; trap effects can be easily included in the LDA formalism.

If we apply the force for a short enough period of time to keep the impurity in the subsonic regime, the impurity velocity saturates to a constant value (Fig. 15(a)). We can determine the effective mass of the polaron by reading off the final velocity of the impurity and dividing the known momentum imparted to the system by this velocity (Fig. 15(b)). As a check, we can compare the 'measured' effective mass in our simulation with that calculated using the saddle point solution to the equations of motion (see Sec. 2.1.4). We see that the measured effective mass matches the saddle

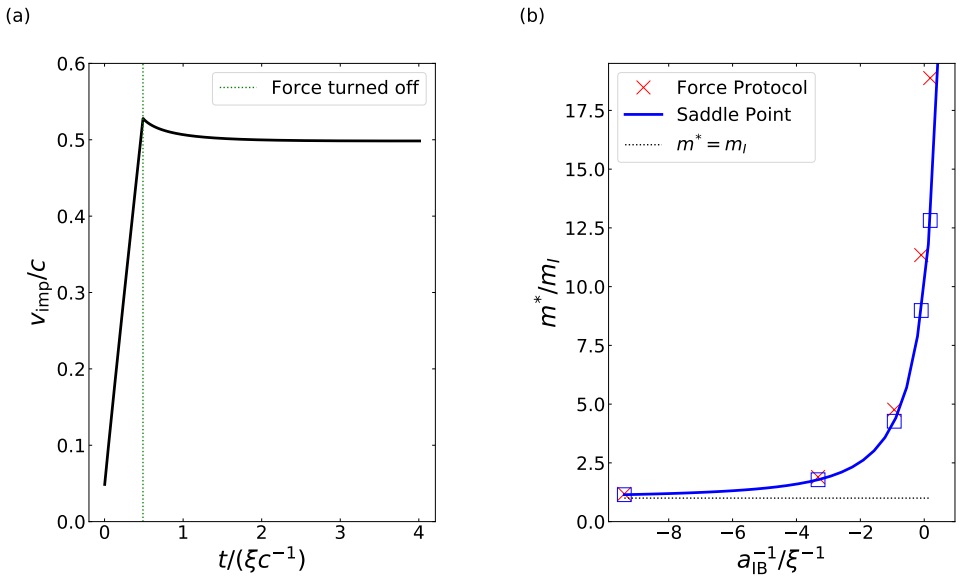

Figure 15: Effective mass protocol fully in subsonic region. (a) Average impurity speed. The impurity velocity increases linearly while the constant external force is applied. The impurity-boson interaction is $a_{\mathrm{IB}}^{-1} = -9.39/\xi^{-1}$ and an external force of $F = 0.21\frac{2\pi c}{\xi^2}$ is applied for $\Delta t = 0.5/(\xi c^{-1})$ to impart momentum $\Delta P = 0.8/(m_I c)$. (b) Mass enhancement. We confirm that the proposed protocol correctly yields a larger effective mass as we increase interaction strength. The system parameters used were a mass ratio of $\frac{m_I}{m_B} = 1.7$, a momentum cutoff $\Lambda = 36.60/\xi$, and an initial polaron state with total momentum $P_0 = 0.15/(m_I c)$.

point calculation fairly well, especially at weak interactions. For strong interactions, we see increasingly large discrepancies that are likely due to non-adiabatic effects during the dynamics of the protocol. While the LDA is exact for an external constant force, the changing of total system momentum in time is likely done too quickly for the impurity's dressing cloud to appropriately adjust into the correct polaron state. We do not see this issue for weak interactions as the impurity is not as strongly dressed. Another way to understand this error is to think of the time-dependent total momentum as a series of infinitesimal quenches; for strong interactions, short time scattering drops the impurity to slower final speeds than would be expected in the ground state. This undershoot in final velocity causes the overshoot in mass enhancement between the force protocol and saddle point solution that we see in Fig. 15(b).

If we repeat this protocol after applying the force long enough to speed the im-

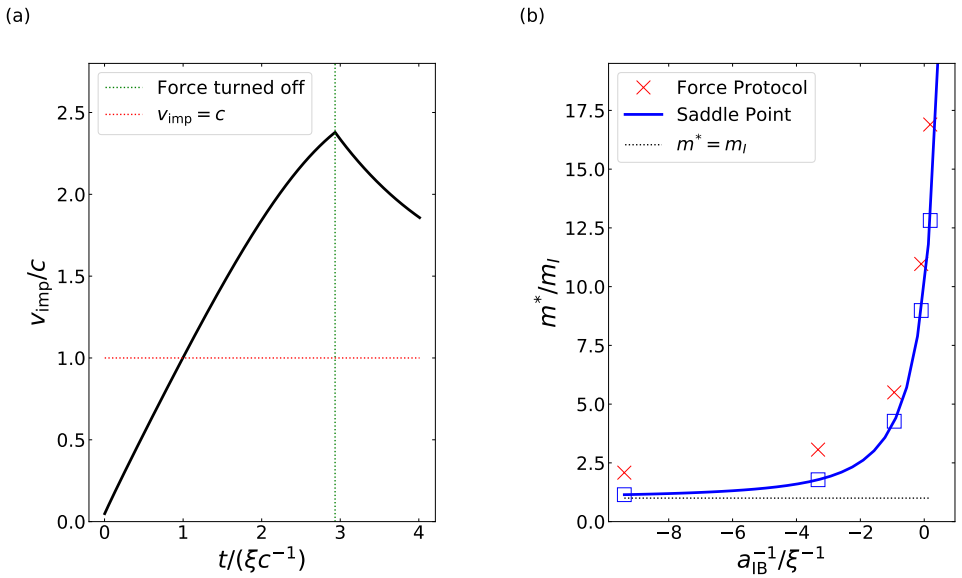

Figure 16: Effective mass protocol partially in supersonic region. (a) Average impurity speed. We see curvature corresponding to dissipation as the external force accelerates the impurity past the speed of sound. The impurity-boson interaction is $a_{\text{IB}}^{-1} = -9.39/\xi^{-1}$ and an external force of $F = 0.21\frac{2\pi c}{\xi^2}$ is applied for $\Delta t = 0.5/(\xi c^{-1})$ to impart momentum $\Delta P = 4.6/(m_I c)$. (b) Mass enhancement. There is error in the 'measured' effective mass at weak interactions. The system parameters used were a mass ratio of $\frac{m_I}{m_B} = 1.7$, a momentum cutoff $\Lambda = 36.60/\xi$, and an initial polaron state with total momentum $P_0 = 0.15/(m_I c)$.

purity up into the supersonic regime, we get different results for weak interactions. We see dissipation represented by a curvature in the velocity as soon as we cross the speed of sound (Fig. 16(a)) which leads to the measured effective mass values drifting from the values determined from the saddle point calculation (Fig. 16(b)). The error with the saddle point calculation is roughly equivalent at strong interactions in both Fig. 15(b) and Fig. 16(b) because the effective mass has increased and the impurity is not actually supersonic in either case. We therefore see that Cherenkov physics rears its head and disrupts the effective mass protocol if the experimental setup is not sufficiently cold so the thermal velocity of impurities is near the speed of sound and/or if the force is applied for long enough that the impurity becomes supersonic.

4.2 BEC Oscillation Protocol

Cherenkov physics also plays an important role in an experimental protocol where we induce dipole oscillations of the BEC and examine the dynamics of the impurity as the interspecies interaction strength is increased.

The protocol is as follows (Fig. 17). We trap both the impurity and the BEC using harmonic traps. A second (displaced) harmonic trap which preferrentially affects the BEC is adiabatically turned on; this causes the condensate density to shift. The first trap affecting the BEC is then suddenly turned off which kicks the BEC into performing dipolar oscillations at the frequency of the second harmonic trap. We assume the impurity is minimally affected by this adiabatic protocol (the bare impurity trap remains unchanged) and before the BEC starts oscillating, enough time has passed for it to form a polaron state with the surrounding atoms. We can then 'measure' time traces of the impurity's average position. From these trajectories, we can compute the frequency response of the impurity's motion as well as velocity time traces (both in the lab frame and the BEC frame). The interaction between the impurity and the BEC causes the BEC oscillations to act as a drive for the impurity. We assume that the inhomogeneous BEC density in the presence of a harmonic trap is given by the following Thomas Fermi profile:

$$n_0(\mathbf{R}) = n_{TF}(\mathbf{R}) + n_G(\mathbf{R}) \tag{4.1}$$

$$n_{TF}(\mathbf{R}) = n_{TF,\text{peak}} \max\left[1 - \left(\frac{x}{R_{TF,x}}\right)^2 - \left(\frac{y}{R_{TF,y}}\right)^2 - \left(\frac{z}{R_{TF,z}}\right)^2, 0\right] \tag{4.2}$$

$$n_G(\mathbf{R}) = n_{G,\text{peak}} e^{-\left(\frac{x}{R_{G,x}}\right)^2 - \left(\frac{y}{R_{G,y}}\right)^2 - \left(\frac{z}{R_{G,z}}\right)^2} \tag{4.3}$$

where $\mathbf{R} = (x, y, z)$. The parameters for the density profile as well as other quantities in the system is given in Table 4.1.

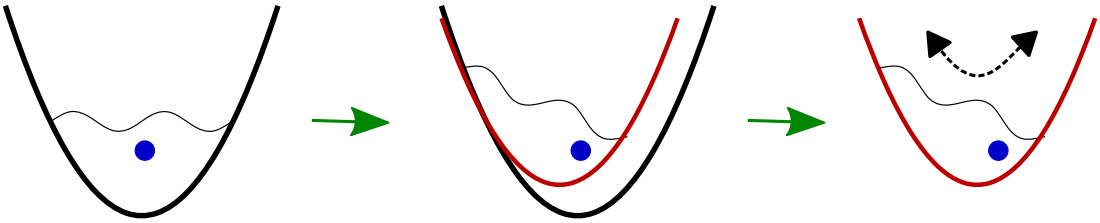

Figure 17: Dipole oscillation protocol. The BEC is confined in a harmonic trap, a second trap is adiabatically turned on, then the first trap is turned off which kicks the BEC into dipole oscillations set by the frequency of the second trap. The impurity is depicted as the blue dot and is trapped in its own harmonic potential (not shown) which remains unchanged during this protocol.

Parameter	Value
Impurity mass (m_I)	39.96 u
Boson mass (m_B)	22.99 u
Boson-boson scattering length (a_{BB})	52 a_0
Bare impurity trap frequency (ω_0)	150 Hz
BEC density Thomas Fermi radii ($R_{TF,x}$,$R_{TF,y}$,$R_{TF,z}$)	(14.4,11.5,95.7) μm
BEC density thermal Gaussian waists ($R_{G,x}$,$R_{G,y}$,$R_{G,z}$)	(95,29,12) μm
BEC peak density (Thomas Fermi) ($n_{TF,\mathrm{peak}}$)	6×10^{13} cm^{-3}
BEC peak density (thermal) ($n_{G,\mathrm{peak}}$)	0.9×10^{13} cm^{-3}
BEC oscillation frequency (ω_{BEC})	80 Hz
BEC oscillation amplitude (initial displacement)	10 μm

Table 4.1: Oscilation Protocol Parameters.

4.2.1 Homogeneous BEC

We first consider the case of a homogeneous BEC; the BEC is still oscillating but the density of the condensate is constant as if its trap was flat and infinitely wide. In reality, a homogeneous BEC is a good approximation if $R_{I,x} \ll R_{TF,x}, R_{G,x}$, meaning that the impurity's position $R_{I,x}$ (in the direction of the BEC's oscillation) is always one to two orders of magnitude smaller than the width of the BEC's density profile, which is set by the Thomas-Fermi radius $R_{TF,x}$ and thermal width $R_{G,x}$ in this direction. In this case, the condensate has a uniform density from the perspective of the impurity.

In Fig. 18, we plot the frequency spectra $I(\omega)$ of the impurity's trajectory as a function of interspecies interaction strength. To this end, we calculate the impurity trajectory $R_{I,x}(t)$ along the BEC oscillation axis and take its Fourier transform

$I(\omega) = \int_0^\infty dt e^{-i\omega t} R_{I,x}(t)$. Note that we compute the spectrum from the impurity's trajectory in the lab frame. In Fig. 18(a) and Fig. 18(c) we plot the frequency spectra for negative and positive scattering lengths respectively. We see that the impurity initially oscillates at its bare trap frequency for weak interactions, and then eventually locks on to the BEC as interactions strength is increased. In Fig. 18(b) and Fig. 18(d) we plot the spectra when we artificially turn off phonon dynamics for negative and positive scattering lengths respectively. The phonons in the polaron state we initialize in are frozen and the impurity only feels the LDA potentials of its bare trap and the ficticious force from the BEC's oscillation. As the impurity has no way to talk to the BEC through phonons, we of course see that the impurity just oscillates at its bare trap frequency. Therefore, phonon dynamics leads to locking in the same way in the same interaction range for both negative and positive scattering lengths.

We can gain insight into the cause of locking by looking at the average impurity velocity in the BEC frame (Fig. 19). For weak interactions, the BEC's oscillation drives the impurity to be supersonic the majority of the time. As interaction strength is increased, phonon emission allows the impurity to dissipate its momentum and the onset of locking coincides with the impurity being able to dissipate momentum quickly enough that it always remains subsonic. Cherenkov physics is therefore sufficient for the impurity motion to lock onto the frequency of the oscillating BEC.

In Fig. 20. we plot the dissipation constant γ computed by fitting the effective oscillator model described in Appendix 4.2.3 to the impurity trajectory. We see that at weak interactions, we recover the expected result from Fermi's golden rule; the dissipation should scale quadratically with the scattering length as the rate of phonon emission from the Fröhlich term of the Hamiltonian is proportional to the square of the interaction constant. This indicates, as the figure confirms, that negative and positive scattering lengths should behave identically in this regime. Differences in the two cases only start arising at stronger interactions.

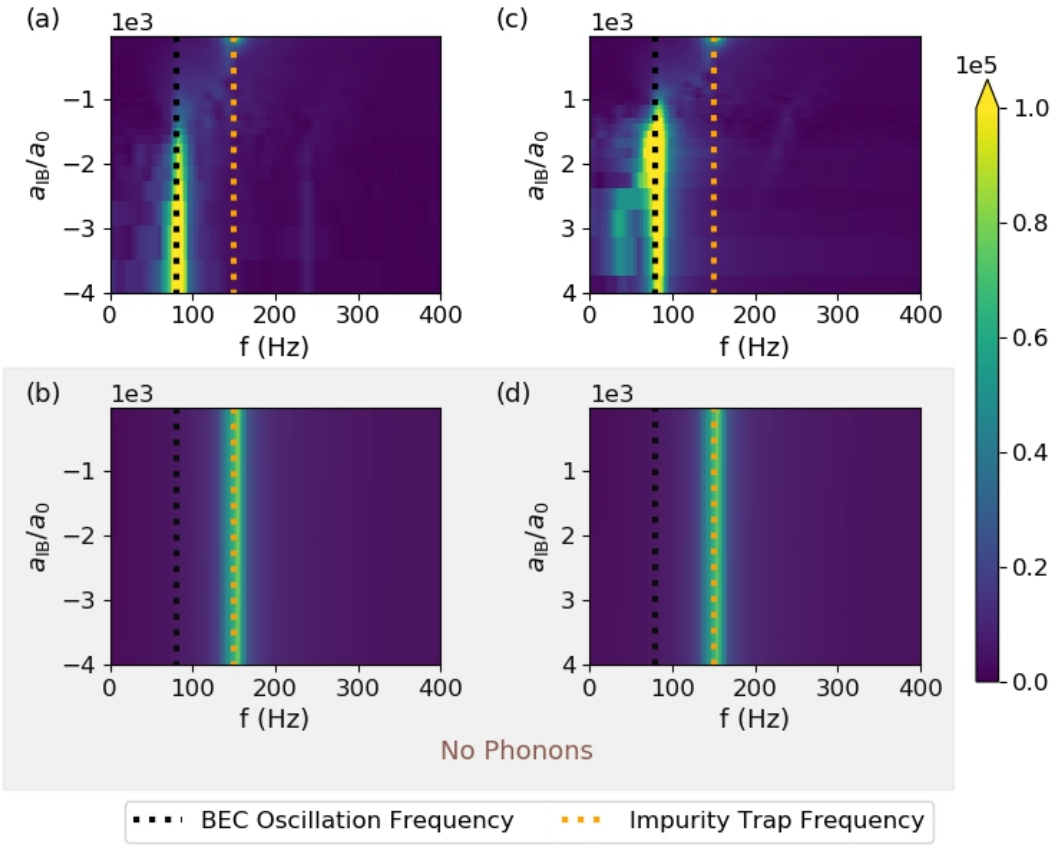

Figure 18: Frequency spectra of impurity trajectory in homogeneous oscillating BEC. (a) Negative scattering lengths and full dynamics. (b) Negative scattering lengths and phonon dynamics turned off. (c) Positive scattering lengths and full dynamics. (d) Positive scattering lengths and phonon dynamics turned off. We see that the phonon dynamics causes the impurity to lock onto the BEC for both negative and positive scattering lengths.

4.2.2 Harmonically Trapped BEC

Now we can examine the case where the density variation of the BEC due to its trap is appreciable over the region that the impurity explores. The polaron energy potential (Sec. 2.2.3) must now be included. The frequency spectra of the impurity trajectory are given in Fig. 21. In Fig. 21(b) we plot the spectra when we artificially turn off phonon dynamics for negative scattering lengths. We see an additional frequency line that exactly corresponds to a harmonic approximation to the effective impurity potential created by the combination of the bare impurity trap potential and the polaron energy potential. A white line corresponding to this harmonic approximation

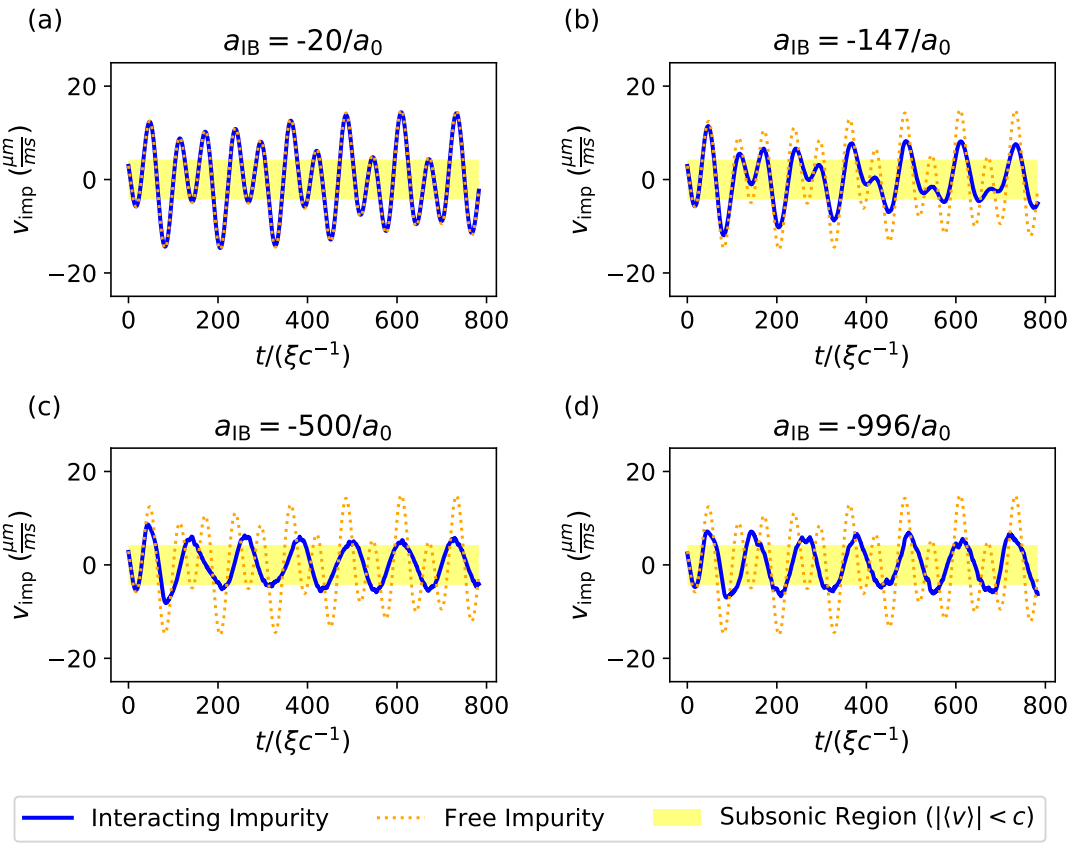

Figure 19: Average impurity velocity in BEC frame for negative scattering lengths. As we go from (a)-(d), the interaction strength is increased and we see that the impurity becomes increasingly confined to the subsonic region. The orange dotted line gives a reference of what the impurity would do if it only saw its bare trap. Note that $\xi c^{-1} = 0.11$ms.

is drawn for reference. The impurity is driven by the BEC's motion and also oscillates according to this effective mean-field potential.

In Fig. 21(a), we turn on phonon dynamics (which are always physically present) and see that they cause a red-shifting of the mean-field potential. This red-shifting is due to increased mass renormalization of the impurity for stronger interactions and is thus a signature of the initial polaron undergoing oscillatory dynamics. Let us take the effective mean-field potential in the absence of phonon dynamics (due to the bare impurity trap and polaron energy potential) to be $V_{MF}(x_I) = \frac{1}{2} m_I \omega_{MF}^2 x_I^2$; the frequency ω_{MF} is what is plotted as the white reference line in Fig. 21(b). We can estimate the mass-renormalized frequency $\tilde{\omega}_{MF}$ by equating $V_{MF}(x_I)$ to $\frac{1}{2} m^* \tilde{\omega}_{MF}^2 x_I^2$

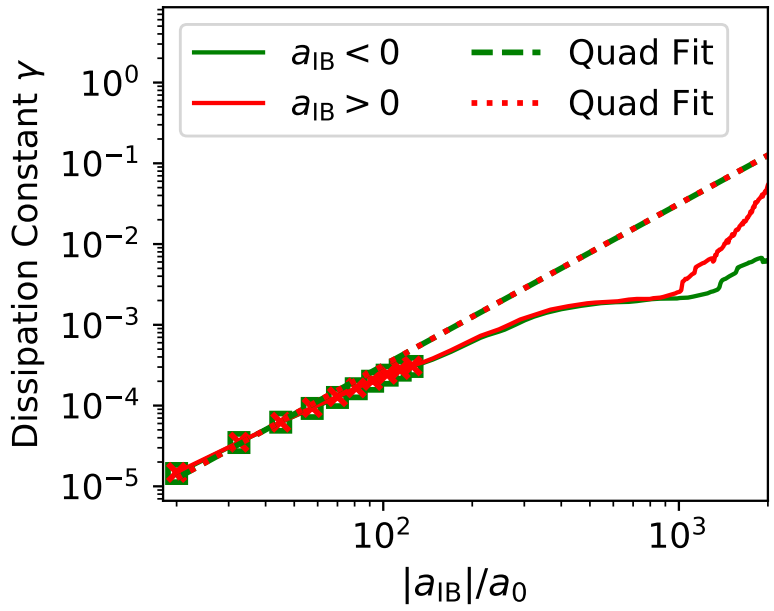

Figure 20: Dissipation constant fit in a homogeneous oscillating BEC. At weak interactions, both negative and positive scattering length trajectories have the same dissipation constant. Example data points are given by the green squares and red X's showing a quantitative match. The dashed green line (dotted red line) shows a quadratic fit to the dissipation constant for negative (positive) scattering lengths; the dissipation depends quadratically on interaction strength for weak interactions. The quadratic fit was done between $|a_{\mathrm{IB}}| \in [0, 50]a_0$.

where m^* is the effective mass of the initial polaron state calculated through Eq. (2.36). This renormalized frequency $\tilde{\omega}_{MF} = \omega_{MF}\sqrt{m/m^*}$ is plotted as the white reference line in Fig. 21(a) and we see that it matches the red-shifted spectral line. We therefore see that dipole oscillations of a BEC can be used as a probe of the effective mass of attractive polarons.

Next, we examine the positive scattering case. Fig. 21(d) shows the case where phonon dynamics are artificially turned off for comparison. We find that the impurity dynamics is unstable and the impurity spends most of its time being supersonic even at strong interactions (not shown). This instability can be thought of as resulting from the large amount of phase space accessible to the impurity when it is not damped by phonon emission and can therefore access high velocities.

When we turn on phonon dynamics (21(c)), the dynamics gets stabilized and we see that the impurity locks onto the BEC. There is also a DC shift that can be

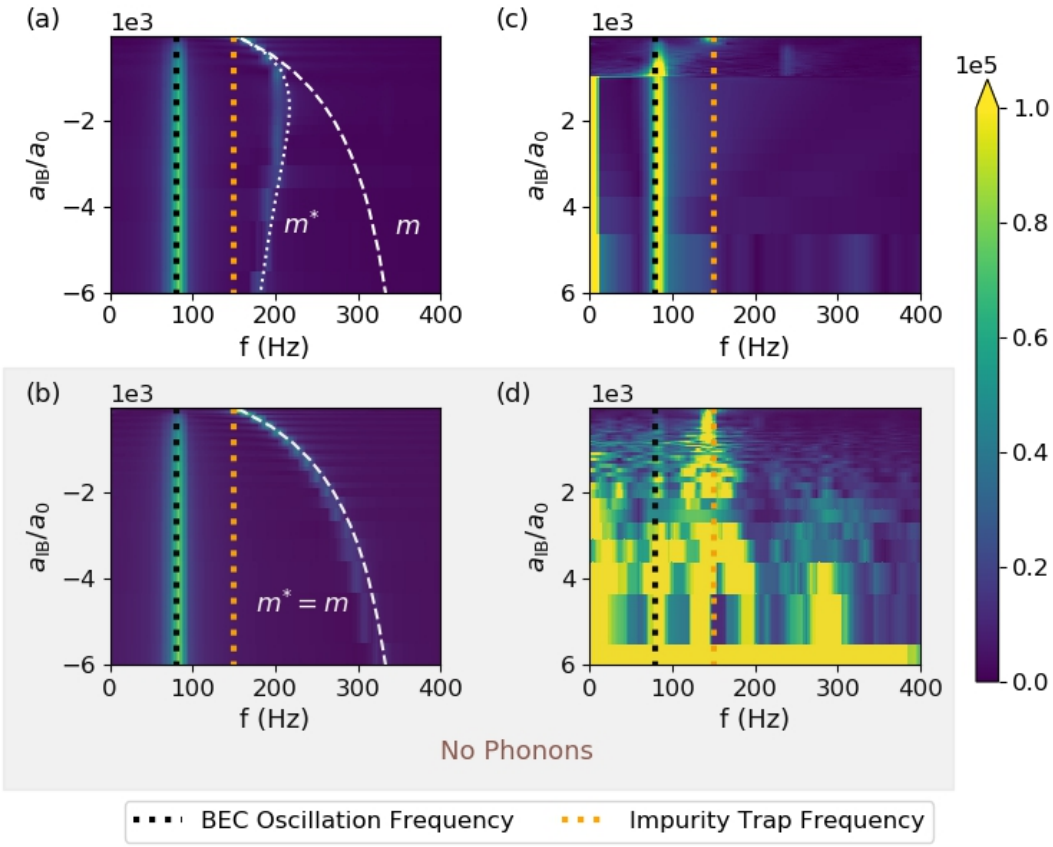

Figure 21: Frequency spectra of impurity trajectory in harmonically trapped oscillating BEC. (a) Negative scattering lengths and full dynamics. The mean-field potential gets red-shifted due to mass renormalization (white line). (b) Negative scattering lengths and phonon dynamics turned off (no mass renormalization). We see a clear frequency line corresponding to the mean-field potential (white lines). (c) Positive scattering lengths and full dynamics. The impurity dynamics is stable and exhibits locking onto the BEC. (d) Positive scattering lengths and phonon dynamics turned off. The impurity dynamics is unstable.

understood by looking at the impurity trajectory plots in the BEC frame shown in Fig. 22. We see that as interaction strength is increased, the impurity locks onto the BEC's motion but bounces between the edges of the BEC. At sufficiently strong interactions, it stops bouncing and gets localized around one edge of the BEC which corresponds to the DC shift. This behavior is consistent with what is seen for repulsive impurity-boson interactions in 1D where the locking of the impurity onto an edge of the BEC was interpreted as a breakdown of the polaron quasiparticle picture [254]. The bare impurity trap and the BEC combine to form a double well potential for

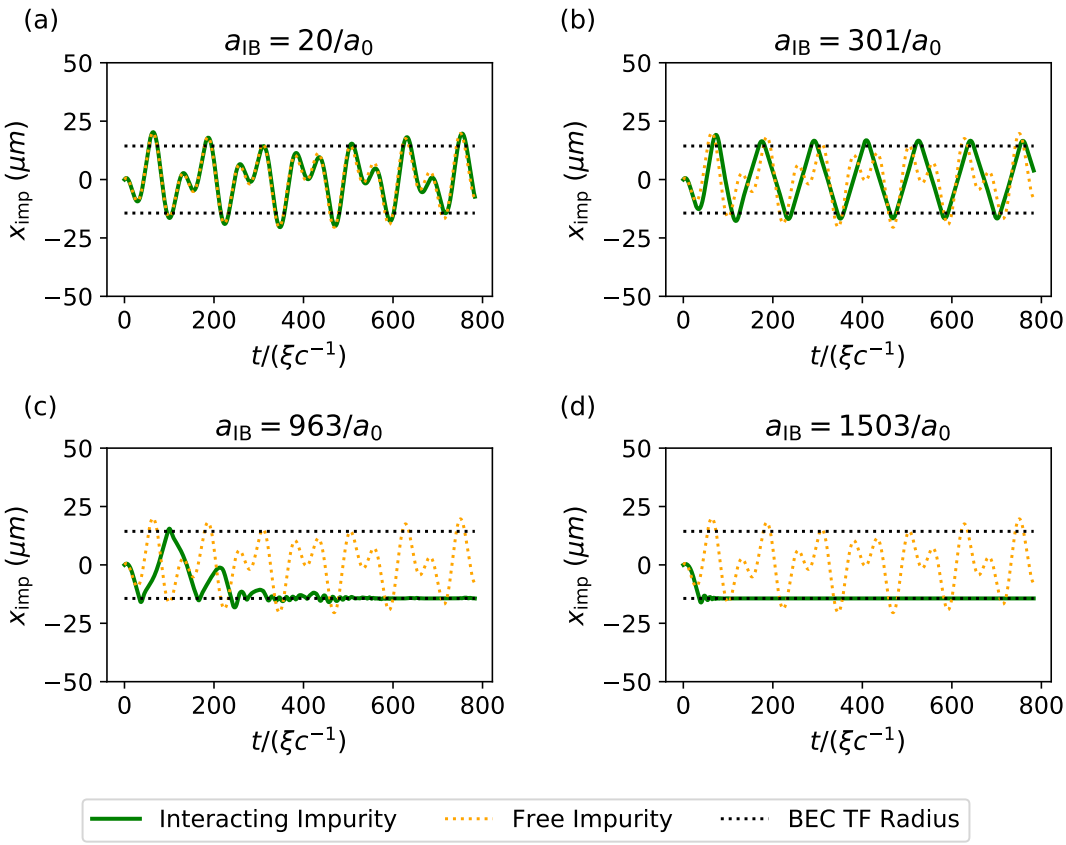

Figure 22: Impurity trajectory in the BEC frame for different interaction strengths. We see that as interaction strength is increased from (a)-(d), the impurity locks onto an edge of the BEC. Note that $\xi c^{-1} = 0.11$ms.

the impurity where for strong enough interactions the impurity gets stuck in one of the wells [254]. We can think of the phonon dynamics as limiting the phase space available to the impurity. After the impurity gets pushed to the edge of the BEC due to strong repulsive interactions it either slides down its bare trap potential towards the BEC as the BEC moves away from it or gets pushed up its bare trap potential as the BEC moves towards it. In either case the impurity is essentially stationary (with respect to the BEC) and does not have enough energy to enter deep into the BEC.

4.2.3 Effective Oscillator Model

Here, we describe an effective driven-dissipative harmonic oscillator model used to fit simulation data in order to gain insight into the relative strength of various physical

mechanisms in the system. Assume the BEC is oscillating in the x-direction, the bare trap on the impurity is in the same direction, there are no other forces acting on the impurity that push it in the y- or z-directions. Also assume that the initial momentum $\mathbf{P}_0$ of the impurity only points in the x direction as well ($\mathbf{P}_0 = (P_0, 0, 0)$). Then the impurity only moves in the x direction; without loss of generality, the impurity position in the BEC frame is $\mathbf{R}_I(t) = (x(t), 0, 0)$ and the impurity position in the lab frame is $\tilde{\mathbf{R}}_I(t) = (x_L(t), 0, 0)$ where $x_L(t) = x(t) + x_{BEC}(t)$ and $x_{BEC}(t) = B_0 \cos(\omega_B t)$ is the position of te BEC's peak density[1].

We would like to write down an effective model for $x(t)$ (or equivalently $x_L(t)$). The effects we want to consider are the potential on the impurity due to the inhomogeneous BEC density, dissipation through Cherenkov radiation, the bare impurity trapping potential, and the ficticious force due to the non-inertial BEC frame. Assuming a harmonic trap on the BEC, the density of the BEC becomes position dependant and the polaron energy E_{pol} becomes position dependent (through its density dependence) and acts as an effective harmonic potential on the impurity. Specifically, we can Taylor expand the potential $V_{pol}(x) \equiv E_{pol}(x)$ in the BEC frame around the peak density of the BEC (assumed at $x = 0$ in the BEC frame) to get $V_{pol}(x) = \frac{1}{2}\left(\frac{d^2 E_{pol}}{dx^2}|_{x=0}\right) x^2 + \mathcal{O}(x^3)$. Defining $\alpha \equiv \frac{d^2 E_{pol}}{dx^2}|_{x=0}$ and dropping higher order terms, this gives a harmonic potential $V_{pol}(x) = \frac{1}{2}\alpha x^2$ that acts on the impurity with an associated force $F_{pol}(x) = -\frac{\partial V_{pol}}{\partial x} = -\alpha x$. We can model the effect of dissipation through Cherenkov radiation using a damping term $F_{damp} = -\xi \dot{x}$ which acts on the impurity's position in the BEC frame. The harmonic bare impurity trap acts on the impurity's position in the lab frame and takes the form $V_{trap}(x_L) = \frac{1}{2} m\omega_0^2 x_L^2$ with an associated force $F_{trap}(x_L) = -\frac{dV_{trap}}{dx_L} = -m\omega_0^2 x_L$. We can rewrite this trapping potential in the BEC frame as $F_{trap}(x) = -m\omega_0^2 (x + x_{BEC})$. Lastly, we have a ficticious force $F_{fict} = -m\ddot{x}_{BEC}$ that acts on the impurity in the non-inertial BEC frame. Newton's equation of motion in the BEC frame thus reads

$$m\ddot{x} + \left(m\omega_0^2 + \alpha\right) x + \xi \dot{x} = m\left(\omega_B^2 - \omega_0^2\right) B_0 \cos(\omega_B t) \tag{4.4}$$

[1] In accordance to the definition in the previous section, we have $B_0 = aR_{TF,x}$

In the lab frame this can be rewritten as

$$\begin{aligned} m\ddot{x}_L + \left(m\omega_0^2 + \alpha\right) x_L + \xi \dot{x}_L \\ = \alpha \left[B_0 \cos\left(\omega_B t\right)\right] + \xi \left[-\omega_B B_0 \sin\left(\omega_B t\right)\right] \end{aligned} \tag{4.5}$$

Note that in the lab frame equation of motion, we get an additional driving term $\xi \dot{x}_{BEC}$ proportional to the damping coeffficient. This term comes from the fact that the Cherenkov damping is really acting as friction in the BEC frame and and therefore drags the impurity around in the original lab frame. We now have the physical interpretations in the lab frame that the impurity trap acts as a standard harmonic potential, the polaron potential E_{pol} both renormalizes this frequency as well as provides an external driving force at the BEC frequency ω_B, and Cherenkov radiation causes both a damping term as well as an external driving force at the BEC frequency ω_B. Therefore we can generally have driving contributions at ω_B due to both the polaron potential as well as the Cherenkov radiation. Locking to the BEC frequency ω_B at strong interactions can therefore be due to either of these effects or a combination of them. Fitting the data to this model to estimate α and ξ will allow us to compare the relative strengths of the effects.

Let us divide by mass in the BEC frame ODE to get

$$\begin{aligned} \ddot{x} + 2\gamma \dot{x} + \left(\omega_0^2 + \beta\right) x \\ = \left(\omega_B^2 - \omega_0^2\right) B_0 \cos\left(\omega_B t\right) \end{aligned} \tag{4.6}$$

where we have defined $2\gamma \equiv \frac{\xi}{m}$ and $\beta \equiv \frac{\alpha}{m}$. The driven-dissipative oscillator model above will either be underdamped, critically damped, or overdamped depending on whether the quantity $\gamma^2 - \omega_0^2 - \beta$ is less than, equal to, or greater than zero respectively. Equivalently, we can define the damping ratio $\rho \equiv \frac{\gamma}{\sqrt{\omega_0^2 + \beta}}$ which determines whether we are underdamped, critically damped, or overdamped depending on whether $\rho < 1$, $\rho = 1$, or $\rho > 1$ respectively. We can solve the ODE in each of these cases subject to initial conditions $x_0 \equiv x\left(t = 0\right)$ and $v_0 \equiv \left(t = 0\right)$ of the impurity in the BEC frame

and then convert the trajectory back to motion in the lab frame. The resulting lab frame trajectories are:

$$x_{L,Un}(t) = c_{1,Un}\cos(\omega t + c_{2,Un})\, e^{-\gamma t} + g\cos(\omega_B t + \varphi) \tag{4.7}$$

$$x_{L,Cr}(t) = (c_{1,Cr} + c_{2,Cr}t)\, e^{-\gamma t} + g\cos(\omega_B t + \varphi) \tag{4.8}$$

$$x_{L,Ov}(t) = \left(c_{1,Ov}e^{\nu t} + c_{2,Ov}e^{-\nu t}\right) e^{-\gamma t} + g\cos(\omega_B t + \varphi) \tag{4.9}$$

where we have defined

$$\omega = \sqrt{\omega_0^2 + \beta - \gamma^2} \tag{4.10}$$

$$\nu = \sqrt{\gamma^2 - \omega_0^2 - \beta} \tag{4.11}$$

$$d = \frac{(\omega_B^2 - \omega_0^2)\, B_0}{\sqrt{\left(\omega_0^2 + \beta - \omega_B^2\right)^2 + 4\gamma^2\omega_B^2}} \tag{4.12}$$

$$\delta = \arctan\left(\frac{2\gamma\omega_B}{\omega_B^2 - \omega_0^2 - \beta}\right) \tag{4.13}$$

$$g = \sqrt{d^2 + B_0^2 + 2dB_0\cos\delta} \tag{4.14}$$

$$\varphi = \arctan\left(\frac{\sin\delta}{\cos\delta + \frac{B_0}{d}}\right) \tag{4.15}$$

which all only depend on γ and β. The constants c_1 and c_2 for each case are equivalent to specifying initial conditions and are given in terms of x_0, v_0, and the above defined

quantities:

$$c_{1,Un} = \sqrt{\left(x_0 - d\cos\left(\delta\right)\right)^2 + \frac{1}{\omega_0^2 + \beta - \gamma^2}\left(v_0 + \omega_B d\sin\left(\delta\right)\right)^2} \tag{4.16}$$

$$c_{2,Un} = -1 * \arctan\left[\frac{1}{\sqrt{\omega_0^2 + \beta - \gamma^2}}\frac{v_0 + \omega_B d\sin\left(\delta\right)}{x_0 - d\cos\left(\delta\right)}\right] \tag{4.17}$$

$$c_{1,Cr} = x_0 - d\cos\left(\delta\right) \tag{4.18}$$

$$c_{2,Cr} = \gamma x_0 + v_0 + \omega_B d\sin\left(\delta\right) - \gamma d\cos\left(\delta\right) \tag{4.19}$$

$$c_{1,Ov} = \frac{1}{2\nu}\left[\left(\nu + \gamma\right)\left(x_0 - d\cos\left(\delta\right)\right) + \left(v_0 + \omega_B d\sin\left(\delta\right)\right)\right] \tag{4.20}$$

$$c_{2,Ov} = \frac{1}{2\nu}\left[\left(\nu - \gamma\right)\left(x_0 - d\cos\left(\delta\right)\right) - \left(v_0 + \omega_B d\sin\left(\delta\right)\right)\right] \tag{4.21}$$

We only need parameters β and γ as well as initial conditions x_0 and v_0 to completely determine the solution. The parameters ω_0, ω_B, and B_0 are specified by the experimental set-up. At extremely weak interactions, the impurity initially oscillates at the bare impurity trap frequency ω_0. We therefore expect to be in the underdamped case at weak interactions with β and γ approximately equal to zero. As we move to stronger interactions, either β,γ, or both will increase and if we achieve locking, we are left with the $g\cos\left(\omega_B t + \varphi\right)$ part of the trajectory. Here, the angle φ gives the phase delay of the impurity behind the BEC's oscillation.

4.3 Summary

We have found that the Cherenkov physics discussed in Chap. 3 can play a prominent role in common ultra-cold atom experimental protocols involving finite momentum impurities immersed in a weakly interacting BEC. An understanding of these effects can give guidance on designing more effective experimental protocols to probe quasiparticle properties like effective mass as well as quasiparticle breakdown. In one such protocol where an external force is applied to dynamically measure a polaron's effective mass, we see accurate results when the impurity is kept subsonic and interactions with the BEC are relatively weak. When impurities are supersonic, the polaron quasi-

particle picture becomes invalid and it remains unclear how a renomarlized impurity mass can be meaningfully defined, as discussed in [325]. In this protocol, impurities that are driven to be supersonic exhibit dissipation that introduces measurement errors. For strong interactions, even when the impurity is kept subsonic, non-adiabatic effects can introduce errors in the effective mass measurement. Therefore impurities must be kept sufficiently cold and slow in such protocols to extract meaningful results.

The other experimental protocol we discussed is to induce dipole oscillations of the BEC and examine the dynamics of the impurity. We see that such oscillations with amplitudes on the order of the BEC's width can drive the impurity to be supersonic; dissipation due to phonon emission is then sufficient to cause the impurity to lock onto the motion of the BEC for strong enough interactions. When the spatial variation of the BEC density becomes visible to the impurity (as is the case in usual experiments), the impurity picks up additional frequencies in it's trajectory aside from just the drive of the BEC's oscillation. For negative scattering lengths, we see a frequency corresponding to the mean-field potential that gets increasingly red-shifted as interaction strength is increased; this is a signature of mass-renormalization of the impurity. For positive scattering lengths, we see stable locking of the impurity onto an edge of the BEC; this is related to a vanishing phase space available to the impurity and is connected to a breakdown of the polaron picture. Dipole oscillation experiments may therefore be a more robust probe of both quasiparticle quantities like the effective mass as well as quasiparticle breakdown.

Ultra-cold atom experiments such as those discussed in this section have the tantalizing possibility of probing quasiparticles in Bose-Fermi mixtures as we transition from a very dilute minority gas, where we consider single impurity atoms, to gases with equal densities. While each limit is theoretically tractable, described by single polaron physics and hydrodynamics respectively, the intermediate regime is difficult to analyze. Experiments would be able to shed unique insight in this regime, including, for example, systems where quasiparticles start to interact with each other.

Part III

Dynamics of open systems: Dissipative spin chains

Chapter 5

Introduction

Closed quantum many-body systems such as the Bose-Fermi mixtures of Chap. 3 model settings where we can neglect the interaction between the degrees of freedom of interest and other degrees of freedom belonging to the environment around the system. In many cases, however, including platforms being developed for quantum technologies such as computing and sensing, this interaction significantly influences the dynamics of the system. Coupling between such 'open' systems and their environment induces dissipation, which often causes a loss of entanglement between the degrees of freedom, and quantum information in the system more broadly, via dephasing and decoherence.

While dissipation usually decoheres the system, it can also be used to prepare correlated quantum states with interesting phenomenology or utility as a resource for quantum information processing [92, 107, 362, 93, 155, 52]. Compared to the conventional use of unitary processes to manipulate a system, the irreversiblity of dissipative dynamics makes it more robust to variations in the initial state and allows for simpler control protocols. The advent of quantum simulators opens up the opportunity to study dissipative dynamics in many-body systems in a controllable fashion, while developing the ability to engineer dissipation to produce scientifically interesting phenomenology or technologically useful quantum resources.

Realizing the potential of such dissipation engineering, however, has been challenging, with experiments thus far using a combination of unitary operations and

dissipation to produce and stabilize entangled states of a small number of qubits [22, 220, 228]. Purely non-unitary preparation of correlated states typically requires dissipation that is non-local in space and can lock the phases of two or more adjacent particles [92]. Correlations generated by such dissipation, even with spatial profiles involving only neighboring particles, can endow a system with exotic character such as non-trivial topological properties [93, 21, 20, 165, 353], quantum critical points without equilibrium counterparts [107, 153, 236, 240], and integrability revival in the presence of a drive [202, 296]. Investigating the dynamics of correlations in many-body systems with non-local dissipation is therefore a promising way to gain insight, for example, into the growth of quantum fluctuations and entanglement in open systems [67, 56, 166].

Before discussing correlations in open systems, however, it is helpful to calibrate ourselves using the extensive literature on correlation dynamics in closed systems. In integrable closed many-body systems, correlations are paradigmatically understood to spread due to entangled pairs of quasiparticles in an initial non-equilibrium state: excitations travel at a finite velocity across the system, with quantum information thereby spreading in a linear light-cone [56, 247, 57, 67, 257, 3]. Such behavior is ubiquitous in generic short-range interacting systems [219] unless the propagation of quantum information is suppressed by slow dynamics or ergodicity breaking [7, 1, 89, 314, 379, 308, 318, 361, 340, 186, 213].

Systems with long-range interactions circumvent the constraints imposed by locality and permit remote degrees of freedom to build up correlations which respect only a milder notion of causality [147, 149, 176, 108, 364, 130, 117, 249, 55, 212, 112, 354, 355]. Specifically, in such systems, the effect of a local perturbation does not generally decay exponentially fast outside a linear light-cone. This feature makes long-range interactions an important ingredient in several theoretical and experimental topics of current interest, such as fast quantum-state transfer [111, 354] and fast scrambling dynamics [145, 26]. Additionally, the cooperative nature of dynamics in long-range interacting systems earns them a special place in the realization of exotic nonequilibrium states of matter [209, 307, 229].

Both short- and long-range interactions with variable strengths can be realized in several atomic and molecular platforms [36, 375, 298, 381, 262, 194, 87], as well as in optical platforms for simulating quantum many-body physics such as photonic waveguide, circuit QED, and cavity QED systems [35, 231, 215, 157, 359, 129, 352, 128, 106, 132, 239, 162, 156, 84, 270, 115, 222, 185, 208, 201, 357, 271, 356, 238, 192, 258]. Photonic or atomic losses are an essential aspect of these platforms, thus requiring coherent and dissipative dynamics to be treated on the same footing. These quantum simulators therefore provide a fitting setting to study correlation dynamics originating from both coherent and dissipative processes.

The case of correlations spreading due to variable range coherent interactions, and the effect of local and collective dissipation on said correlations, has been addressed in a number of platforms at the interface of condensed matter and many-body quantum optics [241, 53, 30, 15, 242, 371, 223, 277, 278]. The case of correlations spreading due to analogous non-local dissipative processes, however, is more poorly understood. Experimental implementations of non-local dissipation with long-range spatial profiles have been proposed in atomic platforms [273, 276], but with limited tunability of the profile, and thereby of the generated correlations and accessible effects. For example, dissipation with a power-law spatial profile may enable the realization of exotic phenomena such as purely non-unitary many-body quantum synchronization [51, 50] or novel non-equilibrium critical states that would be otherwise inaccessible [94]. The ability to easily tune the spatial profile of dissipative channels would therefore open new avenues and applications of dissipation engineering.

In this part of the thesis, we explore how quantum simulators can be used to study the dynamics of correlations generated by dissipation with a widely tunable spatial profile. First, in Chap. 6, we show how a variable spatial profile non-local dissipation channel can be implemented using a cavity-QED quantum simulator. Specifically, we show how a system of cold atoms trapped inside a single-mode optical cavity can be used to simulate a spin chain with effective dynamics described by such a channel. Spatially correlated dissipation naturally arises in atomic ensembles, where it manifests as cooperative phenomenon such as superradiance and subradi-

ance [12, 150]. These ensembles can be geometrically controlled to selectively emit into specified modes by tuning the mean atomic separation with respect to the photon wavelength [338, 244]. The tunability of correlated emission considered in Chap. 6, realized using a magnetic field gradient and a Raman drive with appropriately chosen sideband frequencies, can be considered a synthetic version of the geometric control in atomic ensembles. Cavity QED platforms with this synthetic control therefore allow us to study the non-equilibrium dynamics of quantum correlations beyond conventional cooperative emission phenomenon.

In Chap. 7, we present the formalism of nonequilibrium spin wave theory extended to dissipative systems, and derive equations of motion for any translationally-invariant spin chain undergoing a combination of coherent and dissipative dynamics when the dissipation can be described via Lindblad channels. This formalism constitutes the methodological core of this part of the thesis and is used to analyze the correlation dynamics of the dissipative spin chain of interest in Chap. 8. We study non-local dissipation with both short- and long-range spatial profiles, and find that the system exhibits novel spatio-temporal correlation patterns which we compare to dynamics generated by spin-exchange Hamiltonians with similar interaction profiles in unitary quantum simulators.

Furthermore, we investigate how the behavior of this dissipative channel can be modulated via a uniform external field, implemented either directly with a magnetic field or effectively using an optical field, for dissipation engineering applications. We find that control over the spatial profile and uniform field can be exploited to engineer the profile of correlations in the system, which we show by tailoring the spatio-temporal window over which correlations are present, creating oscillating packets of correlations, and sending the system towards an increasingly squeezed state. The ability to shape correlations enables the manipulation of entanglement dynamics, which we demonstrate by generating entanglement that preferentially enhances metrological sensitivity to a desired spatial mode of an external field.

The work in this part of the thesis, corresponding to Refs. [319] and [320], explores how quantum simulators can be used to study the correlation dynamics of open

many-body quantum systems and compares them with the established paradigm of correlation spreading in closed systems. We also take a step towards utilizing non-local dissipation in quantum simulators to engineer the far-from-equilibrium dynamics of quantum information, with potential applications in quantum metrology, state preparation, and transport.

Chapter 6

Cavity-QED implementation

In this chapter, we show how to implement a non-local dissipation channel using an analog quantum simulator consisting of cold atoms trapped in a single-mode optical cavity. Specifically, we engineer a simulator for the dynamics of a translationally-invariant, one-dimensional many-body quantum spin system (spin chain) undergoing both unitary dynamics and Markovian dissipation with an arbitrary spatial profile. Such interacting spin systems serve as paradigmatic models of magnetic materials and are also relevant to a range of other condensed matter systems [168]. The far-from-equilibrium dynamics and transport in many such systems is still not fully understood, and can be hard to analyze theoretically depending on how strongly correlated the system becomes. Non-local dissipation channels that generate correlations can make the dynamics richer a the cost of increasing the analysis difficulty. Cold atom quantum simulators provide a natural platform to study dynamics in these systems, thereby granting insight into how non-local dissipation can be used to generate novel physics or as a resource for metrological applications.

The state of the system, ρ, evolves according to the quantum master equation in Lindblad form

$$\dot{\rho} = i\left[\rho, \hat{H}\right] + \kappa \sum_{n,m} f_{n,m}\left(\hat{L}_n \rho \hat{L}_m^\dagger - \frac{1}{2}\left\{\hat{L}_m^\dagger \hat{L}_n, \rho\right\}\right), \tag{6.1}$$

where $\hat{H}$ is the Hamiltonian characterizing unitary evolution, $\hat{L}_n$ is the jump operator

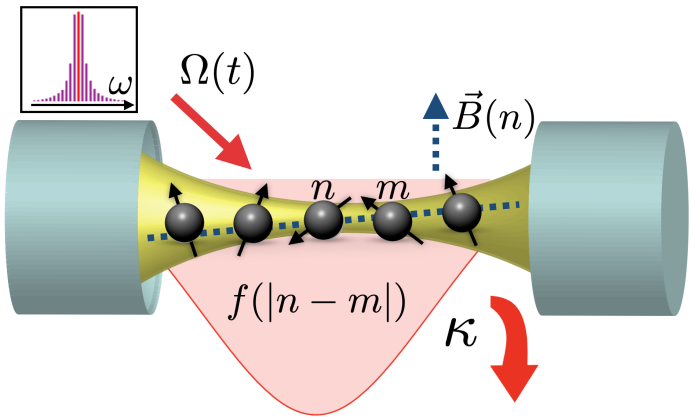

Figure 23: Experimental realization. Spin degrees of freedom are encoded in the internal states of atoms trapped in a leaky optical cavity. A magnetic field gradient, $\mathbf{B}(n)$, and a classical Raman beam, $\Omega(t)$, with multiple sidebands (inset) are used to generate a desired spatial profile, $f(|n-m|)$, of non-local dissipation.

characterizing the loss channel, and $n, m = 1...N$ index the sites of the chain. Here, $f_{n,m}$ is the spatial profile of the dissipation and only depends on the difference $|n-m|$. Independent dissipation, corresponding to $f_{n,m} = \delta_{n,m}$, and collective dissipation, corresponding to $f_{n,m} = 1$, are the two commonly considered scenarios. The former is a common source of decoherence in experiments, while the latter can generate collective entanglement useful for quantum metrology [261, 343, 189, 179, 82, 297, 177]. Both these loss channels are spatially homogeneous and therefore cannot cause correlations to spread in space.

The case of tunably non-local dissipation can be understood as interpolating between independent and collective loss. For example, consider a short-range spatial profile, $f_{n,m} = e^{-|n-m|/\chi}$, where χ is the length scale of the profile. If the system is comprised of atoms coupled to a common cavity mode, with dissipation arising from photons leaking out of the cavity, detection of a leaked photon does not allow one to discern which specific atom emitted the photon. Instead, such a photon can only be traced back to a neighborhood of atoms comprised of approximately χ sites. As χ is decreased or increased, we recover independent and collective dissipation respectively.

Figure 23 schematically depicts how to realize non-local dissipation of spin-1/2 systems using cold atoms trapped in a single-mode optical cavity. The spin states

are encoded in the hyperfine levels of the atoms and the cavity photon mode allows the atoms to communicate with each other, through both coherent interactions and non-local dissipation. There are three key components to this construction. First, a magnetic field gradient makes the energy of the hyperfine levels site-dependent and thereby endows the system with spatial resolution [27, 358, 271]. Second, a classical Raman beam with multiple sidebands provides control over atomic transitions between different spin states [162, 27]. The frequencies of the sidebands can be chosen so that communication between atoms via the cavity mode only depends on the distance between atoms, thereby enforcing translational invariance. The amplitudes of the sidebands determine the rate of internal atomic transitions and dictate the likelihood that two atoms a fixed distance apart communicate with each other, thereby setting the spatial profile of the dynamical channel. Third, cavity photon losses are large enough that the coherent spin-exchange contribution to dynamics is negligible and only dissipative dynamics remains. The three ingredients described above can be used to construct non-local dissipation channels with a variety of jump operators $\hat{L}_n$. Experiments will generally suffer from additional local dissipation arising from spontaneous scattering of individual atoms into free space; we derive conditions for the robustness of our set-up to such losses in Sec. 6.3.

6.1 Non-local losses

Here, we give an experimental construction of a non-local dissipator corresponding to a $\hat{L}_n = \hat{S}_n^-$ loss channel with a translationally invariant spatial profile $f(|n-m|)$, as described in Eq. 6.1. Our proposal is motivated by experiments employing clouds of ^{87}Rb atoms coupled to a single photon mode in an optical cavity. In previous works, the cavity mode can be employed as a resource to mediate spin-exchange coherent interactions among the atoms [84, 85], which can be accompanied by collective dissipation depending on the cooperativity of the cavity. Here we work in a complementary limit and engineer incoherent spin emission with spatial resolution. The premise of our construction is to take a chain of atoms, each with three hyper-

fine levels out of which two are degenerate, trap them inside an optical cavity, and then apply a magnetic field gradient and a Raman beam to the system with several sidebands of tunable frequency and amplitude (see Ref. [162] for a related implementation in photonic waveguides). The magnetic field gradient splits the degeneracy of each atom such that its energy levels form a Λ-configuration; the energies are site-dependent and make the atoms spatially distinct. The Raman beam couples one leg of the Λ-configuration, while the cavity mode couples the other. The cavity mode mediates communication between atoms at different sites, allowing for both coherent atom-atom interactions as well as indistinguishable atomic losses. The choice of frequencies and amplitudes of the sidebands comprising the Raman beam dictates the probability that atoms at different sites communicate with each other through the cavity photon, thereby setting the spatial profile which shapes both coherent interactions and losses. If the cavity is made to be sufficiently leaky, the coherent interactions are washed out and only dissipative dynamics with the desired spatial profile remains.

We now give a detailed construction of the experimental implementation. We consider a one-dimensional chain of N atoms labeled by lattice index $n = 1, .., N$. Each atom has two internal states $|\tilde{g}\rangle_n$ and $|e\rangle_n$. The state $|\tilde{g}\rangle_n$ belongs to a degenerate hyperfine manifold which, under application of an external field, splits as $|\tilde{g}\rangle_n \rightarrow \{|s\rangle_n, |g\rangle_n\}$. We encode the spin 1/2 Hilbert space $\{|\uparrow\rangle_n, |\downarrow\rangle_n\}$ in this ground state manifold. We take $|s\rangle_n$ to be the lower energy state and set its energy to zero without loss of generality. The energy difference between $|s\rangle_n$ and $|g\rangle_n$ is given as $\omega_{g,n}$ and we will refer to the energy difference between $|s\rangle_n$ and $|e\rangle_n$ as $\omega_{e,n}$. These energies are position dependent since they inherit spatial dependence from the external applied magnetic field gradient. In terms of the operators $\hat{\sigma}^n_{ab} = |a\rangle_n \langle b|_n$, with $a, b \in \{s, g, e\}$, the bare atomic Hamiltonian reads

$$\hat{H}_{\mathrm{a}} = \sum_n \left(\omega_{e,n}\hat{\sigma}^n_{ee} + \omega_{g,n}\hat{\sigma}^n_{gg}\right). \tag{6.2}$$

We now dipole-couple the states $|s\rangle_n$ and $|e\rangle_n$ using a Raman driving field $\tilde{\Omega}(t) =$

$\sum_{\alpha=0}^{m_p-1} \Omega_\alpha e^{i\omega_\alpha t}$ where ω_α represents each of the m_p different drive frequencies and Ω_α represents the Rabi frequency (beam amplitude) associated with those frequencies. We can define the frequency $\omega_L \equiv \omega_{\alpha=0}$ as the main frequency and rewrite the driving field in terms of the detunings $\tilde{\omega}_\alpha \equiv \omega_\alpha - \omega_L$ as $\tilde{\Omega}(t) = \Omega(t) e^{i\omega_L t}$ where $\Omega(t) \equiv \sum_{\alpha=0}^{m_p-1} \Omega_\alpha e^{i\tilde{\omega}_\alpha t}$. Note that $\tilde{\omega}_\alpha = 0$ by definition. The dipole coupling between $|s\rangle_n$ and $|e\rangle_n$ is then described by the Hamiltonian

$$\hat{H}_{\mathrm{d}} = \sum_n \left(\frac{\Omega(t)}{2} e^{i\omega_L t} \hat{\sigma}_{se}^n + \frac{\Omega^*(t)}{2} e^{-i\omega_L t} \hat{\sigma}_{es}^n \right). \tag{6.3}$$

We now consider an optical cavity mode that dipole couples $|g\rangle_n$ and $|e\rangle_n$. The photon mode, represented by the operator $\hat{a}$, has a frequency ω_c and couples to atom n through the single-photon coupling g. The bare photon Hamiltonian and the light-matter coupling between atoms and photons are given respectively by

$$\hat{H}_{\mathrm{p}} = \omega_c \hat{a}^\dagger \hat{a}, \tag{6.4}$$

$$\hat{H}_{\mathrm{lm}} = \sum_n \left(g \hat{a} \hat{\sigma}_{eg}^n + g^* \hat{a}^\dagger \hat{\sigma}_{ge}^n \right). \tag{6.5}$$

The total density matrix of the system has dynamics given by the quantum master equation in Lindblad form

$$\frac{d}{dt}\rho = -i \left[\hat{H}, \rho \right] + \mathcal{D}_{\mathrm{leak}}(\rho). \tag{6.6}$$

The last term is the dissipator corresponding to photon losses occurring with rate γ

$$\mathcal{D}_{\mathrm{leak}}(\rho) = \gamma \left(\hat{a}^\dagger \rho \hat{a} - \frac{1}{2} \left\{ \hat{a}\hat{a}^\dagger, \rho \right\} \right). \tag{6.7}$$

When the excited state $|e\rangle$ is largely detuned by $\Delta = |\omega_e - \omega_L|$ from the other atomic and photonic energy scales ($\Delta \gg \Omega_\alpha, g$), one can use a Schrieffer-Wolf transformation to eliminate the state and write an effective Hamiltonian for the remaining atomic Hilbert space. The light-matter interaction coupling at leading order in $1/\Delta$ then

becomes

$$\hat{H}_{\rm lm} = -\sum_n (\frac{g\Omega\left(t\right)}{\Delta}\hat{a}\hat{\sigma}^n_{sg}e^{i(\omega_L-\omega_c-\omega_{g,n})t} + \frac{g^*\Omega^*\left(t\right)}{\Delta}\hat{a}^\dagger\hat{\sigma}^n_{gs}e^{-i(\omega_L-\omega_c-\omega_{g,n})t}). \tag{6.8}$$

Defining, $\eta_\alpha \equiv \frac{\Omega_\alpha g}{\Delta}$ and $\delta_{\alpha,n} \equiv \omega_\alpha - \omega_{g,n} - \omega_c$, the interaction Hamiltonian can be written as

$$\hat{H}_{\rm lm} = -\sum_{n,\alpha}\left[\eta_\alpha\hat{a}\hat{\sigma}^n_{sg}e^{i\delta_{\alpha,n}t} + h.c.\right]. \tag{6.9}$$

The cavity mode mediates communication between atoms. We now assume that the cavity photon loss is large enough that

$$\gamma \gg \eta_\alpha, \quad \gamma \gg \delta_{\alpha,n}, \tag{6.10}$$

and therefore the cavity photon loss occurs on a timescale much faster than the effective dynamics of the spins. The light field can then be adiabatically eliminated and becomes enslaved to atomic operators [2]. The Heisenberg evolution of the light field can then be expanded in powers of ϵ, with $\epsilon = \eta_\alpha/\gamma$ or $\epsilon = \delta_{\alpha,n}/\gamma$:

$$\hat{a}\left(t\right) = i2\sum_{n,\alpha}\left(\frac{\eta^*_\alpha}{\gamma}\hat{\sigma}^n_{gs}e^{-i\delta_{\alpha,n}t}\right) + 2\sum_{n,\alpha}\left(\frac{\delta_{\alpha,n}\eta^*_\alpha}{\gamma^2}\hat{\sigma}^n_{gs}e^{-i\delta_{\alpha,n}t}\right) + \mathcal{O}\left(\epsilon^3\right), \tag{6.11}$$

Before using the above expression to replace the light field in the full Lindblad equation, Eq. (6.6), we can gain insight into the effective dynamics of the system after elimination of the light field by performing this substitution for the equation of motion of a single spin operator:

$$\frac{d}{dt}\hat{\sigma}^n_{gs} = i\hat{a}\ \hat{\sigma}^n_z\sum_\alpha\eta_\alpha e^{i\delta_{\alpha,n}t} \rightarrow -\hat{\sigma}^n_z\sum_{m,\alpha,\beta}\left(\gamma_{\rm eff}\right)_{\alpha,\beta}\left(1 - i\frac{\delta_{\beta,m}}{\gamma}\right)e^{i(\delta_{\alpha,n}-\delta_{\beta,m})t}\hat{\sigma}^m_{gs} + \mathcal{O}\left(\epsilon^3\right), \tag{6.12}$$

where we have defined $\left(\gamma_{\rm eff}\right)_{\alpha,\beta} \equiv 2\eta^*_\alpha\eta_\beta/\gamma$. We see that the motion of the $n^{\rm th}$ atom is conditioned by the motion of the $m^{\rm th}$ one, with $\left(\gamma_{\rm eff}\right)_{\alpha,\beta}$ setting the effective coupling

rate. The leading order contribution to the motion is dissipative dynamics with rate $(\gamma_{\text{eff}})_{\alpha,\beta}$, with the subleading contribution being coherent dynamics with frequency $(\gamma_{\text{eff}})_{\alpha,\beta}\frac{\delta_{\beta,m}}{\gamma}$. When the effective coupling constant, $(\gamma_{\text{eff}})_{\alpha,\beta}$, is much smaller than the minimum detuning between the atomic transition frequencies, we can ignore the off-resonant couplings and only consider the interaction between atoms n and m for which $\delta_{\alpha,n} - \delta_{\beta,m} = 0$. Specifically, we require

$$(\gamma_{\text{eff}})_{\alpha,\beta} \ll \min\{\delta_{\alpha,n} - \delta_{\beta,m}\}, \tag{6.13}$$

where the minimization means the smallest nonzero value of $\delta_{\alpha,n} - \delta_{\beta,m}$. Formally, Eq. (6.13) is derived by taking the long time average of (6.12), and then applying the Sokhotski–Plemelj lemma to extract the singular part of the time integral (resonant process) and the regular part (off-resonant processes). The contribution of the off-resonant term becomes negligible when the condition (6.13) is satisfied (see Ref. [162]). We can then safely restrict the dynamics to the resonance shell $\delta_{\alpha,n} = \delta_{\beta,m}$, which can be restated as

$$\omega_{g,m} - \omega_{g,n} = \tilde{\omega}_\beta - \tilde{\omega}_\alpha. \tag{6.14}$$

In order to introduce spatial addressability in the system, we choose the site-dependent energy shifts as $\omega_{g,n} = \mu n$, which is implemented via an externally imposed linear magnetic field. We also choose the sideband detunings as $\tilde{\omega}_\alpha = \mu\alpha$. After our choice of sideband detunings, the resonance condition Eq. (6.14) reads

$$(\alpha - \beta) = (n - m)\,. \tag{6.15}$$

This selection rule makes pairs of atoms at distance $n - m$ apart interact. The dynamics of a single spin, given by Eq. 6.12, then becomes

$$\frac{d}{dt}\hat{\sigma}^n_{gs} \approx\!\!\rightarrow -\hat{\sigma}^n_z \sum_{m,\beta} (\gamma_{\text{eff}})_{\beta+(n-m),\beta} \left(1 - i\frac{\delta_{\beta,m}}{\gamma}\right) \hat{\sigma}^m_{gs}, \tag{6.16}$$

and we see that the effective coupling rate, $(\gamma_{\text{eff}})_{\beta+(n-m),\beta}$, depends only on the dis-

tance between atoms n and m. The leading order term, corresponding to dissipative dynamics, is therefore translationally invariant. The subleading coherent term, proportional to $\delta_{\beta,m}/\gamma$, however, does have explicit position dependence. We note that if the condition in Eq. (6.13) is violated, then atoms on multiple sites can communicate and even the dissipative dynamics will not be translationally invariant.

We now perform this same adiabatic elimination of the cavity photon on the full Lindblad equation, Eq. (6.6), by replacing $\hat{a}$ with the expression in Eq. (6.11). Keeping terms up to $\mathcal{O}(\epsilon^2)$ in Eq. (6.11), the dissipator given by Eq. (6.7) becomes

$$\mathcal{D}_{\text{leak}}(\rho) \approx 2 \sum_{n,m,\alpha,\beta} (\gamma_{\text{eff}})_{\alpha,\beta} \left(1 + i\frac{(\delta_{\alpha,n} - \delta_{\beta,m})}{\gamma}\right) \times \\ \times e^{i(\delta_{\alpha,n}-\delta_{\beta,m})t} \left(\hat{\sigma}^m_{gs}\rho\hat{\sigma}^n_{sg} - \frac{1}{2}\left\{\hat{\sigma}^n_{sg}\hat{\sigma}^m_{gs}, \rho\right\}\right), \quad (6.17)$$

while the coherent light-matter interaction, given by Eq. (6.9), becomes

$$\hat{H}_{\text{lm}} \approx -i2 \sum_{n,m,\alpha,\beta} (\gamma_{\text{eff}})_{\alpha,\beta} e^{i(\delta_{\alpha,n}-\delta_{\beta,m})t} \left(\hat{\sigma}^n_{sg}\hat{\sigma}^m_{gs} - \hat{\sigma}^n_{sg}\hat{\sigma}^m_{gs}\right) \\ - 2 \sum_{n,m,\alpha,\beta} (\gamma_{\text{eff}})_{\alpha,\beta} \frac{\delta_{\beta,m}}{\gamma} e^{i(\delta_{\alpha,n}-\delta_{\beta,m})t} \hat{\sigma}^n_{sg}\hat{\sigma}^m_{gs}. \quad (6.18)$$

We see that the first term in the above equation vanishes and we are left with

$$\hat{H}_{\text{lm}} \approx -2 \sum_{n,m,\alpha,\beta} (\gamma_{\text{eff}})_{\alpha,\beta} \frac{\delta_{\beta,m}}{\gamma} e^{i(\delta_{\alpha,n}-\delta_{\beta,m})t} \hat{\sigma}^n_{sg}\hat{\sigma}^m_{gs}. \quad (6.19)$$

The master equation for the density matrix describing the system can thus be written as

$$\frac{d}{dt}\rho \approx 2 \sum_{n,m,\alpha,\beta} (\gamma_{\text{eff}})_{\alpha,\beta} \left(1 + i\frac{(\delta_{\alpha,n} - \delta_{\beta,m})}{\gamma}\right) \times \\ \times e^{i(\delta_{\alpha,n}-\delta_{\beta,m})t} \left(\hat{\sigma}^m_{gs}\rho\hat{\sigma}^n_{sg} - \frac{1}{2}\left\{\hat{\sigma}^n_{sg}\hat{\sigma}^m_{gs}, \rho\right\}\right) \\ + i2 \sum_{n,m,\alpha,\beta} (\gamma_{\text{eff}})_{\alpha,\beta} \frac{\delta_{\beta,m}}{\gamma} e^{i(\delta_{\alpha,n}-\delta_{\beta,m})t} \left[\hat{\sigma}^n_{sg}\hat{\sigma}^m_{gs}, \rho\right]. \quad (6.20)$$

If the condition Eq. (6.13) is satisfied, then we can restrict dynamics to the resonance shell defined by Eq. (6.14) and the resulting Lindblad equation is

$$\frac{d}{dt}\rho \approx \left(\frac{4|g|^2\Omega_M^2}{\gamma\Delta^2}\right)\sum_{n,m} f_{n,m}\left(\hat{\sigma}_{gs}^m\rho\hat{\sigma}_{sg}^n - \frac{1}{2}\left\{\hat{\sigma}_{sg}^n\hat{\sigma}_{gs}^m,\rho\right\}\right) + \\ + i\left(\frac{4|g|^2\Omega_M^2}{\gamma\Delta^2}\right)\sum_{n,m}\left[\tilde{f}_{n,m}\hat{\sigma}_{sg}^n\hat{\sigma}_{gs}^m,\rho\right] \quad (6.21)$$

where

$$f_{n,m} = \sum_{(\alpha,\beta);(\alpha-\beta)=(n-m)}\frac{\Omega_\alpha\Omega_\beta^*}{\Omega_M^2} \\ \tilde{f}_{n,m} = \sum_{(\alpha,\beta);(\alpha-\beta)=(n-m)}\frac{\delta_{\beta,m}}{\gamma}\frac{\Omega_\alpha\Omega_\beta^*}{\Omega_M^2}. \quad (6.22)$$

In the above equation, we define Ω_M as the largest Raman sideband amplitude and choose it as a representative scale for the drive. Note that the term in Eq. (6.20) that is proportional to $\delta_{\alpha,n}$ exactly cancels the term proportional to $\delta_{\beta,m}$ when we satisfy the two-atom resonance condition Eq. (6.14).

Collating the conditions, Eq. (6.10) and Eq. (6.13), for adiabatically eliminating the cavity photon, we have:

$$\eta_\alpha \ll \gamma, \quad \delta_{\alpha,n} \ll \gamma, \quad \frac{\eta_\alpha\eta_\beta^*}{\min\{\delta_{\alpha,n}-\delta_{\beta,m}\}} \ll \gamma. \quad (6.23)$$

Recall that in the third condition above, the denominator, $\min\{\delta_{\alpha,n}-\delta_{\beta,m}\}$, is a minimization over processes with $\delta_{\alpha,n} \neq \delta_{\beta,m}$. For any fixed η_α and $\delta_{\alpha,n}$, a sufficiently large cavity decay γ allows all three conditions to be simultaneously satisfied. Later, we show that these conditions can be consistently satisfied by providing numerical estimates using parameters from cavity QED experiments. We note that the condition $\delta_{\alpha,n} \ll \gamma$ is satisfied by choosing a large cavity decay, γ, and a non-zero $\delta_{\alpha,n}$. In fact, we require that $\delta_{\alpha,n} \neq 0$ in order to preserve spatial structure in the dynamics. We can see this by setting $\delta_{\alpha,n} = 0$ in Eq. (6.11) to get $\hat{a}(t) = i\zeta\hat{\sigma}_{gs}$ where $\hat{\sigma}_{gs} = \sum_n \hat{\sigma}_{gs}^n$ and $\zeta = \frac{2}{\gamma}\sum_\alpha \eta_\alpha^*$. Single-atom resonant processes, characterized by $\delta_{\alpha,n} = 0$, therefore

only lead to collective dissipation of all spins in the system, arising from collective emission of the cavity photon, rather than non-local dissipation with spatial structure.

Physically, we can interpret the set-up resulting in Eq. (6.21) as follows. Both non-local dissipation and coherent interactions amongst the spins are mediated by non-resonant virtual photons, corresponding to $\delta_{\alpha,n} \neq 0$, which satisfy the two-atom resonance condition $\delta_{\alpha,n} = \delta_{\beta,m}$. The spatial profile of the resulting non-local dissipation, $f_{n,m}$, is translationally invariant and represents leakage of a cavity photon without certainty about which of the two atoms, n or m, it came from. The spatial profile of the coherent interaction, $\tilde{f}_{n,m}$, represents a spin-exchange between the atoms which is suppressed by a factor $\delta_{\beta,m}/\gamma$ due to the highly lossy cavity. The conditions in Eq. (6.23) represent a regime where the cavity loss, γ, is large enough that: (i) the effective dynamics of each individual spin, occurring through a Λ-process in the atom with rate η_α, occurs slowly compared to the cavity photon loss so the photon only serves to mediate coherent interactions and non-local emission from pairs of spins, (ii) coherent interactions of the spins are suppressed, and (iii) the time-scale of the effective non-local emission from pairs of spins, set by $\tau = 1/\left(\gamma_{\text{eff}}\right)_{\alpha,\beta} \propto \gamma/\eta_\alpha^*\eta_\beta$, is slow enough that off-resonant two-atom processes ($\delta_{\alpha,n} \neq \delta_{\beta,m}$) average to zero and only the resonant two-atom process remains. This resonant two-atom process is a translationally-invariant non-local emission from pairs of atoms.

The quantity $f_{n,m} = f\left(|n-m|\right)$ only depends on the difference $n-m$ and sets the spatial profile of the non-local dissipation. We can design the desired translationally-invariant profile $f_{n,m} = f\left(|n-m|\right)$ of the dissipator by exactly solving $f\left(|n-m|\right) = \sum_{(\alpha,\beta);(\alpha-\beta)=(n-m)} \Omega_\alpha \Omega_\beta^*/\Omega_M^2$. Later, we explicitly show how to numerically invert this equation. Defining $\kappa = |g|^2\,\Omega_M^2/(\gamma\Delta^2)$ and relabeling the projection operators as $\hat{S}_n^- = \hat{\sigma}_{gs}^n/2$ and $\hat{S}_n^+ = \hat{\sigma}_{sg}^n/2$, we have

$$\frac{d}{dt}\rho \approx \kappa \sum_{n,m} f\left(|n-m|\right)\left(\hat{S}_m^-\rho\hat{S}_n^+ - \frac{1}{2}\left\{\hat{S}_n^+\hat{S}_m^-,\rho\right\}\right) + i\left[\kappa\sum_{n,m}\tilde{f}_{n,m}\hat{S}_n^-\hat{S}_m^+,\rho\right] \quad (6.24)$$

The first term in Eq. (6.24) is the desired non-local dissipation while the second term represents coherent spin-exchange interactions mediated by a virtual photon emitted

in the Λ-process within one atom and absorbed via the reverse Λ-process in a second atom a distance $|n-m|$ away [162, 27]. Comparing the expressions for $\tilde{f}_{n,m}$ and $f_{n,m}$ in Eq. (6.22), we see that the coherent dynamics are subleading to the dissipative dynamics. Therefore, when the cavity decay is large enough that $\gamma \gg \delta_{\beta,m}$, the coherent dynamics vanishes and we are left with purely dissipative dynamics with a spatial profile $f(|n-m|)$:

$$\frac{d}{dt}\rho = \kappa \sum_{n,m} f(|n-m|) \left(\hat{S}_n^- \rho \hat{S}_m^+ - \frac{1}{2} \left\{ \hat{S}_m^+ \hat{S}_n^-, \rho \right\} \right) \tag{6.25}$$

which is the non-local $\hat{L}_n = \hat{S}_n^-$ loss channel we aimed to construct. The positivity of this Lindblad map is guaranteed by the positivity of the Raman sideband amplitudes Ω_β that determine $f(|n-m|)$; we require $f(|n-m|=0) \neq 0$ to ensure a positive Lindblad map, which is violated only when all sideband amplitudes are zero and we have no dynamics.

6.2 Engineering the spatial profile

We now show how to construct a desired dissipation profile $f(|n-m|)$ by choosing the Raman sideband amplitudes $\{\Omega_\beta\}$ appropriately. In this section, we work in units where the maximum sideband amplitude is normalized to 1 ($\Omega_M = 1$). The equation we want to invert is

$$\begin{aligned} f(|n-m|) &= \sum_{\alpha,\beta;(\alpha-\beta)=(n-m)} \Omega_\alpha \Omega_\beta^* \\ &= \sum_\beta \Omega_{\beta+(n-m)} \Omega_\beta^*, \end{aligned}$$

with $r \equiv n-m$. For a system of N spins, we have $r = -(N-1), -(N-2), .., 0, ..., (N-2), (N-1)$. Recalling that $f(|n-m|) = f(r)$ is a translationally invariant profile, we have

$$f(r) = \sum_\beta \Omega_{\beta+r} \Omega_\beta^*, \tag{6.26}$$

where we will need $2N-1$ sidebands corresponding to the values that r can take; the sidebands $\{\Omega_\beta\}$ are indexed as $\beta = -(N-1), -(N-2), .., 0, ..., (N-2), (N-1)$. Note that Eq. (6.26) shows that the profile $f(r)$ is simply the discrete autocorrelation of the sideband amplitudes. We can thus make use of the convolution theorem to take the discrete Fourier transform (DFT) of both sides:

$$f(k) = |\Omega_k|^2, \tag{6.27}$$

where we define the DFT as $f(k) = \sum_r e^{-ikr} f(r)$ and $\Omega_k = \sum_\beta e^{-ik\beta}\Omega_\beta$, introducing the inverse DFT as $f(r) = \frac{1}{(2N-1)} \sum_k e^{ikr} f(k)$ and $\Omega_\beta = \frac{1}{(2N-1)} \sum_k e^{ik\beta}\Omega_k$. We know that any choice of $f(|n-m|)$ which yields a physically valid dissipator must be positive semidefinite, and therefore $f(k)$ must be real and non-negative. We can take its square root and get

$$|\Omega_k| = \sqrt{f(k)}. \tag{6.28}$$

Now, we can look for solutions with Ω_k real, thus yielding

$$\Omega_\beta = \frac{1}{(2N-1)} \sum_k e^{ik\beta} \sqrt{f(k)} \tag{6.29}$$

which are the desired sideband amplitudes. One can numerically compute these amplitudes using a fast Fourier transform and then check that the amplitudes yield the desired profile by computing their autocorrelation (Eq. (6.26)). In Fig. 24, we demonstrate this procedure for a long-range spatial profile $f(|n-m|) = \frac{1}{(|n-m|+1)^\alpha}$ and a short-range spatial profile $f(|n-m|) = e^{-|n-m|/\chi}$.

6.3 Parameter estimates

For the construction to hold, we require that the detuning, Δ, and cavity loss rate, γ, are sufficiently large. Specifically, we require that $\Delta \gg \mu N$, $\Delta \gg \omega_L - \omega_c - \omega_{g,n}$, and $\Delta \gg \Omega_M, g$. These conditions result in the excited atomic level $|e\rangle_n$ having approximately the same energy along the entire chain and only participating virtually

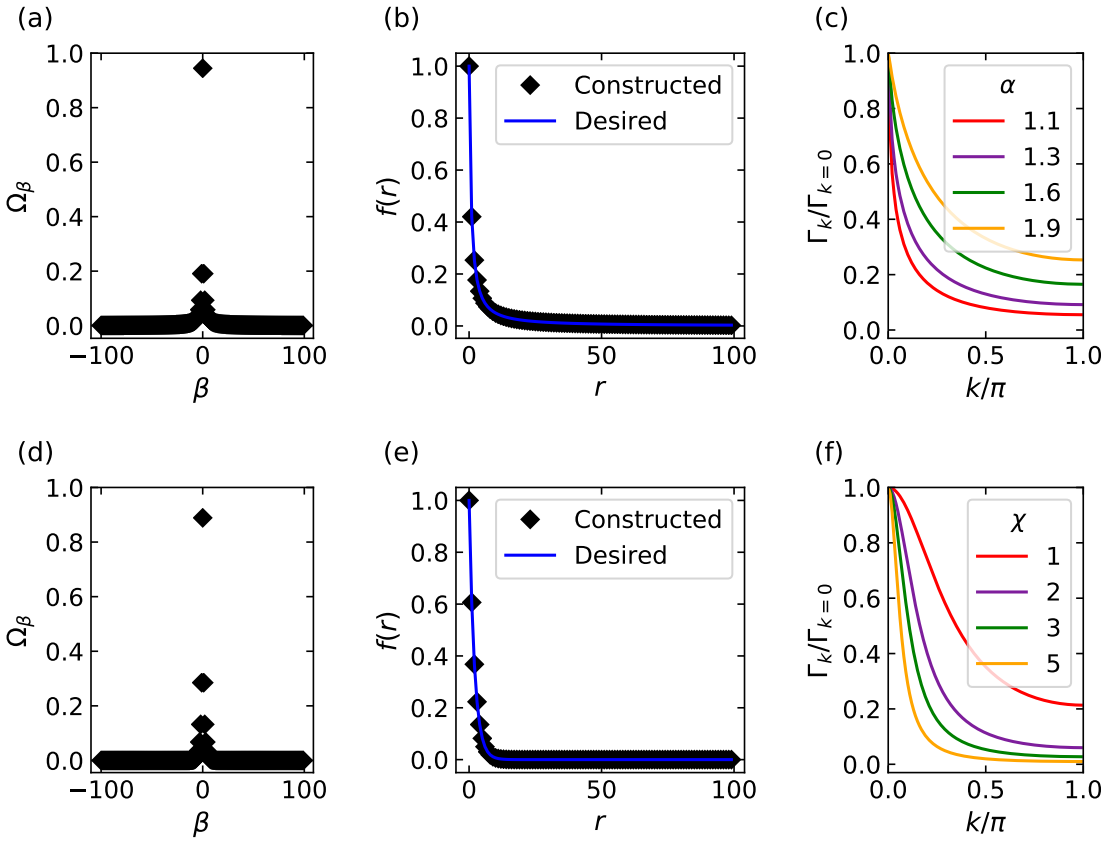

Figure 24: Sideband amplitude construction. (a) Sideband amplitudes required to construct a long-range spatial profile $f(|n-m|) = (|n-m|+1)^{-\alpha}$ on a 100 site chain. (b) Spatial profile resulting from the amplitudes in (a). (c) Fourier transform of the long-range spatial profile. (d) Sideband amplitudes required to construct a short-range spatial profile $f(|n-m|) = e^{-|n-m|/\chi}$ on a 100 site chain. (e) Spatial profile resulting from the amplitudes in (d). (f) Fourier transform of the short-range spatial profile.

in the dynamics. We also require that $\gamma \gg g\Omega_M/\Delta$ and $\gamma >> \delta_{\beta,m}$, which allow us to adiabatically eliminate the photon and suppress coherent spin-exchange interactions respectively. Lastly, we require that $\Delta^2\gamma \gg g^2\Omega_M^2/\min|\omega_{g,n} - \omega_{g,m}|$ so that only the resonant process Eq. (6.14) takes place.

Below we provide estimates for the parameters involved in the experiment of Ref. [84, 85] and show that our construction is accessible to current experimental systems. The number of lattice sites is $N \approx 100$ and it is comparable to the number of sidebands $\approx$ 50-100 in the Raman beam. The Raman beam Rabi frequency $|\Omega|$ and cavity mode coupling g range are on the order of a few MHz. The carrier fre-

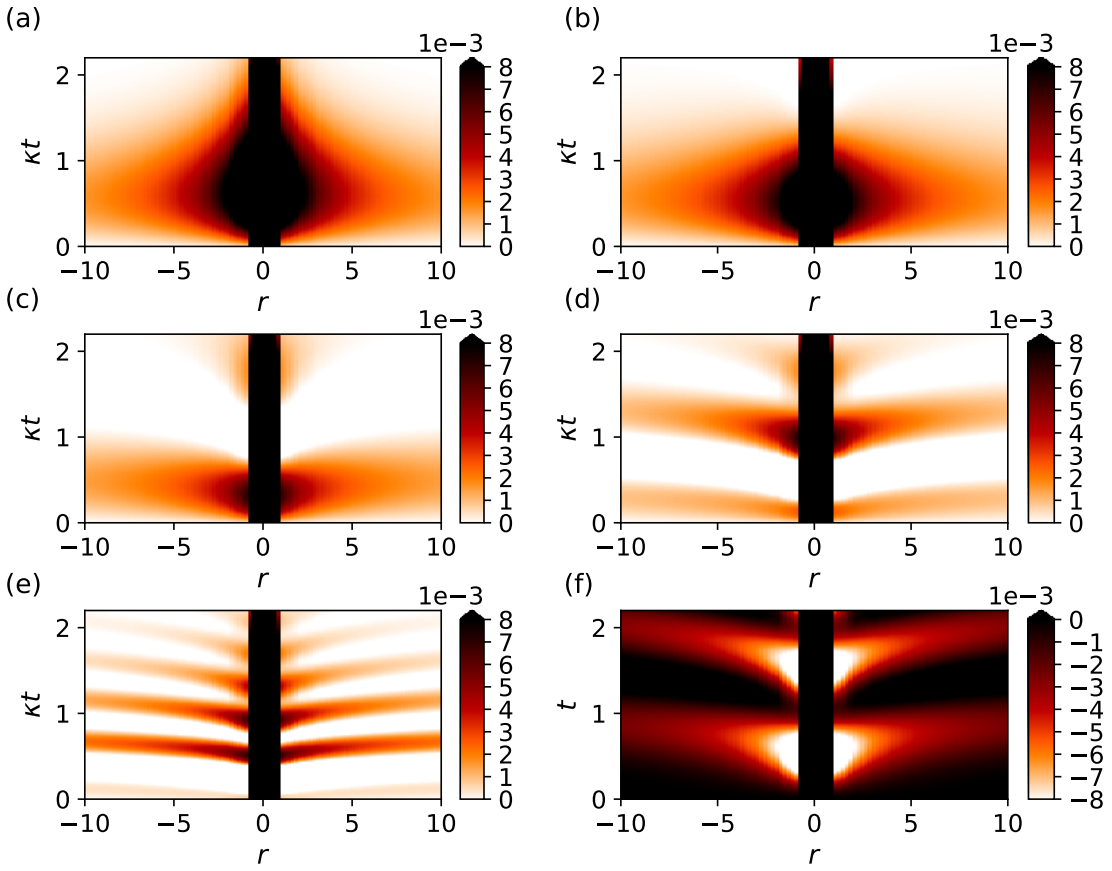

Figure 25: Crossover between dissipative and coherent dynamics. We compute the correlation function $C^{zz}(r,t)$ for a system whose dynamics is comprised of a long-range dissipation channel ($\hat{L}_n = \hat{S}_n^-$) with strength κ and a long-range spin-exchange Hamiltonian with strength η. For both generators, the spatial profile is $f(|n-m|) = (|n-m|+1)^{-\alpha}$ with $\alpha = 1.25$. The system exhibits a crossover between $\eta/\kappa = 0.25$ and $\eta/\kappa = 0.5$. (a) $\kappa = 1.0$, $\eta = 0.0$ (only dissipation). ()b) $\kappa = 1.0$, $\eta = 0.25$. (c) $\kappa = 1.0$, $\eta = 0.5$. (d) $\kappa = 1.0$, $\eta = 1.0$. (e) $\kappa = 1.0$, $\eta = 2.0$. (f) $\kappa = 0.0$, $\eta = 1.0$ (only Hamiltonian). Details on how these correlation dynamics are computed are given in Chaps. 7 and 8.

quency ω_L is $\approx$ 384THz, while the sideband frequencies of the Raman beam satisfy $\max\{|\tilde{\omega}_\alpha - \tilde{\omega}_\beta|\} \approx$ 10kHz. The Zeeman splitting $\omega_{g,n} = \mu n$ on each site is given by a magnetic field $\mu \cdot L \approx$ 500kHz, where L is the length of the cloud. Finally, the cavity decay γ is in the range $\approx$ 200kHz – 10 of MHz. Per these experimental parameters, we can estimate that $\mu N/\Delta \sim 10^{-5}$, $(\omega_L - \omega_c - \omega_{g,n})/\Delta \sim 10^{-4}$, $\Omega_M/\Delta \sim g/\Delta \sim 10^{-4}$, $\delta_{\beta,m}/\gamma \sim 10^{-1}$, $g\Omega_M/(\Delta\gamma) \sim 10^{-4}$, and $g^2\Omega_M^2/(\min|\omega_{g,n} - \omega_{g,m}|\,\Delta^2\gamma) \sim 10^{-1}$. The conditions for achieving the desired effective dynamics are thus satisfied.

While we should safely be able to ignore the coherent spin-exchange dynamics described in Eq. 6.24, we can further examine the robustness of our platform to subleading effects. In Fig. 25, we plot the correlation dynamics when both dissipative and coherent dynamics are present. As the relative strength of the coherent dynamics is increased, the pattern of correlations demonstrates a cross-over between the dissipative confinement pattern discussed in Sec. 8.1 and correlation fronts characteristic of a purely coherent dynamics arising from a spin-exchange Hamiltonian. The dissipative confinement pattern survives even when the coherent dynamics is one-fourth as strong as the dissipative dynamics; the experimental estimate of $\delta_{\beta,m}/\gamma \sim 10^{-1}$ is well below this threshold.

The subleading spin-exchange Hamiltonian rotates the collective spin similar to a uniform external field and one may consider using it to tune the correlation pattern. However, as the spin-exchange dynamics also inherits a spatial profile, it complicates the spread of correlations and therefore makes an inconvenient tool to engineer a desired pattern arising from the dissipative dynamics. A uniform external field cannot create any spatial correlations, and therefore acts as a simple knob that tunes dynamics arising from the dissipator.

We note that such a uniform external field requires an addition to the experimental construction. It can be implemented, for example, by shining an additional multifrequency Raman beam that directly couples the two lower atomic levels with sideband frequencies corresponding to the change in energy splittings on each site. The amplitude ω_F characterizing the strength of this effective magnetic field would be set by the Rabi frequency Ω_x of this additional Raman beam, which typically takes on values between 1kHz to 50kHz in the experiment referenced above.

Lastly, we consider the effect of local losses from spontaneous Raman scattering of the individual atoms into free space. These incoherent spin losses are present in all experiments and introduce undesired decohering effects that deplete the total magnetization of the system. Following Ref. [342], we estimate the number of spontaneous emission events after a time t as $N_\Sigma \simeq N\Sigma t\Omega_M^2/\Delta^2$, with Σ being the decay rate and N being the total number of excitations in the system. The relevant time

scale is set by the rate at which non-local dissipation generates correlations, given by $t \sim 1/\kappa \sim \gamma\Delta^2/g^2\Omega_M^2$. Correlations generated on this time scale are preserved if the number of spontaneous emission events is small compared to the number of atoms in the system: we require $N_\Sigma \ll N$. To satisfy this requirement, we need $\Sigma\gamma/g^2 \ll 1$, which together with the above stated condition of leaky cavity $\gamma \gg g\Omega_M/\Delta$, yields $\Sigma \ll (\Delta/\Omega_M)^2\gamma$. In the setup of Ref. [84, 85], we have $\Omega_M/\Delta \sim 10^{-4}$, and as both Σ and γ are typically of the order of a few MHz, correlations generated from non-local dissipation are protected against scattering into free space for a long window of time. We can alternatively combine the conditions $\Sigma\gamma/g^2 \ll 1$ and $\gamma \gg g\Omega_M/\Delta$ into $g \gg \Sigma\Omega_M/\Delta$, which states that the coupling between the atoms and the cavity mode should be strong enough that coherent cavity-mediated transitions between atomic energy levels should be much more frequent than incoherent transitions due to spontaneous emission. For the parameters of Ref. [84, 85], g and Σ are of the order of a few MHz and $\Omega_M/\Delta \sim 10^{-4}$ so this strong coupling condition is satisfied.

Chapter 7

Generalized nonequilibrium spin-wave theory

In this chapter, we derive the dissipative version of nonequilibrium spin-wave theory (NEQSWT). This formalism allows us to obtain equations of motion for the relevant observables and their correlations in translationally-invariant spin chains governed by a master equation, such as the model, Eq. (6.1). Previously, NEQSWT has been used to study the non-equilibrium dynamics of a variety of unitary systems including interacting spin chains with competing short- and long-range interactions [306, 210, 214, 286], variable-range interactions [209, 212, 211], and those coupled to a cavity mode [384]. Here, we extend the method to dissipative dynamics and derive equations of motion for any system whose dynamics is described by a combination of translationally-invariant Hamiltonians and translationally-invariant Lindblad channels. Our derivation can be used to construct equations of motion for the system constructed in Chap. 6 and investigated in Chap. 8, and more generally for any translationally-invariant spin system whose dynamics is described by a master equation. Many of the models that are either naturally realized or purposefully engineered on quantum simulation platforms fit into this class of systems [36, 29, 157, 164].

The premise of NEQSWT is to assume that the system is well-described by a time-dependent strongly polarized collective spin, with a small number of spin-wave excitations on top of the collective polarization. The motion of the collective spin and

the spin-waves are coupled, as the spin waves produce a back-reaction (or quantum feedback) that self-consistently modifies the mean-field trajectory of the collective spin. As the number of spin-waves is assumed to be small, we can treat the spins as bosons and the dynamics of the system is reduced to the motion of excitations on top of a moving "condensate". Formally, the treatment is a self-consistent time-dependent Hartree approximation of the lowest order Holstein-Primakoff expansion of the spin dynamics. The method is valid when the relevant excitations of the system are spin-waves and during the portion of dynamics in which the spin-wave population remains low. The advantage of NEQSWT is that it allows us to examine the dynamics of a thermodynamically large number of spins whenever the above two conditions are met. This typically results in control of dynamics over a time window significantly larger than what permissible with conventional low order Holstein-Primakoff expansions [6]. Compared to straightforward [230], or cluster [169], mean-field approaches, which can be unstable for driven-dissipative systems, NEQSWT can be considered a systematic improvement which enables the treatment of dissipative quantum many body dynamics using a method with a control parameter.

7.1 Types of channels

We consider translationally-invariant spin systems described by a quantum master equation constructed from a combination of three types of channels, each characterized by a spin operator of the general form

$$\hat{L}_n = c_x^{F,U,D}\hat{S}_n^x + c_y^{F,U,D}\hat{S}_n^y + c_z^{F,U,D}\hat{S}_n^z\,. \tag{7.1}$$

The coefficients $c_{x,y,z}^{F,U,D}$ take arbitrary (complex) values, which can be chosen independently in the various channels of type F, U, and D defined below. We assume $|c_x^{F,U,D}|^2 + |c_y^{F,U,D}|^2 + |c_z^{F,U,D}|^2 = 1$, so the magnitude of each channel is encoded in overall dimensionful coupling constants.

The first type of channel is unitary dynamics from a collective field generated by

the Hamiltonian

$$\hat{H}_F = \omega_F \sum_n \hat{L}_n. \tag{7.2}$$

Clearly, in order for $\hat{H}_F$ to be Hermitian, the coefficients $c^F_{x,y,z}$ appearing in the definition of operators $\hat{L}_n$ must be taken to be real.

The second type of channel is unitary dynamics with spatial character generated by a Hamiltonian

$$\hat{H}_U = \frac{\eta}{s\Gamma_{U,k=0}} \sum_{n,m} f_U\left(|n-m|\right)\left(\hat{L}^\dagger_m \hat{L}_n + h.c.\right) \tag{7.3}$$

where $\Gamma_{U,k} \equiv \sum_{r\in\left\{-\frac{N}{2},\frac{N}{2}\right\}} e^{ikr} f_U\left(|r|\right)$ is the Fourier transform of the spatial profile $f_U\left(|n-m|\right)$, N is the number of spins in the system, and s is the total spin of each spin on the chain (typically taken to be $s = 1/2$). The strength of this term is defined with a factor of $\Gamma_{U,k=0}$ as per the usual Kac renormalization that is used to normalize the contribution of this channel to dynamics in the case that $f_U\left(|n-m|\right)$ is long-range [173]. The coefficients $c^U_{x,y,z}$ appearing in the definition of operators $\hat{L}_n$ may be complex in this case. One can construct arbitrary unitary models of interest featuring two-body spin-spin interactions by combining various building-block Hamiltonians of the above forms, each defined through operators $\hat{L}_n$ of the form (7.1) with different coefficients. For example, one can construct Heisenberg XYZ models with arbitrary spatial modulation of the couplings, including, as relevant limits, one-axis and two-axis twisting Hamiltonians.

The third type of channel is dissipative dynamics generated by a jump operator $\hat{L}_n$ of the form in Eq. (7.1), with arbitrary complex coefficients $c^D_{x,y,z}$ chosen independently from those of the Hamiltonian channels. The contribution of this channel to an adjoint master equation for an operator $\hat{A}$ is

$$\mathcal{D}_D\left(\hat{A}\right) = \frac{\kappa}{s\Gamma_{D,k=0}} \sum_{n,m} f_D\left(|n-m|\right)\left(\hat{L}^\dagger_n \hat{A} \hat{L}_m - \frac{1}{2}\left\{\hat{L}^\dagger_m \hat{L}_n, \hat{A}\right\}\right), \tag{7.4}$$

where we have once again renormalized the dissipative strength with $\Gamma_{D,k=0}$ analogously to above. The usual cases of purely collective (i.e., fully permutationally invariant) dissipation can be recovered by choosing $f_D(|n-m|) = \delta_{n,m}$ for individual dissipation and $f_D(|n-m|) = \text{constant}$ for collective dissipation. Note that the interaction matrix $f_D(|n-m|)$ for a valid Lindblad map must be positive semi-definite; this condition is violated if the same-site component of the spatial profile $f_D(|n-m|=0)$ vanishes. Therefore, a valid dissipative channel will always include a sufficiently strong local (diagonal) term. For this reason, the definition of couplings $f_U(|n-m|) = |n-m|^{-\alpha}$ for $n \neq m$, usually taken for long-range Hamiltonian interactions, does not lead to a well-defined positive Lindblad generator. In the following, we will thus include a hardcore parameter $R > 0$ in the definition of our Lindblad generator spatial profile, entering as

$$f_D(|r|) = \frac{1}{(R+|r|)^{\alpha}}\,. \tag{7.5}$$

The choice $R = 1$ is sufficient to ensure positivity for all values of α. We can see as follows. The spatial profile $f(|n-m|)$ of a valid Lindblad map must be positive semi-definite, which translates to the requirement that the Fourier transform of the function $f(r) := f_{r=|n-m|}$ is a non-negative function, i.e.,

$$\widetilde{f}(k) = \sum_{r=-\infty}^{+\infty} e^{-ikr} f(r) \geq 0\,.$$

This is because translational invariance implies that $\{\widetilde{f}(k), -\pi < k \leq \pi\}$ are proportional to the eigenvalues of dissipator. Spatial profiles of dissipative Lindblad channels must thus be defined such that they satisfy this constraint. For example, a long-range spatial profile can be properly defined for a dissipative channel as $f(r) = 1/(1+|r|)^{\alpha}$. We show in Fig. 26 that the Fourier transform of this profile is positive for all $\alpha > 1$, which is the regime where spatial correlations survive in the thermodynamic limit.

The positivity condition can also be proved analytically. Consider the more general

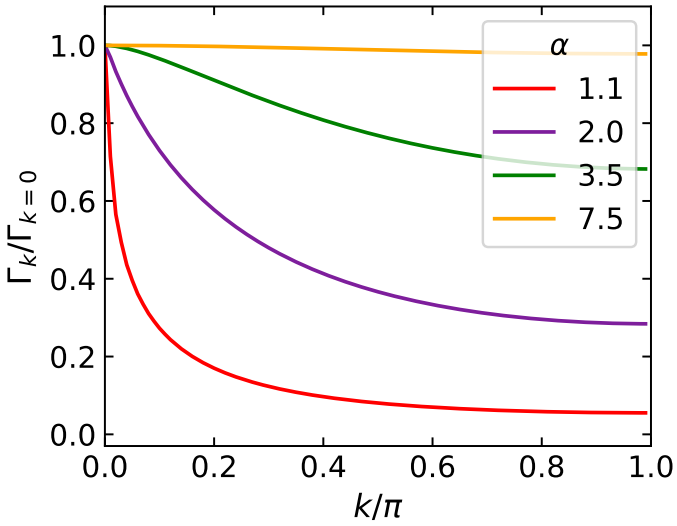

Figure 26: Fourier transform of long-range spatial profile $f(|r|) = (|r|+1)^{-\alpha}$. The function is symmetric across $k = 0$ for $k \in [-\pi, 0]$. The fact that Γ_k is greater than zero for all $\alpha > 1$ ensures that a Lindblad channel with this spatial profile is mathematically well-defined.

form of a long range spatial profile

$$f(r) = \frac{1}{(R+|r|)^{\alpha}} \tag{7.6}$$

with a tunable hardcore parameter R. Let us separate the effects of the local part $f^L(r) = \delta_{r,0}\frac{1}{R^\alpha}$ and the non-local part $f^{NL}(r) = (1-\delta_{r,0})\frac{1}{(R+|r|)^\alpha}$ of the dissipation spatial profile. The Fourier transform is

$$\widetilde{f}(k) = \widetilde{f}^L(k) + \widetilde{f}^{NL}(k) = f(0) + 2\sum_{r=1}^{+\infty}\cos(kr)f(r)\,. \tag{7.7}$$

Note that by construction

$$\int_{-\pi}^{\pi}\frac{dk}{2\pi}\widetilde{f}^{NL}(k) = f^{NL}(0) = 0 \tag{7.8}$$

so the nonlocal part $\widetilde{f}^{NL}(k)$ is equally distributed above and below zero. The local part $\widetilde{f}^L(k)$ is a positive additive constant equal to $f(0)$. Thus, we can choose the value of $f(0)$ to push the full Fourier transform entirely up above the horizontal axis,

thereby realizing positivity. The smaller the R, the larger this constant. A simple sufficient criterion can be proven as follows:
one can choose $R = R(\alpha)$ such that the last inequality holds:

$$f(0) + \min_k \widetilde{f}^{NL}(k) \geq f(0) - \max_k |\widetilde{f}^{NL}(k)| \geq 0\,. \tag{7.9}$$

To do so, we bound

$$\begin{aligned}\max_k |\widetilde{f}^{NL}(k)| &\leq 2\sum_{r=1}^{\infty} \frac{1}{(R+r)^\alpha} \\ &\leq 2\int_0^\infty \frac{dx}{(R+x)^\alpha} = \left(\frac{2R}{\alpha-1}\right)\frac{1}{R^\alpha}.\end{aligned} \tag{7.10}$$

Positivity is guaranteed when this quantity does not exceed $f(0) = 1/R^\alpha$. Thus, we obtain the sufficient criterion

$$R \leq \frac{\alpha-1}{2}\,. \tag{7.11}$$

This bound is not tight, because we majorized $|\min_k \widetilde{f}^{NL}(k)|$ by $\max_k |\widetilde{f}^{NL}(k)|$: For all $1 \leq \alpha < \infty$, the former extremum is realized at $k = \pi$ and the latter at $k = 0$, so the two quantities are always different. In reality, the value $R = 1$ that we chose in our study is sufficient for all α's: for $R = 1$ one has

$$\widetilde{f}(k) = 1 + \mathrm{Re}\left[\sum_{r=1}^{\infty} \frac{e^{ikr}}{(1+r)^\alpha}\right] = 1 + \mathrm{Re}\Big[e^{-ik}\mathrm{Li}_\alpha(e^{ik}) - 1\Big]\,, \tag{7.12}$$

where $\mathrm{Li}_\alpha(z) = \sum_{r=1}^\infty z^r/r^\alpha$ is the polylogarithmic function. The function on the right-hand side is positive in the whole domain $k \in (-\pi, \pi]$, $\alpha \in [1, \infty)$.

Having understood how to choose valid spatial profiles for dissipation channels, we return to the dynamics of an operator $\hat{A}$ under the channels Eqs. (7.2), (7.3), and (7.4) . We can express the total dynamics using an adjoint master equation

$$\frac{d}{dt}\hat{A} = \sum_j \frac{1}{i}[\hat{A}, \hat{H}_j] + \sum_{j'} \mathcal{D}_{j'}\left(\hat{A}\right), \tag{7.13}$$

where the sums run over Hamiltonians and dissipators of the types described above, F,each defined with different coefficients $c^{U,D}_{x,y,z}$. As the system is translationally-invariant, we assume periodic boundary conditions and define the Fourier transform of the spin components as $\hat{S}^{\alpha}_{k} = \sum_n e^{-ikn}\hat{S}^{\alpha}_{n}$ with $\alpha \in \{x, y, z\}$. The inverse transform is given by $\hat{S}^{\alpha}_{n} = \frac{1}{N}\sum_k e^{ikn}\hat{S}^{\alpha}_{k}$. The spins in Fourier space satisfy the commutation relation $[\hat{S}^{\alpha}_{k}, \hat{S}^{\beta}_{k'}] = i\epsilon^{\alpha\beta\gamma}\hat{S}^{\gamma}_{k+k'}$.

We now rotate to a time-dependent frame defined by angles $\theta(t)$ and $\phi(t)$. Specifically, we apply the unitary transformation $\hat{V}(\theta, \phi) = e^{-i\phi\sum_n S^z_n}e^{-i\theta\sum_n S^y_n}$. Letting e_α be the unit vectors of the lab frame, the unit vectors of the rotated frame, $e_{\tilde{\alpha}}$, are given as

$$e_{\tilde{x}} = \begin{pmatrix} \cos\theta\cos\phi \\ \cos\theta\sin\phi \\ -\sin\theta \end{pmatrix}, \quad e_{\tilde{y}} = \begin{pmatrix} -\sin\phi \\ \cos\phi \\ 0 \end{pmatrix}, \quad e_{\tilde{z}} = \begin{pmatrix} \sin\theta\cos\phi \\ \sin\theta\sin\phi \\ \cos\theta \end{pmatrix}. \tag{7.14}$$

We will later choose $\theta(t)$ and $\phi(t)$ so that the z-axis of the rotated frame, $e_{\tilde{z}}$, aligns with the z-component of the collective spin $\hat{S}^{\tilde{\alpha}} = \sum_n \hat{S}^{\tilde{\alpha}}_{n} = \hat{S}^{\tilde{\alpha}}_{k=0}$. The cost of this time-dependent rotation is an additional 'inertial' Hamiltonian

$$\hat{H}_{\mathrm{RF}} = \sin\theta\dot{\phi}\hat{S}^{\tilde{x}} - \dot{\theta}\hat{S}^{\tilde{y}} - \cos\theta\dot{\phi}\hat{S}^{\tilde{z}} \tag{7.15}$$

that contributes to the dynamics. The three types of dynamical channels that contribute to the dynamics of an operator $\hat{\tilde{A}}$ in the rotated frame take thus the form

$$\hat{H}_F = \omega_F \sum_{\tilde{\alpha}\in\{\tilde{x},\tilde{y},\tilde{z}\}} F_{\tilde{\alpha}}\hat{S}^{\tilde{\alpha}}_{k=0} \tag{7.16}$$

$$\hat{H}_U = \frac{2\eta}{\Gamma_{U,k=0}Ns}\sum_k \Gamma_{U,k} \sum_{\tilde{\alpha},\tilde{\beta}\in\{\tilde{x},\tilde{y},\tilde{z}\}} M^{U}_{\tilde{\alpha},\tilde{\beta}}\hat{S}^{\tilde{\alpha}}_{-k}\hat{S}^{\tilde{\beta}}_{k} \tag{7.17}$$

$$\mathcal{D}_D\left(\hat{\tilde{A}}\right) = \frac{\kappa}{\Gamma_{D,k=0}Ns}\sum_k \Gamma_{D,k} \sum_{\tilde{\alpha},\tilde{\beta}\in\{\tilde{x},\tilde{y},\tilde{z}\}} M^{D}_{\tilde{\alpha},\tilde{\beta}}\left(\hat{S}^{\tilde{\alpha}}_{k}\hat{\tilde{A}}\hat{S}^{\tilde{\beta}}_{-k} - \frac{1}{2}\left\{\hat{S}^{\tilde{\alpha}}_{-k}\hat{S}^{\tilde{\beta}}_{k}, \hat{\tilde{A}}\right\}\right) \tag{7.18}$$

where we have defined

$$F_{\tilde{\alpha}}(\theta,\phi) = c_x^F G_{\tilde{\alpha},x} + c_y^F G_{\tilde{\alpha},y} + c_z^F G_{\tilde{\alpha},z} \tag{7.19}$$

$$M^{U,D}_{\tilde{\alpha},\tilde{\beta}}(\theta,\phi) = \left((c_x^{U,D})^* G_{\tilde{\alpha},x} + (c_y^{U,D})^* G_{\tilde{\alpha},y} + (c_z^{U,D})^* G_{\tilde{\alpha},z}\right)\left(c_x^{U,D} G_{\tilde{\beta},x} + c_y^{U,D} G_{\tilde{\beta},y} + c_z^{U,D} G_{\tilde{\beta},z}\right) \tag{7.20}$$

and $G_{\tilde{\alpha}\beta} = e_{\tilde{\alpha}} \cdot e_\beta$ is the projection of the rotated basis vectors on the lab frame basis vectors. The choice of operators $\hat{L}_n$ are encoded in the coefficients $F_{\tilde{\alpha}}(\theta,\phi)$ or $M^{U,D}_{\tilde{\alpha},\tilde{\beta}}(\theta,\phi)$ while the choice of spatial profiles $f_{U,D}(|n-m|)$ are encoded in $\Gamma_{U,k}$, $\Gamma_{D,k}$. Note that the dynamics of the above channels does not decompose into independent dynamics for each wave vector k as sectors of different momenta are coupled via the self-consistent feedback of the $k = 0$ mode.

7.2 Holstein-Primakoff expansion in a moving vacuum

We now bosonize the spins via a lowest-order Holstein-Primakoff transformation [6]

$$\hat{S}_n^{\tilde{z}} = s - \hat{b}_n^\dagger \hat{b}_n, \quad \hat{\tilde{S}}_n^{+} = (2s)^{\frac{1}{2}} \hat{b}_n, \quad \hat{\tilde{S}}_n^{-} = (2s)^{\frac{1}{2}} \hat{b}_n^\dagger \tag{7.21}$$

where $\hat{b}_n^\dagger$ and $\hat{b}_n$ are bosonic creation and annihilation operators representing spin flips along the chain and satisfy canonical commutation relations $\left[\hat{b}_n, \hat{b}_m^\dagger\right] = \delta_{nm}$. In Fourier space, the mapping becomes

$$\hat{S}_k^{\tilde{x}} = \left(\frac{Ns}{2}\right)^{\frac{1}{2}} \left\{\hat{b}_k + \hat{b}_k^\dagger\right\}, \tag{7.22}$$

$$\hat{S}_k^{\tilde{y}} = \frac{1}{i}\left(\frac{Ns}{2}\right)^{\frac{1}{2}} \left\{\hat{b}_k - \hat{b}_k^\dagger\right\}, \tag{7.23}$$

$$\hat{S}_k^{\tilde{z}} = Ns\delta_{k,0} - \sum_{k'} \hat{b}_{k'}^\dagger \hat{b}_{k+k'} \tag{7.24}$$

where $\hat{b}_k^\dagger = \frac{1}{\sqrt{N}} \sum_n e^{ikn} \hat{b}_n^\dagger$ and $\hat{b}_k = \frac{1}{\sqrt{N}} \sum_n e^{-ikn} \hat{b}_n$ are bosonic creation and annihilation operators representing spin-wave excitations. It is useful to work in terms of quadrature operators $\hat{q}_k$ and $\hat{p}_k$ which are expressed in terms of the creation and annihilation operators as $\hat{b}_k^\dagger = \frac{1}{\sqrt{2}} (\hat{q}_k - i\hat{p}_k)$ and $\hat{b}_k = \frac{1}{\sqrt{2}} (\hat{q}_k + i\hat{p}_k)$. Note that these momentum space quadrature operators satisfy the commutation relation $[\hat{q}_k, \hat{p}_{k'}] = i\delta_{k',-k}$. The mapping between spins and bosonic modes can be given in terms of the quadrature operators as

$$\hat{S}_k^{\tilde{x}} = (Ns)^{\frac{1}{2}} \hat{q}_k, \tag{7.25}$$

$$\hat{S}_k^{\tilde{y}} = (Ns)^{\frac{1}{2}} \hat{p}_k, \tag{7.26}$$

$$\hat{S}_k^{\tilde{z}} = Ns\delta_{k,0} - \frac{1}{2} \sum_{k'} \left(\hat{q}_{k'} \hat{q}_{k-k'} + \hat{p}_{k'} \hat{p}_{k-k'} - \delta_{k,0} \right). \tag{7.27}$$

It is also useful to define

$$n_k = \langle \hat{b}_k^\dagger \hat{b}_k \rangle = \frac{1}{2} \langle (\hat{q}_k \hat{q}_{-k} + \hat{p}_k \hat{p}_{-k} - 1) \rangle \tag{7.28}$$

with $n_{k=0}$ corresponding to the condensate density and $n_{k\neq 0}$ corresponding to the occupation of the spin-wave mode at wavevector k. The evolution of the $k = 0$ mode represents the dynamics of the spin-wave vacuum and the evolution of the $k \neq 0$ represents dynamics of spin-waves on top of the moving vacuum. In the thermodynamic limit, we can treat the spin-wave vacuum classically [211, 212], while treating the spin-waves as quantum mechanical excitations. In practice, this amounts to replacing $\hat{S}_{k=0}^{\tilde{z}}$ by a c-number $\langle \hat{S}_{k=0}^{\tilde{z}} \rangle$ and using the total spin-wave density

$$\epsilon(t) = \frac{1}{Ns} \sum_{k\neq 0} n_k(t) = \frac{1}{Ns} \sum_{k\neq 0} \frac{\langle \hat{q}_k(t) \hat{q}_{-k}(t) + \hat{p}_k(t) \hat{p}_{-k}(t) - 1 \rangle}{2} \tag{7.29}$$

as a control parameter for the approximation. The 'time-dependent' part of NEQSWT references choosing the rotating frame angles $\theta(t)$ and $\phi(t)$ at every momentum in time so that the $\tilde{z}$ axis aligns with the collective spin, which amounts to determining the equations of motion for these angles by enforcing $\langle S_{k=0}^{\tilde{x}} \rangle = 0$ and $\langle S_{k=0}^{\tilde{y}} \rangle = 0$. The

position of the collective spin on the Bloch sphere defined in the lab frame is given as $\mathbf{m} = (m^x, m^y, m^z)$ where

$$m^x(t) = \sin\theta(t)\cos\phi(t), \tag{7.30}$$

$$m^y(t) = \sin\theta(t)\sin\phi(t), \tag{7.31}$$

$$m^z(t) = \cos\theta(t). \tag{7.32}$$

This choice extends the validity of spin-wave theory to larger window of dynamics by redefining the spin-wave vacuum, represented by the collective spin, at every point in time so that the total spin-wave density on top of the vacuum remains small [214]. In the dilute regime of $\varepsilon(t) \ll 1$, spin waves behave as free bosonic modes which scatter self-consistently only with the collective magnetization ($k = 0$ mode).

As long as $\epsilon\,(t)$ remains small, the majority of angular momentum in the system resides in the collective $k = 0$ mode (taken to be aligned with the $\tilde{z}$ axis) and higher order terms in the Holstein-Primakoff transformation can be ignored [214, 210]. The system's dynamics can then be described as that of the collective spin on a Bloch sphere with a small density of spin-waves, negligibly reducing the length of this collective magnetization. NEQSWT is valid up to times $\sim 1/\epsilon^2$ (see for instance Refs. [214, 210]). As a practical rule of thumb, the dynamics of spins are faithfully captured as long as the spin-wave density satisfies $\epsilon(t) \lesssim 0.2$ for the effects illustrated in Section 8.1.

We apply the Holstein-Primakoff transformation described above to the adjoint master equation Eq. (7.13). A sufficiently small spin-wave density allows us to truncate the equations of motion for the system at the Gaussian level; expectation values of operators that are more than quadratic in spin-wave operators are negligible in this limit. This approximation then allows for a closed set of non-linear coupled dynamical equations involving only the angles $\theta(t)$ and $\phi(t)$, representing the one-point

correlation functions, and the two-point correlation functions defined below:

$$\Delta_k^{qq}(t) = \langle \hat{q}_k(t)\, \hat{q}_{-k}(t) \rangle , \tag{7.33}$$

$$\Delta_k^{pp}(t) = \langle \hat{p}_k(t)\, \hat{p}_{-k}(t) \rangle , \tag{7.34}$$

$$\Delta_k^{qp}(t) = \frac{1}{2} \langle \hat{q}_k \hat{p}_{-k} + \hat{p}_k \hat{q}_{-k} \rangle . \tag{7.35}$$

The dynamics of these two-point functions act as feedback for the motion of $\theta(t)$ and $\phi(t)$.

Specifically, we substitute the spin operators with bosonic creation and annihilation operators in the Hamiltonian or dissipator and keep contributions that are at most quadratic in bosonic operators. We then substitute quadrature operators for the creation and annihilation operators before computing equations of motion for $\hat{q}_{k=0}$, $\hat{p}_{k=0}$, $\hat{q}_k\hat{q}_{-k}$, $\hat{p}_k\hat{p}_{-k}$, and $\frac{1}{2}(\hat{q}_k\hat{p}_{-k} + \hat{p}_k\hat{q}_{-k})$. The first two quantities and enforcement of $\langle S^{\tilde{x}}_{k=0} \rangle = \langle S^{\tilde{y}}_{k=0} \rangle = 0$ yields equations of motion for the angles $\theta(t)$ and $\phi(t)$ respectively, while the latter three quantities yield equations of motion for the two-point functions given in Eq. (7.33).

It is important to note three technical points. First, we must do the Gaussian approximation in terms of bosonic creation and annihilation operators rather than quadratures as $\hat{b}_k^\dagger \hat{b}_k$ is the quantity that is related to the small parameter ε that we are expanding around; doing the approximation in terms of quadrature operators may yield spurious terms in the final equations due to zero-point quantum fluctuations. Second, we must apply the Holstein-Primakoff transformation and Gaussian approximation at the level of the generators Eqs. (7.16)-(7.18) before calculating the equation of motion for an operator $\hat{\tilde{A}}$; performing the Gaussian approximation after computing the equation of motion may also introduce spurious terms in the final equations. Third, the chain rule for derivatives does not apply to operators evolving under a Lindblad master equation so the equations for the two-point functions must be directly computed [123]; we cannot construct these equations from a product of the equations of motion for the one-point functions as is commonly done when NEQSWT is applied to purely unitary systems.

7.3 Equations of motion

The content of this section is intended as a user guide for assembling equations of motion for arbitrary quantum master equations of the general form considered in this work, corresponding to adjoint master equations that can be expressed as Eq. (7.13). The following are a set of mechanical rules to construct the right-hand side of the equations of motion.

First, we start with the contributions of the Larmor Hamiltonian $\hat{H}_{\mathrm{RF}}$ which will always be present due to the rotation of the reference frame:

$$\begin{aligned}
\frac{d}{dt}\theta &= 0 \\
\frac{d}{dt}\phi &= 0 \\
\frac{d}{dt}\Delta_k^{qq} &= \cos\theta\dot{\phi}\,(2\Delta_k^{qp}) \\
\frac{d}{dt}\Delta_k^{pp} &= -\cos\theta\dot{\phi}\,(2\Delta_k^{qp}) \\
\frac{d}{dt}\Delta_k^{qp} &= -\cos\theta\dot{\phi}\,(\Delta_k^{qq} - \Delta_k^{pp})
\end{aligned} \tag{7.36}$$

Each channel j, given by a choice of one of the generators in Eqs. (7.16)-(7.18), then contributes to the above equations as

$$\frac{d}{dt}\theta \to \frac{d}{dt}\theta + d\theta_j \tag{7.37}$$

$$\frac{d}{dt}\phi \to \frac{d}{dt}\phi + d\phi_j \tag{7.38}$$

$$\frac{d}{dt}\Delta_k^{qq} \to \frac{d}{dt}\Delta_k^{qq} + dQ_j \tag{7.39}$$

$$\frac{d}{dt}\Delta_k^{pp} \to \frac{d}{dt}\Delta_k^{pp} + dP_j \tag{7.40}$$

$$\tag{7.41}$$

$$\frac{d}{dt}\Delta_k^{qp} \to \frac{d}{dt}\Delta_k^{qp} + dW_j \tag{7.42}$$

Below we give the contributions to the equations of motion from each type of channel.

It is useful to define the quantities

$$\xi_{\tilde{\alpha},\tilde{\beta}} = \frac{M_{\tilde{\beta},\tilde{\alpha}}}{M_{\tilde{\alpha},\tilde{\beta}}} = \frac{M^*_{\tilde{\alpha},\tilde{\beta}}}{M_{\tilde{\alpha},\tilde{\beta}}} \tag{7.43}$$

$$\delta^{\eta\xi} = \frac{1}{\Gamma_{k=0} Ns} \sum_{k\neq 0} \Gamma_k \Delta_k^{\eta\xi}. \tag{7.44}$$

defined analogously for each superscript U or D.

The contributions from a $\hat{H}_F$ channel are

$$d\theta_{H_F} = \omega_F F_{\tilde{y}} \tag{7.45}$$

$$d\phi_{H_F} = -\omega_F F_{\tilde{x}} \frac{1}{\sin\theta} \tag{7.46}$$

$$dQ_{H_F} = -2\omega_F F_{\tilde{z}} \Delta_k^{qp} \tag{7.47}$$

$$dP_{H_F} = 2\omega_F F_{\tilde{z}} \Delta_k^{qp} \tag{7.48}$$

$$dW_{H_F} = \omega_F F_{\tilde{z}} \left(\Delta_k^{qq} - \Delta_k^{pp}\right) \tag{7.49}$$

To ease the notation, we drop the superscripts U and D in the coefficients in the following equations for the channels $\hat{H}_L$ and $\mathcal{D}_L$. The contributions from a $\hat{H}_U$ channel are

$$\begin{aligned} d\theta_{H_L} = &-M_{\tilde{x},\tilde{z}} 4\eta \frac{1}{\Gamma_{k=0} Ns} \sum_{k'} \Gamma_{k'} \frac{1}{2} \left\langle \hat{q}_{-k'} \hat{p}_{k'} + \xi_{\tilde{x},\tilde{z}} \hat{p}_{-k'} \hat{q}_{k'} \right\rangle \\ &+ M_{\tilde{y},\tilde{z}} 2\eta \left(1 + \xi_{\tilde{y},\tilde{z}}\right) \left(1 - \varepsilon - \delta_\alpha^{pp} - \frac{1}{Ns} n_{k=0} - \frac{1}{Ns} \Delta_{k=0}^{pp}\right) \end{aligned} \tag{7.50}$$

$$d\phi_{H_L} = M_{\tilde{y},\tilde{z}} \frac{1}{\sin\theta} 4\eta \frac{1}{\Gamma_{k=0} Ns} \sum_{k'} \Gamma_{k'} \frac{1}{2} \left\langle \hat{p}_{-k'} \hat{q}_{k'} + \xi_{\tilde{y},\tilde{z}} \hat{q}_{-k'} \hat{p}_{k'} \right\rangle \tag{7.51}$$

$$- M_{\tilde{x},\tilde{z}} \frac{1}{\sin\theta} 2\eta \left(1 + \xi_{\tilde{x},\tilde{z}}\right) \left(1 - \varepsilon - \delta_\alpha^{qq} - \frac{1}{Ns} n_{k=0} - \frac{1}{Ns} \Delta_{k=0}^{qq}\right) \tag{7.52}$$

$$dQ_{H_L} = M_{\tilde{y},\tilde{y}} \eta \cdot 8 \frac{\Gamma_k}{\Gamma_{k=0}} \Delta_k^{qp} - M_{\tilde{z},\tilde{z}} \eta \cdot 8 \Delta_k^{qp} + M_{\tilde{x},\tilde{y}} 4\eta \left(1 + \xi_{\tilde{x},\tilde{y}}\right) \frac{\Gamma_k}{\Gamma_{k=0}} \Delta_k^{qq} \tag{7.53}$$

$$dP_{H_L} = -M_{\tilde{x},\tilde{x}}\eta \cdot 8\frac{\Gamma_k}{\Gamma_{k=0}}\Delta_k^{qp} + M_{\tilde{z},\tilde{z}}\eta \cdot 8\Delta_k^{qp} - M_{\tilde{x},\tilde{y}}4\eta\left(1+\xi_{\tilde{x},\tilde{y}}\right)\frac{\Gamma_k}{\Gamma_{k=0}}\Delta_k^{pp} \tag{7.54}$$

$$dW_{H_L} = -M_{\tilde{x},\tilde{x}}\eta \cdot 4\frac{\Gamma_k}{\Gamma_{k=0}}\Delta_k^{qq} + M_{\tilde{y},\tilde{y}}\eta \cdot 4\frac{\Gamma_k}{\Gamma_{k=0}}\Delta_k^{pp} \tag{7.55}$$

$$+ M_{\tilde{z},\tilde{z}}\eta \cdot 4\left(\Delta_k^{qq} - \Delta_k^{pp}\right) \tag{7.56}$$

The contributions from a $\mathcal{D}_D$ channel are

$$d\theta_{\mathcal{D}_D} = -iM_{\tilde{x},\tilde{z}}\frac{1}{2}\kappa\frac{1}{\Gamma_{k=0}Ns}\sum_{k'}\Gamma_{k'}\left\langle \hat{q}_{-k'}\hat{p}_{k'} - \xi_{\tilde{x},\tilde{z}}\hat{p}_{k'}\hat{q}_{-k'}\right\rangle \tag{7.57}$$

$$- iM_{\tilde{y},\tilde{z}}\frac{1}{2}\kappa\left(1-\xi_{\tilde{y},\tilde{z}}\right)\left(1-\varepsilon+\delta_\alpha^{pp} - \frac{1}{Ns}n_{k=0} + \frac{1}{Ns}\Delta_{k=0}^{pp}\right) \tag{7.58}$$

$$d\phi_{\mathcal{D}_D} = iM_{\tilde{y},\tilde{z}}\frac{1}{\sin\theta}\frac{1}{2}\kappa\frac{1}{\Gamma_{k=0}Ns}\sum_{k'}\Gamma_{k'}\left\langle \hat{p}_{-k'}\hat{q}_{k'} - \xi_{\tilde{y},\tilde{z}}\hat{q}_{k'}\hat{p}_{-k'}\right\rangle \tag{7.59}$$

$$+ iM_{\tilde{x},\tilde{z}}\frac{1}{\sin\theta}\frac{1}{2}\kappa\left(1-\xi_{\tilde{x},\tilde{z}}\right)\left(1-\varepsilon+\delta_\alpha^{qq} - \frac{1}{Ns}n_{k=0} + \frac{1}{Ns}\Delta_{k=0}^{qq}\right) \tag{7.60}$$

$$dQ_{\mathcal{D}_D} = M_{\tilde{y},\tilde{y}}\kappa\frac{\Gamma_k}{\Gamma_{k=0}} + iM_{\tilde{x},\tilde{y}}\kappa\left(1-\xi_{\tilde{x},\tilde{y}}\right)\frac{\Gamma_k}{\Gamma_{k=0}}\Delta_k^{qq} \tag{7.61}$$

$$dP_{\mathcal{D}_D} = M_{\tilde{x},\tilde{x}}\kappa\frac{\Gamma_k}{\Gamma_{k=0}} + iM_{\tilde{x},\tilde{y}}\kappa\left(1-\xi_{\tilde{x},\tilde{y}}\right)\frac{\Gamma_k}{\Gamma_{k=0}}\Delta_k^{pp} \tag{7.62}$$

$$dW_{\mathcal{D}_D} = iM_{\tilde{x},\tilde{y}}\kappa\frac{\Gamma_k}{\Gamma_{k=0}}\frac{1}{2}\left\langle \hat{q}_k\hat{p}_{-k} - \xi_{\tilde{x},\tilde{y}}\hat{p}_k\hat{q}_{-k} + \hat{q}_{-k}\hat{p}_k - \xi_{\tilde{x},\tilde{y}}\hat{p}_{-k}\hat{q}_k\right\rangle \tag{7.63}$$

Note that the spin-wave density is expressed in terms of two-point correlation functions as $\varepsilon(t) = \frac{1}{Ns}\sum_{k\neq 0} n_k$ where $n_k = \frac{1}{2}\left(\Delta_k^{qq} + \Delta_k^{pp} - 1\right)$. After assembling the contributions of each desired channel to the equations of motion for the collective spin angles and two-point functions, we then plug in the final expression for $\frac{d}{dt}\phi$ into the Larmor term in the equations of motion for the two-point functions. We then

keep terms that are second order in $k \neq 0$ spin-wave operators. As each Larmor term is proportional to $\frac{d}{dt}\phi$ multiplied by a two-point function, we only keep terms in $\frac{d}{dt}\phi$ that are zeroth order in spin-wave operators when substituting the expression. In the above expressions, we have kept terms that are proportional to $\frac{1}{Ns}$ which are necessary to quantify finite size effects. In the thermodynamic limit, these terms vanish. The treatment thus results in a set of differential equations for the collective angles $\theta(t)$ and $\phi(t)$ which are coupled to the $2N$ equations of motion for the two-point correlation functions which represent the dynamics of spin-wave excitations. The coupling between these equations represents the self-consistent part of the method where the quantum fluctuations of spin-waves affects the motion of the spin-wave vacuum and vice-versa.

The initial values of the dynamical variables depend on the choice of initial state. For quasiclassical pure states fully polarized along a given direction, the dynamical variables take the values $\theta(0) = \theta_0$, $\phi(0) = \phi_0$, $\Delta_k^{qq} = \Delta_k^{pp} = 1/2$, and $\Delta_k^{qp} = 0$.

Chapter 8

Correlation dynamics

In this chapter, we investigate a specific spin model which exhibits novel correlation dynamics illustrative of spatially extended dissipation. The system serves as a relatively simple model of the types of interesting correlations that can be generated by spatially extended dissipation. Additionally, as the collective dissipation limit has been studied in past literature [164], the methods used to analyze the system can be benchmarked in this limit. The proposed experimental implementation of the model in an analog quantum simulator is given in Chap. 6 and the formalism used to analyze its dynamics is given in Chap. 7. The system is described via the following purely dissipative non-diagonal Lindblad quantum master equation:

$$\partial_t \hat{\rho} = K \sum_{n,m=1}^{N} f_{n,m} \left(\hat{S}_n^- \rho \hat{S}_m^+ - \frac{1}{2} \{ \hat{S}_n^+ \hat{S}_m^-, \rho \} \right). \tag{8.1}$$

The spatial extension of the dissipation is contained in the translationally-invariant profile $f_{n,m} = f(|n-m|)$, while its strength $K \equiv 2\kappa/(\Gamma_{k=0})$ is renormalized by $\Gamma_{k=0}$ where $\Gamma_k \equiv \sum_{r \in \{-\frac{N}{2}, \frac{N}{2}\}} e^{ikr} f(|n-m|)$ is the Fourier transform of $f_{n,m}$.

In the language of Chap. 7, the system described by Eq. (8.1) has observables $\hat{A}$ that evolve according to the adjoint master equation $\frac{d}{dt}\hat{A} = \mathcal{D}_D\left(\hat{A}\right)$ with:

$$\mathcal{D}_D\left(\hat{A}\right) = \frac{\kappa}{s\Gamma_{k=0}} \sum_{n,m} f(|n-m|) \left(\hat{S}_n^+ \hat{A} \hat{S}_m^- - \frac{1}{2} \left\{ \hat{S}_m^+ \hat{S}_n^-, \hat{A} \right\} \right) \tag{8.2}$$

Note that we drop the superscript D in this section. It is instructive to analyze dynamics described by Eq. (8.2) starting from the case of a long-range spatial profile, $f(|n-m|) = (|n-m|+1)^{-\alpha}$. The Fourier transform, Γ_k, of this profile can be expressed in terms of poly-logarithm functions $\Gamma_k(\alpha) = 1 + 2\mathrm{Re}\left[e^{-ik}\mathrm{Li}_\alpha\left(e^{ik}\right) - 1\right]$ of order α. The inclusion of a hardcore parameter $R = 1$ ensures positivity of Γ_k, as explained in Sec. 7.1. The denominator $\Gamma_{k=0}$ ensures the extensive scaling of the Liouvillian (8.1) in the thermodynamic limit, thus playing a role analogous to the conventional Kac's renormalization of long-range Hamiltonians [58, 176, 55, 364, 365].

When $\alpha = 0$, the dynamics of the collective spin admit an analytical solution in the thermodynamic limit [164, 288]. The mean-field solution becomes exact and can be written in terms of the components of the collective magnetization, $m^x(t) = \sin\theta(t)\cos\phi(t)$ and $m^z(t) = \cos\theta(t)$, which, in this case, is fully described by a spin coherent state moving on the (collective spin) Bloch sphere with azimuthal and polar angles $\phi(t)$ and $\theta(t)$, respectively. The model at $\alpha = 0$, with the addition of a coherent external field representing by a Hamiltonian $\hat{H}_0 = \omega_0 \sum_{n=1}^{N} \hat{S}_n^x$, has been studied in the context of cooperative radiation, optical bistability, and time-crystals [164, 99, 100, 367, 146]. When $\omega_0/\kappa \gtrsim 1$, the total magnetization rolls around the $\hat{x}$ axis with $\langle \hat{S}^z \rangle = 0$. In the opposite limit $\kappa/\omega_0 \gtrsim 1$, the dynamics is damped and quickly attracted towards the southern hemisphere of the Bloch sphere with a non-vanishing $\hat{S}^z$ component.

Choosing $\alpha \neq 0$ introduces spatial resolution to the system and understanding the dynamics requires, in principle, a solution to the full many-body system including connected spin correlation functions of all orders beyond mean-field. In the dissipation-dominated regime $\kappa/\omega_0 \gtrsim 1$, however, the NEQSWT developed in Chap. 7 can be used to treat the system as the number of spin-wave excitations remains sufficiently low over the course of dynamics. In the next section, we analyze dynamics for a system with no external field ($\omega_0 = 0$). As the dissipation channel, Eq. (8.1), is the only generator of dynamics, we are always in the dissipation-dominated regime where NEQSWT remains valid. The case of a non-zero external field ($\omega_0 \neq 0$) is discussed in Ref. [319], with the overall picture unaffected by a small but non-zero ω_0.

For $0 \leq \alpha \leq 1$, the normalization factor diverges, which means that the normalized spectrum of the Lindbladian $(\kappa/s)\Gamma_k/\Gamma_{k=0}$ asymptotically converges to zero for all finite momenta $k \neq 0$. It can be shown that such a spectrum remains discrete in the thermodynamic limit [212, 90]. Away from fine-tuned dynamical critical points, however, the behavior of collective observables in the thermodynamic limit is identical with that of the mean-field model describing the $\alpha = 0$ case. There may be severe finite-size effects for α close to 1. For $\alpha > 1$, however, spin-wave modes get populated as the system evolves out of equilibrium, exerting a finite feedback on the dynamics of the collective spin, which acquire corrections beyond the mean-field. In the next section, we consider this situation.

8.1 Correlation dynamics of non-local dissipation channel

We can gain intuition for the dynamics of quantum correlations generated by Eq. (8.2) by considering the simplest situation of evolution starting from a pure state with a single spin excitation $\rho(0) = |j\rangle\langle j|$, where $|j\rangle \equiv |\downarrow_1 \ldots \downarrow_{j-1}\uparrow_j\downarrow_{j+1} \ldots \downarrow_N\rangle$ and the single up spin is at site j. Time evolution takes place in the restricted Hilbert space spanned by $\{|n\rangle, n = 1, \ldots, N\}$ and the dark state $|\emptyset\rangle \equiv |\downarrow_1 \ldots \downarrow_N\rangle$ which is fully polarized down. The state's dynamics, governed by the master equation Eq. (8.2), admits a simple physical picture: the excitation initially at site j evolves in the single-excitation space subject to the non-Hermitian (imaginary) hopping Hamiltonian

$$\frac{i\kappa}{2s\Gamma_{k=0}} \sum_{n,m} f_{|n-m|} L_n^\dagger L_m \;\rightsquigarrow\; \frac{i\kappa}{2s\Gamma_{k=0}} \sum_{n,m} f_{|n-m|} |n\rangle\langle m| \,. \tag{8.3}$$

This single-particle evolution is diagonal in Fourier space, and each momentum component decays with a different rate proportional to $\Gamma_k/\Gamma_{k=0}$. The probability continuously lost by the single-excitation space accumulates in the dark state. Thus, the excitation initially localized at site j spreads quantum mechanically in the single-excitation sector, generating an initial spreading of quantum correlations with quan-

tum coherence between different single-excitation states. At the same time, each momentum component inhomogeneously decays to the dark state, which generates nontrivial correlation dynamics.

Armed with intuition from the above example, we proceed to examining the dynamics of Eq. (8.1) starting from initial states far away from the dark state. We will consider systems prepared in fully polarized states pointing along an arbitrary direction on the Bloch sphere, identified by spherical angles θ_0, ϕ_0. Furthermore, we consider long-range and short-range spatial profiles $f(r = |n - m|)$ given respectively by

$$f\left(r\right) = \frac{1}{(r+1)^{\alpha}} \qquad \text{or} \qquad f\left(r\right) = \exp(-r/\chi). \tag{8.4}$$

Using Eqs (7.36), we can derive a differential equation for the occupation n_k of the spin-wave excitation at wavevector $k \neq 0$.

$$\frac{d}{dt} n_k = 2\kappa \frac{\Gamma_k}{\Gamma_{k=0}} \left(n_k \cos\theta(t) + \cos^4\left(\frac{\theta(t)}{2}\right)\right). \tag{8.5}$$

The k-dependent prefactor $\Gamma_k/\Gamma_{k=0}$ is positive for both spatial profiles of interest; positivity of the master equation requires $\kappa \geq 0$. Remarkably, for the specific Lindblad channel in Eq. (8.2), the equation of motion for spin-wave occupation given by Eq. (8.5) is a linear differential equation that is not coupled to other NEQSWT variables. The homogeneous term in Eq. (8.5) describes the rate of production of spin-waves and depends on $\cos\theta(t)$; accordingly, it generates or drains spin waves depending on whether the collective magnetization is in the northern ($0 < \theta(t) < \pi/2$) or southern ($\pi/2 < \theta(t) < \pi$) hemisphere of the Bloch sphere. In other words, the transition in the rate of production of spin waves can be understood as a consequence of the spin waves' dynamics being dependent on the instantaneous direction of the collective spin. While the effect of dissipation is creating spin waves on top of a mean field in the northern hemisphere, the same dissipative mechanism results in a reduction of spin-waves with respect to a mean-field in the southern hemisphere. We note that the inhomogeneous decay of spin excitations with different momenta, discussed at the beginning of this section [cf. Eq. (8.3)], is visible in Eq. (8.5) by examining the

point $\theta \simeq \pi$.

Note that this behavior is a result of the choice of dissipation channel, $\hat{L}_n = \hat{S}_n^-$, and does not depend on the choice of spatial profile which only modifies the prefactor $\Gamma_k/\Gamma_{k=0}$ in Eq (8.5). The long-range profile is a power-law decay characterized by power α and results in a prefactor that decays as a a power-law with power related to α. The short-range profile is an exponential decay characterized by a decay length χ and results in a prefactor that is Lorentzian with width proportional to $1/\chi$. The change in spatial profile determines modifications in some non-universal parameters such as the transition time, t^* upon which the system switches from pumping excitations to draining excitations. The spatial profile is, however, important when engineering the dynamics of the system for certain applications.

The mechanism governing the dynamics of spin-wave occupation explains the dynamics of equal time spin-spin correlation functions. As an example, we examine the connected correlation function

$$C^{zz}(r,t) = \langle \hat{S}_n^z(t)\, \hat{S}_{n+r}^z(t)\rangle - \langle \hat{S}_n^z(t)\rangle \langle \hat{S}_{n+r}^z(t)\rangle \tag{8.6}$$

which is directly sensitive to the action of spin losses $\hat{L}_n = \hat{S}_n{}^-$. This function can be expressed in terms of NEQSWT variables as

$$C^{zz}(r,t) = (\sin\theta(t))^2 \sum_{k\neq 0, k>0} \cos(kr)\Delta_k^{qq}. \tag{8.7}$$

We see that there is an overall envelope to the correlation dynamics set by $[\sin\theta(t)]^2$, which grows as the collective spin moves from the north pole of the Bloch sphere to the equator, and shrinks as it moves from the equator to the south pole. Therefore, in the absence of other dynamical channels, we expect the correlations to grow for a period of time and then shrink, with the time t^* upon which the system transitions between these two regimes being dependent on the motion of the collective spin. As the dynamics of spin-wave occupation also increases and decreases depending on the collective spin motion, we expect that the correlation transition time t^* sets the scale

upon which the spin-wave density ε reaches its maximum value before shrinking. Similar to the dynamics of spin-wave occupation, we note that the choice of spatial profile does not qualitatively modify the correlation dynamics. The spatial profile only enters Eq. (8.7) through the dynamics of Δ_k^{qq}.

We now numerically calculate the dynamics of the correlation function, Eq. (8.7), using NEQSWT and analyze both long-range and short-range cases. We start with all the spins in a coherent state pointing slightly above the equator of the Bloch sphere ($\theta(t=0) = 0.4\pi$, $\phi(t=0) = 0$). The qualitative nature of the dynamics for this dissipative channel does not depend on the angle of the initial coherent state; starting too close to the North pole, however, causes the spin-wave density to exceed the threshold treatable by NEQSWT. Our choice of $\theta(t=0) = 0.4\pi$ allows the dynamics to be validly treated with NEQSWT.

The correlation dynamics for the long-range spatial profile is shown in Fig. 27(a). In the first stage of dynamics, correlations exhibit a front scaling as $t \approx r^{\beta}$. The exponent β is plotted in Fig. 27(c), showing that the dissipation strength κ does not play a role in the 'opening' of the correlation function. The exponent β characterizing the scaling follows $\beta \simeq \alpha$; this result can be understood by making the following scaling ansatz for $C^{zz}(r,t)$ in the initial opening stage of correlation spreading dynamics:

$$C^{zz}\left(rt_1^{1/\beta}, t_1\right) = C^{zz}\left(rt_2^{1/\beta}, t_2\right). \tag{8.8}$$

Algebraic manipulation yields the equivalent expressions

$$\begin{aligned} C^{zz}(\zeta r, t) &= \zeta^{\nu} C^{zz}(r,t), \\ C^{zz}(r, \zeta t) &= \zeta^{-\nu\eta} C^{zz}(r,t). \end{aligned} \tag{8.9}$$

Here ζ is a positive rescaling factor while ν and η are the two rescaling exponents for space and time. The above ansatz represents a correlation function front scaling with exponent $\beta = 1/\eta$. As we discuss later, we find that for large distances ($r \gg 1$), the correlation function satisfies $C^{zz}(r,t) \propto 1/r^{\alpha}$. This behavior yields $\nu = -\alpha$ using the first equation in (8.9). Additionally, at short times, correlations grow linearly to

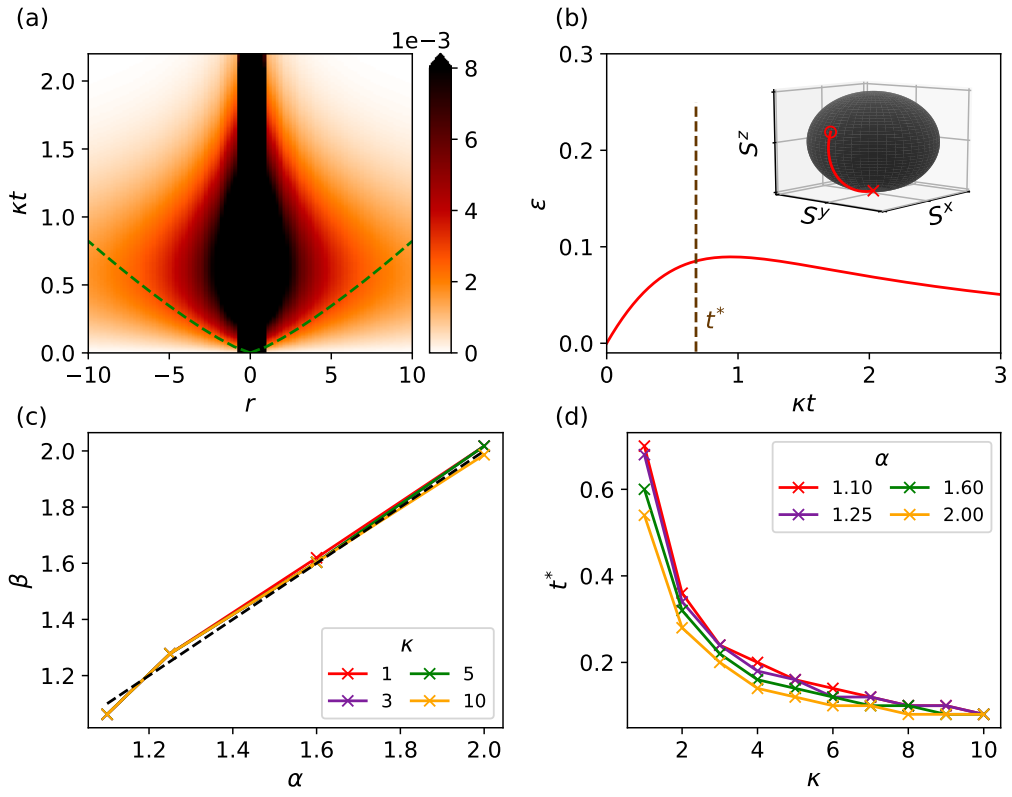

Figure 27: Dynamics of $\hat{L}_n = \hat{S}_n^-$ dissipation with long-range spatial profile $f(|r|) = (|r|+1)^{-\alpha}$. (a) Spreading and contraction of spin correlations described by Eq. (8.6) for $\alpha = 1.25$ and $\kappa = 1.0$; the green dotted line tracks the correlation front which spreads as $t \approx r^\beta$ at short times. (b) Dynamics of the spin wave density and evolution of the collective magnetization on the Bloch sphere (inset) for the same choice of parameters as (a). The density of spin waves has a peak at time t^* where the front of correlations reverses (cf. (a)). (c) Scaling parameter β as a function of α. The black dotted line represents $\beta = \alpha$; we see that $\beta \simeq \alpha$ independent of the dissipation strength κ. (d) Dependence of t^* on α and κ. For all panels we evaluate dynamics in the thermodynamic limit with the initial state of the system representing a spin coherent state pointing in the direction $\theta(t=0) = 0.4\pi$, $\phi(t=0) = 0$.

leading order ($C^{zz}(r, t \to 0) \propto t + \mathcal{O}(t^2)$) as we start with an uncorrelated spin coherent state for which $C^{zz}(r, t=0)$ is vanishing. The second equation in (8.9) therefore implies $\nu\eta = -1$ and combining them, yields $\eta = 1/\alpha$. We therefore see that the correlation front must scale as $t \simeq r^\beta$ with $\beta = \alpha$ as numerically observed. At large α, correlations disappear ($\beta \to \infty$) consistently with the Lindbladian becoming diagonal and representing independent local emission events. This behavior differs from the large α light cone of long-range Hamiltonians which becomes increasingly linear

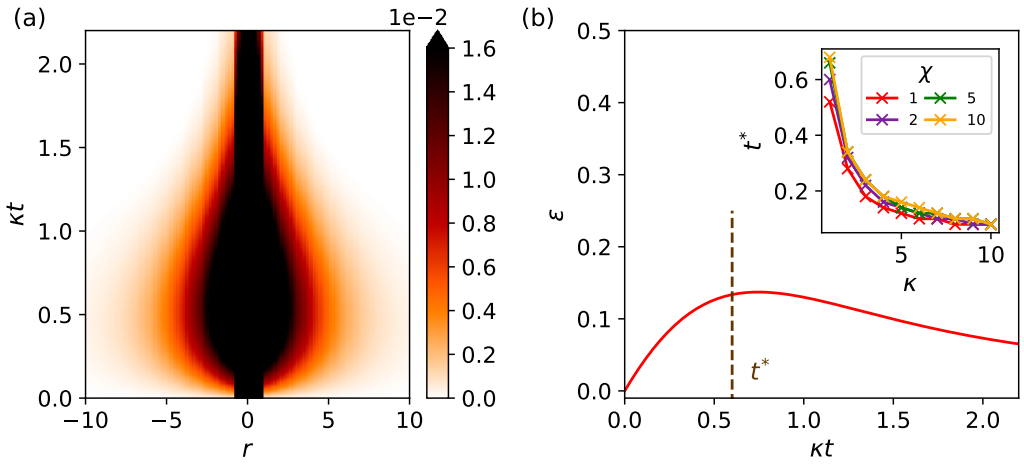

Figure 28: Dynamics of $\hat{L}_n = \hat{S}_n^-$ dissipation with short-range spatial profile $f(|r|) = \exp(-|r|/\chi)$. (a) Spreading and contraction of spin correlations described by Eq. (8.6) for $\chi = 2.0$ and $\kappa = 1.0$. (b) Dynamics of spin-wave density and correlation function transition time (inset). For all panels we evaluate dynamics in the thermodynamic limit with the initial state of the system representing a spin coherent state pointing in the direction $\theta(t = 0) = 0.4\pi$, $\phi(t = 0) = 0$.

($\beta \approx 1$) [118]. As stated in Sec. 7.1, this difference arises from the proper way to define long-range dissipation ($f(|n - m|) = (|n - m| + 1)^{-\alpha}$) versus coherent dynamics ($f(|n - m|) = |n - m|^{-\alpha}$). In the former case, we tend towards independent dissipators for large α, while in the latter case one retrieves nearest-neighbor interactions. Similar phenomenology is retrieved for short-range losses when $\chi \to 0$.

At late times, long-range dissipation has a contractive effect on correlation dynamics. Correlations reach their maximum spread at a time t^* where the spin wave density exhibits a peak. Spin waves are pumped by the second term in the right hand side of Eq. (8.5) which acts as parametric drive, and they are damped by the first term of (8.5) as soon as the collective magnetization enters the southern hemisphere. For sufficiently strong dissipation, the collective magnetization will always eventually enter the southern hemisphere as the south pole is the dark state for strong spin losses. The competition of this self-pumping mechanism and the incoherent depolarization of spins is what leads to the opening and closing of the correlation function. The transition time t^* corresponds to the timescale upon which the spin wave damping term starts to dominate dynamics (see Fig. 27(d)). Correlations vanish in the ab-

sence of spin wave excitations and therefore the correlation function $C^{zz}(r,t)$ shrinks to zero as spin waves are progressively dissipated into the environment for $t > t^*$ (see Fig. 27(b)). At sufficiently late times ($t \gg t^*$), there is negligible spin wave density and the system is almost in a coherent state of spins pointing in a direction near the south pole. Closer inspection into the correlations near the steady state shows that $C^{zz}(r) \propto 1/r^\alpha$ for large inter-spin distances. In fact, this $1/r^\alpha$ decay of correlations appears to hold at all times.

We also examine the correlation dynamics for a short-range spatial profile. Figure 28(a) shows that the correlations follow the same qualitative behavior as the the long-range case (they grow for a period before contracting). The time t^* characterizing this transition is shown in Fig. 28(b) and it corresponds to the time upon which spin-wave excitations reach their maximal value and start decreasing. In both long- and short-range cases, the time scale t^* increases for spatial profiles that decay more slowly in space. However, the dependence on spatial profile is weak and the transition time primarily depends on the decay rate κ which sets the overall time-scale of the dissipation channel. The main difference between long- and short-range dissipative dynamics is that the correlations decay more rapidly in space for the short-range case, as seen by comparing Fig. 27(a) to Fig. 28(a).

The spread and contraction of correlations arising from non-local dissipation is reminiscent of dynamical signatures of confinement in purely unitary spin systems [187, 221, 348, 64]. There, correlations are confined due to bound states in the spectrum of Hamiltonianan which arise from an effective attractive potential for low-lying excitations. Here, however, confinement of correlations is an inherently non-equilibrium phenomenon stemming from the fact that non-local dissipation channels can both create and destroy correlations.

8.2 Correlation engineering using non-local dissipation and a control field

Let us summarize the basic intuition for the dynamics of the non-local dissipation channel analyzed in the previous section. When the collective spin is in the northern hemisphere of the Bloch sphere, the average magnetization of the system is positive and the jump operator $\hat{S}_n^-$ creates spin-waves by lowering the magnetization away from that of a spin-coherent state which is fully polarized upwards. When the collective spin is in the southern hemisphere of the Bloch sphere, the average magnetization of the system is negative and the jump operator destroys spin-waves by lowering the average magnetization towards that of a spin-coherent state which is fully polarized downwards. The collective spin therefore acts as a mobile vacuum for excitations and its position controls whether the dissipation channel predominently creates or destroys correlations carried by these excitations.

This intuition intimates a natural way to engineer correlations generated by the non-local dissipation channel. A uniform external field which guides the motion of the collective spin, and thereby influences when dissipation creates or destroys excitations, can be used to modulate the spatio-temporal correlation pattern created by the $\hat{L}_n = \hat{S}_n^-$ dissipation channel. We demonstrate this control using a field of magnitude ω_F and direction φ. This field is modeled by adding a unitary dynamics channel described by the Hamiltonian $\hat{H} = \omega_F \left(\cos\varphi \hat{S}^x + \sin\varphi \hat{S}^z \right)$ to the non-local dissipation channel described by Eq. 8.2.

In Fig. 29(a)-(d), we show how the long-range confinement pattern of Fig 27 can be modified. Figure 29(b) shows temporal control over the correlation pattern. The window of time during which the system remains correlated before decaying to an uncorrelated state is extended by a factor of approximately five.

Figure 29(d) shows that the confinement pattern can be modulated to exhibit oscillating correlations, which resembles a dissipation-induced limit cycle dressed by quantum fluctuations. This behaviour, however, is metastable and the system reaches a non-oscillatory steady state. For parameters $\alpha \leq 1$, $\varphi = 0$, and $\omega_F \geq \kappa$, the system

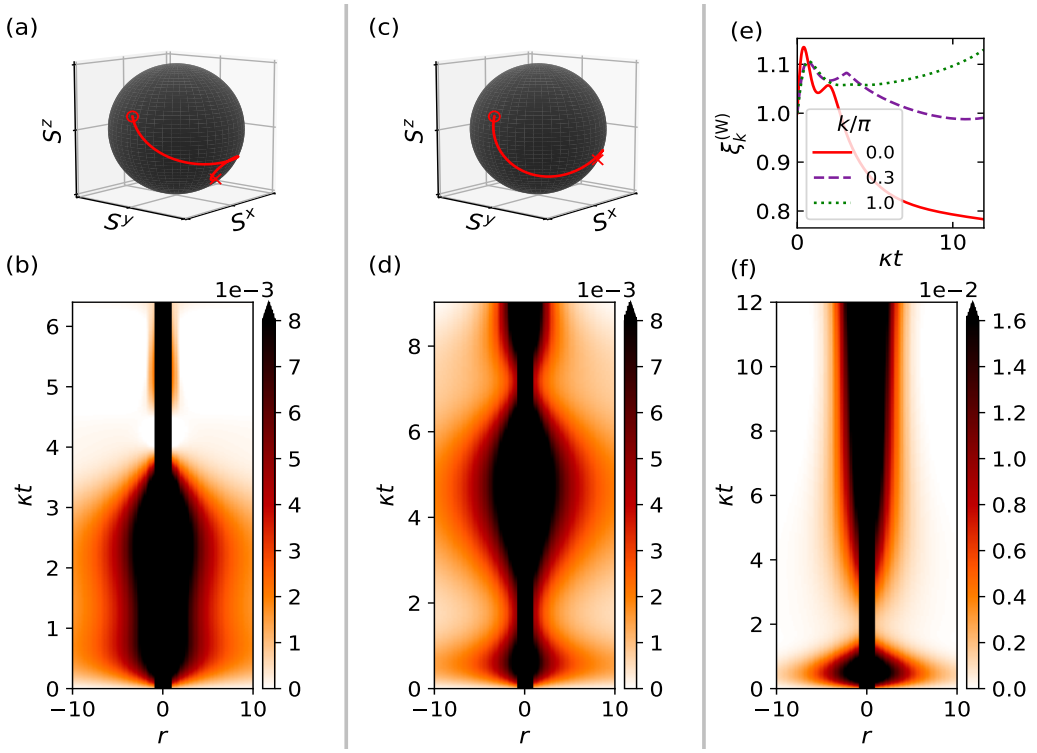

Figure 29: Modulating correlations via a uniform field. We initialize the system in a spin coherent state pointing in the direction $\theta(t=0) = 0.4\pi$, $\phi(t=0) = 0$ for all panels. (a),(b) Collective spin motion and connected correlation function $C^{zz}(r,t)$ for a long-range spatial profile with $\alpha = 1.25$. System parameters are $\kappa = 0.8$, $\omega_F = 1.0$, and $\varphi = 0.25\pi$. (c),(d) Collective spin motion and connected correlation function $C^{zz}(r,t)$ for a long-range spatial profile with $\alpha = 1.1$. System parameters are $\kappa = 0.95$, $\omega_F = 1.0$, and $\varphi = 0.1\pi$. (e),(f) Squeezing parameter and connected correlation function $C^{zz}(r,t)$ for a short-range spatial profile with $\chi = 3.0$. System parameters are $\kappa = 1.2$, $\omega_F = 1.0$, and $\varphi = 0$.

is fully described by the classical motion of the collective spin and exhibits persistent oscillations [164]. However, for $\alpha > 1$, we find that these oscillations are eventually washed out by many-body fluctuations.

In Fig. 29(e)-(f), we manipulate the short-range confinement pattern of Fig 28 via the uniform field. Specifically, we send the system to an increasingly correlated state at late times in a fashion reminiscent of traditional dissipative state preparation schemes [92].

Many such schemes try to leverage collective dissipation to prepare metrologically useful states [81]. Collective dissipation limits the system to sensing uniform external fields. Non-local dissipation, however, may be able to prepare metrologically useful

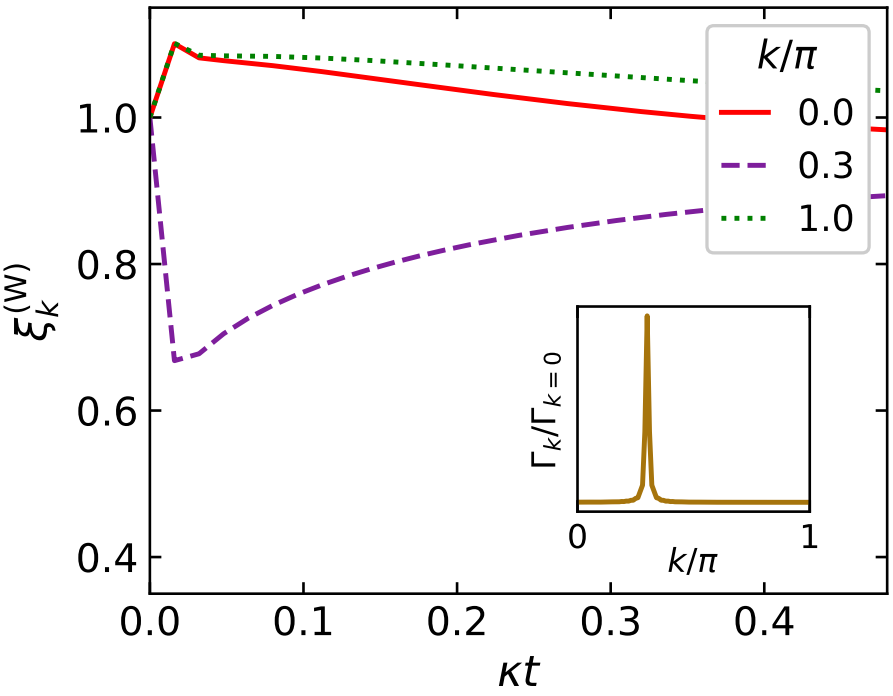

Figure 30: Preferentially squeezing a target wavevector. Spatial squeezing parameter for a spatial profile $f_{n,m} = \cos(k^*|n-m|)\, e^{-|n-m|/\chi}$ with $\chi = 50$ and $k^* = 0.3\pi$. System parameters are $\kappa = 0.8$, $\omega_F = 1.0$, and $\varphi = 0$. The system is initialized in a spin coherent state pointing in the direction $\theta(t=0) = 0.4\pi$, $\phi(t=0) = 0$. The figure inset shows that the Fourier transform of the spatial profile is peaked around k^*.

states for sensing spatially varying fields. We can explore this potential by examining the finite wavevector squeezing parameter

$$\left(\xi_k^{(\mathrm{W})}\right)^2 = \min_{\boldsymbol{e}_\perp}\left\{\frac{2^{\delta_{k\neq 0}} N\langle \Delta\left(\boldsymbol{e}_\perp \cdot \mathrm{Re}\{\hat{\boldsymbol{S}}_k\}\right)^2\rangle}{|\langle \boldsymbol{e}_s \cdot \hat{\boldsymbol{S}}_{\mathrm{tot}}\rangle|^2}\right\}. \tag{8.10}$$

where $\hat{\boldsymbol{S}}_k = \sum_n e^{-ikn}\hat{\boldsymbol{S}}_n$ and $\delta_{k\neq 0} = 1$ if $k \neq 0$ and 0 otherwise. In Sec. 8.3, we show that $\xi_k^{(\mathrm{W})}$ is a generalization of the Wineland collective squeezing parameter [370, 227], and quantifies metrologically useful entanglement when sensing a particular spatial mode of a spatially varying field.

Figure 29(e) shows that different wavevectors exhibit varying amounts of squeezing depending on the Fourier transform of the spatial profile, given by $\Gamma_k = \sum_{r=n-m} e^{ikr} f(|r|)$. Modes with larger Γ_k will get squeezed more at short times. This fact can be exploited

to preferentially squeeze a target mode k^*.

We demonstrate this control in Fig. 30, where we show the dynamics of $\xi_k^{(\mathrm{W})}$ for a spatial profile $f_{n,m} = \cos(k^*|n-m|)\, e^{-|n-m|/\chi}$ with $k^* = 0.3\pi$. The figure inset shows that Γ_k is a Lorentzian of width χ peaked at k^*. We see that the $k = k^*$ mode is squeezed more than other modes, including the collective $k = 0$ mode which witnesses pairwise entanglement. Furthermore, squeezing at k^* seems to antisqueeze other modes. The correlation dynamics arising from a non-local dissipation channel can thus be engineered using a uniform control field to generate states which act as a resource for sensing spatially varying external fields.

8.3 Finite wavevector squeezing parameter

Here, we show that the finite wavevector squeezing parameter described in the previous section acts as a witness of metrologically useful entanglement for the task of measuring a spatial Fourier component of an external field. Consider a spatially varying magnetic field $\mathbf{B}(\mathbf{r}) = (0, 0, B(\mathbf{r}))$ pointing in the z-direction of the coordinate system applied to a spin chain of N spins represented by operators $\hat{\mathbf{S}}_n$, where n indexes the position of each spin. If the field is applied for a time t, the effect on a system state ρ_0 is

$$\rho_0 \to \rho_t(\{B_n\}) = \hat{U}(t)\, \rho_0 \hat{U}(t)^\dagger \tag{8.11}$$

where $\hat{U}(t) = \exp\{i\hat{H}t\}$, $\hat{H} = \sum_{n=1}^{N} B_n \hat{S}_n^z$, and $B_n = B(\mathbf{r}_n)$. Letting $\mathbf{r}_n = na$ and setting the lattice constant as $a = 1$, we can decompose the magnetic field in terms of Fourier components as $B_n = \frac{2}{N}\sum_k B_k \cos(kn)$ with $k \in \frac{2\pi}{N}\{1, N\}$. The Fourier components are given by the inverse transform $B_k = \sum_n B_n \cos(kn)$. Our goal is to estimate B_{k^*} for a desired wavevector $k = k^*$ using M measurements performed on the state ρ_t, given that the magnetic field strengths $\{B_n\}$ are unkown a priori. Estimating B_{k^*} thus amounts to estimating a linear function

$$f(\boldsymbol{\alpha}, \boldsymbol{\theta}) = \boldsymbol{\alpha} \cdot \boldsymbol{\theta} \tag{8.12}$$

of unknown parameters $\boldsymbol{\theta} = \{B_n\}$ and known coefficients $\boldsymbol{\alpha} = \{\cos(k^* n)\}$. The precision bounds, known as Cramer-Rao bounds, for such multiparameter estimation tasks were derived in Ref. [110]. Let Θ_{k^*} be the estimator of B_{k^*}, with a mean $\mathbb{E}[\Theta_{k^*}]$ and variance $\Delta(\Theta_{k^*})^2$. The lower bound on the variance sets the maximum achievable precision of the estimator. If the initial state ρ_0 has no entanglement, then $\Delta(\Theta_{k^*})^2 \geq \Delta_{\mathrm{SQL}}(\Theta_{k^*})^2$ where

$$\Delta_{\mathrm{SQL}}(\Theta_{k^*})^2 = \frac{N}{Mt^2}\frac{1}{2^{\delta_{k^*\neq 0}}} \tag{8.13}$$

is known as the standard quantum limit (SQL). We have used the shorthand $\delta_{k^*\neq 0} = 1$ if $k^* \neq 0$ and zero otherwise. If we allow entanglement in the initial state ρ_0, then $\Delta(\Theta_{k^*})^2 \geq \Delta_{\mathrm{HL}}(\Theta_{k^*})^2$ where

$$\Delta_{\mathrm{HL}}(\Theta_{k^*})^2 = \frac{1}{Mt^2} \tag{8.14}$$

is known as the Heisenberg limit (HL). The key point is that $\Delta_{\mathrm{SQL}}(\Theta_{k^*})^2 / \Delta_{\mathrm{HL}}(\Theta_{k^*})^2 \propto N$, therefore entanglement allows a factor N scaling improvement in the precision of the estimator. Importantly, as the generators $\{\hat{S}_n^z\}$ commute with each other, the Heisenberg limit can in principle be saturated with an optimal choice of initial state ρ_0 and measurement protocol.

In order to put the above expressions for the SQL and HL in a more familiar context, consider the quantity $\phi_0 = \frac{1}{N} B_{k^*=0}$ and its estimator Φ_0. This quantity corresponds to measuring the uniform component of the magnetic field and has precision limits

$$\Delta_{\mathrm{SQL}}(\Phi_0)^2 = \frac{1}{NMt^2}, \tag{8.15}$$

$$\Delta_{\mathrm{HL}}(\Phi_0)^2 = \frac{1}{N^2 Mt^2}, \tag{8.16}$$

which are the usual expressions for the single parameter estimation problem typically considered in quantum-enhanced metrology.

We can similarly gain intuition for the $k^* \neq 0$ case by framing it as a single

parameter estimation problem. Let us define the Fourier transformed spin operators as $\hat{\boldsymbol{S}}_k = \sum_n e^{-ikn}\hat{\boldsymbol{S}}_n$, with the inverse transform being $\hat{\boldsymbol{S}}_n = \frac{1}{N}\sum_k e^{ikn}\hat{\boldsymbol{S}}_k$. Then, we can write the Hamiltonian generating evolution due to the magnetic field as $\hat{H} = \frac{2}{N}\sum_k B_k \operatorname{Re}\{\hat{S}^z_k\}$ where $\operatorname{Re}\{\hat{\boldsymbol{S}}_k\} = \sum_n \cos(kn)\,\hat{\boldsymbol{S}}_n$. The variance of the estimator Θ_{k^*} is then bounded by generator of B_{k^*} in $\hat{H}$ [284, 110, 5]. Specifically, we have $\Delta(\Theta_{k^*})^2 \geq \Delta_{\mathrm{G}}(\Theta_{k^*})^2$ where $\Delta_{\mathrm{G}}(\Theta_{k^*})^2 = 1/(Mt^2 4\Delta\left(\hat{G}_{k^*}\right)^2)$ and $\hat{G}_{k^*} = \partial\hat{H}/\partial B_{k^*} = \frac{2}{N}\operatorname{Re}\{\hat{S}^z_{k^*}\}$. This yields the precision bound

$$\Delta_{\mathrm{G}}(\Theta_{k^*})^2 = \Delta_{\mathrm{SQL}}(\Theta_{k^*})^2 \frac{2^{\delta_{k^*\neq 0}}}{16}\frac{N}{\Delta\left(\operatorname{Re}\{\hat{S}^z_{k^*}\}\right)^2}. \tag{8.17}$$

The bound in Eq. (8.17) is typically looser than the one in Eq. (8.14), but provides intuition for how decreasing the variance of the operator $\hat{S}^z_{k^*}$ increases the potential precision in the estimate of B_{k^*}.

We now give an example of an estimator that can exploit squeezing of this variance to provide a metrological advantage. Consider an experiment that makes M measurements of an observable $\hat{\mu}$ on the state $\rho_t(\theta)$ that depends on the unknown parameter of interest, θ. Let the expected value of this observable be $\bar{\mu} = \operatorname{Tr}\{\hat{\mu}\rho_t(\theta)\} \equiv f(\theta)$, where we have made the dependence on θ explicit, and the sample average of the measurements be $\bar{\mu}_M$. The method of moments (MOM) estimator is defined as the value of θ for which the expectation value $\bar{\mu}$ equals the sample average: $\Theta_{\mathrm{mom}} = f^{-1}(\bar{\mu}_M)$ [284]. We have $\bar{\mu}_M = f(\Theta_{\mathrm{mom}})$, and in the limit of many measurements, the law of large numbers states that $\bar{\mu}_M \approx \bar{\mu} = f(\theta)$. Therefore, we expect $\Theta_{\mathrm{mom}} \approx \theta$ and we can expand $\bar{\mu}_M = f(\Theta_{\mathrm{mom}})$ around $\Theta_{\mathrm{mom}} = \theta$:

$$f(\Theta_{\mathrm{mom}}) \approx f(\theta) + \left.\frac{\partial f}{\partial\theta}\right|_\theta (\Theta_{\mathrm{mom}} - \theta). \tag{8.18}$$

Plugging in $\bar{\mu}_M$ and $\bar{\mu}$, we have

$$\bar{\mu}_M \approx \bar{\mu}(\theta) + \left.\frac{\partial\bar{\mu}}{\partial\theta}\right|_\theta (\Theta_{\mathrm{mom}} - \theta). \tag{8.19}$$

The convenient aspect of the MOM estimator is that the value Θ_{mom} can be extracted directly from the experimental sample average $\bar{\mu}_M$. Extracting the estimate, however, requires knowledge of the functional form $\bar{\mu}(\theta)$, or its inverse, as is the case in the usual Ramsey metrology protocol where typically $\bar{\mu}(\theta) \propto \cos^2(\theta)$. Alternatively, the MOM estimate can be extracted using the above Taylor expansion if we know a calibration value θ_c that is close to the true unknown value θ, as well as $\bar{\mu}(\theta_c)$ and $\frac{\partial \bar{\mu}}{\partial \theta}|_{\theta_c}$ with high precision [5]:

$$\bar{\mu}_M \approx \bar{\mu}\left(\theta_c\right) + \left.\frac{\partial \bar{\mu}}{\partial \theta}\right|_{\theta_c} \left(\Theta_{\text{mom}} - \theta_c\right). \tag{8.20}$$

In either case, the variance of the estimator can be calculated in the limit of large M by identifying $\Delta\left(\Theta_{\text{mom}}\right)^2 \approx \left(\Theta_{\text{mom}} - \theta\right)^2$ and $\Delta\left(\bar{\mu}(\Theta_{\text{mom}})\right)^2 \approx M\left(\bar{\mu}(\Theta_{\text{mom}}) - \bar{\mu}(\theta)\right)^2$ in Eq. (8.19), or by replacing $\theta \to \theta_c$ in these expressions and then using them with Eq. (8.20). Letting $\hat{G}_\theta = \partial \hat{H}/\partial\theta$, we have $\frac{\partial \bar{\mu}}{\partial \theta}|_{\theta_c} = -it\text{Tr}\{\left[\hat{G}_\theta, \hat{\mu}\right] \rho_t(\theta)\}$. The variance of the MOM estimator is then

$$\Delta\left(\Theta_{\text{mom}}\right)^2 = \frac{\langle \Delta\left(\hat{\mu}\right)^2 \rangle}{Mt^2 |\langle \left[\hat{G}_\theta, \hat{\mu}\right] \rangle|^2} \tag{8.21}$$

where $\langle \cdot \rangle = \text{Tr}\{\cdot \rho_t(\theta)\}$. For our problem to estimate $\theta = B_{k^*}$, we have $\hat{G}_\theta = \frac{2}{N}\text{Re}\{\hat{S}^z_{k^*}\}$. We pick a measurement observable $\hat{\mu} = \boldsymbol{e}_\perp \cdot \text{Re}\{\hat{\boldsymbol{S}}_{k^*}\}$ where $\boldsymbol{e}_\perp$ represents a unit vector in the plane perpendicular to both the mean spin direction, $\boldsymbol{e}_s$, and the direction of the external magnetic field, $\boldsymbol{e}_z$. The variance of our MOM estimate for B_{k^*} is

$$\Delta_{\text{mom}}\left(\Theta_{k^*}\right)^2 = \frac{N}{Mt^2} \frac{N\langle \Delta\left(\boldsymbol{e}_\perp \cdot \text{Re}\{\hat{\boldsymbol{S}}_{k^*}\}\right)^2 \rangle}{|\langle \boldsymbol{e}_s \cdot \hat{\boldsymbol{S}}_{\text{tot}} \rangle + \langle \boldsymbol{e}_s \cdot \text{Re}\{\hat{\boldsymbol{S}}_{2k^*}\} \rangle|^2} \tag{8.22}$$

$$= \frac{N}{Mt^2} \frac{N\langle \Delta\left(\boldsymbol{e}_\perp \cdot \text{Re}\{\hat{\boldsymbol{S}}_{k^*}\}\right)^2 \rangle}{4|\sum_n \cos^2\left(k^* n\right) \langle \boldsymbol{e}_s \cdot \hat{\boldsymbol{S}}_n \rangle|^2} \tag{8.23}$$

$$\leq \frac{N}{Mt^2} \frac{N\langle \Delta\left(\boldsymbol{e}_\perp \cdot \text{Re}\{\hat{\boldsymbol{S}}_{k^*}\}\right)^2 \rangle}{4|\langle \boldsymbol{e}_s \cdot \hat{\boldsymbol{S}}_{\text{tot}} \rangle|^2} \tag{8.24}$$

where $\hat{\boldsymbol{S}}_{\text{tot}} = \hat{\boldsymbol{S}}_{k=0} = \sum_n \hat{\boldsymbol{S}}_n$ and we have used the fact that spin operators satisfy the commutation relation $\left[\hat{S}_k^\alpha, \hat{S}_{k'}^\beta\right] = i\varepsilon^{\alpha\beta\gamma}\hat{S}_{k+k'}^\gamma$ for $\alpha, \beta, \gamma \in \{x, y, z\}$. We can thus upper bound the variance of the MOM estimator as

$$\Delta_{\text{mom}}^{\text{ub}}\left(\Theta_{k^*}\right)^2 = \Delta_{\text{SQL}}\left(\Theta_{k^*}\right)^2 \xi_{k^*}^2 \tag{8.25}$$

with

$$\xi_{k^*}^2 = \frac{2^{\delta_{k^*\neq 0}} N \langle \Delta\left(\boldsymbol{e}_\perp \cdot \text{Re}\{\hat{\boldsymbol{S}}_{k^*}\}\right)^2 \rangle}{|\langle \boldsymbol{e}_s \cdot \hat{\boldsymbol{S}}_{\text{tot}} \rangle|^2}, \tag{8.26}$$

For $k^* = 0$, we get Wineland's metrological squeezing parameter [284], and therefore Eq. (8.26) serves as a generalization of Wineland's parameter to the case of sensing specific Fourier components of a spatially varying field. If $\xi_{k^*}^2 < 1$, then a MOM estimator can exploit entanglement in the system to measure this Fourier component with a precision beyond the standard quantum limit. The estimator requires that we can measure $\langle \boldsymbol{e}_\perp \cdot \text{Re}\{\hat{\boldsymbol{S}}_{k^*}\}\rangle$. Using the Fourier decomposition of $\hat{\boldsymbol{S}}_{k^*}$, this requires computing $\langle \boldsymbol{e}_\perp \cdot \hat{\boldsymbol{S}}_n \rangle$, which can easily be extracted from simultaneous projective measurements of $\langle \hat{S}_n^z \rangle$ of each spin after rotation of $\boldsymbol{e}_\perp$ to the $\boldsymbol{e}_z$ basis. Such measurements are routinely performed in cold atom systems using flourescence imaging to determine the occupation of the atoms in each of their internal states (corresponding to spin up and spin down).

In general, if we are trying to characterize the metrological utility of a state ρ_0 with a fixed mean spin direction $\boldsymbol{e}_s$, we can presume control over the direction of the external magnetic field $\mathbf{B}(na)$ that is being sensed and align it for greatest sensitivity. The metrological gain to sense a Fourier component at wavevector k of the field can then be quantified via the finite wavevector squeezing parameter

$$\left(\xi_k^{(\text{W})}\right)^2 = \min_{\boldsymbol{e}_\perp}\left\{\frac{2^{\delta_{k\neq 0}} N \langle \Delta\left(\boldsymbol{e}_\perp \cdot \text{Re}\{\hat{\boldsymbol{S}}_k\}\right)^2 \rangle}{|\langle \boldsymbol{e}_s \cdot \hat{\boldsymbol{S}}_{\text{tot}} \rangle|^2}\right\}, \tag{8.27}$$

where the minimization is performed over all directions $\boldsymbol{e}_\perp$ that are perpendicular to the mean spin direction $\boldsymbol{e}_s$. One should be careful in the interpretation of the

above generalized squeezing parameter. The spin operators at a given wavevector k do not form a closed spin algebra, and therefore there is no single Bloch sphere that can be associated with this spin mode. Therefore, the usual intuition of squeezing a quadrature of the spin on its Bloch sphere does not hold. Nonetheless, Eq. (8.27) does quantify the amount of metrological gain that can be achieved due to entanglement in the state using projective measurements of local spin operators (e.g. $\langle \hat{S}_n^z \rangle$). The reason is that reducing the variance of the generator of the estimated parameter helps increase the precision of the estimate, as described in Eq. (8.17). In general, the precision of this MOM estimator is worse than the optimal precision set by Eq. (8.14), but one may hope to find squeezing values, $(\xi_k^{(\mathrm{W})})^2$, which scale as $1/N$ and therefore provide the same scaling advantage. More optimal estimators can saturate the bound of Eq. (8.14) [110, 291, 292, 327, 372].

8.4 Discussion

In this part of the thesis, we have shown how quantum simulators may be used to investigate the open system dynamics of quantum many-body systems as well as dissipative quantum information processing. Compared to purely unitary strategies, dissipative protocols may hold unique advantages in a variety of applications as irreversible dynamics is stable to variations in the initial state. We have checked, for instance, that the dynamical features shown in Figs. 27, 28, and 29 do not depend qualitatively on the choice of initial state. In contrast, the dynamical confinement of correlations in long-range interacting unitary quantum simulators requires careful preparation of the initial state [187, 221, 348, 64].

The spread of correlations in unitary long-range quantum simulators has proven a fruitful area of inquiry for understanding entanglement dynamics in many-body systems [149, 364, 117]. By choosing a spatial profile $f_{n,m} = (|n-m|+1)^{-\alpha}$, our platform turns into a non-Hermitian analogue of such systems, thus opening an opportunity to explore how the purely dissipative character of dynamics affects entanglement spreading. The far-from-equilibrium dynamics of many closed quantum spin

chains is still not fully understood despite much theoretical effort [168]. Dissipative channels which can generate correlations open the door to richer dynamics, but can make the system harder to analyze. Quantum simulators are thus a valuable tool to study these systems.

The correlation function in Eq. (8.6) can be experimentally measured by state-selective fluorescence imaging [283]. Initially preparing a spin texture alternatively allows one to track the dynamics of the system with direct measurements of the local magnetization [85], potentially revealing novel transport mechanisms assisted by non-local dissipation. Our platform also offers the prospect of studying quantum information scrambling [238, 28] and novel phase transitions [94] in purely dissipative cavity QED simulators.

Furthermore, the ability to squeeze the system at desired wavevectors may be useful for spatially-resolved magnetometry, thus providing an advantage over systems employing homogeneous, collective dissipation [82], which can only squeeze the collective spin mode. Realizing our platform's potential for spatial magnetometry requires optimizing the choice of profile, $f_{n,m}$, and jump operator, $\hat{L}_n$, characterizing the non-local dissipation channel to maximally decrease the value of $\xi_k^{(\mathrm{W})}$ within the Heisenberg limit (see Appendix 8.3). Feedback conditioned on emitted photons and use of ensembles of atoms may offer additional routes towards increased metrological sensitivty [85, 315, 216, 77, 191].

From a methodological perspective, there are several interesting directions that could be explored with formalisms that go beyond the limitations of the NEQSWT developed in Chap. 7. For example, we plan to extend the generalized NEQSWT to a Hartree-Fock treatment of non-linear effects beyond the leading order Holstein-Primakoff expansion. This would allow us to analyze systems with sizeable spin-wave densities, enabling the study of systems with highly correlated initial states, as well as exploring the possibility of dynamical phase transitions arising from competition between unitary dynamics generated by a Hamiltonian and dissipative dynamics generated by a Lindblad channel.

In order to provide a closer benchmark with cavity-QED quantum simulation

experiments and explore regimes where coherent and dissipative dynamics of the cavity compete, a method to treat the combined light-matter system is required. We envision the possibility of extending variational many-body methods [336] to study how correlations spread in the system when the cavity photon cannot be adiabatically eliminated and will therefore participate in the dynamics of the atoms. When the photon linewidth is decreased, the spatio-temporal spin correlation patterns may get modified in non-trivial ways [178].

Part IV

Dynamics of practical systems: NMR spectroscopy

Chapter 9

Introduction

In the prior two parts of the thesis, we explored how quantum simulation can be used to study the closed and open system dynamics of physics systems of fundamental scientific interest. Quantum simulation also has potential utility for many applications of practical interest, including quantum chemistry systems such as the FeMo cofactor of nitrogenase with relevance to industrial fertilizer production [295], material science systems such as perovskites with relevance to solar energy [125], and physics systems such as high-temperature superconductors with relevance to fusion energy and defense applications [38]. Useful quantum simulation of these systems, however, will likely require fault tolerant quantum computers or simulators that will take an appreciable amount of time to develop. It is therefore interesting to consider if there are any practical applications where near- and intermediate-term quantum simulators can add value.

This part of the thesis explores quantum simulation in the context of an application of significant scientific and industrial relevance: nuclear magnetic resonance (NMR) spectroscopy. NMR spectroscopy is used both fundamental biochemistry as well as pharmaceutical drug development. The essence of the technique is to infer information about the structure and dynamics of molecules based on observations of the dynamics of their nuclear and electronic spins. In most NMR experiments, the difference in orientations of the molecules in the sample, either due to rapid rotation in liquid-state samples or random orientations fixed during sample preparation in

solid-state samples, causes decoherence in the quantum dynamics of the many-body spin system describing the relevant degrees of freedom in the experiment. NMR experiments can thus be described by the dynamics of noisy quantum spins, which gives hope to simulate them with noisy near- and intermediate-term quantum simulators; the idea is to simulate one noisy spin system with another noisy effective spin system. Such simulations can prove very useful in inferring the molecule's chemical information of interest, and great effort has been invested in developing NMR simulation tools that run on classical computers [196]. Quantum hardware which more naturally simulates spin dynamics may have a natural advantage for certain contexts that are hard to simulate on classical computers.

The dynamics of NMR systems can vary widely depending on the experimental protocol that is used. Some experiments can be described by purely closed systems, such as those discussed in Part II, with a phenomenological decay added to the computed signal. Other experiments must be described with open systems, such as those discussed in Part III, as the chemical information of interest is contained in the dissipative dynamics itself. The generic NMR experiment thus contains information in both the unitary (closed) and dissipative (open) dynamics of the spins, and simulations must capture both types of dynamical channels. Here, we focus on simulations of NMR experiments which are accurately described by unitary dynamics, including many common liquid-state NMR protocols such as COSY, or ensemble averages over unitary dynamics, including solid-state NMR and ESR protocols such as DEER. We leave the case of dissipation-dominated protocols such as NOESY for future work.

We start by giving a background on the utility and challenge of NMR simulation in Chapter 10. In Chapter 11, we develop quantum algorithms to aid in the analysis of NMR experiments by simulating the spin dynamics in these experiments, and argue that noisy quantum simulators may still hold a practical advantage over classical computers for this application. In Chapter 12, we discuss both completed and proposed experimental demonstrations of the algorithm on a digital ion trap quantum computer and an analog superconducting quantum simulator respectively.

Near-term quantum computers and simulators are noisy and scaling their use

beyond proof-of-principle experiments is likely to rely upon software-hardware co-design, with error-aware algorithms and protocols optimized for the platforms they are run on. Therefore, in Chapter 13, we show how knowledge of noise in a system can be exploited to improve the design of gate-based quantum simulation algorithms, and concretely demonstrate the utility of our error-mitigation strategy in the context of NMR simulation.

Chapter 10

NMR spectroscopy

Nuclear magnetic resonance (NMR) spectroscopy is a widely used tool in materials chemistry and structural biology, providing insight into the structure, conformational dynamics, reaction state, and chemical environment of molecules [218]. NMR is employed to probe the structure of promising photovoltaic candidates [193] as well as medically-relevant biomolecules such as the intrinsically disordered proteins that cause Alzheimer's and Parkinson's [294, 102]. Despite their versatility, NMR experiments can be difficult to interpret, often requiring numerical simulation of the molecule's nuclear spin dynamics [294, 104]. The spin correlations in these quantum systems can spread in an exponentially large state space, making simulation on classical computers intractable for large molecules as well as for emerging experimental protocols such as zero-field NMR [351, 23].

In this chapter, we first present the spin Hamiltonian describing the effective dynamics of nuclear spins in an NMR system. We then give the initial state and observable measured during an NMR experiment. The NMR simulation task is to use a classical or quantum computer to simulate a quantum system which starts in this initial state, undergoes dynamics described by the appropriate spin Hamiltonian, and then has the appropriate observable measured. We close with a discussion on when this type of simulation is useful in the analysis of NMR experiments, and when these simulations are hard to perform on classical computers.

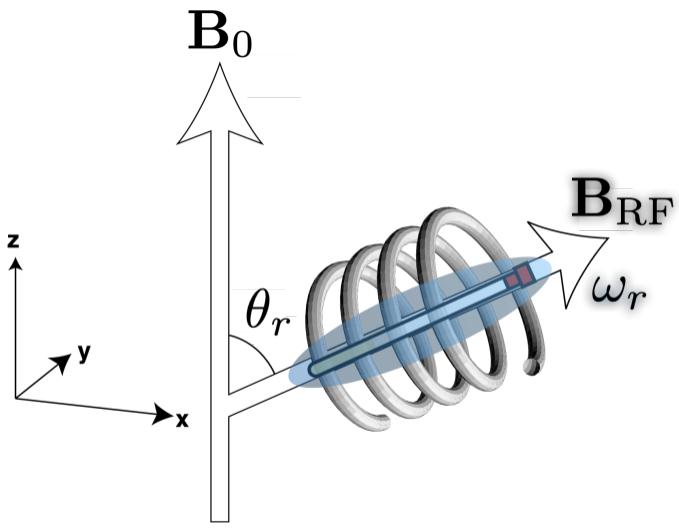

Figure 31: Orientation of a NMR Experiment. Modified from Ref. [218].

10.1 NMR Spin Hamiltonian

Consider a heteronuclear spin-$\frac{1}{2}$ system consisting of N_S nuclear spins $\left\{\hat{S}_i\right\}$ and N_I nuclear spins $\left\{\hat{I}_i\right\}$ of a different type. We assume that the (liquid or solid state) sample is placed in a superconducting magnet which produces a constant magnetic field oriented along the z-direction. The sample is attached to a rotor which can rotate the sample at a frequency ω_r around an axis that is tilted at a polar angle θ_r with respect to the solenoid axis (see Fig. 31). Additionally, there is an RF coil around the sample with the coil orientated along the rotor axis; this coil is used to both apply RF pulses on the spins as well as read out the free-induction decay (FID) signal which the NMR experiment measures.

The lab-frame spin Hamiltonian modeling the system can be built from the following terms:

- Larmor terms from the external magnetic field

$$\hat{H}_{0,S} = \omega_{0,S}\hat{S}^z_{\mathrm{tot}} \tag{10.1}$$

$$\hat{H}_{0,I} = \omega_{0,I}\hat{I}^z_{\mathrm{tot}} \tag{10.2}$$

where the Larmor frequencies are $\omega_{0,(S,I)} = -\gamma_{(S,I)}B_0$, the gyromagnetic ratios

of the S and I nuclei are $\gamma_{(S,I)}$, and the external Zeeman field is $\mathbf{B}_0 = B_0\mathbf{u}_z$. Note that we have defined the total spin operators as $\hat{S}^\alpha_{\text{tot}} = \sum_{i=1}^{N_S} \hat{S}^\alpha_i$ and $\hat{I}^\alpha_{\text{tot}} = \sum_{i=1}^{N_I} \hat{I}^\alpha_i$.

- RF field (assumed resonant with the Larmor frequencies):

$$\hat{H}_{\text{RF},S}(t) = -\omega_{\text{RF},S}\left(\cos(\omega_{0,S}t + \phi_{\text{RF}})\,\hat{S}^x_{\text{tot}} + \sin(\omega_{0,S}t + \phi_{\text{RF}})\,\hat{S}^y_{\text{tot}}\right) \tag{10.3}$$

$$= -\omega_{\text{RF},S}\hat{R}^z_S(\omega_{0,S}t + \phi_{\text{RF}})\,\hat{S}^x_{\text{tot}}\hat{R}^{z\dagger}_S(\omega_{0,S}t + \phi_{\text{RF}}) \tag{10.4}$$

$$\hat{H}_{\text{RF},I}(t) = -\omega_{\text{RF},I}\left(\cos(\omega_{0,I}t + \phi_{\text{RF}})\,\hat{I}^x_{\text{tot}} + \sin(\omega_{0,I}t + \phi_{\text{RF}})\,\hat{I}^y_{\text{tot}}\right) \tag{10.5}$$

$$= -\omega_{\text{RF},I}\hat{R}^z_I(\omega_{0,I}t + \phi_{\text{RF}})\,\hat{I}^x_{\text{tot}}\hat{R}^{z\dagger}_I(\omega_{0,I}t + \phi_{\text{RF}}) \tag{10.6}$$

where $\omega_{\text{RF},(S,I)} = \left|\frac{1}{2}\gamma_{(S,I)}B_{\text{RF}}\sin\theta_r\right|$ and the RF field is given as $\mathbf{B}_{\text{RF}}(t) = B_{\text{RF}}\cos\left(\omega_{0,(S,I)}t + \phi_{\text{RF}}\right)(\sin\theta_r\mathbf{u}_x + \cos\theta_r\mathbf{u}_z)$. Note that we have defined the rotation operators $\hat{R}^\alpha_S(\phi) = e^{-i\phi\hat{S}^\alpha_{\text{tot}}}$ and $\hat{R}^\alpha_I(\phi) = e^{-i\phi\hat{I}^\alpha_{\text{tot}}}$.

- Chemical shifts corresponding to the average electron distribution response to external magnetic fields (shielding):

$$\hat{H}_{0,S}(\Theta, \{\theta_r, \omega_r t\}) = \omega_{0,S}\sum_{i=1}^{N_S}\mathbf{h}_{S_i}(\Theta, \{\theta_r, \omega_r t\})\cdot\hat{\mathbf{S}}_i \tag{10.7}$$

$$\hat{H}_{0,I}(\Theta, \{\theta_r, \omega_r t\}) = \omega_{0,I}\sum_{i=1}^{N_I}\mathbf{h}_{I_i}(\Theta, \{\theta_r, \omega_r t\})\cdot\hat{\mathbf{I}}_i \tag{10.8}$$

where the lab-frame shifts $\mathbf{h}_{(S,I)_i}(\Theta(t), \{\theta_r, \omega_r t\})$ depend on the orientation of the molecule Θ in the rotor frame, taken to be the stationary frame of the sample, which in turn can vary in time in liquid samples due to thermally caused molecular rotation, as well as purposeful rotation of the sample at angle θ_r and frequency ω_r (often done for solid samples). If we fix the orientation of the molecule at time $t = 0$ and diagonalize the chemical shift tensor $\mu^{\alpha\beta}_{(S,N)} = \gamma_{(S,N)}h^\alpha_{(S,I)_i}B^\beta_0$, the eigenvectors represent the three directions in which an applied external field will cause a chemical shift in the same direction. We call this set of orthogonal eigenvectors the 'principal axis system'

(PAS) and the eigenvalues $\mathbf{h}^{P}_{(S,I)_i}$ are the princpal chemical shifts which do not depend on the molecular orientation, and therefore contain intrinsic information about the molecule. We can relate the the principal shifts to the lab-frame shifts as $h^{\alpha}_{(S,I)_i} = \sum_{\beta,\eta} \tilde{\mathcal{R}}^{\alpha\eta}(\theta_r, \omega_r t)\, \mathcal{R}_i^{\eta\beta}(\Theta)\, h_i^{P,\beta} \mathcal{R}_i^{\beta\eta}(\Theta)\, \tilde{\mathcal{R}}^{\eta\alpha}(\theta_r, \omega_r t)$ where $\alpha, \beta, \eta \in \{x, y, z\}$ and $\mathcal{R}_i(\Theta)$ is the orientation-dependent rotation matrix that rotates the PAS to the rotor frame, and $\tilde{\mathcal{R}}(\theta_r, \omega_r t)$ is the rotation matrix the rotates the rotor frame to the lab-frame where the external field $\mathbf{B}_0$ is pointing in the z-direction.

We define the isotropic chemical shift as the average of the principle shifts: $h^{\text{iso}}_{(S,I)_i} = \frac{1}{3}\left(h^{P,x}_{(S,I)_i} + h^{P,y}_{(S,I)_i} + h^{P,z}_{(S,I)_i}\right)$. For liquid state NMR without any rotor, rapid molecular tumbling causes the orientation-dependence of the lab-frame shift to average out leaving us with the leading contribution $h^{\alpha}_{(S,I)_i} = h^{\text{iso}}_{(S,I)_i}$. Furthermore, for high-field NMR, typically only the $h^{z}_{(S,I)_i}$ term contributes. Chemical shift anisotropy (CSA) is the deviation of the molecular orientation-dependent lab-frame shift from the isotropic shift leads, and this CSA acts as a relaxation mechanism that is secondary to dipolar relaxation but still important. We can roughly think of the CSA as the deviation of $h^{z}_{(S,I)_i}(\Theta)$ from the average value of the principal chemical shifts intrinsic to the molecule.

- Direct dipolar coupling between nuclear spins ('through-space' coupling):

$$\hat{H}_{D,SS}(\Theta, \{\theta_r, \omega_r t\}) = \sum_{i<j}^{N_S} K_{S_i,S_j}\left(\hat{\mathbf{S}}_i \cdot \hat{\mathbf{S}}_j - 3\left(\hat{\mathbf{S}}_i \cdot \mathbf{u}_{S_i,S_j}\right)\left(\hat{\mathbf{S}}_j \cdot \mathbf{u}_{S_i,S_j}\right)\right) \quad (10.9)$$

$$\hat{H}_{D,II}(\Theta, \{\theta_r, \omega_r t\}) = \sum_{i<j}^{N_I} K_{I_i,I_j}\left(\hat{\mathbf{I}}_i \cdot \hat{\mathbf{I}}_j - 3\left(\hat{\mathbf{I}}_i \cdot \mathbf{u}_{I_i,I_j}\right)\left(\hat{\mathbf{I}}_j \cdot \mathbf{u}_{I_i,I_j}\right)\right) \quad (10.10)$$

$$\hat{H}_{D,SI}(\Theta, \{\theta_r, \omega_r t\}) = \sum_{i=1}^{N_S}\sum_{j=1}^{N_I} K_{S_i,I_j}\left(\hat{\mathbf{S}}_i \cdot \hat{\mathbf{I}}_j - 3\left(\hat{\mathbf{S}}_i \cdot \mathbf{u}_{S_i,I_j}\right)\left(\hat{\mathbf{I}}_j \cdot \mathbf{u}_{S_i,I_j}\right)\right) \quad (10.11)$$

where $\mathbf{r}_{(S,I)_i,(S,I)_j} = r_{(S,I)_i,(S,I)_j}\mathbf{u}_{(S,I)_i,(S,I)_j}$ is the dipole vector connecting spin $(S,I)_i$ and $(S,I)_j$ with magnitude $r_{(S,I)_i,(S,I)_j}$ and direction $\mathbf{u}_{(S,I)_i,(S,I)_j}$. The

coupling constant $K_{(S,I)_i,(S,I)_j} = \frac{\mu_0}{4\pi}\gamma_{(S,I)_i}\gamma_{(S,I)_j}r^{-3}_{(S,I)_i,(S,I)_j}$ contains the dependence on the distance between the spins, while the direction $\mathbf{u}_{(S,I)_i,(S,I)_j} = \mathbf{u}_{(S,I)_i,(S,I)_j}(\Theta, \{\theta_r, \omega_r t\})$ contains the dependence on the molecule's orientation and rotor frame (defined by θ_r and $\omega_r t$). The dependence on Θ causes the primary relaxation mechanism in solid state NMR, with the distance dependence of the relaxation rate (encoded in $K_{(S,I)_i,(S,I)_j}$) allowing information to be inferred about the physical structure of the molecule.

- Indirect exchange (J) coupling between nuclear spins mediated by shared electron orbitals ('through-bound' coupling):

$$\hat{H}_{J,SS} = \sum_{i<j}^{N_S} \left(2\pi J_{S_i,S_j}\right) \hat{\mathbf{S}}_i \cdot \hat{\mathbf{S}}_j \tag{10.12}$$

$$\hat{H}_{J,II} = \sum_{i<j}^{N_I} \left(2\pi J_{I_i,I_j}\right) \hat{\mathbf{I}}_i \cdot \hat{\mathbf{I}}_j \tag{10.13}$$

$$\hat{H}_{J,SI} = \sum_{i=1}^{N_S}\sum_{j=1}^{N_I} \left(2\pi J_{S_i,I_j}\right) \hat{\mathbf{S}}_i \cdot \hat{\mathbf{I}}_j \tag{10.14}$$

  where $J_{(S,I)_i,(S,I)_j}$ are the J-coupling constants. The value of the J-coupling constant contains information about the bond torsion angles in the molecule, and therefore allows information to be inferred about the chemical structure of the molecule.

Note that the electric quadrupole interaction is very important for systems of spins that are greater than spin-$\frac{1}{2}$, but vanishes for spin-$\frac{1}{2}$ systems due to symmetry. In principle, for spin-$\frac{1}{2}$ systems, we should also include the spin-rotation interaction between the nuclear spin and the magnetic fields arising from the current generated by the molecules rapid motion, but this is typically irrelevant for liquid and solid state NMR; the interaction only contributes a third order relaxation mechanism behind the anisotropic dipolar interaction and the chemical shift anisotropy.

(10.15)

The overall Hamiltonian for a generic NMR system is then given as

$$\hat{H}_f(t) = \hat{H}_{0,S} + \hat{H}_{0,S}(t) + \hat{H}_{D,SS}(t) + \hat{H}_{J,SS} \tag{10.16}$$

$$+ \hat{H}_{0,I} + \hat{H}_{0,I}(t) + \hat{H}_{D,II}(t) + \hat{H}_{J,II} \tag{10.17}$$

$$+ \hat{H}_{D,SI}(t) + \hat{H}_{J,SI} \tag{10.18}$$

with the addition of $\hat{H}_{\mathrm{RF},S}(t)$ and/or $\hat{H}_{\mathrm{RF},I}(t)$ depending on if the RF field is applied at any given moment.

Typical parmeter values and scales in the system are

- $\theta_r = \theta_m \equiv \cos^{-1}\left(\frac{1}{\sqrt{3}}\right)\mathrm{rad} \approx 54.7^\circ$
- $\omega_r/2\pi \sim 1\mathrm{kHz} - 100\mathrm{kHz}$
- $\omega_{0,(S,I)} \sim 10\mathrm{MHz} - 1000\mathrm{MHz}$ (assuming a Zeeman field of $B_0 \sim 5\mathrm{T} - 20\mathrm{T}$)
- $\omega_{\mathrm{RF},(S,I)}/2\pi \sim 1\mathrm{kHz} - 200\mathrm{kHz}$
- chemical shifts: typically $10^{-4} \times \omega_{0,(S,I)} \sim 1\mathrm{kHz} - 100\mathrm{kHz}$
- dipolar coupling: $K_{(S,I)_i,(S,I)_j}/2\pi \sim 10\mathrm{kHz}$ for nuclei that are relatively close by (e.g. two ${}^1H$ that are ~$0.2\mathrm{nm} = 0.02\text{Å}$ apart)
- $J_{(S,I)_i,(S,I)_j}/2\pi \sim 1\mathrm{Hz} - 200\mathrm{Hz}$
- $\frac{\gamma_S}{\gamma_I} \sim 3 - 5$ where we have chosen[1] $\gamma_S > \gamma_I$ WLOG, and correspondingly $\frac{\omega_{0,S}}{\omega_{0,I}} \sim \frac{\omega_{\mathrm{RF},S}}{\omega_{\mathrm{RF},I}} \sim 3-5$ so the Larmor and RF Rabi frequencies for different nuclear species are off-resonant with each other
- temperature: room temperature corresponding to $k_B T/2\pi \sim 40\mathrm{THz}$

For high-field NMR experiments, which are those with a large external Zeeman field, we therefore have four broad scales in the system: THz (temperature), MHz (Larmor frequency, RF control field frequencies), kHz (chemical shifts, dipolar coupling, RF Rabi frequency, rotor frequency), Hz (J-coupling). For zero-field NMR, experiments

[1] e.g. let S be ${}^1\mathrm{H}$ and I be ${}^{13}\mathrm{C}$

the Zeeman field, chemical shifts, and RF fields vanish, and we add a DC magnetic field of 1G (corresponding to a Rabi frequency of $\omega_{\mathrm{DC},(S,I)} \sim 1\mathrm{kHz} - 10\mathrm{kHz}$) to apply pulses; the scales becomes THz (temperature), kHz (dipolar coupling, DC Rabi frequency, rotor frequency), Hz (J-coupling).

NMR is also used to study chemical exchange processes which involve one nuclei dynamically exchanging its environment with another (e.g. through bond rearrangement). This exchange changes the chemical shifts and J-coupling parameters. For fast exchange that is averaged out on the time-scale of NMR experiments, the chemical shifts and J-coupling parameters are a weighted average of the parameters before and after the exchange with the weight given by a temperature-dependent (reaction) equilibrium constant. The NMR spectrum can thus be measured at several different temperatures and the chemical shifts and J-couplings of each state of the reaction, as well as the enthalphy and entropy differences between states, can be determined by fitting. In this fast exchange case, no change is made to the Hamiltonian used in the NMR simulation and the chemical shifts and J-coupling parameters are just interpreted as the average parameters at the temperature of the given experimental spectrum that serves as the baseline for inference. For medium and slow exchange that is comparable to the timescale of NMR experiments, we add a time-dependence to the chemical shifts and J-couplings, with these parameters now evolving according to a classical rate equation with a temperature-dependent rate. Note that for the chemical shifts, this time-dependence is in addition to the time-dependence arising from changes in the molecules orientation. Information about the chemical exchange for medium and slow exchange processes can then be observed in the individual spectrum itself, in addition to comparison to spectra at different temperatures.

Recently, 'nanoscale' NMR has been demonstrated [224, 16], which uses NV centers in diamond to polarize and measure NMR signals in samples that are at the sub-μm scale (approximately cubic nanometers, or nm length scale) in both high- and low-field settings. This allows for NMR experiments on systems of $10^2 - 10^3$ nuclear spins, which is much smaller than the 10^{14} spins (corresponding to a macroscopic sample length scale) used in conventional NMR. Such an improved resolution

allows for NMR experiments on smaller volume samples and lower magnetic fields (making the experiment smaller and cheaper), as well as on single biological macromolecules (e.g. a single protein) that is attached to the diamond surface. Nanoscale NMR can be thought of as producing the same NMR signal as conventional NMR; the Hamiltonian and simulation protocol doesn't change, though the molecular orientation will remain fixed if single molecule NMR is done with a sample that is not rotating. Resolution of the technique must be significantly improved, however, before it is competitive with conventional NMR.

10.2 Experimental Protocol and Measurement

The NMR experiment is initialized by polarizing the spins in the sample into the an uncorrelated product state of spins pointing in the $+z$-direction. The typical way to do this in conventional high-field NMR is to turn on a strong external Zeeman field in the $+z$-direction and let the sample relax into thermal equilibrium at room temperature. The initial state of the system is then approximately $\rho_0 = \frac{1}{Z}\exp\left\{-\beta\hat{H}_0\right\}$ with $\hat{H}_0 = \hat{H}_{0,S} + \hat{H}_{0,I}$, where we have assumed that the Larmor frequencies $\omega_{0,(S,I)}$ are much larger than other scales in the system Hamiltonian so we can ignore other Hamiltonian terms. The room temperature of the experiment is a much higher scale than the Larmor frequencies, however, so we can approximate the state further as being at high-temperature: $\rho_0 \approx \frac{1}{Z}\left(\hat{I} - \beta\hat{H}_0\right)$. The system then undergoes time-evolution, with the RF field on or off at various times. We can describe this evolution with the operator $\hat{U}(t,0) = \mathcal{T}\exp\left(-i\int_0^t ds\hat{H}(s)\right)$ where

$$\hat{H}(t) = \hat{H}_f(t) + \sum_{n=0}^{\mathcal{N}-1} \text{rect}\left(\frac{t-t_n}{\tau_n}\right)\hat{H}_{\text{RF}}^{(n)}(t)$$

where $\hat{H}_{\text{RF}}^{(n)}(t) \in \left\{\hat{H}_{\text{RF},S}(t), \hat{H}_{\text{RF},I}(t), \hat{H}_{\text{RF},S}(t) + \hat{H}_{\text{RF},I}(t)\right\}$, τ_n is the duration of each RF pulse and t_n is the center time of the window it is applied in. The state of the system after this evolution is $\rho(t) = \hat{U}(t,0)\rho_0\hat{U}^\dagger(t,0)$. The NMR experiment then measures the total transverse magnetization of one of the nuclear species, described

by observable $\hat{S}^{+}_{\text{tot}}$ or $\hat{I}^{+}_{\text{tot}}$, as a function of time t. This measured signal is called the free induction decay (FID) and its Fourier transform yields the NMR spectrum. Depending on the spin species that is measured, the FID signal can thus be described as

$$S_A(t) = \left\langle \hat{A}^{+}_{\text{tot}}(t) \right\rangle = \text{Tr}\left\{ \hat{A}^{+}_{\text{tot}} \rho(t) \right\} \tag{10.19}$$

where $\hat{A}^{+}_{\text{tot}}(t) = \hat{U}^{\dagger}(t,0)\, \hat{A}^{+}_{\text{tot}} \hat{U}(t,0)$ and $A \in \{S, I\}$ is the species of nuclear spin we measure. Plugging in the approximation of the initial state, we have

$$S_A(t) \approx -\lambda \left(\text{Tr}\left\{ \hat{A}^{+}_{\text{tot}}(t) \left(\hat{S}^{z}_{\text{tot}} + \frac{\gamma_I}{\gamma_S} \hat{I}^{z}_{\text{tot}} \right) \right\} \right) \tag{10.20}$$

where $\lambda \sim \omega_{0,S} / \left(2^{N_S + N_I} \beta\right)$ is an experimentally fit proportionality constant. In physics language, the FID above takes the form of an infinite temperature two-point correlation function. The Fourier transform of the FID yields the NMR spectrum. If the time-evolution is composed of several independently chosen times, $\hat{U}(t,0) \leftarrow \hat{U}(t_n)$, each time t_n will be associated with a separate frequency variable ω_n. Each of these frequencies is considered a 'dimension' and we get a multi-dimensional spectrum. Multi-dimensional NMR protocols are useful, for instance, in analyzing larger molecules where the usual 1D NMR spectrum becomes too degenerate to analyze.

10.3 The simulation challenge in NMR

Here, we discuss when NMR simulation is useful in the analysis of NMR experiments. We indicate when these simulations are hard to perform on classical computers, even when using gold-standard software packages such as Spinach [154]. From the intersection of these two characteristics, we identify the contexts in which we may look for a practically useful quantum advantage in simulation of NMR experiments.

10.3.1 Types of magnetic resonance experiments

Metabolomics

Metabolites are small molecules that drive critical mechanisms in cells such as energy production and storage, signal transduction, and apoptosis [171]. Studying them can grant deep insight into disease processes, drug toxicity, and cell function [302]. NMR and mass spectroscopy are the two most widely used tools to characterize metabolites. NMR experiments on metabolites are typically analyzed by comparison to reference data and chemical standards. This approach is quite successful without requiring simulation. However, a large portion of the metabolite space is unmapped and performing experiments to populate this reference space is currently untenable. Simulations may therefore be useful populating the metabolite reference space 'in silico' [41]. As metabolites are typically very small, classical computers are well-capable of efficiently performing these simulations.

Natural product, organic, and protein biochemistry

Liquid-state NMR is one of the most widely used tools in the study of biomacromolecules such as proteins, nucleic acids, carbohydrates, and lipids. NMR is essential in characterizing the structure and function of these intermediate to large molecules when they do not crystalize, have functional differences in a crystalline or frozen state compared to their natural solution environment, or when we are interested in their dynamics [74]. While NMR enables de novo structure characterization of molecules such as proteins with applications both in fundamental biochemistry [374] and drug discovery [133], interpreting the spectra and inferring chemical structure can be challenging. Chemists are trained to accurately extract the Hamiltonian parameters (chemical shifts, J-couplings, and internuclear distances) from multidimensional NMR experiments and then perform structure assignment. The sophisticated, and complicated, set of heuristics that are used to perform this analysis usually lead to accurate results.

Simulation can be critical, however, in validating the final set of parameters and

structure for large organic compounds [104]. Most experiments in this category are high-field, liquid-state protocols which are reasonably easy to simulate on classical computers using software like Spinach [154]. On the other hand, certain key protocols such as NOESY that are useful for de novo structure characterization of proteins involve dipolar relaxation on large molecules. The correlations generated by the dipolar interaction and the size of the molecule make the dynamics of the system hard to simulate classically. The largest NOESY simulation performed using classical hardware is that of ubiquitin [104], a protein whose weight of 8.6 kDa corresponds to approximately 1000 coupled spins. Biomolecular NMR experiments, however, are routinely performed on proteins weighing up to 50 kDa with new techniques such as deuteration starting to enable experiments on molecules weighing hundreds of kDa [159]. There is therefore a wide range of biomolecular NMR experiments where simulation would be useful for structural validation but is currently infeasble using classical computers.

Solid-state chemistry

NMR experiments are also used to study the structure and dynamics of rigid and semi-rigid solid systems that appear in biochemistry, such as membrane proteins and amyloid fibrils, as well as materials chemistry, such as polymers, battery materials, photovoltaic perovskites, solid state catalysts, and metal-organic frameworks [294, 66]. The utility of solid-state NMR in these contexts is its ability to selectively probe inter-atomic interactions, and therefore information about the chemical structure, three-dimensional structure, and dynamics of both ordered and disordered systems at the atomic level [294]. The technique is thus complementary to other structural characterization methods such as X-ray crystallography and cryo-EM which provide a more 'average' structural description and struggle to fully characterize disordered systems without long-range order or periodicity [66]. Solid-state NMR is thus an important tool in biochemistry to study binding between biomacromolecules and small molecules, protein and ligand dynamics with functional importance, and chemical processes such as protonation reactions, as well as an important tool in materials

chemistry to investigate disorder properties that play a critical role in the chemical reactivity of, for example, organometallic catalysts [294].

The downside of solid-state NMR compared to other structural characterization methods which produce spatial density maps, however, is that it is more difficult to interpret and infer structural information from NMR spectra as the information is encoded in the frequency domain. The presence of quadrupolar nuclei can make interpretation even more complicated, although the quadrupolar interaction embeds additional structural information into the spectrum and is therefore useful if the information can be extracted [66]. Computational simulation and fitting is thus often required to infer structural parameters from solid-state NMR experiment [294]. As an example, consider Ziegler-Natta catalysts (ZNCs) which are one of the most important catalysts used in the industrial production of polyolefins such as polyethylene and polypropylene that form the foundation of many chemical industries. Despite their industrial success, these catalysts are poorly understood at the molecular level and their heterogeneous disordered composition makes solid-state NMR a well-suited investigative tool compared to other structural characterization methods. Due to in part to the presence of quadrapolar nuclei in the material, computational simulation and fitting is required to interpret NMR experiments on ZNCs and other organometallic catalysts [32, 34, 33, 252].

The synergetic combination of solid-state NMR experiments and computational simulations to study structurally complex systems has coalesced into the developing field of 'NMR crystallography' [14, 13, 49]. Density functional theory is the primary computational tool used to provide ab initio predictions of NMR parameters from structural models of the system. Spin dynamics simulations then form a natural bridge from the NMR parameters to computed NMR spectra that can be compared with experiment. These spin dynamics simulations are very challenging to do on classical computers for two reasons. Firstly, the dynamics of the system is dominated by a coherent dipolar interaction whose long-range character generates an appreciable amount of correlations between the hundreds of spins required to describe the sample. Secondly, the orientations of the molecules in the sample are static but randomly

distributed, and we must average over an ensemble of orientations ('powder average'). Therefore, while it is often possible to simulate solid-state NMR experiments using classical computers, these simulations can be extremely resource intensive, especially for large systems.

Electron spin resonance (ESR) and electron pair resonance (EPR)

ESR and EPR experiments are widespread in chemistry, biology, physics, and material science. In biochemical contexts, the protocol is to prepare molecules with radicals, cryogenically freeze the sample, and then study the dynamics of the electronic spins interacting via a dipolar interaction. Such protocols give valuable distance information that can be used to probe the structure, reactivity, and mechanisms of systems ranging from catalysts, photosystems, and molecular conductors to biological macromolecules such as proteins and nucleic acids [303, 299, 313]. A simple example of this type of experiment is the DEER protocol, where we try to extract the distance between a pair of electrons. This distance, however, varies slightly between molecules in the sample as they are frozen in slightly different configurations. We are tasked with identifying the distance distribution that results in the experimental trace.

Simulation is often critical to interpret ESR and EPR experiments, but can be challenging and the most time-consuming aspect of the study [303, 373]. While the number of spins in the system is small so their dynamics is generally not difficult to simulate, there are now two ensembles we must average over. The first is the orientation (powder) average, and the second is the distribution of distances between electrons. For experiments such as Gd^{3+}-label DEER involving spins greater than 1/2, the dynamics itself becomes more difficult, which, combined with the large amount of ensemble averaging, can cause the simulation to take months using classical computers [234].

Zero- and ultralow-field (ZULF) NMR

ZULF NMR was developed with the goals of achieving cheaper liquid-state biomolecular NMR and more precise determination of interaction constants related to bond

angles [351, 369]. While a lower magnetic field enables these goals, interpretation of the spectrum becomes more challenging and requires simulation to analyze as the interactions dominate and we can no longer interpret the spectrum based on perturbations of chemical shift frequencies. The strong interactions, however, make the dynamics hard to simulate on classical computers for systems of even intermediate sizes. From an application perspective, however, ZULF experiments may be less relevant to chemistry and more useful for testing Standard Model physics [54].

10.3.2 Searching for a practical quantum advantage

We can therefore identify two characteristics of NMR contexts where simulation is required to analyze the experiment but is hard to perform on classical computers. The first characteristic is when the dynamics of the spins is hard. This typically occurs when we have large systems in which the long-range dipolar interactions are relevant, either in the coherent or relaxation dynamics of the system. NOESY protocols on large proteins are an example of this context. The second characteristic is when we have to ensemble average over many parameters, such as orientations and distances, in the Hamiltonian. Regardless of the size of the system or complexity of the dynamics, the requirement to run several parallel simulations to compute the ensemble average makes the simulation task challenging. ESR and EPR experiments are an example of where even modestly sized systems, especially when involving spins greater than 1/2, can be hard to simulate due to the massive ensemble of parameters we must average over even though the systems are small enough that their dynamics itself is tractable. Solid-state NMR of large systems, especially when involving quadrupolar nuclei with spins greater than 1/2, is a context where both of these characteristics appear; the dynamics of the spins is hard due to coherent dipolar interactions and we must ensemble average over orientations.

We should therefore focus on NMR contexts with either of these two characteristics are present when seeking a practical quantum advantage in NMR simulation. The quantum algorithms presented in the next chapter open the possibility for seeking such an advantage. Specifically, Sec 11.1 discusses the simulation of NMR dynamics on a

quantum device, and Sec 11.2 discusses how ensemble averaging can be performed. The combination of these two algorithms confers memory and time advantages over classical simulation, allowing for efficient simulation of NMR experiments that can be modeled using purely coherent dynamics, including solid-state NMR and ESR/EPR. A quantum algorithm that captures NMR experiments with dissipative dynamics would enable simulation of practically-useful liquid-state relaxation protocols such as NOESY on large proteins, and is an ongoing effort. Quantitative metrics for comparing the efficiency of classical and quantum simulations are memory (classical memory and number of qudits), elapsed real time of the simulation, and number of parallelizable runs of the simulation that must be performed for contexts requiring ensemble averaging.

Performing a quantum simulation that surpasses classical computers in solid-state NMR or liquid-state relaxation NMR on large, application-relevant systems will require quantum hardware that is appreciably more mature than what is currently available. We can thus consider two avenues to demonstrate value from near-term quantum hardware. First, we can perform quantum simulations of ZULF NMR experiments. While these experiments may not have as much practical utility as solid-state NMR or liquid-state relaxation NMR, classical computers start struggling with the simulation of even intermediate-sized molecules; near-term quantum hardware therefore has a chance of demonstrating an advantage on a classically hard system. In Sec. 12.1, we take an initial step in this direction by demonstrating a proof-of-principle quantum simulation of a ZULF experiment that is still easily simulable on classical computers. The second avenue is to use quantum hardware to simulate a subsystem of a large solid-state NMR or liquid-state relaxation NMR experiment, while feeding this simulation result into a larger computation on a classical computer. In Part V, we discuss such hybrid quantum-classical algorithms where quantum hardware acts as an accelerater rather than a replacement for classical computers.

Chapter 11

Quantum simulation of NMR spectra

In the previous chapter, we described when simulation is useful to analyze NMR experiments and when these simulations are classically challenging. We now explore how quantum hardware may be used to simulate NMR experiments and how this quantum simulation may prove advantageous is classically challenging contexts. Here, we focus on spectroscopic NMR protocols, which are those that do not rely on dipolar relaxation or relaxation due to chemical shift anisotropy. Developing a quantum algorithm for such relaxation protocols is an ongoing work.

11.1 Computing the FID

In this section, we describe a quantum algorithm that can be used to simulate a diverse array of spectroscopic NMR experiments, including protocols with multiple dimensions, solid-state samples, and different isotope labeling. The algorithm is a generalization of that presented in Ref. [329]. The basic idea is to simulate the dynamics of the nuclear spins via an effective spin Hamiltonian with the appropriate terms [218] after initializing the system in a high temperature state [330], or by effectively achieving this thermal state by sampling from computational basis states of the quantum machine [329]. Multidimensional protocols can be simulated by inserting single-qubit rotations into the time-evolution and isotope labeling is incorporated by the choice of basis states that the qubits are prepared in and by the choice of qubits

to measure at the end of the simulation. The algorithm can therefore be considered a direct simulation of the average spin dynamics occuring during an NMR experiment.

Our goal is to compute the FID, Eq. (10.19) or equivalently Eq. (10.20), on quantum hardware rather than compute the NMR spectrum itself as done in Ref. [330]. We will then take the Fourier transform of the computed FID to get the spectrum as is done in the NMR experiment itself. Computing the time-domain signal instead of the frequency-domain signal allows us to transparently simulate all the different flavors of NMR protocols by implementing the pulse sequence determining each protocol directly on the quantum device.

We perform the simulation by implementing the NMR experiment's initial state, unitary dynamics, and measured observable on a quantum computer or simulator. The measured observable, $\hat{A}^{+}_{\text{tot}}$, directly maps to the natural computational basis measurement on the quantum device after $\pi/2$ single qubit rotation performed on each qubit. The unitary dynamics $\hat{U}(t)$ can either be implemented in a digital fashion via a quantum circuit composed of several quantum gates, or in an analog fashion by engineering the device's native dynamics to mimic $\hat{U}(t)$. Both of these routes can be challenging to implement efficiently, and strategies to do so are discussed in Chapter 12. The NMR experiment's initial thermal Gibbs state can either be directly implemented on the quantum device by exploiting ancilla qubits [330], or by repeating the simulation with several of the computational basis states that are naturally prepared via single qubit rotations [329]. We focus on the latter approach here.

We can calculate the FID, Eq. (10.20), as follows. The eigendecomposition of operator $\hat{S}^{z}_{\text{tot}} + \frac{\gamma_I}{\gamma_S}\hat{I}^{z}_{\text{tot}}$ is $\left\{|m_{S,I}\rangle = |m_S, m_I\rangle\,; m_{S,I} = m_S + \frac{\gamma_I}{\gamma_S} m_I\right\}$ where $\{|m_S\rangle\,; m_S\}$ and $\{|m_I\rangle\,; m_I\}$ are the eigendecompositions of $\hat{S}^{z}_{\text{tot}}$ and $\hat{I}^{z}_{\text{tot}}$ respectively. We thus have

$$S_A(t) \approx \lambda \sum_{m_{S,I}} m_{S,I} \langle m_{S,I}(t)|\hat{A}^{+}_{\text{tot}}|m_{S,I}(t)\rangle \tag{11.1}$$

where $|m_{S,I}(t)\rangle = \hat{U}(t,0)|m_{S,I}\rangle$. Each term in the sum above is computed by preparing the computational basis state $|m_{S,I}\rangle$ on the quantum device via single qubit rota-

tions, implementing the time-evolution unitary $\hat{U}(t,0)$, and measuring $\hat{A}^{+}_{\text{tot}}$ via single qubit rotations followed by a projective measurement in the computational basis. Note that in the case of zero field NMR, A doesn't correspond to a single spin species, but instead the measurement $\hat{A}^{+}_{\text{tot}} \rightarrow \hat{S}^{+}_{\text{tot}} + \frac{\gamma_I}{\gamma_S}\hat{I}^{+}_{\text{tot}}$ is made. By computing each term in Eq. 11.1 and summing them, we get the FID. There are, however, an exponential number of terms in the sum. This would, in principle, prevent the algorithm for being computationally tractable for large molecules with many spins. Fortunately, we do not actually have to compute every term of the sum. By sampling a polynomial number of basis states, each corresponding to a term in the sum, we can estimate the FID within a desired mean-squared error [329]. Specifically, uniform sampling of basis states in the sum or importance sampling basis states according to the square of their magnitization can always be used to estimate the FID with $\mathcal{O}\left((N_S + N_I)^2\right)$ samples, compared to the $2^{N_s+N_I}$ terms in the sum. The NMR experiment can thus be simulated efficiently on quantum devices as long as we can efficiently implement the time-evolution unitary $\hat{U}(t,0)$.

The hope for a quantum advantage over classical computers performing this simulation stems from the belief that this time-evolution is more natural, and therefore less resource intensive, to implement on quantum hardware compared to classical computers. The difficulty of implementing $\hat{U}(t,0)$ depends on the system studied in the NMR experiment and the protocol that is chosen. In many cases, the dynamics itself is fairly classical, without the spins appreciably developing higher order correlations. These cases can be simulated efficiently using classical computers. Other contexts, however, such as much of solid-state NMR, are classically hard to simulate as discussed in Chapter 10. It is in these contexts where a quantum simulation may prove advantageous.

We note that that the algorithm described in this section can also be used to simulate liquid-state NMR protocols where dipolar relaxation and relaxation from chemical shift anisotropy are relevant. The rapid molecular tumbling underlying these processes are incorporated by allowing the molecular orientation Θ, appearing in the dipolar interaction and chemical shift terms of the model in Sec. 10.1, to vary in

time. However, the scale separation between the molecular tumbling and the internal spin dynamics makes implementation of the time-evolution unitary challenging on a quantum device. In classical simulation of NMR experiments, relaxation processes are taken into account by deriving a Redfield master equation to second order and replacing the time-dependent parameters in this equation of motion with their average over the rapid motional tumbling. We explore a way to capture the spirit of this treatment by deriving an effective Floquet Hamiltonian for the system and then making a similar second-order approximation in ongoing work.

11.2 Ancilla-assisted ensemble averaging

In Chapter 10, we explained that NMR simulation is classically challenging when (1) the time-evolution unitary $\hat{U}(t,0)$ is hard to implement, and (2) when we must ensemble average simulations over different Hamiltonian parameters to match the experimental spectrum. The algorithm in the prior section sought a quantum advantage in challenge (1), hoping that the dynamics is more natural to implement on quantum hardware. Here, we focus on extending the algorithm to seek a quantum advantage in challenge (2). The material in this section corresponds to the work in Ref. [322].

As a concrete context, consider solid-state NMR experiments and electron spin resonance (ESR) experiments such as DEER. In both cases, the effective Hamiltonian of Sec. 10.1 can often be reduced to

$$\hat{H} = \omega_{0,S} \sum_{i=1}^{N_S} h_i \hat{S}_i^z + \sum_{i<j} d_{ij} \left(2\hat{S}_i^z \hat{S}_j^z - \frac{1}{2} \left(\hat{S}_i^+ \hat{S}_j^- + \hat{S}_i^- \hat{S}_j^+ \right) \right) \tag{11.2}$$

where we have taken a homonuclear system for simplicity and applied the secular approximation that is valid for large external fields. The coupling constant is

$$d_{ij} = -\frac{\mu_0 \gamma_i \gamma_j \hbar}{4\pi r_{ij}^3} \frac{1}{2} \left(3\cos^2 \Theta_{ij} - 1 \right) \tag{11.3}$$

where Θ_{ij} is the angle between the dipole vector between the spins and the z-axis,

which is chosen as the quantization axis, and r_{ij} is the distance between the spins. In solid-state NMR and ESR experiments, the orientation of each molecule in the sample takes a uniformly random but static value during the experiment. We can define a molecule's orientation as $\Omega = (\alpha, \beta, \gamma)$, where α, β, and γ are Euler angles. The different orientations correspond to the Θ_{ij} in Eq. (11.3) takings different values. We can therefore simulate the experiment by computing the spectrum for an ensemble of Hamiltonians, Eq. (11.2), each corresponding to a different orientation Ω_k. DEER experiments typically consist of two electron spins a distance r apart. During the experiment, the sample is cryogenically frozen and each molecule in the sample freezes in a slightly different conformation. This causes r to take slightly different values for each molecule, and therefore in DEER experiments we must also ensemble average over this distance.

Performing the ensemble average over orientations, known as the powder average, and possibly over distances is challenging for classical computers even after parallelizing the computation. This parallelization can be done naturally in one shot on a quantum device, however, by exploiting ancilla degrees of freedom in a superposition. Let the Hamiltonians $\hat{H}_k = \hat{H}(\Omega_k, r_k)$ correspond to Eq. (11.2) parameterized by a specific orientation Ω_k and, in the case of a DEER experiment, distance r_k. We can perform the ensemble average using an ancilla system either comprised of discrete degrees of freedom formed by an ancillary set of qubits, or comprised of a continuous degree of freedom formed by an ancillary bosonic mode. We describe both approaches as well as their advantages and disadvantages below.

11.2.1 Averaging using discrete ancilla

Define the unitary operators $\hat{U}_k(t) = e^{-i\hat{H}_k t}$. Then, the circuit in Fig. 32 provides a construction whereby the ensemble averaged FID can be computed on the quantum device in the same amount of time it takes to compute a single FID. Specifically, we use M ancilla qubits to simultaneously averaging over 2^M configurations. The idea is as follows. Let $|k\rangle$ represent the state of the ancilla register, with $k = \{0...00, 0...01, 0...10, 0...11, ..., 1...11\}$. The integer corresponding to each binary

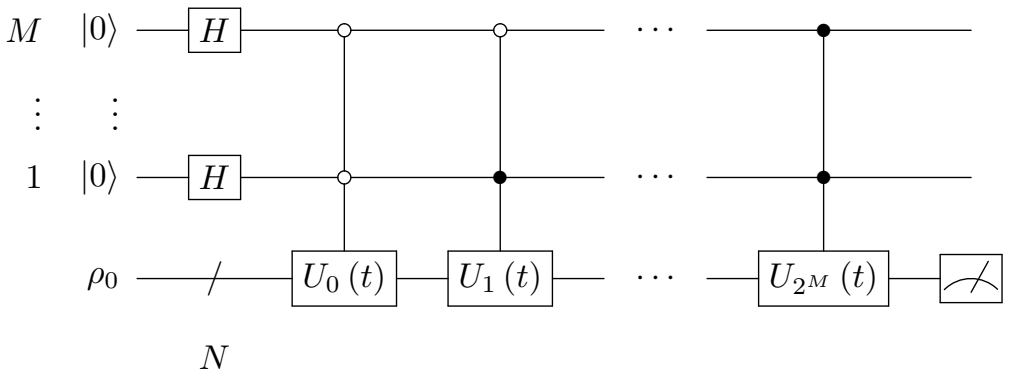

Figure 32: Circuit to compute ensemble averaged FID at time t. Each U_k corresponds to a different configuration of the system (Ω_k, r_k).

string k labels the 2^M configurations that we average over. The circuit in Fig. 32 implements the time evolution

$$\hat{U}_{\text{comb}}(t) = \sum_k |k\rangle\langle k| \otimes \hat{U}_k(t) \tag{11.4}$$

after preparing the combined system in the state $\rho_{\text{comb}} = \left(\sum_{k,k'} |k\rangle\langle k'|\right) \otimes \rho_0$ where ρ_0 is the initial state of the system representing the NMR spins. We can either have ρ_0 be the thermal Gibbs state or the appropriate computational basis state as discussed in Sec. 11.1. The observable we measure is $\hat{I} \otimes \hat{S}^+_{\text{tot}}$, where $\hat{I}$ is the identity operator on the ancilla system. The measurement performed by the circuit is therefore

$$\begin{aligned}
\tilde{S}(t) &= \text{Tr}\{\hat{U}_{\text{comb}}(t)^\dagger \rho_{\text{comb}} \hat{U}_{\text{comb}}(t)\} && (11.5)\\
&= \sum_{k,k'} \text{Tr}\{|k\rangle\langle k'| \otimes \left(\hat{U}_k^\dagger(t) \hat{S}^+_{\text{tot}} \hat{U}_{k'}(t)\right)\} && (11.6)\\
&= \sum_k \text{Tr}\{\hat{U}_k^\dagger(t) \hat{S}^+_{\text{tot}} \hat{U}_k(t)\} && (11.7)\\
&= \sum_{k=1}^{2^M} S_k(t) && (11.8)
\end{aligned}$$

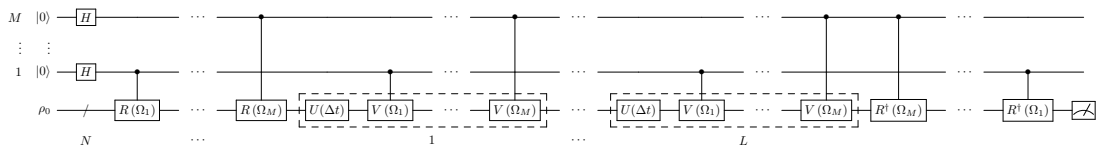

Figure 33: Circuit to efficiently compute orientation averaged FID at time t. The $R(\Omega_k)$ and $V(\Omega_k)$ are composed of a sequence of single qubit rotations, making the ancilla-controlled version of these operations a sequence of two-qubit gates.

where $S_k(t) = \mathrm{Tr}\{\hat{U}_k^\dagger(t)\hat{S}_{\mathrm{tot}}^+\hat{U}^k(t)\}$ is the FID for a particular configuration k of the system. Dividing $\tilde{S}(t)$ by the total number of configurations, 2^M, therefore gives us the desired ensemble averaged FID. We note that the observable $\hat{I}\otimes\hat{S}_{\mathrm{tot}}^+$ corresponds to not measuring the ancilla register; measuring the ancilla would collapse the computation into a single sample of the FID $S_k(t)$ instead of the producing the full ensemble average.

Typically, we desire to average over $\mathcal{O}(10^3)$ to $\mathcal{O}(10^4)$ orientations in solid-state NMR and ESR, and $\mathcal{O}(10^3)$ distances in ESR experiments requiring distance-averaging such as DEER. Therefore, 10-15 ancilla qubits are sufficient for orientation averaging and 20-25 ancilla qubits are sufficient for both orientation and distance averaging. This is a modest resource overhead for being able to simultenously do the entire ensemble averaging in one pass of the quantum computation. The difficulty in practice, however, appears in efficiently implementing the ancilla-controlled unitaries $|k\rangle\langle k|\otimes\hat{U}_k(t)$. In Fig. 33, we give a way to efficiently implement these operations for orientation averaging.

Define the operator

$$\hat{R}(\Omega_k) = e^{-i\varphi_k\mathbf{n}_k\cdot\hat{\mathbf{S}}_{\mathrm{tot}}} \tag{11.9}$$

where $\mathbf{n}_k$ and φ_k are the unit vector and angle that rotates the z-axis to the orientation Ω_k. This operator is composed from single qubit rotations on the system spins. Next, assume we implement the time-evolution $\hat{U}(t)$ via the discretization

$$\hat{U}(t) \approx \left[\hat{U}(\Delta t)\right]^L \tag{11.10}$$

where $\Delta t = t/L$ and L is an integer. In the limit of large L, Eq. (11.10) becomes an equality. This formula captures both digital simulation via product formulas and analog simulation via Hamiltonian engineering (see Chapter 12). In the former, $\hat{U}(\Delta t)$ represents one Trotter step, while in the latter, $\hat{U}(\Delta t)$ represents one Floquet cycle. We now introduce the operator

$$\hat{V}\left(\Omega_k\right) = e^{-i\Delta t \sum_i h_i \hat{\mathbf{S}}\cdot(\mathbf{e}_z - \mathbf{n}_k)} \tag{11.11}$$

where $\mathbf{e}_z$ is the unit vector in the z-direction. First consider implementing the orientation ensemble average of evolution under Eq. (11.2) without the chemical shift term. Then, we allow each of the M ancilla qubits to perform a global rotation $\hat{R}(\Omega_m)$ on the system conditioned on state of the qubit. Specifically, the m^{th} ancilla performs the controlled operation $|0\rangle\langle 0| \otimes \hat{I} + |1\rangle\langle 1| \otimes \hat{R}(\Omega_m)$ at the beginning of the circuit and undoes this rotation at the end of the circuit. The dipolar interaction Hamiltonian will thus be transformed by one of the 2^M following rotations

$$\{\, \hat{R}\left(\Omega_1\right), \hat{R}\left(\Omega_2\right), ..., \hat{R}\left(\Omega_M\right), \hat{R}\left(\Omega_1 + \Omega_2\right), \hat{R}\left(\Omega_1 + \Omega_3\right), ..., \hat{R}\left(\sum_{m=1}^{M} \Omega_m\right) \} \tag{11.12}$$

depending on the bitstring of the ancilla register. Note that we have used the shorthand $\hat{R}(\Omega_m + \Omega_{m'}) = \exp\{-i\left(\varphi_m \mathbf{n}_m + \varphi_{m'} \mathbf{n}_{m'}\right) \cdot \hat{\mathbf{S}}_{\text{tot}}\}$. The M orientations that we specify by choosing the rotations performed by individual ancilla qubits ends up generating 2^M orientations via this construction. We must therefore ensure that we pick the M rotations such that the 2^M rotations uniformly cover the sphere in order to achieve the desired uniform orientation average.

Now let us add the chemical shift term of Eq.(11.2) back in. The problem with the above construction is that while the rotations map the dipolar interaction to another orientation, they also rotate the chemical shift term so that it no longer generates the desired precession around the z-axis. Instead, it will generate precession around the rotated axis. If the time-evolution is implemented in a discretized manner as in Eq. (11.10), then we can fix this error by inserting in ancilla-controlled $\hat{V}(\Omega_m)$ during

each time-evolution step. The commutation error between this operation and the time-evolution unitary $\hat{U}(\Delta t)$ vanishes in the limit of a large number of discretization steps L. We get the circuit in Fig. 33 by combining the initial global rotations $\hat{R}$ and the chemical shift 'fixing' operations $\hat{V}$ in each discretization step. Crucially, the ancilla-controlled versions of these two operations are just two-qubit gates between individual ancilla qubits and individual system qubits, thereby allowing an efficient implementation on quantum hardware as long as the system has the right connectivity between qubits.

The ancilla qubits never interact with each other, but each ancilla needs to be able to interact with all of the system qubits. Trapped ion systems natively have this connectivty, while new architectures of Rydberg atom simulators also have such a capability. Superconducting devices are usually designed with nearest neighbor connectivity, but have the potential to be fabricated in more complex qubit topologies if there is sufficient motivation.

The resource overhead of the ancilla-enabled orientation averaging scheme is M ancilla qubits and $L * M * N$ additional two-qubit gates in the worst case, where N is the number of system qubits and L is the number of discretization steps. Typically, we get a sufficiently low discretization error with $L \approx 10^3$ and can cover the required number of orientations with $M \approx 10 - 15$. For solid-state NMR, we may have $N \approx 10^2 - 10^3$ spins, while for DEER we have $N = 2$. Therefore, a quantum device with 15 qubits and sufficient fidelity to perform around 10^4 two-qubits gates can produce a orientation-averaged DEER spectrum for a single spin distance r.

The orientation averaging in DEER experiments, however, can be performed analytically under common approximations [373]; the distance averaging is the more costly operation. It would be interesting to explore if the spirit of Fig. 32 can be distilled into an efficient construction for ensemble distance averaging, just as Fig. 33 provides such a construction for ensemble orientation averaging. Unlike the orientational average, however, the composition of two ancilla-controlled rotations which correspond to different distance choices does not also correspond to an easily understandable choice of distance. Motivated by the continuous nature of the $1/r^3$

distance term that we would like to average over, we explore an ancilla-assited averaging scheme using a continuous ancilla degree of freedom instead of the discrete Hilbert space of a set of qubits.

11.2.2 Averaging using continuous ancilla

Consider a system of spins evolving according to Eq. (11.2). Our goal is to simultaneously average over a continuous distribution of interaction constants d_{ij}, which is determined by the distribution of angles Θ_{ij} and positions r_{ij}. The angles are uniformly distributed over the unit sphere, while the position distribution typically looks like a smooth combination of a few Gaussians [373]. The idea is to couple the spins describing the NMR system to an ancillary bosonic mode whose state can be described by a continuous wavefunction. By appropriately choosing the wavefunction of the bosonic mode, we can average over the continuum of distance or orientation values in the spin Hamiltonian.

We first illustrate the key idea. Consider two qubits coupled to a bosonic mode. Assuming we can implement a gate

$$\hat{U}_{xi}(\phi) = e^{-i\phi\hat{x}\hat{H}_{\text{int}}} \tag{11.13}$$

where $\hat{x}$ is a quadrature operator of the bosonic mode and $\hat{H}_{\text{int}}$ is the interaction term of the spin Hamiltonian we are trying to average over. For two qubits, we will have

$$\hat{H}_{\text{int}} = d_{12}\left(2\hat{S}_1^z\hat{S}_2^z - \frac{1}{2}\left(\hat{S}_1^+\hat{S}_2^- + \hat{S}_1^-\hat{S}_2^+\right)\right). \tag{11.14}$$

The idea is that by placing the resonator in a state with Wigner function $W(x,p)$ such that $p(x) = \int dpW(x,p)$ corresponds to the distribution of the exchange constants

$$d_{12} = -\frac{\mu_0\gamma_i\gamma_j\hbar}{4\pi r_{12}^3}\frac{1}{2}\left(3\cos^2\Theta_{12} - 1\right), \tag{11.15}$$

we can simultaneously average the DEER spectrum over all d_{12} corresponding to the distribution of the distances r_{12} and angles Θ_{12}. Specifically, let the initial state of

the system be $|\psi_0\rangle = |\psi_0^{(s)}\rangle\,|\psi_0^{(r)}\rangle$, where $|\psi_0^{(s)}\rangle$ and $|\psi_0^{(r)}\rangle$ are the initial states of the spin system and resonator respectively. Expanding the resonator state in the position basis, we have $|\psi_0^{(r)}\rangle = \int dx\sqrt{p(x)}\,|x\rangle$. We are interested in an observable of the form

$$S_x(\phi) = \langle\psi_0|\,\hat{U}_{xi}^\dagger(\phi)\hat{S}_{\text{tot}}^x\hat{U}_{xi}(\phi)\,|\psi_0\rangle\,. \tag{11.16}$$

By expanding out $\hat{U}_{xi}(\phi)$, acting term by term on $|\psi_0\rangle$, and recombining terms into an exponential, we get

$$S_x(\phi) = \int dx\; p(x)\,\langle\psi_0|\,\hat{U}_i^\dagger(\phi,x)\hat{S}_{\text{tot}}^x\hat{U}_i(\phi,x)\,|\psi_0\rangle\,. \tag{11.17}$$

where $\hat{U}_i(\phi,x) = e^{-i\phi x\hat{H}_{\text{int}}}$. Thus, if we are able to prepare a bosonic state such that $p(x)$ corresponds to the desired distribution $p(d_{12})$, then we can simultaneously do the ensemble average over both r_{12} and Θ_{12}.

The full protocol consists in three steps: First, prepare the bosonic mode in a state given by Wigner function $W(x,p)$ such that $\int dpW(x,p) = p(x)$ and the qubits in $|\psi_0\rangle$. Then, act with $\hat{U}_{ix}(\phi)$ on the mode and qubits. Finally, measure $\hat{S}_{\text{tot}}^x$.

As a simple benchmark, we first demonstrate the continuous averaging idea for the Ising Hamiltonian

$$\hat{H}_{\text{int}} = 4J\hat{S}_1^z\hat{S}_2^z, \tag{11.18}$$

with the spins in an initial $|\uparrow_x\uparrow_x\rangle$ and bosonic mode having a wavefunction corresponding to a Gaussian distribution $p(J) = \mathcal{N}(J, \mu = 2\sqrt{2}, \sigma^2 = 0.5)$. This wavefunction corresponds to preparing the bosonic mode in a coherent state, and more precisely, a squeezed displaced state with squeezing $\xi = 0$ and displacement $\alpha = 2$. The interaction Hamiltonian Eq. (11.18) is not an overly simplistic choice as DEER time evolution can be written as a pure Ising model without local magnetic fields in certain limits [373].

In Fig. 34 we simulate the time evolution of the magnetization $4\langle\sum_i \hat{S}_i^x\rangle$ under the Ising model, averaged over the Gaussian distribution of J couplings. We compare two averaging methods. In "brute force averaging", we calculate $4\langle\sum_i \hat{S}_i^x\rangle$ using a

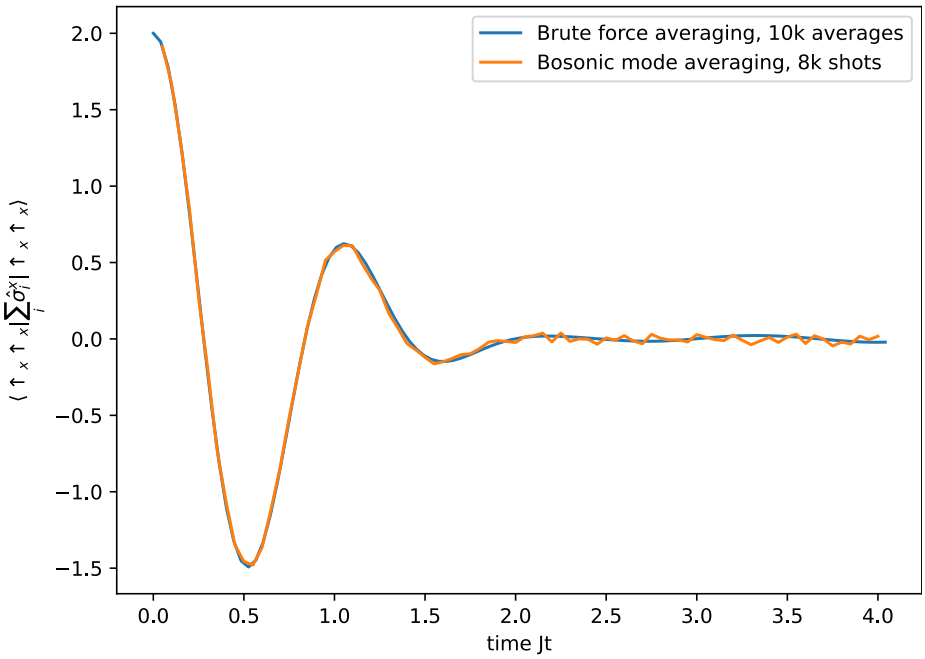

Figure 34: Comparison of brute force sampling versus the averaging employing the Bosonic mode. We use a Trotter step $0.1/J$ for the Bosonic mode averaging.

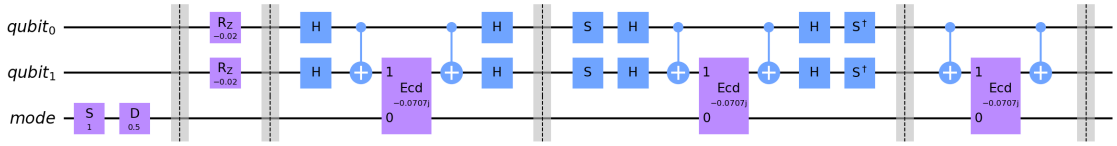

Figure 35: The circuit required to prepare the mode in the powder average distribution (first two gates before the barrier), and then act on it with the Trotter step (rest of circuit) corresponding to the Hamiltonian of interest.

fixed J employing only spin evolution and then averaging over many such runs. In "bosonic mode averaging", we use the method discussed above, i.e. coupling to a bosonic mode prepared in a squeezed displaced state and then time evolved with the Trotterized circuit shown in Fig. 35. We chose a Trotter step of $0.1/J$ and the bosonic operations are implemented with "Bosonic Qiskit" [347]. We see that the continuous ancilla-assisted averaging using the bosonic mode accurately reproduces the ensemble averaged observable of interest.

The remaining challenge is thus experimental implementation of this scheme on quantum simulator platforms such as circuit QED systems comprised of superconducting transmon qubits coupled to a microwave resonator acting as the bosonic

mode, a chain of trapped ions where the transverse phonon mode along the chain provides the bosonic mode, or cavity QED systems consisting of Rydberg atoms in a microwave cavity where the cavity photon acts as the bosonic mode. The two issues that must be addressed are engineering a coupling of the form Eq. (11.13) using the interaction Hamiltonian in Eq. (11.14), and preparing the state of the bosonic mode such that it corresponds to distributions of interest that appear in NMR and ESR experiments.

Circuit QED and trapped ion platforms do not naturally implement a boson-controlled interaction with the dipolar spin Hamiltonian in Eq. (11.14). They can, however, implement a controlled interaction with a flip-flop spin Hamiltonian of the form

$$\hat{H}_{\text{int}} = J\hat{x}\left(\hat{S}_1^+\hat{S}_2^- + \hat{S}_1^-\hat{S}_2^+\right). \tag{11.19}$$

We can then use an appropriate train of single-qubit rotations applied to the two qubits to Floquet-engineer the dynamics such that they approximately behave according to a desired dipolar interaction Hamiltonian on average [71, 383]. For example, the pulse sequence

$$\mathcal{P} = \{R_x(\pi/2), \tau; R_y(-\pi/2), \tau; R_y(\pi), \tau; R_y(\pi/2), \tau; R_x(-\pi/2), R_z(\pi)\} \tag{11.20}$$

where we first apply a pulse $R_x(\pi/2)$ on the two qubits, then undergo evolutionunder the native Hamiltonian for a time τ, then apply a pulse $R_y(-\pi/2)$ on the two qubits, and so on would yield the effective Hamiltonian

$$\hat{\tilde{H}}_{\text{int}} = J\hat{x}\left(2\hat{S}_1^z\hat{S}_2^z + \frac{1}{2}\left(\hat{S}_1^+\hat{S}_2^- + \hat{S}_1^-\hat{S}_2^+\right)\right). \tag{11.21}$$

Application of a π-rotation around the z-axis on one of the qubits then flips the relative sign between the flip-flop part of the interaction and the Ising part of the interaction. Specifically,

$$R_1^z(\pi)^\dagger\hat{\tilde{H}}_{\text{int}}R_1^z(\pi) = J\hat{x}\left(2\hat{S}_1^z\hat{S}_2^z - \frac{1}{2}\left(\hat{S}_1^+\hat{S}_2^- + \hat{S}_1^-\hat{S}_2^+\right)\right). \tag{11.22}$$

where we have chosen to do the rotation around the first qubit. We can then reintroduce the chemical shift terms via Trotterization after each Floquet cycle:

$$\hat{U}\left(t\right)_{\text{ave}} = R_1^z\left(\pi\right)^\dagger \left[R_1^z\left(h_1\frac{t}{r}\right) R_2^z\left(h_1\frac{t}{r}\right) \hat{\tilde{U}}_{\text{int}}\left(\frac{t}{r}\right)\right]^r R_1^z\left(\pi\right) \tag{11.23}$$

where r is the Trotter step and

$$\begin{aligned}\hat{\tilde{U}}_{\text{int}}\left(\frac{t}{r}\right) = R_z\left(\pi\right) R_x\left(-\pi/2\right) \hat{U}_{\text{int}}\left(\frac{t}{4r}\right) R_y\left(\pi/2\right) \hat{U}_{\text{int}}\left(\frac{t}{4r}\right) R_y\left(\pi\right) \times \\ \times \hat{U}_{\text{int}}\left(\frac{t}{4r}\right) R_y\left(-\pi/2\right) \hat{U}_{\text{int}}\left(\frac{t}{4r}\right) R_x\left(\pi/2\right)\end{aligned} \tag{11.24}$$

with $\hat{U}_{\text{int}}\left(t\right)$ being given as

$$\hat{U}_{\text{int}}\left(t\right) = \exp\left\{J\hat{x}\left(\hat{S}_1^+\hat{S}_2^- + \hat{S}_1^-\hat{S}_2^+\right)t\right\} \tag{11.25}$$

in terms of the native ancilla-controlled interaction in the system. The time-evolution in Eq. (11.23) then corresponds to dynamics generated by the effective Hamiltonian

$$\hat{H}_{\text{ave}} = h_1\hat{S}_1^z + h_2\hat{S}_1^z + J\hat{x}\left(2\hat{S}_1^z\hat{S}_2^z - \frac{1}{2}\left(\hat{S}_1^+\hat{S}_2^- + \hat{S}_1^-\hat{S}_2^+\right)\right) \tag{11.26}$$

to leading order. Initializing the bosonic mode in the appropriate state then gives the desired ensemble-averaged dynamics. This hybrid digitial-analog combination of Trotterization, Floquet-engineering, and a native operation of the quantum simulator is a powerful approach to generating complicated Hamiltonians which are useful for different applications. In comparison to circuit QED and trapped ion platforms, Rydberg atoms in microwave cavities may be able to directly implement the boson-controlled dipolar interaction [88, 75]. However, Trotterization may still be required to introduce the chemical shift terms.

We now discuss preparation of the bosonic state such that its wavefunction corresponds to the NMR ensemble of interest. In many cases, the distribution $p(x)$ we would like to average over can be expressed as a sum of a few Gaussian distribu-

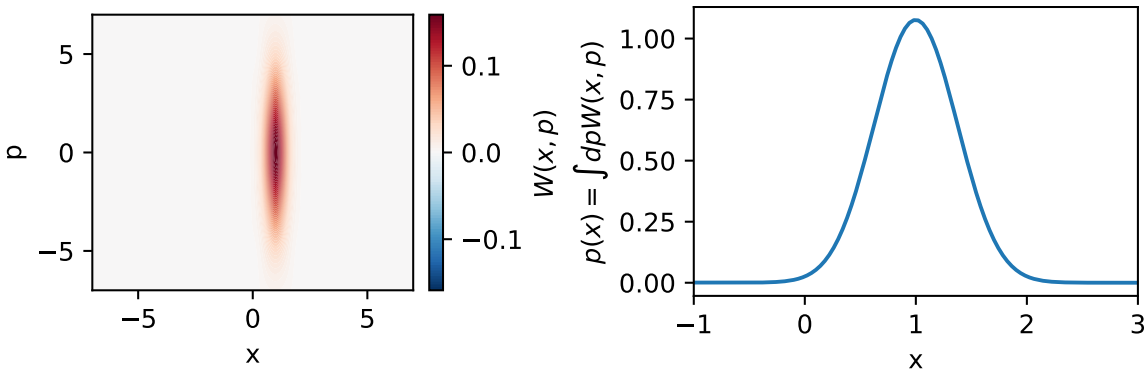

Figure 36: Wigner function of a squeezed displaced state, and the integral over position p.

tions [373]. We can write down such a Gaussian mixture model as

$$p(x) = \sum_i \mathcal{N}_i(x, \mu_i, \sigma_i), \tag{11.27}$$

where μ_i, σ_i are the mean and the standard deviation of the Gaussian

$$\mathcal{N}(x, \mu, \phi) = \frac{1}{\sqrt{2\pi\sigma^2}} \exp\left(-\frac{(x-\mu)^2}{2\sigma^2}\right). \tag{11.28}$$

We can then decompose the ensemble averaged observable of interest as $S(\phi) = \sum_i S_i(\phi)$, where

$$S_i(\phi) = \int dx\, \mathcal{N}_i(x, \mu_i, \theta_i) \langle\psi_0| \hat{U}_i^\dagger(\phi, x) \hat{S}_{\text{tot}}^x \hat{U}_i(\phi, x) |\psi_0\rangle. \tag{11.29}$$

Hence, instead of preparing the full distribution $p(x)$ in experiment, we can instead perform a few experiments in which we only need to prepare a Gaussian and then sum over the results in the end to get $S(\phi)$. The benefit of this decomposition is that it such Gaussian distributions correspond to a wavefunction of a bosonic mode in a squeezed-displaced state. Such states are relatively straightforward to prepare in microwave cavities and trapped ion chains.

We now discuss how to take an arbitrary Gaussian distribution of interest and prepare the corresponding state in bosonic platforms by using displacements and

squeezing. Specifically, the squeezing operator is given by

$$S(\xi) = \exp\left(-\frac{1}{2}(\xi^* \hat{a}^2 - \xi(\hat{a}^\dagger)^2)\right). \tag{11.30}$$

One can then show that for real squeezing $\xi = \xi^*$, the probability distribution along x is a Gaussian with mean zero and standard deviation $\sigma^2 = \exp(-2\xi)/2$.

The displacement operator displaces the vacuum state to a coherent state $|\alpha\rangle = \hat{D}(\alpha)|0\rangle$ and is given by

$$\hat{D}(\alpha) = \exp(\alpha\hat{a}^\dagger - \alpha^*\hat{a}), \tag{11.31}$$

in terms of the bosonic raising/lowering operators $\hat{a}^\dagger, \hat{a}$. Choosing a purely real $\alpha^* = \alpha$, we displace along $\hat{x} = (\hat{a}^\dagger + \hat{a})/\sqrt{2}$. When displacing the vacuum state, we find that the probability distribution along x is a Gaussian with mean $\mu = \sqrt{2}\alpha$.

Combining these two results, we find that if we first squeeze the vacuum with real ξ and *then* displace by real α while choosing the parameters as

$$\xi = -\frac{\ln(2\sigma^2)}{2}, \tag{11.32}$$

$$\alpha = \frac{\mu}{\sqrt{2}}, \tag{11.33}$$

the marginal of the Wigner function $\int dp W(x,p)$ is exactly given by Eq. (11.28) (see Fig. 36).

Note that first displacing and then squeezing yields a different result. Moreover, the exact form of the parameters ξ depends on the definition of $\hat{x}$ in terms of raising/lowering operators, which is not unique. Therefore, for our protocol to work, we need to make sure that $\hat{x}$ is defined in the same way when deriving the gates acting on the bosonic mode in U_{xi}.

In principle, a bosonic wavefunction corresponding to $p(x)$ can also be prepared directly by using ancilla qubits and performing conditional displacements and squeezing. This way, the amount of displacement can be steered by the state of the qubit and therefore a direct superposition of Gaussians can be obtained. We would then avoid the need for several repetitions of the experiment, each corresponding to a sin-

gle Gaussian, but pay the price of a more complicated state preparation protocol and the associated increase in experimental errors.

Chapter 12

Experimental demonstration of NMR simulation

Here, we discuss efforts to experimentally demonstrate the algorithms presented in Chap. 11. There are two modalities of simulation which differ in how they implement the time-evolution unitary

$$U_{\mathrm{NMR}}\left(t_1, ..., t_M\right) = \prod_{m=1}^{M} U_H\left(t_m\right) U_{\mathrm{rot}}^{(m)} \tag{12.1}$$

describing the NMR system's dynamics, where $U_H\left(t_m\right) = e^{-iHt_m}$ and $U_{\mathrm{rot}}^{(m)}$ describe the spin dynamics and global rotations in step m of the protocol respectively. Digital quantum simulation involves decomposing $U_H\left(t_m\right)$ into a sequence of discrete quantum gates that are implemented on the simulator's qubits, while analog simulation tries to engineer the native dynamics of the simulator to mimic $U_H\left(t_m\right)$. Both approaches are worth exploring as they each have advantages and disadvantages. In Sec. 12.1, we discuss a digitial simulation experiment performed in a trapped ion system, corresponding to the work in Ref. [321]. In Sec. 12.2, we discuss an analog simulation experiment that is currently being performed in a superconducting qubit system.

12.1 Digital simulation in trapped ions

We perform the first proof of principle of quantum NMR simulation by simulating a zero-field NMR experiment on a trapped-ion quantum computer [105]. The quantum computer implements a sequence of unitary rotations and entangling interactions on $^{171}Yb^{+}$ ion qubits to implement the quantum circuit that emulates the NMR experiment 12.1.2. Specifically, we compute the spectrum of selectively isotope labeled acetonitrile, with four NMR-active nuclear spins, and show that the resonance frequencies in the spectrum quantitatively match the experimental NMR data from Ref. [206], while the peak intensities match in their ordering. We obtain high spectral resolution within the resource limitations of the trapped-ion device by exploiting compressed sensing techniques [42] and a state-of-the-art quantum circuit synthesis algorithm [380]. These techniques can be used to reduce the resource cost of simulating classically hard NMR systems, and are likely to prove useful in quantum simulations of hard systems that appear in quantum chemistry and condensed matter physics [8]. We give resource estimates for quantum simulations of hard NMR systems, showing how the dephasing commonly present in nuclear spin dynamics may enable such simulations on near-term quantum hardware.

12.1.1 Overview of experiment

First let us discuss zero-field 1D NMR protocols. Recall that an NMR experiment involves polarizing the nuclear spins of a sample via an external magnetic field or a chemical process, letting the spins evolve in time, and measuring the average magnetization of the system. The measured time-dependent magnetization is called the free induction decay (FID), and its Fourier transform yields the NMR spectrum. Letting the operators $\{\mathbf{S}_i\}$ represent the nuclear spins, the initial state of the system when polarized via a magnetic field can be described as $\rho_0 \approx I + \lambda \tilde{S}^z_{\text{tot}}$, where I is the identity operator and $\tilde{S}^z_{\text{tot}} = \sum_i \gamma_i S^z_i$, with γ_i being the gyromagnetic ratio of the nuclear isotope i. In the case of a 1D NMR experiment, the measured FID corresponds to

the quantity

$$\mathrm{FID}\,(t) = \mathrm{Tr}\left[U\,(t)^{\dagger}\,\tilde{S}^{z}_{\mathrm{tot}} U\,(t)\,\tilde{S}^{z}_{\mathrm{tot}}\right], \tag{12.2}$$

where $U\,(t) = \exp\left(-iHt/\hbar\right)$ produces the time-evolution of the system generated by a Hamiltonian H. The evolution of liquid-state molecular samples is typically well captured by

$$H = \sum_{i,j} 2\pi J_{ij}\mathbf{S}_i \cdot \mathbf{S}_j + \sum_i \omega_i S^x_i, \tag{12.3}$$

where we have taken Planck's constant $\hbar = 1$. The J-couplings $\{J_{ij}\}$ characterize the strength of bond-mediated exchange interactions and the chemical shifts $\{h_i\}$ represent local magnetic screening around nuclei in different chemical environments in response to an external magnetic field [218].

Zero-field NMR protocols have no external magnetic field and the chemical shifts are all zero. Instead, the sample is polarized via a chemical process and only the J-couplings contribute to the system's dynamics. The resulting spectra can have narrower resonance lines than conventional high-field NMR due to high absolute field homogeneity and stability [206, 351, 23], allowing more accurate determination of the J-couplings, which in turn encode information about the molecular bond angles. Furthermore, zero-field protocols open the possibility of portable and cheaper experiments as they obviate the need for cryogenically cooled superconducting magnets which produce high fields. Recent experimental progress with nitrogen-vacancy centers in diamond has opened an additional avenue towards zero- and low-field NMR, possibly allowing spectroscopy of samples at the nanoscale [232, 346, 224]. Despite their advantages, a significant limitation of zero-field protocols is that their spectra are hard to interpret without access to reliable computational simulations of the NMR experiment. As the dynamics in zero-field experiments are dominated by interactions between spins, quantum correlations build up rapidly and render classical simulations of even intermediate scale molecules intractable [272]. Zero-field experiments are therefore one of the first NMR settings where quantum computers and simulators may provide computational advantage.

We compute the zero-field spectrum of acetonitrile, a compound which is com-

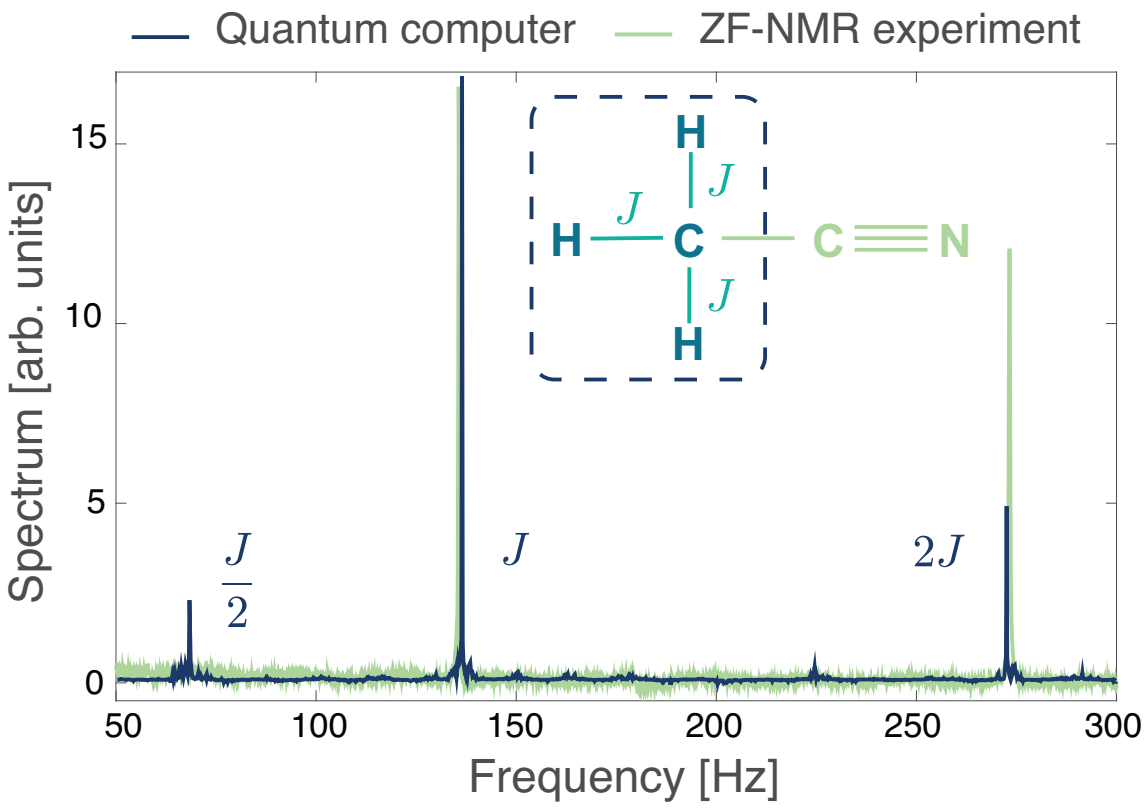

Figure 37: Zero-field spectrum of acetonitrile computed on an ion-trap quantum computer compared with the NMR experiment performed in Ref. [206]. The inset shows the chemical structure of acetonitrile, highlighting the methyl group that was probed in the experiment.

monly used as an industrial solvent. The molecule is isotope labeled to have four NMR-active spin-1/2 nuclei, a ^{13}C and three ^{1}H, that make up a methyl group (see inset in Fig. 37). There are three non-zero J-couplings, corresponding to the three $^{13}\mathrm{C} - {}^{1}\mathrm{H}$ bonds, all with value $J = 136.2$ Hz. The FID signal of Eq. (12.2) can be computed on a quantum computer by initializing the system qubits in basis states with a positive average magnetization, enacting time-evolution under the Hamiltonian via an appropriate quantum circuit, Eq. (13.1), and then measuring the average magnetization of the system. We write this measurable as

$$\mathrm{FID}\,(t) = \sum_{\tilde{m}_n > 0} \tilde{m}_n \,\langle \tilde{m}_n(t)|\tilde{S}^z_{\mathrm{tot}}|\tilde{m}_n(t)\rangle\,, \tag{12.4}$$

where $\{|\tilde{m}_n\rangle\,;\tilde{m}_n\}$ are the eigenstates and eigenvalues of $\tilde{S}^z_{\mathrm{tot}}$, and $|\tilde{m}_n(t)\rangle = U(t)\,|\tilde{m}_n\rangle$.

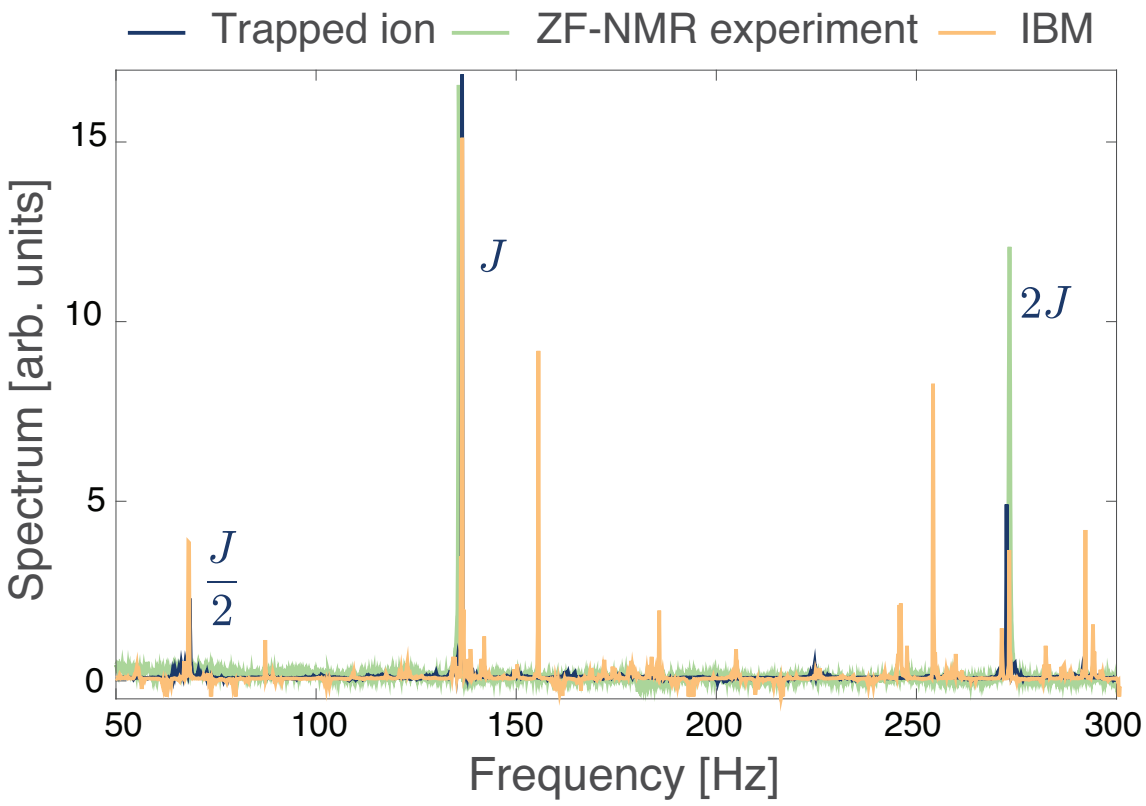

Figure 38: Zero-field spectrum of acetonitrile computed on an ion-trap quantum computer and IBM superconducting quantum computer compared with the NMR experiment performed in Ref. [206]

For a system of N spins, the sum in Eq. (12.4) can have a number of terms that scales exponentially with N, potentially negating any quantum computational advantage. The sampling cost can, however, always be reduced to $\mathcal{O}\left(N^2\right)$ terms via either uniform sampling of basis states in the sum or importance sampling basis states according to a distribution proportional to the square of the states' magnitization ($\tilde{m}_n^2$). The advantage of quantum simulation is thus preserved after incuring a polynomial sampling overhead [329].

Figure 37 shows the spectrum we compute on an ion trap quantum computer in comparison with the seminal zero-field NMR experiment of Ref. [206]. We see that the quantum computation accurately reproduces the resonances at frequencies J and $2J$. Specifically, the corresponding resonance frequencies extracted from the quantum simulation are 136.20 ± 0.09 Hz and 272.41 ± 0.09 Hz, which are within 1σ of the exact frequencies of 136.2 Hz and 272.4 Hz. The extracted resonance frequency

uncertainty is Fourier limited; a Lorentzian fit to the reconstructed peaks results in a width smaller than the frequency grid spacing. We therefore take half the grid spacing as the uncertainty. Given that the zero-field NMR experiment can only resolve the spectral peaks within 0.1 Hz [206], we demonstrate that quantum computers can simulate NMR experiments within their spectral resolution.

The spectrum computed on the ion trap quantum computer has peak intensities that match the ordering of peaks in Ref. [206], but has a quantitative mismatch with spectral weight transferred from the resonance at $2J$ to an additional resonance at $J/2$ that is not present in the NMR experiment. This additional spectral peak arises from a combination of errors in the quantum computer and the high-symmetry of the molecule, which induces dynamical recurrences that are captured by the specific method we use to synthesize the time-evolution circuits. Such artifacts are unlikely to appear in classically intractable NMR simulations whose large, strongly correlated molecules typically do not exhibit dynamical recurrences. Furthermore, we provide a simple method to remove artifact peaks in future experiments even for the small, highly symmetric systems where they may occur 12.1.3. To illustrate that the quantative agreement between the ion trap computation and Ref. [206] is non-trivial, we also compute the same zero-field spectrum on a IBM cloud service superconducting quantum computer (ibm-perth). The result, shown in Fig. 38, manifests several additional spurious peaks and a larger amplitude mismatch than the ion experiment. We attribute this worse performance to control errors in the superconducting device and the fact that the time-evolution circuits, synthesized via an optimization algorithm describe below, have about 1.5-2 times more two-qubit gates than the ion circuits due to the expressivity of the native two-qubit gate on each device. Specifically, the ion system uses a variable angle Molmer-Sorenson interaction, which appears better suited to the quantum simulation of Eq. (13.1) than the CNOT gate of the superconducting system.

In order to calculate the spectrum, we first compute the FID, Eq. (12.4), at a non-uniform random sampling of time points lower than the Nyquist rate. We synthesize the time-evolution quantum circuits using the numerical optimization algorithm in

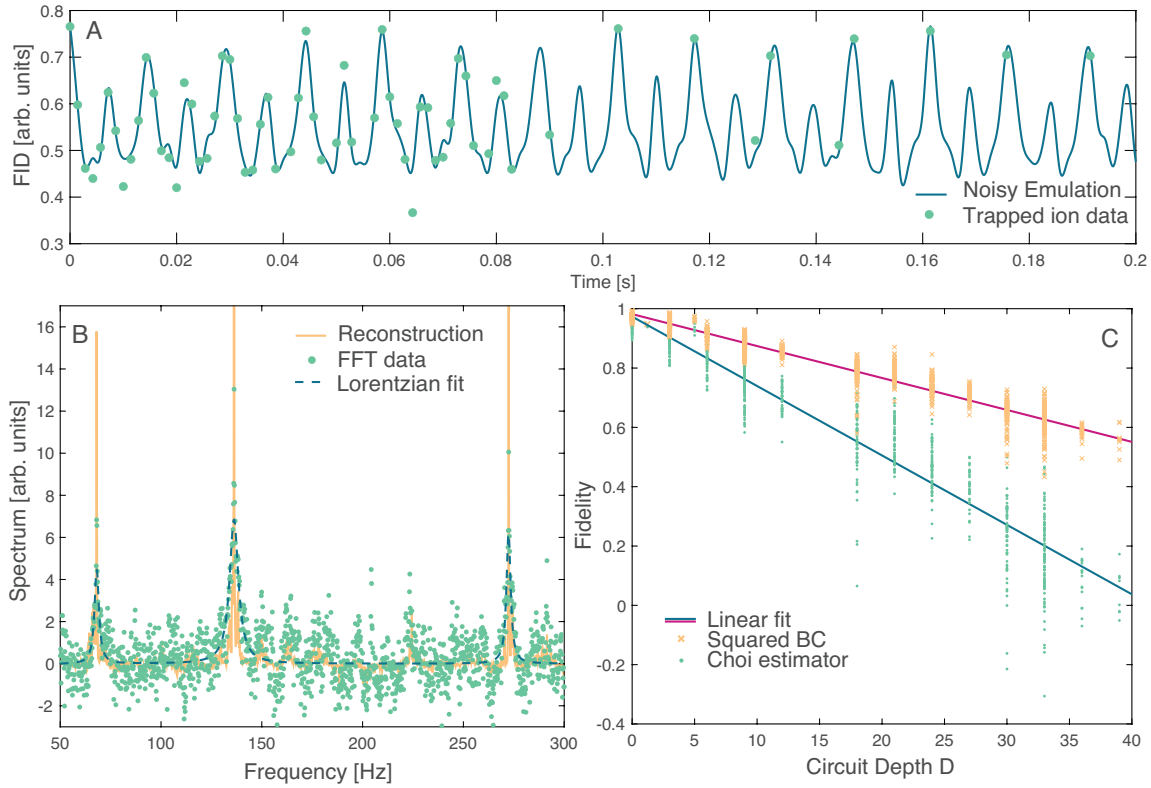

Figure 39: Compressed sensing reconstruction & Benchmarking. (A) Comparison of the FID of a noisy quantum circuit emulation (blue line) and the non-uniform, sparsely sampled points experimentally measured on the trapped-ion quantum computer (green circles). The noise is modeled by two-qubit gates subject to both amplitude and phase damping with rates 0.005 and 0.035 respectively. (B) NMR spectrum extracted from the digital quantum simulation, where the spectrum is the real part of the Fourier transform of the FID. Green dots show the spectrum after replacing unsampled points of the FID with zeros. Dashed blue line shows the best (under ℓ_1-norm) Lorentzian fits to this zero-padded data. Solid yellow line shows the reconstructed spectrum after applying the IST-S algorithm. The y-axis is rescaled (zoomed-in) compared to Fig. 37 to make the features more visible. (C) Fidelity of quantum simulation. The yellow crosses show the squared Bhattacharyya coefficient and the green dots show a fidelity estimator recently introduced by Choi et al. [70] as a function of the circuit depth measured in the number of two-qubit gates.

Ref. [380] after tailoring it to the gate set and qubit topology of the trapped ion device 12.1.2. This numerical synthesis procedure efficiently produces low-depth circuits but is limited to a small number qubits. It can, however, be a useful tool when simulating larger systems 12.1.2.

The undersampled FID measured in experiment is reconstructed into a spectrum by a recovery algorithm which assumes that the time domain signal is sparse in the

frequency domain. The sparsity assumption holds true for 1D NMR spectra of simple molecules and also for higher-dimensional NMR spectra of larger complex molecules. Indeed, higher-dimensional NMR was developed for the purpose of generating sparse, and therefore interpretable, spectra for biological macromolecules such as large proteins. These two steps – non-uniform sampling (NUS) and spectral reconstruction – form the basis of compressed sensing. Compressed sensing techniques have their root in information theory [95], but have been further developed in the experimental NMR community where they can drastically reduce the data collection burden [42]. While these techniques have recently been used in quantum sensing [9], we demonstrate their use in quantum simulation experiments to similarly reduce the computational cost [8]. In Fig. 39A we plot a noisy emulation of the ion trap experiment at all values of the uniform dense time grid and compare to the NUS points that were actually collected in the experiment. Experimental data was collected up to times $t = 6$ 12.1.2, but is only shown up to $t = 0.2$ to allow a clear comparison to the noisy emulation. We use a sine-weighted Poisson gap NUS schedule that is dense at short times as it has been shown to reduce reconstruction artifacts [163]. Figure 39B shows the spectrum resulting from Fourier transforming the experimental data before running the reconstruction algorithm. We see that the signal-to-noise ratio in this raw spectrum is poor due to NUS artifacts, with a Lorentzian fit to the peaks resulting in an uncertainty of approximately 1 Hz. The same spectrum is shown after we run the iterative soft thresholding (IST-S) reconstruction algorithm; the signal-to-noise is dramatically improved, with the uncertainty reducing by an order of magnitude to approximately 0.1 Hz. The reconstructed spectrum matches the spectrum resulting from fully sampled noisy emulation 12.1.2. Experimentally, only 102 out of the 4096 time points were collected, indicating that compressed sensing reduced the computational burden of the experiment by more than a factor of 40. This reduction is particularly crucial for experiments with slow repetition rates.

In Fig. 39C, we asses the quality of the trapped-ion simulation by comparing the outputs of all 102 circuits ($\times$ 8 initial states) with the ideal outputs resulting from a noiseless circuit emulation. These synthesized circuits, each corresponding to a

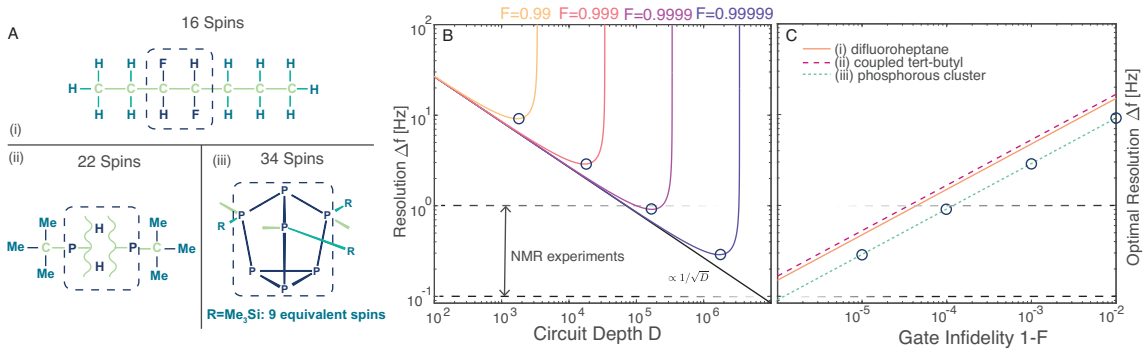

Figure 40: Scaling up to classically hard simulations. (A) Chemical structures of (i) anti-3,4-difluoroheptane [196] (ii) a system with two coupled tert-butyl groups and (iii) the $B[ACR_9]_3$ phosphorous system [245]. Light green atoms do not contribute to the NMR signal and dashed boxes indicate strongly interacting clusters who's circuit synthesis can significantly speed up the quantum computation 12.1.4. (B) Experimental design curves for $(Me_3Si)_3P_7$ (panel A(iii)), showing $1/\sqrt{D}$ scaling, where D is the circuit depth, of the frequency resolution up to a minimally achievable width set by the decoherence of the quantum computer. The circuit depth is measured by the number of fully-connected two-qubit gates. (C) Optimal resolution for all three molecules. The circles indicate the resolution at optimal circuit depth and the dashed black horizontal lines indicate the resolution accessible in NMR experiments.

time t, have varying circuit depths according to the entanglement generated in the system at that time 12.1.3. The Bhattacharyya coefficient (BC), which provides an upper bound for the fidelity of the prepared quantum state 12.1.3, indicates that a typical two-qubit gate operation was enacted with fidelity at most 98.9%. The BC is an informative metric for states with high fidelities, but it saturates to a value of 0.5 for the random states that the system tends to after decoherence runs its course. We therefore also examine the Choi fidelity estimator of Ref. [70], which is a more intuitive metric for low fidelity states as random states will be mapped to a fidelity close to zero. The Choi fidelity yields an estimate of 97.7% fidelity per operation enacted in the trapped-ion experiment.

While the present experiment is performed on state-of-the-art quantum hardware, it is still easily tractable on a classical computer. In order to elucidate the hardware resources required to scale quantum simulations to classically hard NMR experiments, we examine three challenging systems that are at the border of what is classically

simulable. The compounds are are depicted in Fig. 40A. Each system can be simulated on a classical computer using Spinach [154], an advanced classical simulation package, in several hours, provided access to 32 CPU cores, 128 GB RAM, and a graphics card as powerful as the Titan V. The interaction graphs characterizing the molecules' nuclear spin Hamiltonians have a compact structure, and are composed of strongly interacting clusters of four to seven spins which are weakly connected to other clusters. The compact nature of the interaction graphs—which give rise to rapidly spreading strong correlations—makes these systems hard to simulate on a classical computer, even though these NMR experiments can be described without the long-range dipolar interactions that are central to other challenging NMR protocols.

We estimate the resources required to simulate these systems using a quantum computer by using product formulas to prescribe circuits that implement time-evolution under the Hamiltonian of Eq. (13.1). While there are many quantum algorithms that implement quantum dynamics, product formulas are considered to have the lowest resource overhead and be most suitable for early quantum devices [68, 69]. We exploit both the cluster structure of the nuclear interactions as well as inherent dephasing in the NMR experiment to further reduce the cost 12.1.4.

In Fig. 40B, we plot the achievable linewidth Δf of the NMR spectrum as a function of the circuit depth D for quantum computers with various levels of decoherence. We assume the time-evolution quantum circuits are designed using a clustered first order product formula, a schematic of which is depicted in Fig. 41. We define the circuit depth as the number of fully connected two-qubit gates, as available in ion trap quantum computers [105]. We observe a $1/\sqrt{D}$ scaling, reminiscent of the standard quantum limit, up to a critical depth where the decoherence of the quantum computer takes over. At any given value of the gate fidelity F there is an optimal circuit depth $\sim 1/\log(1/F)$ arising from a competition between algorithmic error and decoherence, resulting in linewidth $\Delta f \sim \sqrt{\log(1/F)}$. Fig. 40C depicts the expected optimal linewidth for the molecules in Fig. 40A. While we clearly observe that the larger molecules from Fig. 40A are considerably harder to simulate than the four spin methyl group that was computed here, it should be noted that these curves are

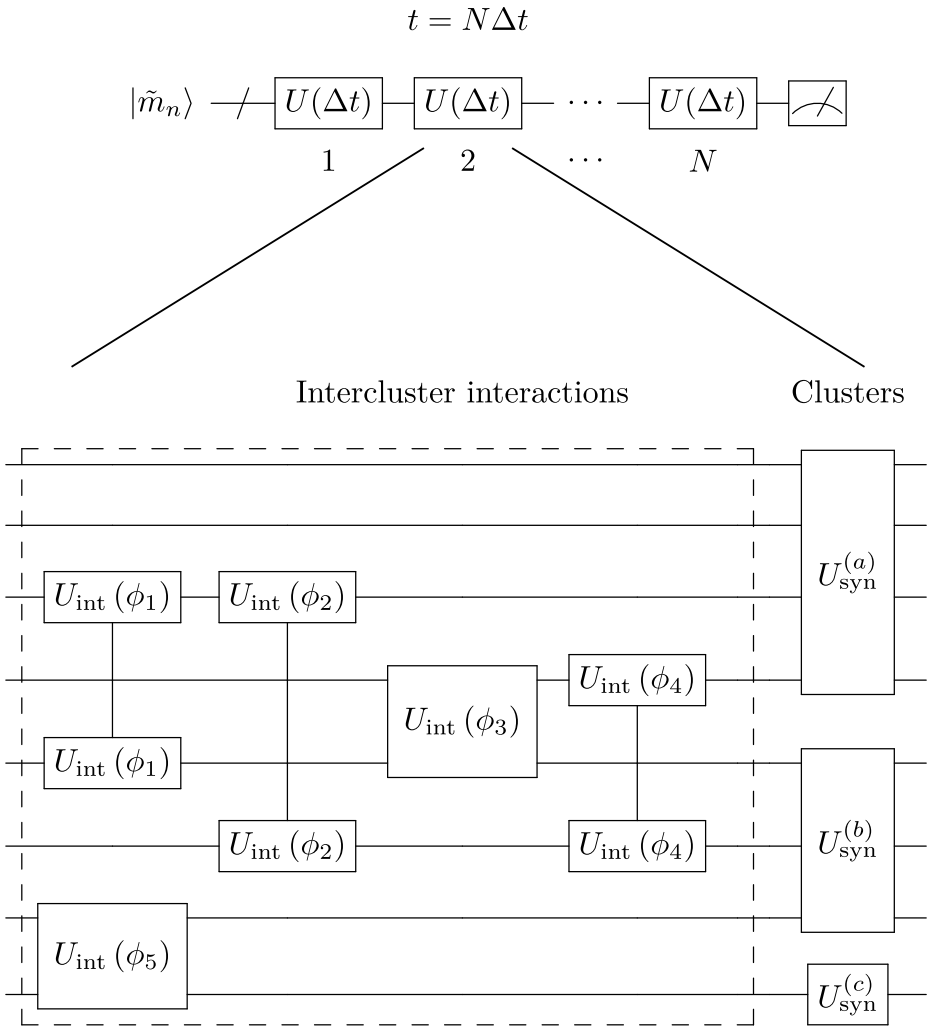

Figure 41: Schematic of quantum circuits simulating the time-evolution of challenging NMR systems. The total time-evolution is split into N identical increments. Each increment is composed of numerically synthesized circuits enacting the time-evolution of strongly interacting clusters of spins, along with two-qubit gates enacting interactions between spins from different clusters. An example of a numerically synthesized circuit is given in 12.1.2.

expected to saturate for Hamiltonians corresponding to clustered molecules. To simulate the phosphorus cluster (Fig. 40A(iii)) to the same level as the physical NMR experiment, we expect to require circuits of $O(10^5)$ gates with a typical gate infidelity of $O(10^{-4})$, an infidelity that is two orders of magnitude better than the present experiment. Such infidelities have been achieved in small trapped-ion systems [121, 18], and future scaling strategies hold great promise for reaching the above performance metrics [46].

Our demonstration provides the first proof of principle that quantum computers can simulate NMR spectra within experimental resolution. Simulations of NMR experiments on quantum hardware would not only be invaluable to analyzing conventional NMR experiments in systems consisting of hundreds to thousands of spins [104] but could also help realize the full potential of emerging modalities that explore strong spin-correlations such as zero-field, low-field, and nanoscale NMR. These latter protocols generate spectra that are especially difficult to interpret without computational simulations, which in turn can prove classically intractable for systems of even a few tens of spins [250].

While scaling quantum NMR simulations to classically intractable systems will be challenging, it should be noted that the resource projections in Fig. 40 are significantly less demanding than most other near-term quantum computing applications [68, 195, 131]. The physical reason behind the reduced resource cost is that dephasing is inherent in the dynamics of nuclear spin systems, with a rate given by the finite line-width of spectral peaks in NMR experiments. Quantum simulations can tolerate decoherence in the quantum device as long as it is less than the dephasing rate of the spin system [329]. NMR thus provides a natural task where we can seek a practical quantum advantage from near-term quantum devices: simulation of noisy spin systems using noisy quantum computers.

12.1.2 Methods

Data collection

NMR simulation circuits are run on a trapped ion quantum computer that uses the $^2S_{1/2}$ states of $^{171}Yb^+$ ions as the qubit states. We trap 15 ions in a chain for the simulation, and the circuits use 4 of those ionic qubits. Before each circuit iteration, ions are cooled using Doppler cooling and Raman sideband cooling, and then reset to the logical $|0\rangle$ state via optical pumping. The qubit state is manipulated using 355-nm pulsed Raman beams. Single qubit gates are implemented using SK1 pulses [**?**], and two-qubit gates are mediated by Mølmer-Sørensen interactions [**?**] —these gates

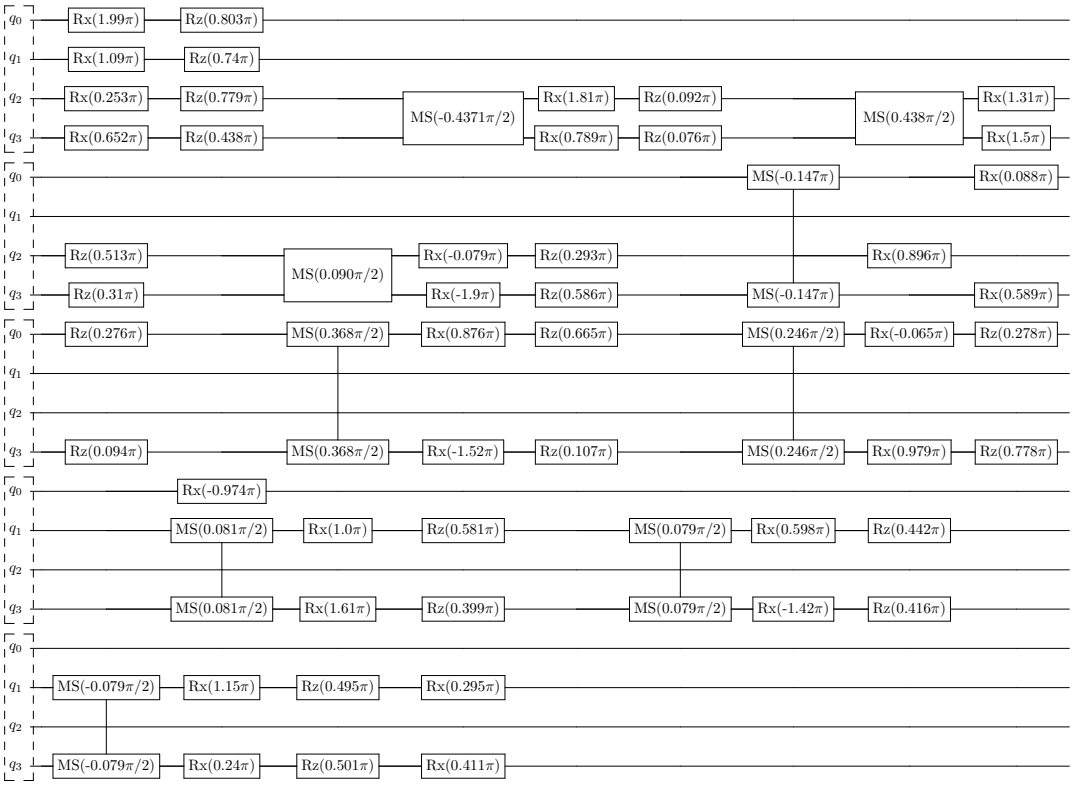

Figure 42: Time-evolution circuit. Example time-evolution circuit generated by numerical synthesis algorithm corresponding to $t = 0.07$ s. Circuit is split into five rows and read top to bottom, with the start of each row indicated by a dashed box around the four qubits in the experiment.

are run sequentially. We measure the qubit states by shining 369-nm light resonant on the $^2S_{1/2} \rightarrow {}^2P_{1/2}$ cycling transition that scatters photons.

The time series data used to construct the NMR spectrum of acetonitrile was collected over the course of 12 days, during which the quantum computer's hardware remained unchanged. The data consists of a 1000 shots of 102 different circuits, for which 8 different initial states were prepared. While running circuits on the quantum machine, we perform system calibrations of trap voltages and gate amplitudes every hour to mitigate effects of system drift on circuit performance. We do not correct for state preparation and measurement (SPAM) errors in this study, and a table of our system's SPAM characterization is presented in Ref. [105].

Time-evolution circuit synthesis

We use the numerical optimization algorithm in Ref. [380] to synthesize the circuits implementing the time-evolution unitary $U(t) = \exp(-iHt/\hbar)$, with the Hamiltonian given in Eq. (12.5). The algorithm implements a bottom-up approach, building the single- and two-qubit gate decomposition of a n-qubit unitary by iteratively searching for a m-qubit gate decomposition with $m < n$. Initially, m is set to $n - 1$. The algorithm is hardware topology and gateset aware; to specialize for the trapped-ion system, we allow all-to-all connectivity of qubit interactions and choose Mølmer-Sørensen gates with variable angles as the interaction gate.

We choose a unitary error of $\epsilon = 10^{-2}$, with the synthesis algorithm producing a circuit in terms of Mølmer-Sørensen (MS) gates and generic single-qubit rotations that approximates the true time-evolution unitary within this error. We then iteratively perform a X-Z-X decomposition of each single-qubit rotations, commuting the trailing X rotation through each MS gate before decomposing the next single-qubit rotation. This optimization results in roughly two Z rotations and two X rotations after each MS gate. As Z rotations are implemented virtually in the trapped-ion system, the final circuit has only two physical single-qubit rotations for each MS gate, and thus the physical circuit depth is reduced compared to the initial output of the synthesis algorithm. An example of the final optimized circuit is shown in Fig. 42. Typically, the produced circuits were composed of up to 40 MS gates and 80 physical single-qubit gates.

Compressed sensing

A general function in the frequency-domain that is nonzero in a specified frequency window can be reconstructed by Fourier transforming a corresponding time-domain signal that is uniformly sampled at the Nyquist rate. If the function is known to be sparse in the frequency domain, however, the time signal can be undersampled by choosing a non-uniform subset of time points which still capture the relevant information in the frequency domain [95]. The missing points on the original uni-

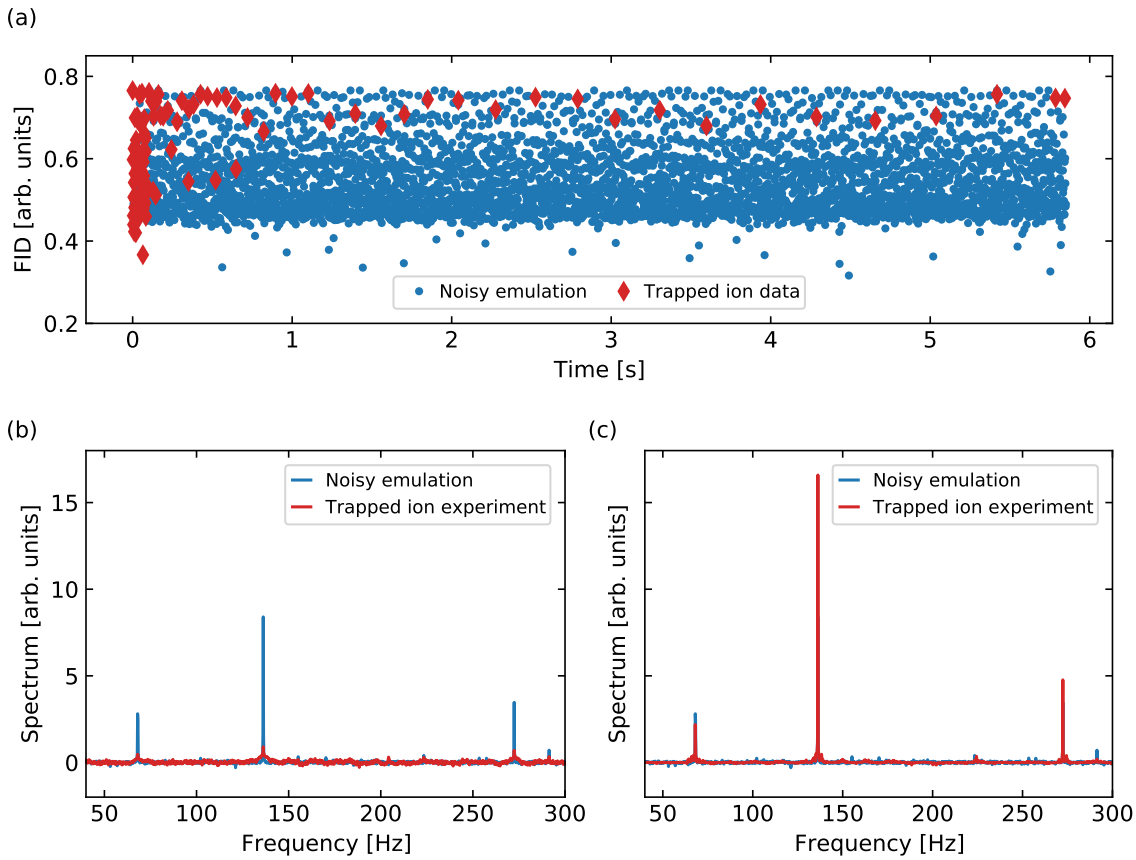

Figure 43: Compressed sensing reconstruction. (a) Comparison of the FID for noisy quantum circuit emulation on a fully sampled uniform time grid of 4096 points (blue circles) and the 99 data points experimentally measured on the ion trap device (red diamonds). (b) Fourier transform of the FID after replacing unsampled points with zeros. (c) Reconstructed spectrum after applying the iterative soft thresholding algorithm. The noise is modeled by two-qubit gates subject to both amplitude and phase damping with rates 0.005 and 0.035 respectively.

form time grid create artifacts in Fourier transform of the signal, however, which must then be removed using a compressed sensing reconstruction algorithm that exploits the assumed sparsity of the frequency signal. NMR spectra are often sparse as they are composed of a series of Lorentzian peaks, and therefore compressed sensing techniques allow for a dramatic reduction in the sampling required during an NMR experiment [42].

This sparsity can also be exploited in quantum simulations of NMR experiments by computing the FID at only the undersampled time points and then reconstructing the spectrum. We compute the FID at 102 out of the $N_s = 4096$ time points on the

uniform grid, choosing the points according to a sine-weighted Poisson gap schedule. Such schedules have been shown to reduce undersampling artifacts [163]. The points are randomly chosen with the likelihood to pick a point $m+1$ on the uniform grid, given we have picked a point m, set by a Poission distribution with mean proportional to $\sin(\alpha\pi m/N_s)$. Specifically, we choose $\alpha = 0.5$, resulting in a schedule that is dense at short times before becoming increasingly sparse at later times. We find that this choice allows for much larger compression compared to a schedule with uniformly distributed gaps between points, or a schedule that is also dense at late times (corresponding to $\alpha = 1$). After computing the undersampled FID, we reconstruct the spectrum using the iterative soft thresholding (IST-S) algorithm [42].

In Fig. 43(a), we plot the FID computed via noisy emulations for all 4096 time points, and compare with the 102 points that were experimentally computed. This plot corresponds to Fig. 39A, but with the quantities depicted over the full time grid. In Fig. 43(b), we plot the spectrum computed after padding the experimental data with zeros for all time points that were not computed. We see that there is some signal at the spectral peaks expected from the noisy emulation, but the signal-to-noise is very large. The zero-padded spectrum in this plot corresponds to the green dots in Fig. 39B. In Fig. 43(c), we plot the compressed sensing reconstruction of the experimentally computed spectrum, and see that the signal-to-noise is dramatically improved. The reconstructed spectrum in this plot corresponds to the yellow curve in Fig. 39C.

Scaling to larger systems

The numerical optimization algorithm we use is likely to be limited to producing time-evolution circuits for systems of up to $\sim$ 7 spins [380]. This tool can still prove useful, however, when scaling to large, classically-intractable NMR simulations by exploiting the cluster structure of these molecules (see Fig. 40A). The strongly-interacting clusters are usually formed from 4-7 spins, and the optimization algorithm can be used to synthesize the time-evolution circuit for each cluster. These circuits can then be combined with a Trotter formula to implement the time-evolution of the

entire systems [69]. Compared to a Trotter decomposition of the entire system, such a hybrid approach can reduce the overall circuit depth, as discussed in Sec. 12.1.4. Furthermore, at the level of discretization estimated in Fig. 40, the simulation times are small enough that the optimization should converge very quickly, potentially enabling real-time compilation of the overall time-evolution circuit.

We note that numerical circuit synthesis of small subsystems and compressed sensing techniques form a synergistic combination of tools. For example, cluster-exploiting Trotter formulas allow for an overall reduction in resource cost at all simulation times, while compressed sensing non-uniform sampling schedules may sample more densely from short times where the resource cost is smallest. On the hardware side, the all-to-all connectivity of trapped ions makes them well-suited to the interaction graphs within clusters, and may allow comparatively smaller gate counts for the cluster evolution circuits. The relatively slow cycle time of ion devices is ameliorated by compressed sensing techniques, which reduce the number of time points that must be sampled. The combination of numerical circuit synthesis, which exploits the clustered interaction structure of a system, and compressed sensing, which exploits sparsity of the observable of interest in the transform domain, may similarly prove useful for quantum simulations in quantum chemistry and condensed matter systems where both of these characteristics are often present [8].

12.1.3 Spectral peak at J/2

The acetonitrile spectrum we compute on the trapped ion quantum computer, depicted in Fig. 37, exhibits a resonance at frequency $J/2$ which does not appear in the NMR experiment of Ref. [206]. Here, we explain the origin of this additional peak and discuss how to prevent such artifacts from appearing in future experiments.

The zero-field nuclear spin Hamiltonian of acetonitrile is

$$\hat{H} = J\left(\hat{\mathbf{S}}_1 + \hat{\mathbf{S}}_2 + \hat{\mathbf{S}}_3\right) \cdot \hat{\mathbf{S}}_4, \tag{12.5}$$

where $\{\hat{\mathbf{S}}_1, \hat{\mathbf{S}}_2, \hat{\mathbf{S}}_3\}$ represent the three ^{1}H and $\hat{\mathbf{S}}_4$ represents the ^{13}C. The eight positive

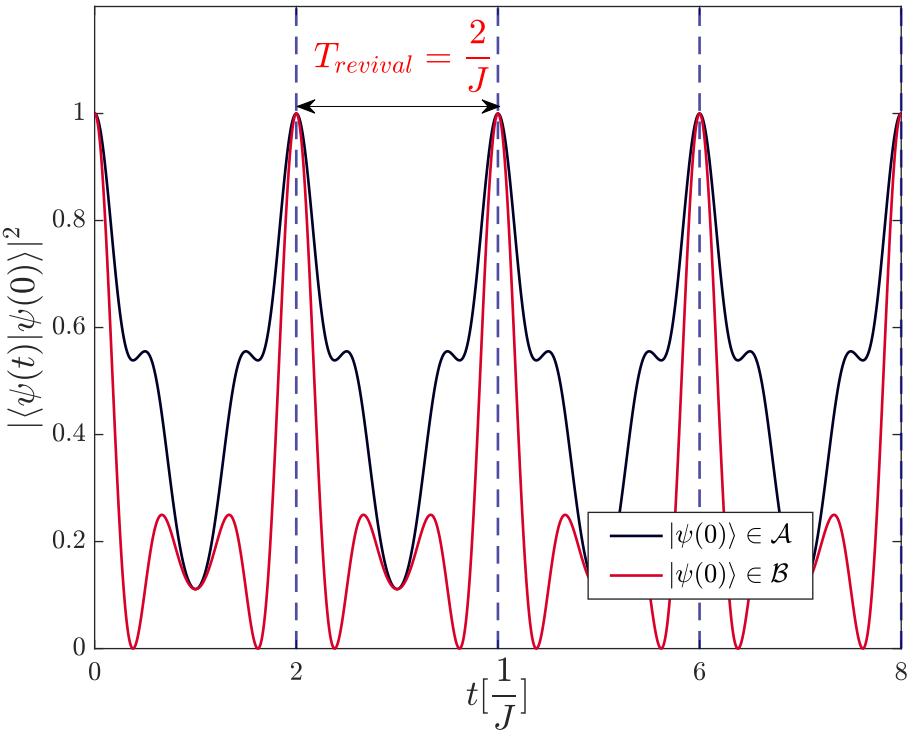

Figure 44: Magnetization basis state revivals. A system initialized in state $|\psi(0)\rangle$ selected from magnetization basis states $\mathcal{A} = \{\tilde{m}_1, \tilde{m}_3, \tilde{m}_5\}$ and $\mathcal{B} = \{\tilde{m}_4, \tilde{m}_6, \tilde{m}_8\}$ undergoes revivals with a period $2/J$.

magnetization states used to compute the FID, see Eq. (12.4), and their magnetizations are

$$
\begin{aligned}
|\tilde{m}_1 = 1.626\rangle &= |0000\rangle & \tilde{m}_1 &= 1.626 \\
|\tilde{m}_2 = 1.626\rangle &= |0001\rangle & \tilde{m}_2 &= 1.374 \\
|\tilde{m}_3 = 1.626\rangle &= |0010\rangle & \tilde{m}_3 &= 0.626 \\
|\tilde{m}_4 = 1.626\rangle &= |0011\rangle & \tilde{m}_4 &= 0.374 \\
|\tilde{m}_5 = 1.626\rangle &= |0100\rangle & \tilde{m}_5 &= 0.626 \\
|\tilde{m}_6 = 1.626\rangle &= |0101\rangle & \tilde{m}_6 &= 0.374 \\
|\tilde{m}_7 = 1.626\rangle &= |1000\rangle & \tilde{m}_7 &= 0.626 \\
|\tilde{m}_8 = 1.626\rangle &= |1001\rangle & \tilde{m}_8 &= 0.374
\end{aligned}
$$

The small, four spin Hilbert space of the NMR active nuclear spins of the molecule

along with the molecules highly symmetric nature—as codified by the single interaction scale J in Eq. (12.5)—combine to yield perfect revivals when the system is prepared in six of the above magnetization basis states. These states can be grouped into the triads $\mathcal{A} = \{\tilde{m}_1, \tilde{m}_3, \tilde{m}_5\}$ and $\mathcal{B} = \{\tilde{m}_4, \tilde{m}_6, \tilde{m}_8\}$ and we depict their revivals in Fig. 44. When viewed in the energy eigenstate basis, each of these six magnetization basis states only has weight on energy eigenstates whose eigenvalues are integer multiples of $J/2$. Consequently, all energies relevant to the dynamics are commensurate with a smallest splitting of $J/2$, which leads to the state reviving with perfect fidelity at this frequency. The revival of each state is mirrored in its entanglement dynamics. Each magnetization state begins in an unentangled product state, non-monotonically accrues entanglement over a period $T = \frac{2}{J}$, and then dis-entangles as it returns to the original product state. The high symmetry and small size of the molecule therefore causes the dynamics to defy usual expectations of ergodicity, with the entanglement of a system initially prepared in one of the states in $\mathcal{A}$ or $\mathcal{B}$ oscillating at a frequency $J/2$ instead of growing monotonically in time.

The numerical optimization algorithm, Ref. [380], we use to synthesize time-evolution circuits for each time point reflects this oscillating entanglement in the gate depth of the synthesized circuits. Specifically, times at which the system is more heavily entangled correspond to deeper circuits with a larger number of two-qubit gates, as can be seen in Fig. 45.

Noise in the system affects deeper circuits more than shallower ones, and therefore imprints the $J/2$ entanglement oscillation onto the experimentally measured observable by lowering the fidelity of the signal at this frequency. We can gain visibility into this process by computing the average Bhattacharyya coefficient (BC) between the measured basis state populations and noiseless emulations of the circuits for each time point. The BC is defined as

$$\mathrm{BC} = 1 - \frac{1}{2} \sum_j \left(\sqrt{p(j)} - \sqrt{q(j)} \right)^2, \tag{12.6}$$

where j runs over all computational basis states, and $p(j)$ and $q(j)$ are the correspond-

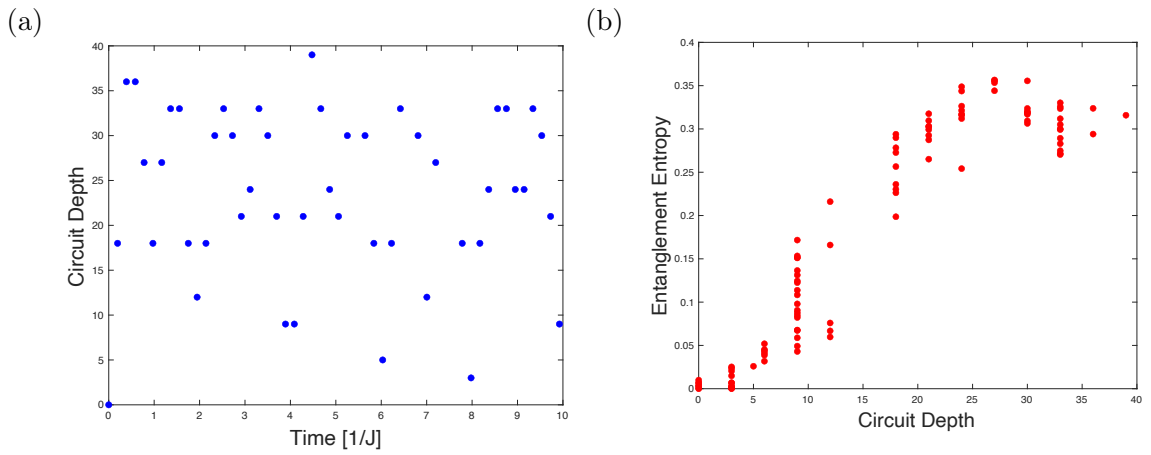

Figure 45: Synthesized circuit depth and entanglement. (a) Two-qubit gate count of synthesized time-evolution circuits for each FID evolution time measured on the trapped-ion device. (b) Entanglement entropy of the system at a particular evolution time compared to the two-qubit gate count of the circuit implementing that evolution. We average the final entanglement entropy for systems initialized in each of the eight magnetization basis states used to compute the FID.

ing occupation probabilities, given by the diagonal elements of the density matrix, of the two states beings compared. The BC gives a measure of the fidelity of the experimental runs and we plot it for every experimentally measured time point in Fig. 46(a). We see that it varies as a function of time, and these oscillations correspond to time-evolution circuits that have a larger two-qubit gate count as shown in Fig.39C. In Fig. 46(b), we use the same compressed sensing algorithm used to compute the NMR spectrum to reconstruct the Fourier transform of the the BC dynamics depicted in Fig. 46(a). We observe a sharp peak at $J/2$, confirming that the fidelity of the experimental oscillates at a frequency of $J/2$. These oscillations corresponding to oscillating depths of the synthesized circuits, which in turn reflect the entanglement revivals of the molecule's underlying dynamics. The above story confirms why noisy circuit simulations, such as the one depicted in Fig. 39A, also exhibit this $J/2$ resonance peak in the computed NMR spectrum regardless of the type of decoherence channel used to simulate noise.

Artifact peaks such as the $J/2$ resonance can easily be removed in future experiments. By padding all time-evolution circuits so that they have roughly the same depth as the deepest synthesized circuit, the noise in the system can no longer imprint

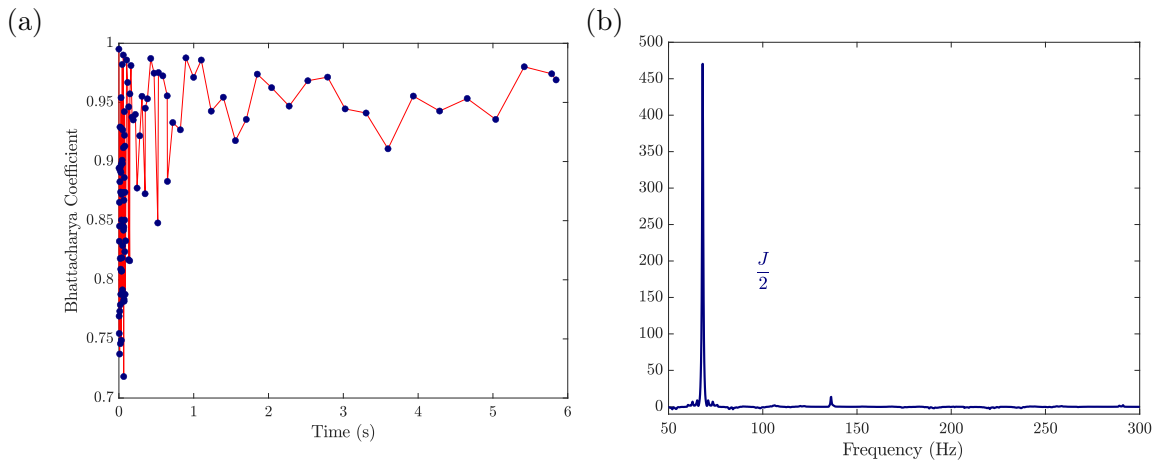

Figure 46: Bhattacharyya coefficient between trapped ion measurements and noiseless emulation of the experiment. (a) BC vs evolution time. (b) Compressed sensing reconstruction of the frequency spectrum of the BC. We see that the BC, a measure of the fidelity of the system, only varies at the frequency $J/2$ with which the system's entanglement, and therefore circuit depth, oscillates.

any frequency on the measured signal as the gate depths no longer oscillate. We show in Fig. 47 that such padding dramatically decreases the height of the $J/2$ peak in noisy circuit simulations of the experiment. The padding will, however, slightly decrease the overall fidelity of the computed FID as every point will be subject to as much noise as the deepest time-evolution circuit. If we desire to compute the maximum fidelity signal allowable by hardware, we can compute FID twice - once with padded circuits and once without. Any feature that vanishes in the padded experiment can be removed from the higher fidelity non-padded experiment.

Lastly, we note that artifact peaks are unlikely to appear during quantum simulations of the majority of NMR experiments, and become increasingly unlikely when scaling to classically intractable systems. Small molecules which do not exhibit the high degree of symmetry exhibited in Eq. (12.5) are unlikely to exhibit the dynamical revivals at the heart of artifact peaks. Larger systems, including those with some symmetry, are even less likely to exhibit revivals as entanglement spreads throughout the system. In fact, classically intractable systems are intractable precisely because quantum correlations spread quickly throughout the system. Furthermore, quantum simulation algorithms that generalize to larger systems, such as product formulas, typ-

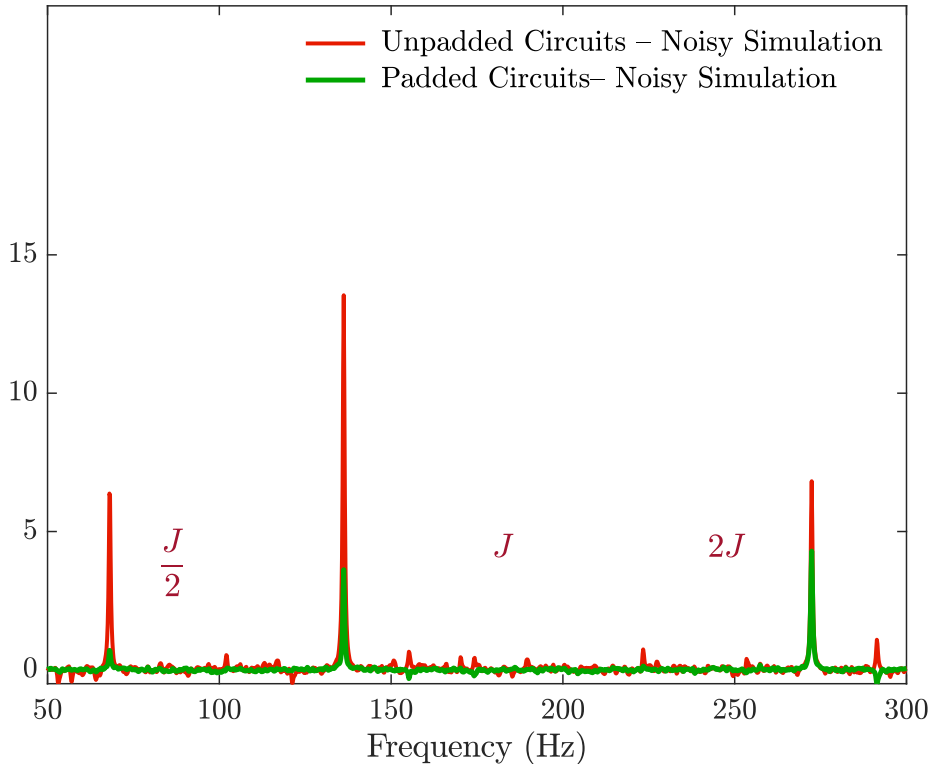

Figure 47: Noisy circuit simulation. The zero-field NMR spectrum of acetonitrile computed using noisy circuit simulations with and without padding. The padded circuits no longer have depths that oscillate in accordance with the system's entanglement, and therefore do not exhibit the artifact peak at $J/2$. Noise was simulated by by adding a depolarizing channel to each gate, with a rate of 10^{-3} for single-qubit gates and 10^{-2} for two-qubit gates.

ically have gate depths that monotonically increase with the simulation time. This relationship is also directly true for analog quantum simulation. Noise in these cases will lead only to a broadening of spectral peaks, and cannot imprint any artifact frequencies on the measured signal. Therefore, artifact peaks are unlikely to be a common concern during quantum simulations of NMR experiments. Even in small, highly symmetric systems where the peaks might appear, circuit padding is a cheap way to remove these artifacts.

12.1.4 Resource Estimates for NMR simulation

The standard Hamiltonian simulation task (e.g. by Suzuki-Trotter product formula, hereafter product formula), seeks to approximate exact unitary dynamics within a

finite precision ϵ (clarified below). However, the spectral resolution—alternatively, the line-width—of NMR experiments are set by the dephasing of the nuclear spins. The inherent dephasing in the experiments we seek to simulate reduces the resource cost simulation compared to purely coherent systems. In what follows, we show how this discrepancy between the standard Hamiltonian simulation task (simulating a unitary to finite *precision*) and the task of employing Hamiltonian simulation as a sub-routine to compute an NMR spectrum (with finite *spectral resolution*) can yield gate counts that are several orders of magnitude smaller for the latter task, making it tractable on NISQ devices. To perform Hamiltonian simulation, we proceed by using a variant of first-order product formula that exploits the clustered structural motif present in many molecules that are classical challenging to simulate. In what follows, we first elucidate the distinction between the standard Hamiltonian simulation task and the task at hand and provide bounds on the requisite two-qubit gate fidelity and gate counts for computing NMR spectra with finite resolution. We round out our discussion by providing commutator bounds relevant to estimating the quantum resources required to simulate the NMR spectra of molecules with a clustered interaction structure.

Approximating Hamiltonian Dynamics for NMR Simulations

We begin by clarifying the difference between a standard Hamiltonian simulation task and the task of using Hamiltonian simulation to simulate NMR experiments. We consider performing Hamiltonian simulation via first order Trotterization, a simple but powerful and gate efficient method for simulating Hamiltonian dynamics. Keeping our discussion somewhat general for the moment, let's say we have a Hamiltonian $H = \sum_\mu h_\mu$, composed out of a number of N_c terms h_μ. We'd like to replace the time-evolution operator $U = e^{-i\Delta t H}$, for some small time-step Δt by our simple product formula:

$$\tilde{U} = \prod_{\mu=1}^{N_c} e^{-i\Delta t h_\mu}.$$

It follows from Baker-Campbell-Hausdorff (BCH), by keeping only lowest order contributions in Δt, that

$$\|U - \tilde{U}\| \leq \frac{(\Delta t)^2}{2} \sum_{\mu=1}^{N_c} \| \sum_{\nu>\mu} [h_\nu, h_\mu] \|, \tag{12.7}$$

as obtained in Ref. [68]. Consequently, we could also write the fidelity of the simulation as

$$\mathcal{F}_{\delta t} = \|U\tilde{U}\| \geq e^{-\beta(\Delta t)^2/2}, \quad \text{where} \quad \beta = \sum_{\mu=1}^{N_c} \| \sum_{\nu>\mu} [h_\nu, h_\mu] \| \tag{12.8}$$

Let's say we'd like to evolve for a total time $T = r\Delta t$, then the total fidelity will be

$$\mathcal{F}_{PF}(T) = \prod_{i=1}^{r} \mathcal{F}_{\delta t_i} = e^{-r\beta(\delta t)^2/2} = \exp\left(-\frac{\beta T^2}{2r}\right), \tag{12.9}$$

If we want a precision ϵ, then we need $\mathcal{F} = 1 - \epsilon \approx e^{-\epsilon}$. This sets the Trotter number r to achieve a precision ϵ:

$$r_\epsilon = \frac{\beta T^2}{2\epsilon}. \tag{12.10}$$

Achieving this can be quite challenging for even intermediate times, in particular in NISQ settings.

The task of simulating the relevant dynamics corresponding to an NMR experiment does not, however, require the approximation of unitary dynamics generated by the Hamiltonian to finite, time-independent precision ϵ. It requires instead the simulation of a spectrum to finite spectral resolution Δf. In an NMR experiment, $\Delta f \sim \gamma$, the dephasing rate of a single nuclear spin in experimentally interrogated sample. Thus, the task of simulating an NMR experiment with resolution Δf is equivalent to simulating Hamiltonian dynamics of a sample of N spins in which each spin decoherences independently with an *effective* dephasing rate $\gamma = \frac{\Delta f}{2\pi}$. Such dephasing exponentially degrades the fidelity, vis-a-vis perfect unitary dynamics given by the Hamiltonian, as $\mathcal{F}_{NMR} \sim e^{-\gamma N t}$. Thus, there is a subtle but essential distinction between the task of approximating a unitary to multiplicative error ϵ and performing Hamiltonian simulation to compute a spectrum with finite spectral res-

olution Δf. If, for the moment, we neglect decoherence in our quantum hardware and consider only algorthmic error due to our product formula, as given in 12.9, then setting $\mathcal{F}_{PF}(T) = \mathcal{F}_{NMR}(T)$ we find a upper bound for the minimal necessary Trotter number:

$$r_{NMR} = \frac{\beta T}{2\gamma N}. \tag{12.11}$$

As typical experiments interrogate regimes up to where $\gamma T \sim 1$, the number of Trotter steps r is reduced by a factor of $\frac{N}{\epsilon}$ as compared to the case of fixed precision—for the examples examined in Fig. 40, this corresponds to a $O(10^3 - 10^4)$-fold decrease in the number of steps required to realize the longest dynamics relevant to experiment.

For a more careful estimate of the necessary resources, we also account for the decrease in fidelity due to decoherence in our quantum hardware. We describe the decaying fidelity of our experiment due to hardware error as $\mathcal{F}_h(T) \sim F^{rN_g}$, where F is the two-qubit gate fidelity, r is the Trotter number, and N_g is the number of two-qubit gates required to realize a particular Trotter step. Note that by such a description, we assume that hardware error and algorithmic error are independent of each other and that two-qubit gates dominate the hardware error. The product of $\mathcal{F}_h(T)$ and $\mathcal{F}_{PF}T$ must be greater than or equal to $\mathcal{F}_{NMR}$ in order to perform reliable simulation. We obtain, the following requirement:

$$-N_g \log(F) + \beta(\Delta t)^2/2 \leq \gamma N \Delta t. \tag{12.12}$$

This will have a solution for the Trotter time step Δt as long as

$$F \geq e^{-\gamma N \Delta t / N_g}. \tag{12.13}$$

Requiring our quantum simulation fidelity to match the fidelity of the experiment —thereby recasting 12.12 as an equality —and re-arranging, we can establish an equation for $\gamma \sim \Delta f$:

$$\gamma = \frac{1}{N}\left(\frac{\Delta t \beta}{2} - \frac{N_g \log(F)}{\Delta t}\right) \tag{12.14}$$

By optimizing over the Trotter step Δt, we can set the ultimate resolution Δf_{opt} of our experiment:

$$\Delta f_{opt} = \frac{\gamma_{opt}}{2\pi} = \frac{1}{2\pi N}\sqrt{2 N_g \beta \log(1/F)} \tag{12.15}$$

Note that this optimal resolution is a simple function of the fidelity of the quantum hardware employed, given by F, and the efficiency of the algorithm used, as encoded by β and N_g. On the hardware side, improving gates and thereby improving the gate fidelity, parametrized by F, would lower the resolution. Similarly, on the algorithmic side, finding more efficient circuits to realize a single Trotter step (lowering N_g) or better product formulae (lowering β), would improve the resolution—in what follows, we provide strategies on how to achieve both of these algorithmic improvements.

Commutator Bounds for Clustered Hamiltonians

As implied by Eq. (12.15), decreasing β, defined above in Eq. (12.8) and representing the magnitude of the commutator error, would improve the resolution of the simulation. In what follows, we compute β, assuming an NMR Heisenberg Hamiltonian with clustered interactions, first in the standard way and then by taking advantage of the cluster motif. We show that by doing the latter, we can reduce β substantially.

Before beginning this program, it is useful to establish some intuition for how clustered interactions reduce β vis-a-vis the case of all-to-all couplings. If we take an all-to-all model with some typical coupling $J/\sqrt{N}$ (taking into account Kac normalization to keep the energy extensive in the system size N), we find

$$\beta = O(J^2 N^2), \quad \text{such that} \quad r \sim \left(\frac{JN}{\gamma}\right)^2 (\gamma T). \tag{12.16}$$

The situation changes for clustered Hamiltonians where each spin typically interacts with a sub-extensive number of spins k. For each term in the latter, only k terms

contribute in the commutator and there are kN terms, yielding:

$$\beta \sim k^2 N J^2, \quad \text{such that} \quad r \sim \left(\frac{Jk}{\gamma}\right)^2 (\gamma T). \tag{12.17}$$

Note that, due to the clustered nature of the interactions, r does not scale with N: Increasing the number of spins does not increase the Trotter number.

Having established an heuristic derivation for the scaling of β and thereby the Trotter number, we turn to the present situation of a Heisenberg model with local fields.

$$H = \sum_{ij} J_{ij}(S_i^x S_j^x + S_i^y S_j^y + S_i^z S_j^z) + \sum_i h_i S_i^z. \tag{12.18}$$

where all terms can be labeled by $\mu = (i, j, \sigma)$, indicating the bond and the operator that is acted with. If we perform a scheme which alternates all Ising-XX gates with all Ising-YYs and all Ising-ZZs, then β is comprised of three terms, defined below: β_1, β_2, β_3.

We first bound β_1, given by:

$$\beta_1 = \sum_{ij} |J_{ij}| \| \sum_{kl} J_{kl}[S_k^y S_l^y + S_k^x S_l^x, S_i^z S_j^z] \|, \tag{12.19}$$

Straightforward algebra brings us to

$$\beta_1 = \sum_{ij} |J_{ij}| \| \sum_k \left(2J_{ki}(S_k^x S_i^y - S_k^y S_i^x)S_j^z + 2J_{kj}(S_k^x S_j^y - S_k^y S_j^x)S_i^z \| \right). \tag{12.20}$$

where the fact that $J_{ij} = J_{ji}$ is used. We therefore have:

$$\beta_1 \leq \sum_{ij} 2|J_{ij}| \sum_k \left(\| J_{ki}(S_k^x S_i^y - S_k^y S_i^x)S_j^z + J_{kj}(S_k^x S_j^y - S_k^y S_j^x)S_i^z \| \right), \tag{12.21}$$

which can again be bounded as:

$$\beta_1 \leq 2 \sum_{ij} |J_{ij}| \sum_k \left| J_{ki} \| (S_k^x S_i^y - S_k^y S_i^x)S_j^z \| + |J_{kj}| \| (S_k^x S_j^y - S_k^y S_j^x)S_i^z \| \right). \tag{12.22}$$

Computing the norm directly—$\|(S_k^x S_i^y - S_k^y S_i^x) S_j^z\| = 1/4$ —we arrive at:

$$\beta_1 \leq \sum_{ijk} |J_{ik}||J_{ki}| \tag{12.23}$$

We can similarly bound β_2, which is given by:

$$\beta_2 = \sum_{ij} |J_{ij}| \| \sum_{kl} J_{kl} [S_k^y S_l^y, S_i^x S_j^x] \|, \tag{12.24}$$

as

$$\beta_2 \leq \frac{1}{2} \sum_{ijk} |J_{ik}||J_{kj}| \tag{12.25}$$

Finally there are local field terms, which if we do them together with the ZZ gates would give

$$\beta_3 = \sum_{i} |h_i| \| \sum_{kl} J_{kl} [S_k^y S_l^y + S_k^x S_l^x, S_i^z] \|, \tag{12.26}$$

which gives

$$\beta_3 = 2 \sum_{i} |h_i| \| \sum_{k} J_{ki} (S_k^x S_i^y - S_k^y S_i^x) \|, \tag{12.27}$$

and thus

$$\beta_3 \leq \sum_{ij} |h_i||J_{i,j}| \tag{12.28}$$

However, one can obtain a tighter bound by treating the Z-gates as a single global gate. Doing so yields:

$$\tilde{\beta}_3 = \| \sum_{kl} J_{kl} [S_k^y S_l^y + S_k^x S_l^x, \sum_i h_i S_i^z] \|, \tag{12.29}$$

in which case we'd arrive at

$$\tilde{\beta}_3 \leq \frac{1}{2} \sum_{ij} |h_i - h_j||J_{i,j}| \leq \beta_3. \tag{12.30}$$

Therefore, we have that the total spectral norm of the nested commutator β is

bounded by:

$$\beta \leq \beta_1 + \beta_2 + \tilde{\beta}_3 \leq \frac{3}{2}\sum_{ijk} |J_{ik}||J_{kj}| + \frac{1}{2}\sum_{ij} |h_i - h_j||J_{i,j}|. \tag{12.31}$$

For many molecules, the interactions between nuclear spins follows a clustered motif. In particular, we examine the computational resources to simulate classically hard molecules that are composed of strongly-interacting clusters tethered together with weakly interacting links. We leverage the clustered motif by performing a variant of first-order Trotter formula wherein the dynamics of the small clusters are numerically synthesized to high precision, using for example the algorithm of Ref. [380], while weak interactions between such clusters are rendered via a pairwise Trotter decomposition of the Hamiltonian.

To understand how this modifies β, we consider the following Hamiltonian:

$$H = H_c + \sum_{i,j} J_{i,j}(S_i^x S_j^{x,c} + S_i^y S_j^{y,c} + S_i^z S_j^{z,c}) + \sum_i h_i S_i^z, \tag{12.32}$$

and

$$H_c = \sum_{k,l} V_{k,l}(S_k^{x,c} S_k^{x,c} + S_k^{y,c} S_l^{y,c} + S_k^{z,c} S_l^{z,c}) + \sum_k h_k S_k^{z,c}, \tag{12.33}$$

where the superscript simply indicates that the operator belongs to the cluster H_c. If we could synthesize the Hamiltonian of the cluster efficiently (see below), we find:

$$\beta \leq \frac{3}{2}\sum_{i,j,k} |J_{i,k}V_{k,j}| + \frac{3}{2}\sum_{i,j,k} |J_{i,k}J_{k,j}| + \frac{1}{2}\sum_{i,k} |J_{i,k}||h_k - h_i|. \tag{12.34}$$

By comparing Eq. (12.34) with Eq. (12.31), we see that the latter avoids terms with intra-cluster couplings (i.e. terms like $V_{i,j}V_{k,l}$). For the cases considered in Fig. 40, making use of the cluster structure in this manner reduces the Trotter number by one to two orders of magnitude. We note that classical NMR simulation algorithms also reduce their resource cost by exploiting structure in the molecule's interaction graph using spiritually similar decompositions of the system's dynamics [154]

12.2 Analog simulation in superconducting devices

In Sec. 12.1, we discussed how quantum simulation of NMR experiments can tolerate decoherence in quantum devices due to decoherence in the NMR system itself. This allowed a dramatic reduction in the resource cost for digital quantum simulation of theese systems. In comparison, quantum simulations of classically hard quantum chemistry [26] and condensed matter systems [27] may have a lower tolerance to device decoherence than NMR systems as the dynamical systems being simulated in these settings do not explicitly contain dissipation. The tolerance towards decoherence in NMR simulation can also be exploited by analog quantum simulation via Hamiltonian engineering of quantum devices, providing an alternative route to digital quantum simulation via quantum circuits. Analog simulators may be easier to realize in the near-term [9], and the fact that NMR systems only explore a set fraction of state space due to decoherence means that the analog device need only be engineered to access the same fraction of space, as opposed to digital quantum computers which are designed to have universal control and access to the full exponentially large state space. Here, we discuss a concrete proposal for analog quantum simulation of NMR systems on superconducting devices.

12.2.1 Superconducting devices

In Fig. 48, we show an eight qubit chip composed of four flux-tunable grounded transmon system qubits and four flux-tunable grounded transmon 'coupler' qubits. The system qubits are the qubits we perform computations with, while the coupler qubits are used to tunably couple adjacent system qubits [376]. The system implements of a hard-core Bose-Hubbard model that can be mapped to the following spin Hamiltonian [378]:

$$H_{\mathrm{SC}} = \sum_i \omega_i S_i^z + \sum_{\langle ij \rangle} 4J_{ij} \left(S_i^+ S_j^- + S_i^- S_j^+ \right) \tag{12.35}$$

(a) (b)

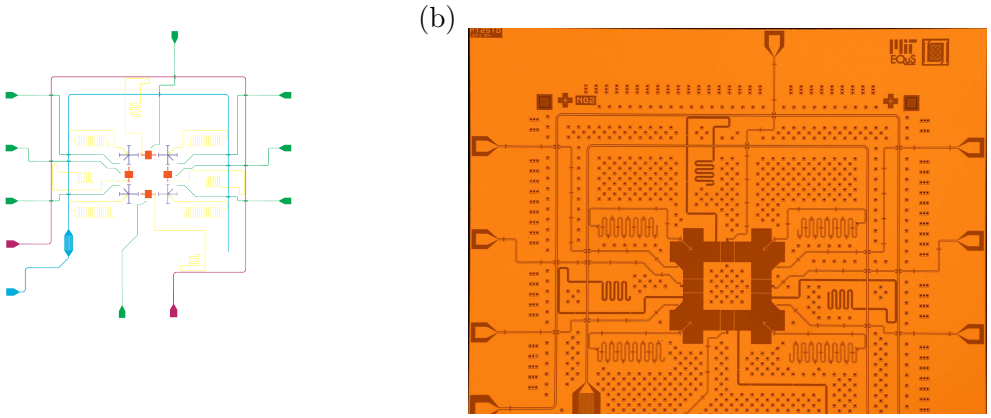

Figure 48: Tunable coupler superconducting chip for proposed analog simulation experiment. (a) False color. (b) Optical micrograph. The tunable couplers on the chip are a few μm in size..

where the spin operators S_i represent system qubits. The effective nearest-neighbor coupling J_{ij} between adjacent system qubits can be tuned by modulating the frequency of the coupler qubits. The sweet spot frequency of the system and coupler qubits are offset by approximately 1 GHz, allowing us to effectively turn off the interaction between adjacent system qubits, as well as to partially compensate for the parasitic ZZ interaction in the system. The chip therefore constitutes a 2x2 grid of system qubits with frequencies that can be tuned between 4.5 GHz - 3.0 GHz and effective nearest-neighbor interactions that can be tuned from +5 MHz to −30 MHz.

12.2.2 Hamiltonian engineering

We would like to manipulate the system so that the native dynamics of the chip, described by Eq. (12.35) is turned into the appropriate NMR Hamiltonian, described in Sec. 10.1. A framework to systematically construct pulse sequences to do this is described in Ref. [71]. The idea is to discretize the total time-evolution into several (Floquet) cycles, each of which constitutes a sequences pulses implementing global rotations on the spins interspersed with evolution under the system's native Hamiltonian. If the total time is discretized into a sufficiently large number of cycles, the effective dynamics of the system can be described via average Hamiltonian theory. We can think of the framework in Ref. [71], which was experimentally demonstrated in

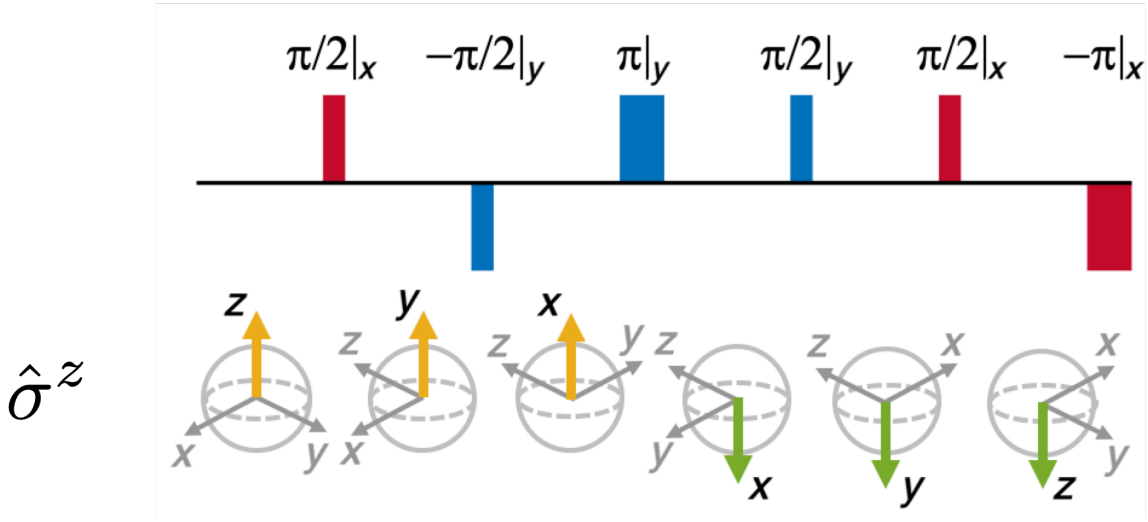

Figure 49: Pulse sequence that echos out local S_i^z terms and symmetrizes the flip-flop interaction.

Ref. [383], as a generalization of dynamical decoupling pulse sequences that have long been used in NMR experiments. Here, we utilize these pulse sequences to engineer the native Hamiltonian of a quantum device into an effective Hamiltonian implementing an analog quantum simulation of a different target system.

For example, the pulse sequence in Fig. 49 echos out the local S_i^z terms in Eq. (12.35) while symmetrizing the flip-flop interaction, transforming it into

$$H_{\text{av}} = \sum_{\langle ij \rangle} \mathbf{S}_i \cdot \mathbf{S}_j \tag{12.36}$$

A similar pulse sequence that symmetrizes the interaction but keeps the S_i^z terms will implement the NMR Hamiltonian Eq. (13.1). Such a Hamiltonian is a good description of many liquid-state NMR experiments, including multidimensional experiments such as COSY. We demonstrate the by simulating the COSY90 spectrum of rotenone, a 22 spin pesticide, using the true Hamiltonian Eq. (13.1) (Fig. 50), and using the native superconducting Hamiltonian Eq. (12.35) with the appropriate pulse sequence (Fig. 51).

We see that both 2D spectra match quite well, with a few discretization artifacts in Fig. 51 that are not present in the true spectrum depicted in Fig. 50. These artifacts

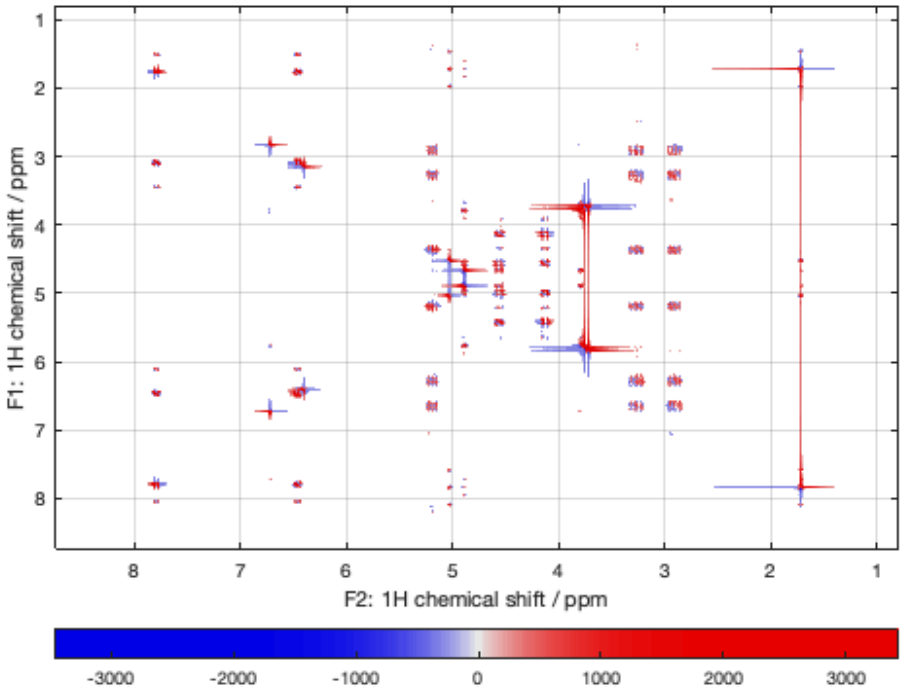

Figure 50: COSY90 spectrum of rotenone computed via the true NMR Hamiltonian.

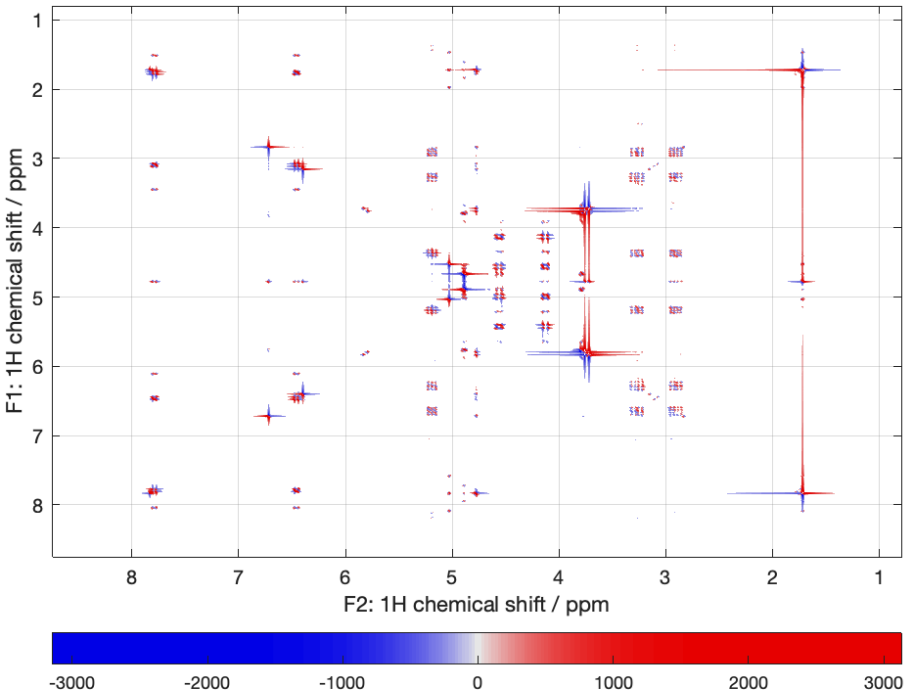

Figure 51: COSY90 spectrum of rotenone computed via pulse sequences applied on top of the native superconducting Hamiltonian.

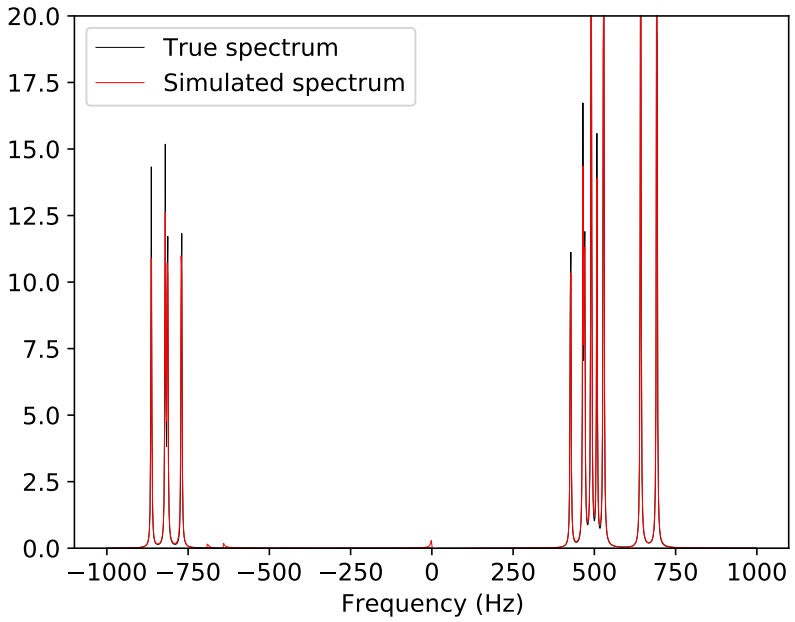

Figure 52: Proposed quantum simulation of threonine. The 'True spectrum' corresponds to dynamics evolving under the true NMR Hamiltonian, while the 'Simulated spectrum' corresponds to a noisy simulation of the superconducting chip with appropriate puse sequences to modify its native dynamics.

will vanish if we split the time-evolution into a larger number of Floquet cycles.

12.2.3 Proposed test systems

The rotenone molecule is too large to compute on the chip in Fig. 48. Instead, we propose to simulate the spectrum of the amino acid threonine. By deuterating the hydrogens in the molecule and leaving the nitrogen unlabeled, we are left with a linear chain of four carbon spins that can be simulated on the superconducting chip. In Fig. 52, we show a simulation of the 1D NMR spectrum computed using the true NMR Hamiltonian, Eq. (13.1), and one computed from a noisy simulation of the superconducting chip with the appropriate pulse sequence to modify its native dynamics. We hope the replace the 'True spectrum' curve with one experimentally computed in a NMR lab, and the 'Simulated spectrum' curve with one experimentally computed on the superconducting chip.

In addition to this analog quantum simulation the NMR spectrum via the algo-

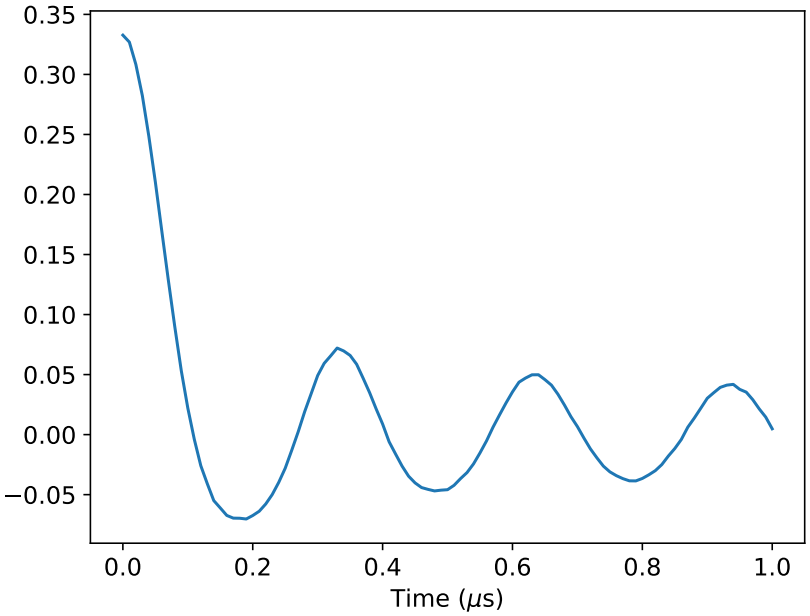

Figure 53: Proposed quantum simulation of nitroxide radical DEER spectrum. Simulation is computed from dynamics evolving under the true NMR Hamiltonian and orientation (powder) averaged across 3200 orientations.

rithm of Sec. 11.1, we also intend on a minimal demonstration of the ancilla-assisted orientation averaging described in Sec. 11.2. We will simulate the DEER trace of a pair of nitroxide radicals with a single ancilla qubit allowing us to average over two orientations at a time. A simulation of the trace we wish to produce is depicted in Fig. 53. While this trace is simple, it serves as a proof of principle demonstration and benchmark of hardware.

Chapter 13

Co-design of digital quantum simulation

In the previous chapter, we discussed digital quantum simulation of NMR experiments, and how scaling to large, classically hard systems will likely require a product formula decomposition of the time-evolution unitary (see Fig. 41). Such formulas implement terms of the Hamiltonian via quantum gates. In real hardware, however, control errors in the system often result in an applied gate being different from the intended one. A common challenge in all such gate-based quantum simulation, therefore, is to optimize the quantum circuit implementing the product formula for a particular NISQ platform. Specifically, the discretization ('Trotter') error in the product formula is reduced by increasing the number of gates, while hardware noise in the system causing decoherence leads to error that typically worsens as the number of gates increases. To achieve the best performance of the algorithm, we must therefore determine both the optimal number of gates and the optimal parameters for these gates in order to account for noise. The focus of this chapter is to provide insight into these questions which lie at the heart of software-hardware co-design of gate-based quantum simulation.

More generally, understanding the principles of co-design and error-mitigation is essential to realize the potential of quantum computers, as hardware noise usually wipes out the effects responsible for quantum advantages [197]. Even fault-tolerant

quantum computers of the future will rely on the characterization and mitigation of noise. The existence of a fault tolerance threshold is only rigorously defined when errors are assumed to be independent; this Markovian idealization is only true when spatial and temporal correlations in the noise die off quickly [269, 266, 289]. The magnitude of independent errors, in turn, affects the resource cost of the system, with noisier systems requiring a larger overhead of physical qubits per logical qubit. For near-term noisy, intermediate-scale platforms, characterizing the noise in a system is even more critical. Practical applications will require the co-design of protocols optimized to different hardwares. Indeed, understanding the nature of noise in a system can enable tailored quantum-control and error mitigation that improves desired performance metrics [279, 205]. In some cases, noise can even be exploited as a feature of the system to simulate the dynamics of complicated many-body models [345].

The three categories of error in quantum computations and simulations are state preparation and measurement (SPAM) errors, incoherent errors, and coherent errors. The first category corresponds to errors occuring at the beginning and end of the computation respectively. State preparation error corresponds to the initial state prepared on the hardware being different from the intended one, and may occur due to the probabilistic nature of projective measurements used to initial the system. Measurement error arises as quantum observables have inherent uncertainty and hence their expectation value can only be determined with a certainty set by the number of measurement samples. The second category, incoherent error, arises from coupling between the qubits and their environment, with these interactions causing the internal state of the qubit to change. The last category, coherent error, occurs when a desired unitary transformation of the system imparts an angle different than intended. These unitary errors are the focus of this chapter and arise due to limitations of the platform's analog control hardware or the dynamics of the physical qubits [300]. Over the course of a quantum computation or simulation, such unitary errors accumulate and dephase the system state, killing the coherent effects responsible for a quantum advantage and degrading the fidelity of any simulation. In trapped ions, for example, one dominant source of decoherence is the ions' collective motion, which is

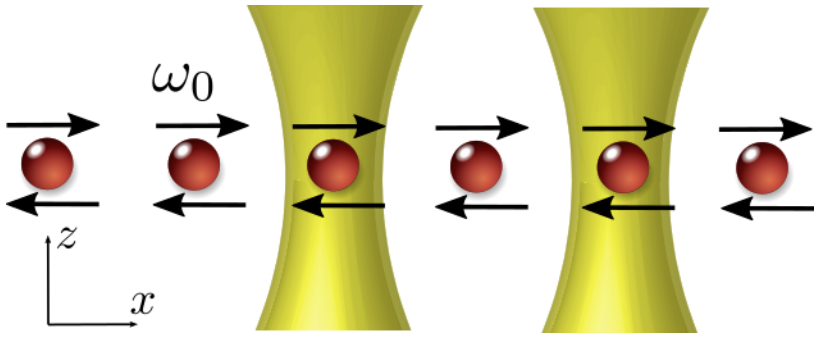

Figure 54: Chain of trapped ions collectively moving at frequency ω_0 in the x direction. Ions explore different parts of the beam waist of lasers (yellow) that apply unitary gates, thus accumulating an incorrect phase.

thermally excited due to electric field fluctuations from trap electrodes. While the internal qubit states of the ions are not directly affected by this motion, the Molmer-Sorenson gate, used as the standard two-qubit entangling gate, is implemented via individually addressed lasers and imparts an erroneous phase to the qubit states, as depicted in Fig. 54. The source of this noise can be understood as the phonon mode associated with the center of mass of the chain having an energy that undergoes diffusion due to heating from electric field fluctuations. We find that this slow diffusion of the phonon in energy space causes the unitary error to be non-Markovian, with correlations arising between gates applied at different times during an experiment.

In this chapter, we demonstrate how to exploit knowledge of the noise underlying a system to optimize gate-based quantum simulations. To provide a concrete example, we do so in the context of simulating the dynamics of a Heisenberg spin model in a system of trapped ions. We first introduce the quantum simulation task and associated gate-based algorithm. Then, we derive a theoretical noise model describing unitary errors from thermal ion motion in trapped ion systems and provide a protocol to experimentally extract the latent variable underlying the model. We discuss how temporal correlations in the noise induce an optimal gate depth of the quantum simulation circuit. These correlations cause the error in the simulation arising from motional noise to accumulate as the gate depth is increased, while the Trotter error associated with discretization of the time-evolution decreases as the gate depth is increased. The competition of these two errors induces an optimal gate depth.

Next, we provide a platform-independent framework for optimal feedforward control of unitary gate errors, which involves applying gates with angles that are modified to compensate for the predicted noise in the system. We illustrate the utility of feedforward control in the trapped ion implementation of simulating the Heisenberg Hamiltonian, showing that feedforward control partially mitigates both discretization error and decoherence error in the simulation output.

Our work provides three results that are generally applicable to the co-design of gate-based quantum algorithms beyond the discussed simulation task: *(i)* the understanding that non-Markovian correlations are the root cause of decoherence and the subsequent limitation on gate depth in any platform where unitary errors are the dominant noise, *(ii)* a method to optimally leverage noise characterization to mitigate unitary gate errors via feedforward control, and *(iii)* an accurate model of unitary gate errors arising from thermally-excited ion motion in trapped ion systems. The material in this chapter corresponds to the work in Ref. [324].

13.1 Hamiltonian simulation

To provide a concrete context for our discussion, we focus on the specific task of simulating the time-evolution, $\hat{U}(t) = \exp(-iHt/\hbar)$, of a system whose dynamics is generated by thethe Heisenberg Hamiltonian,

$$\hat{H} = \sum_{i,j} J_{ij} \hat{\mathbf{S}}_i \cdot \hat{\mathbf{S}}_j + \sum_i h_i \hat{S}_i^x. \tag{13.1}$$

This paradigmatic model not only describes many NMR systems, as discussed in previous chapters, but also describes the magnetic properties of many insulating crystals [79] and appears in the study of thermalization in quantum systems [264, 225, 275].

Many near-term quantum algorithms and simulations focus on the task of estimating the expectation value of some observable after time-evolution, with the value of such observables often being less susceptiable to noise than the full system state [349].

In this vein, we also benchmark the quality of gate-based quantum simulation of Eq. (13.1) with the spectrum simulation task discussed in Ch. 11 and experimentally demonstrated in Ch. 12. Specifically, we compute the NMR spectrum

$$A(\omega) = \mathrm{Re} \int_0^\infty dt \cdot e^{i\omega t - \gamma t} S(t) \tag{13.2}$$

where

$$S(t) = \langle \hat{S}^z_{\mathrm{tot}}(t)\, \hat{S}^z_{\mathrm{tot}} \rangle \tag{13.3}$$

$$= \mathrm{Tr}\left[e^{i\hat{H}t} \hat{S}^z_{\mathrm{tot}} e^{-i\hat{H}t} \hat{S}^z_{\mathrm{tot}} \rho_0 \right] \tag{13.4}$$

is the total magnetization response function and $\rho_0 = \frac{\hat{I}}{\mathrm{Tr}[\hat{I}]}$ is the initial state of the spin system.

We implement this time-evolution using a first-order Trotter decomposition into gates commonly used in trapped ion platforms. Specifically, we split the total time-evolution into r Trotter steps yielding $\hat{U}(t) = \left[\hat{U}(\Delta t)\right]^r$ where $\Delta t = \frac{t}{r}$. The unitary $\hat{U}(\Delta t) = e^{-i\hat{H}\Delta t}$ is then approximated with the Suzuki-Trotter product formula

$$\hat{U}_1(\Delta t) = e^{-i\left(\sum_i h_i \hat{S}^x_i\right)\Delta t} \left(\Pi_{\langle ij \rangle} e^{-i\hat{S}^z_i \hat{S}^z_j (2J_{ij}\Delta t)} \right) \times \\ \times \left(\Pi_{\langle ij \rangle} e^{-i\hat{S}^y_i \hat{S}^y_j (2J_{ij}\Delta t)} \right) \left(\Pi_{\langle ij \rangle} e^{-i\hat{S}^x_i \hat{S}^x_j (2J_{ij}\Delta t)} \right) \tag{13.5}$$

where $\langle ij \rangle$ corresponds to all unique pairs of spins as $J_{ij} = J_{ji}$ in the Hamiltonian. Furthermore, we only include pairs of spins where $J_{ij} \neq 0$. The total time-evolution is then given by $\hat{U}_1(t) = \left[\hat{U}_1(\Delta t)\right]^r$. Defining the two-qubit gates $\hat{U}^{\alpha\alpha}(\phi_{ij}) = \exp\{-i\hat{S}^\alpha_i \hat{S}^\alpha_j \phi_{ij}\}$ where $\phi_{ij} = 2J_{ij}\Delta t$, single-qubit rotation gates $\hat{R}^\alpha_i(\phi) = e^{-i\hat{S}^\alpha_i \frac{\phi}{2}}$,

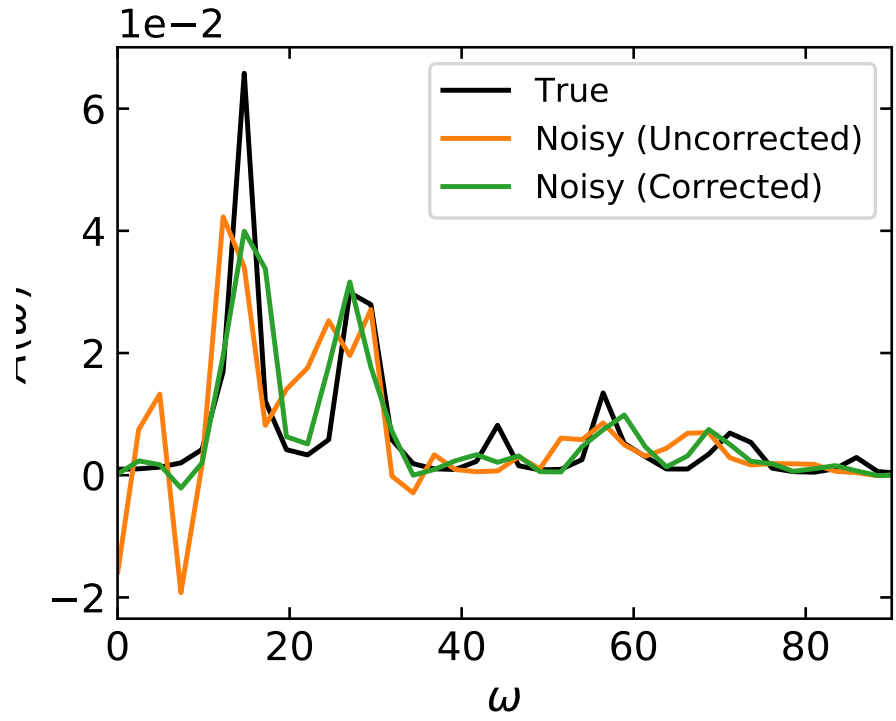

Figure 55: Example spectrum without noise (black), with Trotter error and unitary noise (orange), and noise with feedforward control (green) for a system of four spins evolving under the Heisenberg Hamiltonian, Eq. (13.1). The phonon heating rate is taken to be $c_2 = 0.02$ ms^{-1} and the noisy spectra are averaged over 40 runs. The uncorrected noisy spectrum is computed using 200 gates and the corrected noisy spectrum is computed using 500 gates, which are the gate depths for which each spectrum is closest to the noiseless spectrum, as quantified by the Hellinger distance between the spectra.

and angles $\phi_i = 2h_i\Delta t$, the quantum circuit for time evolution is given by

$$\begin{aligned}\hat{U}_1(t) = \Pi_{m=1}^{r}\{&\left(\Pi_i \hat{R}_i^y\left(-\frac{\pi}{2}\right)\right)\left(\Pi_i \hat{R}_i^z\left(-\phi_i\right)\right)\times \\ &\times\left(\Pi_{\langle ij\rangle}\hat{U}^{xx}\left(\phi_{ij}\right)\right)\left(\Pi_i \hat{R}_i^y\left(\frac{\pi}{2}\right)\right)\times \\ &\times\left(\Pi_i \hat{R}_i^z\left(-\frac{\pi}{2}\right)\right)\left(\Pi_{\langle ij\rangle}\hat{U}^{xx}\left(\phi_{ij}\right)\right)\times \\ &\times\left(\Pi_i \hat{R}_i^z\left(\frac{\pi}{2}\right)\right)\left(\Pi_{\langle ij\rangle}\hat{U}^{xx}\left(\phi_{ij}\right)\right)\}\end{aligned} \quad (13.6)$$

where we apply gates from right to left. The Trotter decomposition, Eq. (13.6), is expressed in terms of the Molmer-Sorensen gates, $\hat{U}^{xx}(\phi_{ij})$, and single qubit rotations that are commonly used in trapped ion computations.

Assuming that enough measurements are made during a computation to ignore measurement errors in the expection values, $\langle \hat{S}^z_{\text{tot}}(t) \rangle$, the computed spectrum will still include discretization errors from Trotterization and unitary gate errors from the ion motion described in Sec.13.2. The feedforward control discussed in Sec.13.4 can help mitigate the latter. Figure 55 shows an example spectrum (black), the same spectrum with both Trotter and unitary noise (orange), and the noisy spectrum with feedforward control (green).

13.2 Trapped Ion Noise Model

Trapped ions have emerged as a leading platform for quantum computation and simulation due to their long coherence times, identical nature, and negligible idle errors [197, 62]. The ions in these systems crystalize into a chain after being tightly confined in two directions via an oscillating electric field. Entanglement between the qubits is generated by a laser-induced interaction between states that is mediated by the collective motion of ions. Usually, the motional modes along the tightly confined transverse direction are used for these operations as they are less sensitive to electric field fluctuations arising from the electrodes generating the trap. These fluctuations do, however, excite the weakly confined longitudinal modes of the chain. The deviation of the ions from their lattice positions causes them to experience erroneous intensities from the individudally addressed laser beams used to implement different operations. As the longitudinal motion of the ions heats up, these errors build into a dominant form of noise that limits the operational time window of the system [62]. Here, we develop a noise model for errors arising from this longitudinal heating, ignoring other possible sources of error in trapped ion systems that may be more prevelant in different operational regimes of the device.

We first characterize the gate error in the system due to longitudinal movement of the ions in the x-direction, depicted in Fig. 54. The individually addressed single- and two-qubit gates in trapped ion systems are enacted by shining a narrowly focused laser on a single or pair of ion lattice sites respectively. The gates take the form $\hat{U}(\phi) =$

$\exp\left(-i\phi\hat{A}\right)$, where $\hat{A}$ is either a single spin operator, $\hat{S}_j^\alpha$, acting on a site j, or the bilinear, $\hat{S}_i^x\hat{S}_j^x$, acting on a pair of sites. These gates form a sufficient set for universal quantum computation. The phase of the gate is $\phi = \Omega t_g$, where t_g is the duration of the laser pulse, and Ω is the Rabi frequency set by the electric field amplitude of the laser. This amplitude typically has a Gaussian spread in the longitudinal direction which carries over to the Rabi frequency: $\Omega(x) = \Omega_0 \exp(-x^2/(2\sigma^2))$ where Ω_0 represents the maximum beam intensity and σ characterizes the beam width. The collective motion of the ions in the longitudinal direction can be decomposed in terms of normal modes with frequencies ω_m. During application of a gate, these motional oscillations cause the ions to feel a position-dependent Rabi frequency that is less than the desired Ω_0. Our goal is to derive the distribution of the erroneous phase ϕ that is applied when inputing an angle $\phi_{\text{in}} = \Omega_0 t_g$. In general, this distribution will evolve in time as the longitudinal phonon modes are heated, leading to larger amplitude oscillations. We therefore also seek to determine how the erroneous Rabi frequency, and therefore the phases $\phi(t)$ and $\phi(t')$, are correlated at different times. Temporal correlations over a sufficiently long timescale can limit the fidelity of computations in the system, even after feedforward optimization of individual gates.

In many common trapping schemes, electric field fluctuations from electrodes trapping the ions are primarily responsible for heating the longitudinal phonons [47]. Here, we consider systems utilizing such trapping schemes. The lowest frequency phonon mode, characterized by ions oscillating in phase at frequency ω_0, typically dominates the gate error as the field fluctuations are roughly uniform over the chain [62]. The gate application time, t_g, is usually much longer than the timescale set by ω_0 so we can assume that the effective Rabi frequency, $\overline{\Omega}(t)$, that an ion feels during a gate initiated at time t only depends on the average position of the ion:

$$\overline{\Omega}(t) = \Omega_0 \exp\left(-\frac{\overline{x}^2(t)}{2\sigma^2}\right) \tag{13.7}$$

where $\overline{x}(t) = \frac{1}{t_g}\int_t^{t+t_g} ds\,\langle\hat{x}(s)\rangle$ and $\hat{x}$ is the position operator of the ion. Letting $\hat{p}$ be the canonically conjugate ion momentum operator, we define the usual bosonic

creation and annihilation operators $\hat{a}^\dagger = (\hat{x} - i\hat{p})/\sqrt{2}$ and $\hat{a} = (\hat{x} + i\hat{p})/\sqrt{2}$. The average ion position only depends on the average energy of the harmonic motion: $\overline{x}^2(t) = \hbar \langle \hat{n}(t) \rangle / (m\omega_0)$ where m is the mass of the ion and $\hat{n} = \hat{a}^\dagger \hat{a}$ is the occupation number.

We must describe the dynamics of the ions' harmonic motion in order to compute the distribution and correlations of the Rabi frequencies, and by extention the phases of the unitary gate. Letting the state of the system be $\rho(t)$, we can model the dynamics with the Lindblad master equation

$$\begin{aligned} \frac{d}{dt}\rho = & -\frac{i}{\hbar}\left[\hbar\omega_0\hat{n}, \rho\right] \\ & + \gamma_+ \left(\hat{a}^\dagger \rho \hat{a} + \frac{1}{2}\left\{ \hat{a}\hat{a}^\dagger, \rho \right\} \right) \\ & + \gamma_- \left(\hat{a} \rho \hat{a}^\dagger + \frac{1}{2}\left\{ \hat{a}^\dagger \hat{a}, \rho \right\} \right), \end{aligned} \tag{13.8}$$

where the first term represents the coherent harmonic oscillation of the ions, the second term represents an increase in the oscillation amplitude at rate γ_+, and the third term represents a decrease in the oscillation amplitude at rate γ_-. These latter two terms describe the incoherent dynamics of the ions resulting from backgrond electric field fluctuations. Assuming that this background field exists in a thermal state at temperature T, the ions' oscillation amplitude changes at rates $\gamma_+ = \gamma \mathcal{N}(\omega_0, T)$ and $\gamma_- = \gamma(\mathcal{N}(\omega_0, T) + 1)$, where $\mathcal{N}(\omega_0, T) = 1/\left(e^{\hbar\omega_0/k_B T} - 1\right)$ is the Bose-Einstein distribution of the electric field occupation. We assume that the background electric field is at infinite temperature so both these rates are equal and redefine γ such that $\gamma_+ = \gamma_- = \gamma$. We also assume that the laser pulse enacting the gate does not affect the ions' motional state; in this sense, it is a weak measurement rather than a strong measurement which would collapse the ions' motion into a particular eigenstate of the occupation $\hat{n}$.

In typical trapped ion experiments, the initial preparation of the system involves cooling it close to its motional ground state. We therefore assume that the initial motional state of the system is the phonon vacuum $\rho(t_0) = |0\rangle\langle 0|$. Dynamics under

Eq. (13.8) will then evolve the system into a harmonically oscillating coherent state undergoing a diffusive random walk in its amplitude. It therefore makes sense to describe the system state in terms of its P-function representation:

$$\rho = \int d^2\alpha P\left(\alpha, \alpha^*, t\right) |\alpha\rangle \langle\alpha| \tag{13.9}$$

where $\{|\alpha\rangle\}$ are coherent states that form a basis for the system. The dynamics of the system is then captured by a Fokker-Planck equation for the P-function, $P\left(\alpha, \alpha^*, t\right)$,

$$\frac{d}{dt}P = \left\{ i\omega_0 \left(\frac{\partial}{\partial\alpha}\alpha - \frac{\partial}{\partial\alpha^*}\alpha^* \right) + \gamma \frac{\partial^2}{\partial\alpha\partial\alpha^*} \right\} P. \tag{13.10}$$

The Green's function of the Fokker-Planck equation, expressed in the rotating frame of the phonon mode with frequency ω_0, is

$$K\left(\alpha', t'|\alpha, t\right) = \frac{1}{\pi\gamma\left(t' - t\right)} \exp\left\{ -\frac{|\alpha' - \alpha|}{\gamma\left(t' - t\right)} \right\}, \tag{13.11}$$

which can be interpreted as the probability to find the ions in state $|\alpha'\rangle$ at time t' given that they were in state $|\alpha\rangle$ at time t. This Green's function can be used to compute the probability distribution and correlations of observables expressed in the coherent state basis. Letting $\phi\left(\tau\right) = \overline{\Omega}\left(\tau\right) t_g$ be the angle imparted by a unitary gate applied at time τ in the experiment, when the phonon mode is in state $|\alpha\left(\tau\right)\rangle$, the Rabi phase of the qubit will advance by an angle

$$\phi\left(\tau\right) = \phi_{\text{in}} \exp\left\{ -\left(\frac{a_{\text{osc}}}{a_{\text{laser}}} \right)^2 |\alpha\left(\tau\right)|^2 \right\}, \tag{13.12}$$

where $a_{\text{osc}} = \sqrt{\hbar/(m\omega_0)}$ and $a_{\text{laser}} = \sqrt{2}\sigma$ are the characteristic length scales of the harmonic oscillator and Gaussian laser respectively. The probability distribution of the angle can then be computed as

$$p_\phi\left(\phi; \tau, c_2\right) = \frac{1}{c_2\tau}\frac{1}{\phi}\left(\frac{\phi}{\phi_{\text{in}}} \right)^{\frac{1}{c_2\tau}} \Theta\left(\phi_{\text{in}} - \phi\right), \tag{13.13}$$

where we have defined the heating rate constant

$$c_2 = \gamma \left(\frac{a_{\text{osc}}}{a_{\text{laser}}} \right)^2 \tag{13.14}$$

and the Heaviside step function, $\Theta(\phi_{\text{in}} - \phi)$, encodes the fact that the time-averaged Rabi frequency felt by the ion cannot be more than spending all its time at the center of the laser where its intensity is strongest. The distribution of angles, Eq. (13.13), is the noise model we need for feedforward control. Note that it only depends on a single latent variable, $\lambda = c_2\tau$, representing the amount of diffusion the ions' motion has undergone.

We can gain insight into the angle distribution by examining the average and typical angles that are applied by the gate,

$$\phi_{\text{avg}} = \mathbb{E}_\phi[\phi] = \frac{\phi_{\text{in}}}{1+\lambda} \tag{13.15}$$

$$\phi_{\text{typ}} = \exp(\mathbb{E}_\phi[\log\phi]) = \phi_{\text{in}} e^{-\lambda}. \tag{13.16}$$

We see that at late experimental times compared to the rate c_2 such that $\lambda \to \infty$, both the average and typical angles go to zero. Physically, the amplitude of the ions' oscillation becomes so large that the ion never spends time inside the laser beam and hence its internal qubit state is not changed. While the average angle algebraically decays to zero at late times, the typical angle becomes very small as τ crosses $1/c_2$, thus showing that c_2 sets the timescale where we can coherently manipulate the qubits in an experiment.

We can further understand the effects of noise on a quantum computation or simulation by examining the correlation between two Molmer-Sorenson gates applied

at a time Δ_τ apart,

$$\mathrm{Corr}\left(\phi(\tau+\Delta_\tau)\phi(\tau)\right) = \frac{\mathrm{Cov}\left(\phi(\tau+\Delta_\tau)\phi(\tau)\right)}{\sqrt{\mathrm{Var}\left(\phi(\tau)\right)\mathrm{Var}\left(\phi(\tau)\right)}}$$

$$= \frac{\tau}{\tau+\Delta_t}\frac{\sqrt{\left(1+2c_2\tau\right)\left(1+2c_2(\tau+\Delta_\tau)\right)}}{1+2c_2\tau+c_2\Delta_\tau+c_2^2\tau\Delta_\tau} \quad (13.17)$$

Taking the limit at late times, we have

$$\lim_{\tau\to\infty}\mathrm{Corr}\left(\phi(\tau+\Delta_\tau)\phi(\tau)\right) = \frac{1}{1+\frac{1}{2}c_2\Delta_\tau}+\mathcal{O}\left(\frac{1}{\tau}\right), \quad (13.18)$$

which shows that c_2 also sets the temporal correlation length between different gates. Given that the gate application time, t_g, is small compared to typical values of c_2 in trapped ion experiments, the unitary gate errors will be temporally correlated.

As a limiting case, we can examine how the noisy gate angles are distributed at short times when the ions are very close to the center of the laser beam. By simultaneously taking the limits $\phi\to\phi_{\mathrm{in}}$ and $c_2\tau\to 0$ in Eq. (13.13), we get the short time distribution

$$p_\phi^{\mathrm{short}}\left(\phi;\tau,c_2\right) = \frac{1}{c_2\tau\phi_{\mathrm{in}}}e^{-\frac{(\phi_{\mathrm{in}}-\phi)}{c_2\tau\phi_{\mathrm{in}}}}\Theta\left(\phi_{\mathrm{in}}-\phi\right). \quad (13.19)$$

This expression can equivalently be derived by Taylor expanding Eq. (13.12) as $\phi\left(\tau\right)=\phi_{\mathrm{in}}\left(1-(\frac{a_{\mathrm{osc}}}{a_{\mathrm{laser}}})^2|\alpha\left(\tau\right)|^2\right)$ and computing the probability distribution of gate angles using the Green's function given in Eq. (13.11). The exponential distribution of gate angles described in Eq. (13.19), valid at short times, is in agreement with the ion noise model discussed in Ref. [62].

We now give a protocol to experimentally extract the value of c_2 which characterizes the noise in a particular trapped ion set-up. Prepare a system of two qubits in the computational basis state $|\downarrow\downarrow\rangle$, wait a time τ, and apply a gate $\hat{U}_{xx}\left(\phi\right)=\exp\left(-i\phi\hat{S}_i^x\hat{S}_j^x\right)$ with an input angle ϕ_{in}. Then, do a projective measurement in the computational basis state to extract the return probability of the system being in the

$|\downarrow\downarrow\rangle$ state. If there was no noise in the system, this probability would be

$$P_{\downarrow\downarrow} = \langle\downarrow\downarrow| \hat{U}_{xx}(\phi_{\text{in}}) |\downarrow\downarrow\rangle = \cos^2\left(\frac{\phi_{\text{in}}}{4}\right) \tag{13.20}$$

for all τ. With unitary gate error due to the ions' motion, the probability becomes

$$\overline{P}_{\downarrow\downarrow}(\phi_{\text{in}}, c_2\tau) = \mathbb{E}_\phi\left[\cos^2\left(\frac{\phi}{4}\right)\right] \tag{13.21}$$

$$= \cos^2\left(\frac{\phi_{\text{in}}}{4}\right) + \frac{\phi_{\text{in}}^2 c_2\tau}{8+16c_2\tau}{}_1F_2(1+\frac{1}{2c_2\tau}, \frac{3}{2}, 2+\frac{1}{2c_2\tau}, -\frac{\phi_{\text{in}}^2}{16}), \tag{13.22}$$

where ${}_1F_2$ is the generalized hypergeometric function. This average return probability is directly related to the moment generating function of Eq. (13.13). Measuring Eq. (13.21) for different input angles, ϕ_{in}, and wait times, τ, yield curves that can be used to fit the value c_2. We give examples of these curves in Fig. 56(a). In Fig. 56(b), we show how the return probability can differentiate between the noise model derived here and and typical phase damping. The latter leads to a return probability characterized by an exponentially decaying oscillations with a constant phase shift dependent on the input angle. Armed with knowledge of the noise model, Eq (13.13), and a method to experimentally determine the latent variable, c_2, we now illustrate how non-Markovian correlations in the noise induce an optimal gate depth when implementing a quantum algorithm.

13.3 Optimal gate depth

We can gain insight into how non-Markovian correlations amongst gates induce an optimal gate depth in a quantum algorithm by first considering a single one- or two-qubit gate $\hat{U}(\phi_{\text{tot}}) = \exp\left(-i\phi_{\text{tot}}\hat{A}\right)$ of the form discussed in Sec 13.2. Let us discretize this gate into r Trotter steps: $\hat{U}(\phi_{\text{tot}}) = \left[\hat{U}(\phi)\right]^r$ where $\phi = \phi_{\text{tot}}/r$ and $\hat{U}(\phi) = \exp\left(-i\phi\hat{A}\right)$. The expected angle applied by the total sequence $\hat{U}(\phi_{\text{tot}})$ is

$$\mathbb{E}[\phi_{\text{tot}}] = r\mathbb{E}_\phi[\phi] \tag{13.23}$$

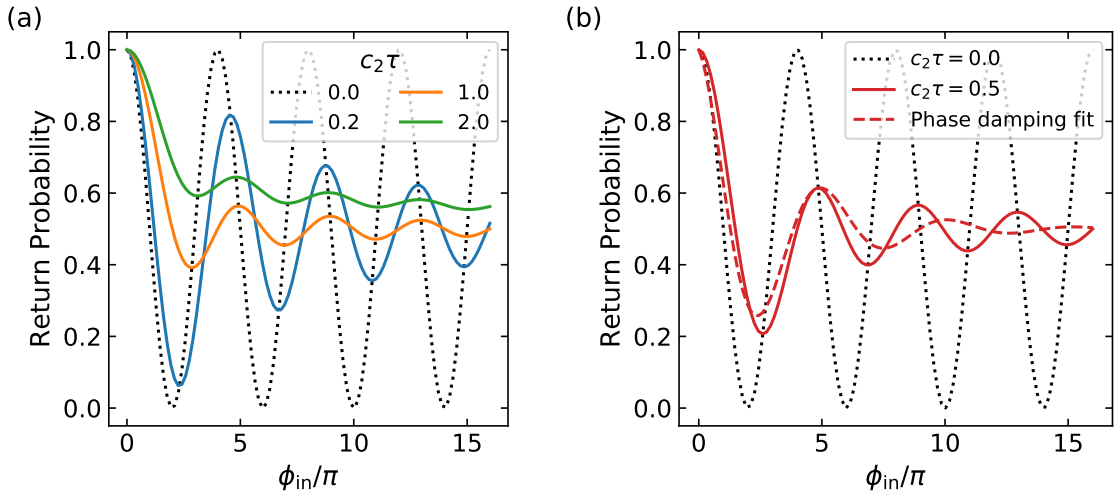

Figure 56: Return probability predictions for experimental protocol to extract c_2. (a) Curves for different wait times, τ, as a function of input angle ϕ_{in}. (b) Difference between derived noise model and phase damping.

where $\mathbb{E}_\phi[\phi]$ is the average angle applied by $\hat{U}(\phi)$. If the unitary gate errors in the system were Markovian, and therefore uncorrelated, the variance in the total angle would be

$$\text{Var}(\phi_{\text{tot}}) = r\text{Var}(\phi) \tag{13.24}$$

where $\text{Var}(\phi)$ is the variance in the angle applied by $\hat{U}(\phi)$. Regardless of the source of unitary error, this variance of each discretized gate will typically be proportional to $\mathbb{E}_\phi[\phi]^2$. Letting the constant of proportionality be β, defined through $\text{Var}(\phi) = \beta\mathbb{E}_\phi[\phi]^2$, the noise-to-signal ratio of the total gate sequence becomes:

$$\eta = \frac{\sqrt{\text{Var}(\phi_{\text{tot}})}}{\mathbb{E}[\phi_{\text{tot}}]} = \frac{\sqrt{\beta}}{r}. \tag{13.25}$$

As a concrete example, if we take the noise model developed in Sec. 13.2 and ignore temporal correlations, we have $\beta = (c_2\tau)^2/(1+2c_2\tau)$. This constant β is computed by assuming that each gate angle is independent and identically distributed according to Eq. (13.13). We see that $\eta \to 0$ as $r \to \infty$, implying that discretizing the total intended gate, $\hat{U}(\phi_{\text{tot}})$, into a large number of steps can fully mitigate the unitary error in the system, thus allowing for application of a perfect gate $\hat{U}(\phi_{\text{tot}})$. If Markovian

noise arising from longitudinal phonon heating was the only source of errors in the system, a generic gate-based quantum algorithm can then be implemented without any errors by discretizing each of its gates as described above. Such an error-free quantum circuit contradicts the decoherence caused by heating-induced unitary errors in real experiments, and hence the assumption that longitudinal phonon heating leads to Markovian noise on the qubit degrees of freedom is flawed. Correlations between the unitary gate errors must be responsible for decoherence in experiments, with an optimal gate depth being set by the timescale upon which this decoherence becomes too large.

To give a concrete example of how this optimal gate depth arises, we turn to the Hamiltonian simulation task described in Sec. 13.1. The computed spectrum will have errors both due to discretization via the Trotter decomposition, Eq. (13.6), and unitary gate noise due to heating of the ions' motion as described in Sec. 13.2. Trotter error decreases as the number of gates in the circuit is increased, while unitary errors accumulate as the numer of gates is increased. Therefore, there is an optimal gate count balancing Trotter error and accumulated unitary error.

We can quantify the error in the computation use two different metrics. The first is to compute the average fidelity

$$F\left(t\right)=|\frac{1}{2^{n}}\mathrm{Tr}\{\hat{U}_{1}\left(t\right)^{\dagger}\hat{U}\left(t\right)\}|^{2}, \tag{13.26}$$

where $\hat{U}\left(t\right)=e^{-i\hat{H}t}$, with $\hat{H}$ given by Eq. (13.1), is the desired time evolution operator and $\hat{U}_{1}\left(t\right)$ is the noisy Trotterized evolution we implement in the quantum circuit, given by Eq (13.6), with noisy gate angles. Given that computation of a spectrum requires implementing time-evolution for a series of different times in order to generate samples of the FID $S(t)$, we can define the time-integrated fidelity

$$F_{\mathrm{int}}=\frac{1}{T}\int_{0}^{T}F\left(t\right) \tag{13.27}$$

where T is the last sampled time. The optimal gate depth is then determined by the largest value of F_{int}. This metric is not biased towards any particular choice of

observable.

Alternatively, we can quantify the error in the spectrum by computing the Hellinger distance

$$D_H^2\left(A_i, A_j\right) = \frac{1}{2}\int \frac{d\omega}{2\pi}\left(\sqrt{A_i(\omega)} - \sqrt{A_j(\omega)}\right)^2 \tag{13.28}$$

between a noiseless spectrum, $A_i(\omega)$, generated by the perfect time evolution operator, $\hat{U}\left(t\right) = e^{-i\hat{H}t}$, and a noisy spectrum, $A_j(\omega)$, generated by a noisy Trotterized evolution, $\hat{U}_1\left(t\right)$. At the optimal gate depth, the Trotterized spectrum will have the most overlap with the true noiseless spectrum according to the Hellinger distance. This metric is biased towards the computation of the spectrum.

The optimal gate depth with the corresponding average fidelity and Hellinger distance for an example noisy computation is shown in Fig. 59 and Fig. 60 respectively, and we discuss these results in the next section. The total amount of error in the noisy computation can be reduced by appropriately modifying the angles of the gates comprising the quantum simulation circuit, Eq. (13.6), a method known as feedforward control. We develop a systematic, platform-independent protocol to determine the modificatied gate angles in the next section. We then illustrate the benefits of the feedforward control in the context of the Hamiltonian simulation task by showing improvements in the fidelity and Hellinger distance for an example Hamiltonian of the form in Eq. (13.1).

13.4 Feedforward Control

A quantum computation or simulation involves applying a unitary operation $\hat{U}$ to a system of qubits. Often, this unitary transformation is a composite of several single- and two-qubit unitary gates $\hat{U}\left(\phi\right) = \exp\left(-i\phi\hat{A}\right)$, with $\hat{A}$ typically linear or bilinear in spin-1/2 operators, $\hat{S}_j^{\alpha} = \hat{\sigma}_j^{\alpha}/2$. A unitary error in the system manifests as application of $\hat{U}\left(\phi\right)$ when we intend to apply $\hat{U}\left(\phi_p\right)$. We usually do not have deterministic knowledge of the value of the incorrect angle, ϕ, and therefore describe it with a probability distribution $p_{\phi}\left(\phi;\phi_{\text{in}},\lambda\right)$, where λ is a vector of latent variables characterizing the physical noise underlying the system and ϕ_{in} is the angle we input

when applying the gate. If the gate was noiseless, we would have $p_\phi(\phi; \phi_{\text{in}}, \lambda) = \delta(\phi - \phi_{\text{in}})$ and would input $\phi_{\text{in}} = \phi_p$, where ϕ_p is the desired output gate angle. The idea of feedforward control is to appropriately adjust the input gate angles of the computation to reduce the error accumulated from incorrect gate angles.

Formally, let the total unitary describing the actual computation be $\hat{U} = \prod_{m=1}^{M} \hat{U}_m\left(\phi^{(m)}\right)$, where $\hat{U}_m\left(\phi^{(m)}\right) = \exp\left(-i\phi^{(m)}\hat{A}_m\right)$. The desired computation is $\hat{U}_p = \prod_{m=1}^{M} \hat{U}_m\left(\phi_p^{(m)}\right)$. As the output angles are probabilistic, a particular manifestation of the output computation $\hat{U}$ depends on the joint probability distribution $p_\phi(\phi; \phi_{\text{in}}, \lambda)$, where ϕ_{in} and ϕ are the m different input and output angles respectively. The goal of feedforward control is to pick the optimal input angles, ϕ_{in}^*, such that the computation $\hat{U}$ is close to $\hat{U}_p$ on average. In general, ϕ_{in}^* will depend on both the set of desired output angles, ϕ_p, and the latent noise variables, λ.

Optimizing over the entire computation, however, can be challenging as it requires knowledge of the full joint distribution, p_ϕ, which is generally non-trivial to compute, even for the model presented in Sec. 13.2. Additionally, even if possible, such an optimization may not generalize well to other computations represented by different gate sequences. We therefore focus on optimizing each individual unitary gate independently of the others, which amounts to neglecting correlations between unitary gate errors and assuming that they are independent and identically distributed according to the marginal distribution, p_ϕ. Mathematically, this amounts to the factorization of the joint distribution: $p_\phi = \prod_{m=1}^{M} p_{\phi^{(m)}}$. Temporal correlations in the physical noise underlying the system lead to correlations in the angles ϕ that are not captured by such a factorization. Feedforward optimization of individual gates can therefore only partially mitigate the error in the overall computation. However, such an optimization is immediately applicable to all computations, $\hat{U}$, as it done at the level of individual gates.

The error due to applying a gate $\hat{U}(\phi)$ when we desire to apply $\hat{U}(\phi_p)$ can be quantified by the gate fidelity

$$F(\phi, \phi_p) = |\frac{1}{2^n}\text{Tr}\{\hat{U}(\phi)^\dagger \hat{U}(\phi_p)\}|^2, \tag{13.29}$$

which describes the expected fidelity of an n-qubit gate for a random state drawn uniformly from the n-qubit state space [268]. For example, let us consider a unitary gate corresponding to $\hat{A} = \hat{S}_i^\alpha \hat{S}_j^\alpha$ describing an interaction between two qubits i and j. The fidelity then takes the simple form $F(\phi, \phi_p) = \cos^2((\phi - \phi_p)/4)$. The figure of merit we want to optimize with feedforward control is the average fidelity over all possible wrong angles ϕ,

$$\mathcal{F}(\phi_{\text{in}}, \phi_p, \lambda) = \int d\phi p_\phi(\phi; \phi_{\text{in}}, \lambda) F(\phi, \phi_p). \tag{13.30}$$

The optimal input angle is then

$$\phi_{\text{in}}^*(\phi_p, \lambda) = \arg\max_{\phi_{\text{in}}} \mathcal{F}(\phi_{\text{in}}, \phi_p, \lambda) \tag{13.31}$$

Calculation of this optimal feedforward angle requires knowledge of the control landscape defined by the dependence of the figure of merit, Eq. (13.30), on the input angle ϕ_{in} and desired output angle ϕ_p. This landscape can either be numerically mapped out with experimental measurements, or analytically computed after developing a theoretical description of the noise underlying the system.

As a concrete example of the latter approach, the distribution $p_\phi(\phi; \phi_{\text{in}}, \lambda)$ for the trapped ion noise discussed in Sec 13.2 is given by Eq. (13.13). The ion noise is paramterized by a single latent variable, $\lambda = c_2\tau$, which can be experimentally extracted by measuring the return probability Eq. (13.21). The figure of merit for feedforward control, Eq. (13.30), is this case can be analytically computed:

$$\begin{aligned}\mathcal{F}(\phi_{\text{in}}, \phi_p, c_2\tau) = &\frac{1}{2} + \frac{1}{2}\cos\left(\frac{\phi_{\text{in}}}{2}\right)\cos\left(\frac{\phi_p}{2}\right) + \\ &+ \frac{\phi_{\text{in}}^2 c_2\tau}{8 + 16c_2\tau}\cos\left(\frac{\phi_p}{2}\right){}_1F_2\left(1 + \frac{1}{2c_2\tau}, \frac{3}{2}, 2 + \frac{1}{2c_2\tau}, -\frac{\phi_{\text{in}}^2}{16}\right) + \\ &+ \frac{\phi_{\text{in}}}{4 + 4c_2\tau}\sin\left(\frac{\phi_p}{2}\right){}_1F_2\left(\frac{1}{2} + \frac{1}{2c_2\tau}, \frac{3}{2}, \frac{3}{2} + \frac{1}{2c_2\tau}, -\frac{\phi_{\text{in}}^2}{16}\right).\end{aligned} \tag{13.32}$$

The optimal input angle, $\phi_{\text{in}}^*(\phi_p, c_2\tau)$, for the trapped ion noise is the angle which

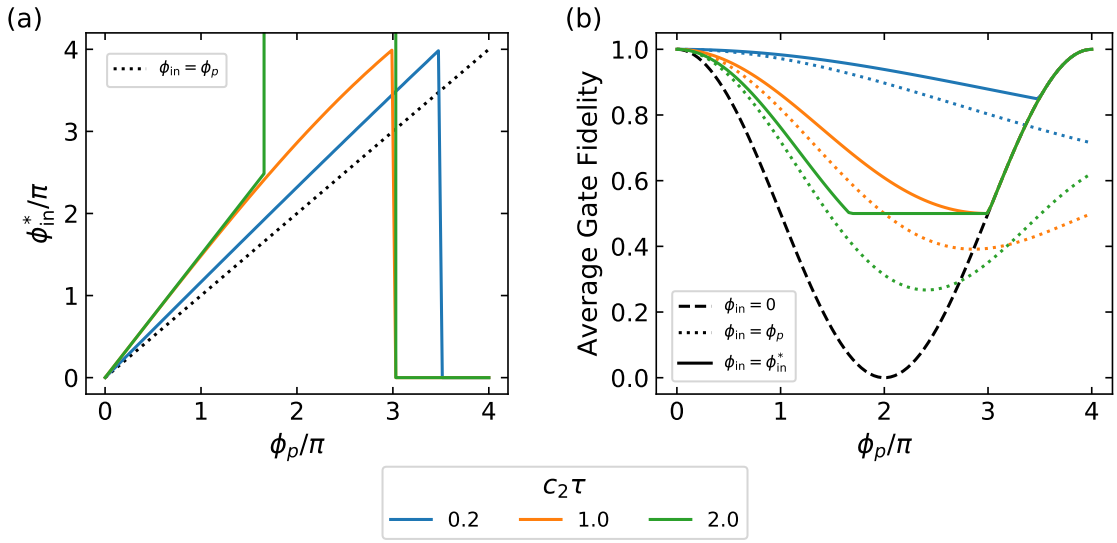

Figure 57: Optimal feedforward control characterization. (a) Optimal input angle. (b) Average gate fidelity. The black dashed line depicts the fidelity if no gate is applied and the dotted lines represent the fidelity if the desired output angle, ϕ_p, is directly taken as the input to the gate.

satisfies the condition

$$\mathcal{F}\left(\phi_{\text{in}}^*, \phi_p, c_2\tau\right) = F\left(\phi_{\text{in}}^*, \phi_p\right), \tag{13.33}$$

where we recall that $F\left(\phi, \phi_p\right) = \cos\left((\phi - \phi_p)/4\right)$ is the fidelity of a gate imparting angle ϕ when we desire to apply ϕ_p. We implement feedforward control by taking each desired output gate angle, ϕ_{ij}, of the $\hat{U}^{xx}$ gates in Eq. (13.6) as ϕ_p at the experimental time τ that the gate is applied. The optimality condition, Eq. (13.33), is then solved numerically for each such gate and the angle ϕ_{in}^* is input into the noisy gate rather than ϕ_{ij}.

We show the optimal input angle, Fig 57(a), and average gate fidelity, Fig 57(b), for a range of desired output angles ϕ_p. First, we note that the optimal feedforward angle, ϕ_{in}^*, always yields a better average fidelity than inputing ϕ_p. We see that for small output angles, there is always a finite optimal input angle. For sufficiently large output angles, however, the optimal input angle is $\phi_{\text{in}}^* = 0$, meaning we do not apply the gate. These angles are such that doing nothing leads to a better fidelity than any non-zero gate we apply. Furthermore, for times $\tau > c_2$, meaning that the ions' collective motion has undergone a considerable amount of diffusion in the ion chain

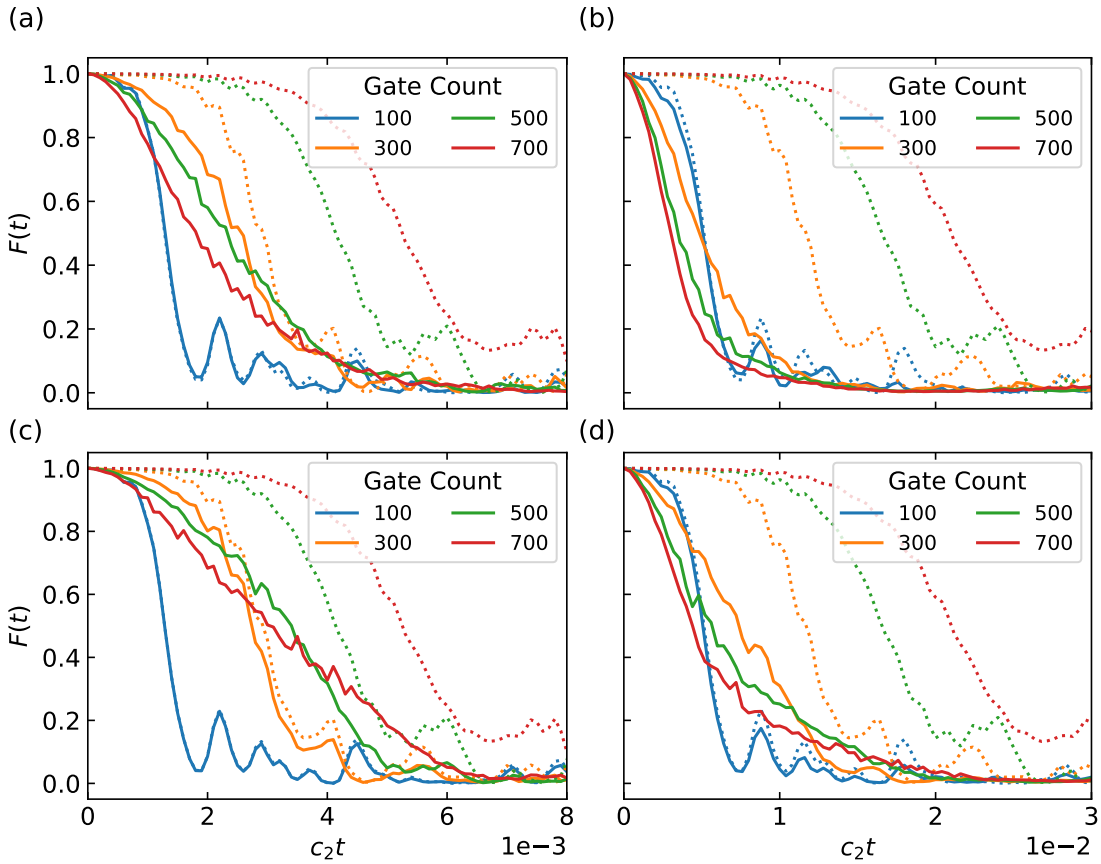

Figure 58: Time dependent fidelity of noisy Trotterized time evolution for a system of four spins evolving under the Heisenberg Hamiltonian, Eq. (13.1). Solid curves include both heating noise and Trotter error, while the dotted curves include only Trotter error and are given as a noiseless reference. (a) $c_2 = 0.005$ ms^{-1} and no feedforward correction. (b) $c_2 = 0.02$ ms^{-1} and no feedforward correction. (c) $c_2 = 0.005$ ms^{-1} with feedforward correction. (d) $c_2 = 0.02$ ms^{-1} with feedforward correction. The noisy computations are averaged over 40 runs.

configuration under consideration, there is an intermediate range of angles where the optimal thing to do is apply a maximally strong laser pulse to make ϕ_{in}^* as large as possible. In this case, the gate essentially applies a random phase to the state and yields an average fidelity of 1/2.

To benchmark the utility of the feedforward control, we implement with Hamiltonian simulation task of Sec 13.1 using optimal input angles computed from Eq. (13.33). In Fig. 58,we plot an example of the time-dependent fidelity, Eq. (13.26), for different heating rate and gate counts with and without feedforward control. We see that for low gate counts such as computations with 100 gates, the drop in fidelity comes

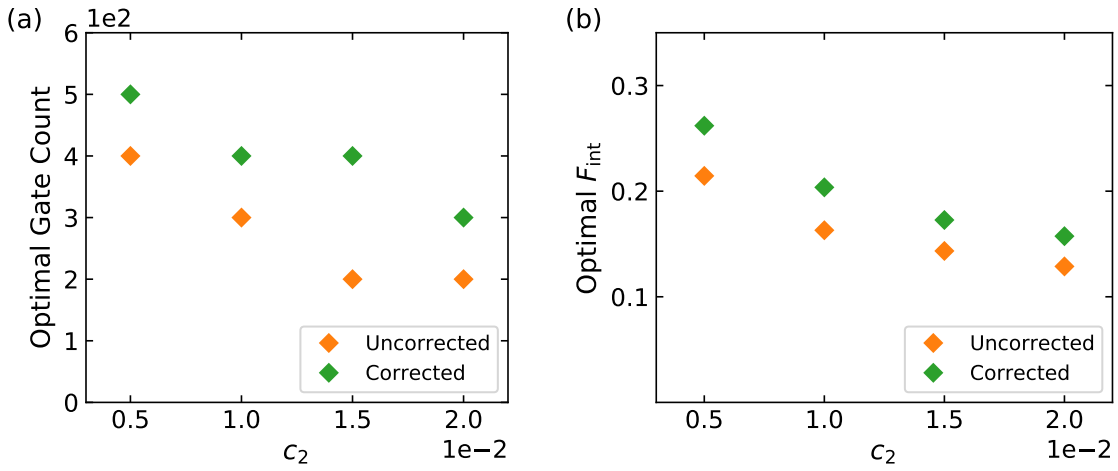

Figure 59: Optimal fidelity resulting from balancing Trotter and decoherence errors for a system of four spins evolving under the Heisenberg Hamiltonian, Eq. (13.1). The heating rate c_2 is given in units of ms^{-1}. (a) Optimal gate count. (b) Integrated fidelity. The noisy computations are averaged over 10 runs.

almost fully from Trotter error without heating noise having much of an effect. For larger gate counts, heating noise becomes the dominant cause of the drop in fidelity. While the fidelity for the zero heating case gets continuously better with increased gate count, finite heating causes computations with sufficiently large gate counts to decrease the overall fidelity.

Feedforward control can improve the situation in two different ways, which can be seen by comparing, for example, the 300 gate and 700 gate curves. The first effect is to improve the total fidelity over all time values, as quantified by the improvement in F_{int}, Eq.(13.27), depicted in Fig. 59. This improvement indicate that the computation of $\hat{U}_1(t)$ is closer on average to the desired computation $\hat{U}(t)$ for all values of t, with the feedforward corretion bringing the fidelity of a computation closer to the upper bound set by the Trotter error. The second effect is that for computations with large gate counts, the fidelity for samples at late times, corresponding to large values of t, is improved more signficantly than for short time samples. This improvement causes the fidelity to have a more shallow decay, and creates windows of time samples where it may be more advantageous to use circuits with different gate counts. For example, in Fig. 58(c), a computation with 300 gates is advantageous for samples with $c_2 t \lesssim 3$, while a computation with 700 gates is advantageous for samples with

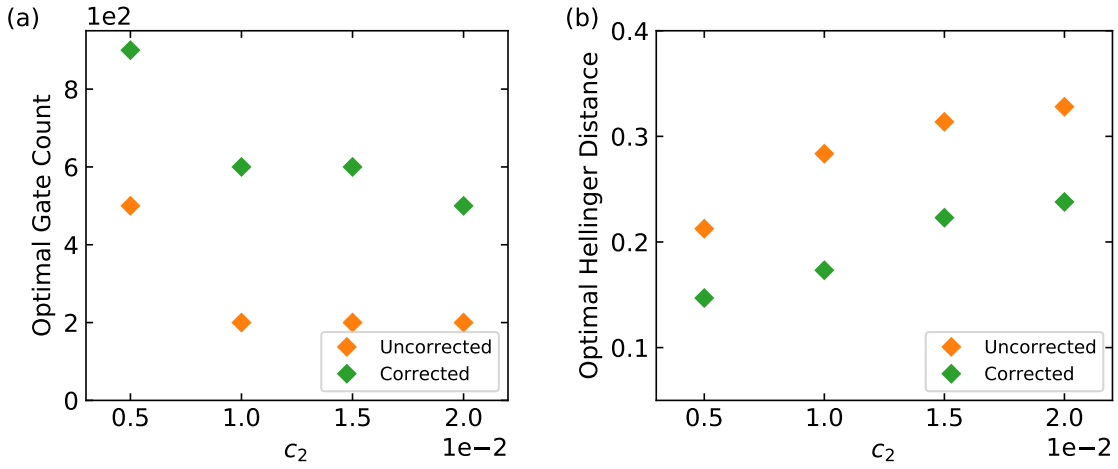

Figure 60: Optimal spectra resulting from balancing Trotter and decoherence errors for a system of four spins evolving under the Heisenberg Hamiltonian, Eq. (13.1). The heating rate c_2 is given in units of ms^{-1}. (a) Optimal gate count. (b) Hellinger distance between optimal noisy spectra and noiseless spectrum. The noisy computations are averaged over 10 runs.

$c_2 t \gtrsim 3$. The significance of this result is that a particular observables of interest may have information that is more concentrated in a particular time window. For example, the resolution between peak of the spectrum, Eq. (13.2), comes from samples at late times. Therefore, the optimal gate count determined by the accuracy of the spectrum may be larger than the optimal gate count determined by the integrated fidelity. Indeed, this is what is seen when comparing Fig. 59 and Fig. 60.

In Fig. 60(a) and (b), we show the optimal gate count and associated Hellinger distance of spectra computed both with and without the feedforward correction. We see that the accuracy of the optimal noisy spectrum is significantly improved. An example spectrum for a system with heating rate $c_2 = 0.02\ \text{ms}^{-1}$ is depicted in Fig. 55. The feedforward control both directly mitigates decoherence error from the motion of the ions and indirectly reduces the Trotter error by increasing the optimal gate count. Therefore, by effectively increasing the optimal gate depth of the circuit, feedforward control can be used to partially mitigate both discretization error and accumulated unitary gate error in the system.

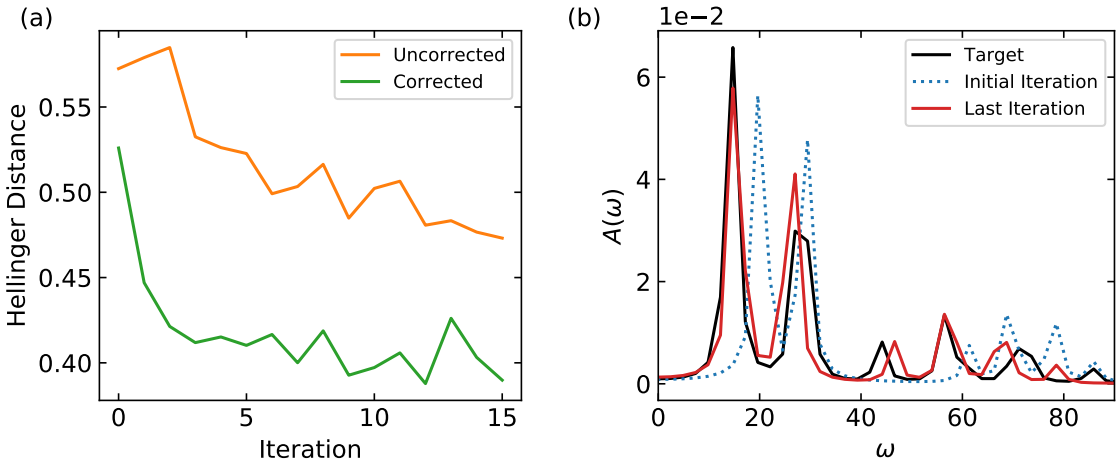

Figure 61: Simulation of NMR inference algorithm with motional noise and Trotter error for a system of four spins. At each update step of the protocol, noisy spectra computed from a set of sample Hamiltonians are used to calculate the next update step (a) Hellinger distance between the average Hamiltonian's noisy spectrum and the target spectrum with and without feedforward correction. (b) Spectrum comparison. We take the average Hamiltonians found at the initial and last iterations of the noisy inference protocol and simulate what its spectrum would be if there was no noise. The fact that the last spectrum is significantly closer to the target spectrum compared to the initial spectrum gives a visual indication of the improvement in the underlying Hamiltonian during the inference protocol. The phonon heating rate is taken to be $c_2 = 0.02$ ms^{-1} and the noisy spectra are computed with 500 gates and averaged over 10 runs.

13.5 Discussion

This improvement in the quality of the Hamiltonian simulation can be helpful for practical applications, such as the NMR spectrum inference task discussed in Ref. [328]. In that work, a hybrid quantum-classical algorithm is used to infer the parameters of a Hamiltonian, Eq. (13.1), that models the system of nuclear spins which produce a given experimental NMR spectrum. The premise of the algorithm is to iteratively simulate the spectrum corresponding to different Hamiltonian parameters on quantum hardware and guess parameters that are closer to the target experimental spectrum using classical optimization techniques. After a sufficient number of iterations, the learned Hamiltonian parmeters can be used to gain insight into the chemical structure of the sample that produced the given NMR spectrum. In Fig. 61, we demonstrate the benefit of feedforward correction in this inference algorithm. Figure 61(a) shows

the Hellinger distance between the average noisy Trotterized spectrum and a given target spectrum at each iteration of the protocol. We see that the feedforward correction allows the algorithm to converge faster, as the increased resolution in the simulated spectra allows the classical optimization to more easily guess better Hamiltonian parameters. In Fig. 61(b), we take the Hamiltonian parameters for the initial and last iterations of the noisy protocol with feedforward correction and compute the corresponding spectra without noise to compare how well the learned parameters correspond to the true parameters underlying the given target spectrum. We see that even though the quantum simulation is noisy, we are still able to iteratively infer the Hamiltonian parameters underlying the target spectrum.

We have shown how to tailor gate-based quantum simulation algorithms for particular hardware platforms. Specifically, we demonstrate how knowledge of hardware noise leading to unitary gate errors can be exploited to implement feedforward control to improve the simulation outcome. The ion noise model we derive applies to an array of computations and simulations performed in trapped ions, and feedforward control can be used to mitigate noise in these applications. In addition to feedforward control, it may be possible to incorporate feedback control to mitigate the motional noise. For example, the motional state of an an ancilla ion can be periodically measured. Such a strong measurement would restart the ions' diffusion process, effectively reducing the time τ over which the system undergoes diffusion. Knowledge of the motional state can then be used to generate feedforward corrections until they are recalibrated by the next measurement.

Other common quantum platforms such as superconducting qubits and Rydberg atoms also suffer from unitary gate errors. For example, charge and flux noise are amongst the dominant source of errors in superconducting platforms, but dispersive coupling in the system can cause correlated coherent errors that are appreciable as well [188, 190]. In Rydberg atom systems, leakage errors due to blackbody radiation-induced transitions and radiative decay are the dominant error channels, but coherent errors arising from the finite temperature atoms feeling different laser amplitudes can be appreciable [76]. The physical mechanisms underlying coherent errors in super-

conducting and Rydberg platforms are quite different from that of trapped ions and understanding the structure of the optimal feedforward correction in these systems may provide insight into which quantum algorithms and simulations are best suited to different platforms.

Part V

Conclusion and Outlook

The goal of this thesis was to progress towards answering practically useful questions using quantum simulators by improving our understanding of which platforms suit different application contexts, and when a digital, analog, or hybrid simulation approach is appropriate. We specifically focused on simulating the dynamics of many-body systems, as this is believed to be one of the first contexts in which early quantum hardware (either late-stage NISQ or early fault tolerant machines) may aid in an application of practical relevance [68, 80]. In Part II, we explored analog quantum simulation of the closed system dynamics of Bose-Fermi mixtures using ultracold atoms. In Part III, we explored analog quantum simulation of the open system dynamics of spin chains using ultracold atoms coupled to optical cavities. In Part IV, we explored digital, analog, and hybrid quantum simulation using trapped ions and superconducting circuits in a context of practical relevance: NMR spectroscopy. NMR experiments are fundamentally about spin dynamics, with different protocols admitting descriptions as closed or open systems. Here, we draw connections between the topics examined in different parts of the thesis, synthesizing key lessons learned and open questions that emerge.

The quantum Cherenkov transition uncovered in Part II can be framed as a dissipative dynamics phenomenon when viewed from the point of view of the fast impurity [204]. When the impurity is slow, it emits a fixed amount of excitations into the bath, while when it is sufficiently fast, it dissipates momentum by emitting a diverging number of excitations into the bath. Dissipation into the bath mediates the dynamics of the impurity and the Loschmidt echo can be used to signify a qualitative transition between these two dynamical regimes. This behavior is spiritually analogous to the dissipative spin chain studied in Part III, where the cavity photon forming the bath mediated dissipative dynamics in the system, with correlation functions of the system spins signifying a transition between two qualitatively different regimes of dynamics: one where spin-wave excitations are created and other where they are destroyed. The analogy between the two systems brings to mind a long-standing question in modern physics: is there a notion of non-equilibrium universality in many-body systems? Universality, the idea that diverse phenomenon

with completely different microscopic origins can be classified and predicted using a handful of underlying characteristics such as dimension and symmetry, is one of the most successful concepts in our understanding of many-body systems in equilibrium. It remains unclear whether non-equilibrium phenomenon in closed quantum many-body systems can similarly be described by a few underlying principles, and whether opening the system and admitting dissipative dynamics changes the answer [237]. Two organizing questions that arise from Parts II and III are (1) can we define a non-equilibrium phase of matter, and (2) can entanglement or a similar metric be used as an order parameter to characterize non-equilibrium universality? Progress on these questions would have fundamental implications for both condensed matter and high-energy physics.

Ultracold atom analog quantum simulators seem ideally suited to study the question of non-equilibrium universality due to their natural implementation of various boson, fermion, and spin models in the thermodynamic limit. Coupling the atoms to an optical cavity allows a degree of tunability of the models that enables exploration of various dynamical systems. Indeed, cold atoms in optical cavities have been used to explore various dynamical transitions in both closed and open systems [25, 44, 200, 208, 94, 259, 382, 96, 304, 113]. These works largely explore the dynamics of collective spin models that are limited to semi-classical behavior. A promising next step would be to use the tricks employed in Part III, namely magnetic field gradients and side-bands, to endow the system with spatially-resolved interactions that endow the system with true many-body character and see how this affects the previously investigated dynamical transitions.

The dissipation engineering tricks developed in Part III are also relevant to the practical application of NMR simulation discussed in Part IV. While we focused on NMR protocols that can be described by (possibly ensemble-averaged) closed system dynamics, many of the most interesting protocols of scientific and pharmaceutical relevance have dissipative dynamics take center stage. For example, NOESY is a protocol that uses dipolar relaxation in the system to infer the relative positions of spins, and thereby learn about the structure of the molecule. NOESY is used widely

to determine the structure of proteins, which in turn can be used to screen different drug targets [133]. Both the dynamics of these relaxation spectroscopy protocols and the dynamics of the spin chains in Part III are described by a master equation characterized by some power spectral density of noise. We can thus ask if we can engineer the dynamics of analog quantum simulators, either in using cold atoms coupled to an optical cavity or superconducting devices in a circuit-QED platform, to mimic the power spectral density of spins in salient relaxation NMR protocols. A possible starting point is to engineer qubits on a superconducting chip to mimic an inversion-recovery NMR experiment, where one qubit would act as the spin of interest and we drive the remaining qubits to engineer an effective bath. More generally, Floquet engineering may enable a path to directly simulate relaxation NMR protocols on otherwise unitary quantum simulators as the relaxation dynamics in NMR arises from the system spins themselves rather than an external bath. Mathematically, truncating the Floquet Hamiltonian at second order and replacing second-order interaction terms with their rotational expectation values may capture the usual master equation treatment of relaxation NMR.

In addition to using the dissipation engineering methods Part III to engineer the dynamics of quantum simulators, the open system correlation dynamics investigated itself may prove useful in bounding the errors in quantum simulations. We know from the trapped ion heating dynamics investigated in Part IV that noise in quantum simulators can often be correlated and non-Markovian. Studying how correlations generated by correlated dissipation spread may therefore allow us to generalize the types of error bounds derived in Ref. [116] to quantum simulations of systems with variable range interactions such as molecules that appear in NMR experiments.

We can also take inspiration in the reverse direction, and see if some of the philosophies in NMR spectroscopy can inform our understanding and control of quantum simulation. Specifically, NMR spectroscopy is limited to a single observable, the total magnetization of the system, and therefore extracts information about the underlying spin dynamics by manipulating the spins with a series of sophisticated pulse trains. We can identify how external control fields similarly made the dynamics of the systems

studied in Parts II and III more visibile. Specifically, an external force applied to the mobile impurity in Part II drove it into the supersonic Cherenkov regime, which manifested in experimentally visible signatures of dissipative dynamics. In Part III, an external control field was able to repeatedly drive the system through its two regimes of dynamics (creating and destroying excitations), making this behavior more visible in experimentally measureable correlation functions. We can thus ask the following question: can we define a quantum optimal control problem where we fix the available measurements in a quantum many-body system and optimize how external control fields are applied such that we can effectively learn the dynamics of excitations in the system? This scenario is the inverse of current Hamiltonian learning and verification proposals, where we fix the dynamics of the system and pick optimal measurements that will let us learn the dynamics effectively [160, 80]. In both cases, we wish to learn the dynamics of the quantum many-body system, but in one case we pick the control fields and fix the measurement while in the other case we fix the control field and pick the measurements.

Progress on this optimal control question may be relevant for NMR experiments themselves. Modern NMR is performed using a radiofrequency (RF) coil to probe the spins. In the last few years, people have shown that quantum sensors such as nitrogen-vacancy (NV) centers in diamond can couple to spins in biomolecules and perform NMR experiments [224]. Compared to the classically coupled RF coil, the coherent nature of the coupling between the NV center and the biomolecule, along with other memory qubits in the diamond that can coherently interact with the NV center, opens the tantalizing possibility of extracting more information from biomolcules than conventional NMR experiments. Exploring this possibility, however, requires determining the optimal manipulation of the limited quantum resources in the diamond and the molecule itself in order to extract salient information about the molecule's spin dynamics.

Answering practically useful questions using quantum simulators in the near-term will likely require a similarly clever use of different available resources. For example, we may use hybrid digital-analog quantum simulation to realize complicated dynam-

ical models while embedding the simulation in a larger classical simulation. Such embedding frameworks have been developed for the electronic structure problem in both condensed matter and quantum chemistry contexts [366]. Two contexts where such embedding methods could enable quantum simulators to add value to scientifically and practically useful applications are high-termperature superconductivity and NMR experiments. Cold atom simulations of the Fermi-Hubbard model [80], and strongly correlated limits of the model that manifest as Bose-Fermi mixtures [184] may be able to shed light on qualitative aspects of high-temperature superconductors if simulations are performed on large enough systems for long enough times. Embedding cold atom analog quantum simulation of these models inside simulations on classical computers may enable quantatively accurate results faster than waiting for cold atom experimental platforms to reach low enough errors to perform the entire simulation themselves.

For NMR experiments, hybrid quantum simulations of solid-state NMR or liquid-state relaxation NMR (such as NOESY) on different platforms embedded inside classical computer simulations using software built on state-space decomposition such as Spinach [196] may enable NMR structure validation of molecules larger than classical computers can accompish by themselves. This structure validation would be useful for both fundamental biochemistry studies as well as drug discovery using screening flows [133]. Enabling quantum simulators to add value, even in a limited capacity, to fundamental material science and biochemistry as well as the development of high-temperature superconductors and novel drugs would give quantum technology a keystone near-term application.

Just as the early and modest commercial success of the transistor radio paved a path to personal computers, a near-term application of quantum hardware with modest impact may buy the quantum science and technology ecosystem enough time to reach fully fault-tolerant quantum computers and realize the promise they bring.

Bibliography

[1] Dmitry A. Abanin, Ehud Altman, Immanuel Bloch, and Maksym Serbyn. Colloquium: Many-body localization, thermalization, and entanglement. *Rev. Mod. Phys.*, 91:021001, May 2019.

[2] G. S. Agarwal, R. R. Puri, and R. P. Singh. Atomic schrödinger cat states. *Phys. Rev. A*, 56:2249–2254, Sep 1997.

[3] Vincenzo Alba and Pasquale Calabrese. Entanglement and thermodynamics after a quantum quench in integrable systems. *Proceedings of the National Academy of Sciences*, 114(30):7947–7951, 2017.

[4] A. Alexandrov and J. Ranninger. Theory of bipolarons and bipolaronic bands. *Physical Review B*, 23(4):1796–1801, 1981.

[5] Sanah Altenburg, Michał Oszmaniec, Sabine Wölk, and Otfried Gühne. Estimation of gradients in quantum metrology. *Phys. Rev. A*, 96:042319, Oct 2017.

[6] Alexander Altland and Ben D Simons. *Condensed matter field theory*. Cambridge university press, 2010.

[7] P. W. Anderson. Absence of diffusion in certain random lattices. *Phys. Rev.*, 109:1492–1505, Mar 1958.

[8] Xavier Andrade, Jacob N. Sanders, and Alán Aspuru-Guzik. Application of compressed sensing to the simulation of atomic systems. *Proceedings of the National Academy of Sciences*, 109(35):13928–13933, 2012.

[9] K. Arai, C. Belthangady, H. Zhang, N. Bar-Gill, S. J. DeVience, P. Cappellaro, A. Yacoby, and R. L. Walsworth. Fourier magnetic imaging with nanoscale resolution and compressed sensing speed-up using electronic spins in diamond. *Nature Nanotechnology*, 10(10):859–864, 2015.

[10] Javier Argüello-Luengo, Alejandro González-Tudela, Tao Shi, Peter Zoller, and J. Ignacio Cirac. Analogue quantum chemistry simulation. *Nature*, 574(7777):215–218, 2019.

[11] Javier Argüello-Luengo, Alejandro González-Tudela, Tao Shi, Peter Zoller, and J. Ignacio Cirac. Quantum simulation of two-dimensional quantum chemistry in optical lattices. *Phys. Rev. Research*, 2:042013, Oct 2020.

[12] Ana Asenjo-Garcia, M Moreno-Cardoner, Andreas Albrecht, HJ Kimble, and Darrick E Chang. Exponential improvement in photon storage fidelities using subradiance and "selective radiance" in atomic arrays. *Physical Review X*, 7(3):031024, 2017.

[13] Sharon E. Ashbrook and Paul Hodgkinson. Perspective: Current advances in solid-state nmr spectroscopy. *The Journal of Chemical Physics*, 149(4):040901, 2018.

[14] Sharon E. Ashbrook and David McKay. Combining solid-state nmr spectroscopy with first-principles calculations – a guide to nmr crystallography. *Chem. Commun.*, 52:7186–7204, 2016.

[15] Yuto Ashida, Keiji Saito, and Masahito Ueda. Thermalization and heating dynamics in open generic many-body systems. *Phys. Rev. Lett.*, 121:170402, Oct 2018.

[16] Nabeel Aslam, Matthias Pfender, Philipp Neumann, Rolf Reuter, Andrea Zappe, Felipe Fávaro de Oliveira, Andrej Denisenko, Hitoshi Sumiya, Shinobu Onoda, Junichi Isoya, and Jörg Wrachtrup. Nanoscale nuclear magnetic resonance with chemical resolution. *Science*, 357(6346):67–71, 2017.

[17] G. E. Astrakharchik and L. P. Pitaevskii. Motion of a heavy impurity through a bose-einstein condensate. *Phys. Rev. A*, 70:013608, Jul 2004.

[18] C. J. Ballance, T. P. Harty, N. M. Linke, M. A. Sepiol, and D. M. Lucas. High-fidelity quantum logic gates using trapped-ion hyperfine qubits. *Phys. Rev. Lett.*, 117:060504, Aug 2016.

[19] Mari Carmen Bañuls, Rainer Blatt, Jacopo Catani, Alessio Celi, Juan Ignacio Cirac, Marcello Dalmonte, Leonardo Fallani, Karl Jansen, Maciej Lewenstein, Simone Montangero, Christine A. Muschik, Benni Reznik, Enrique Rico, Luca Tagliacozzo, Karel Van Acoleyen, Frank Verstraete, Uwe-Jens Wiese, Matthew Wingate, Jakub Zakrzewski, and Peter Zoller. Simulating lattice gauge theories within quantum technologies. *The European Physical Journal D*, 74(8):165, 2020.

[20] C-E Bardyn, Mikhail A Baranov, Enrique Rico, A Imamoglu, Peter Zoller, and Sebastian Diehl. Majorana modes in driven-dissipative atomic superfluids with a zero chern number. *Physical review letters*, 109(13):130402, 2012.

[21] Charles-Edouard Bardyn, Mikhail A Baranov, Christina V Kraus, Enrique Rico, A Imamoglu, Peter Zoller, and Sebastian Diehl. Topology by dissipation. *New Journal of Physics*, 15(8):085001, 2013.

[22] Julio T Barreiro, Markus Müller, Philipp Schindler, Daniel Nigg, Thomas Monz, Michael Chwalla, Markus Hennrich, Christian F Roos, Peter Zoller, and Rainer Blatt. An open-system quantum simulator with trapped ions. *Nature*, 470(7335):486–491, 2011.

[23] Danila A. Barskiy, Michael C. D. Tayler, Irene Marco-Rius, John Kurhanewicz, Daniel B. Vigneron, Sevil Cikrikci, Ayca Aydogdu, Moritz Reh, Andrey N. Pravdivtsev, Jan-Bernd Hövener, John W. Blanchard, Teng Wu, Dmitry Budker, and Alexander Pines. Zero-field nuclear magnetic resonance of chemically exchanging systems. *Nature Communications*, 10(1):3002, 2019.

[24] Bela Bauer, Sergey Bravyi, Mario Motta, and Garnet Kin-Lic Chan. Enabling quantum leap: Quantum algorithms for quantum chemistry and materials, 2019.

[25] Kristian Baumann, Christine Guerlin, Ferdinand Brennecke, and Tilman Esslinger. Dicke quantum phase transition with a superfluid gas in an optical cavity. *Nature*, 464(7293):1301–1306, 2010.

[26] Ron Belyansky, Przemyslaw Bienias, Yaroslav A. Kharkov, Alexey V. Gorshkov, and Brian Swingle. Minimal model for fast scrambling. *Phys. Rev. Lett.*, 125:130601, Sep 2020.

[27] Gregory Bentsen, Tomohiro Hashizume, Anton S. Buyskikh, Emily J. Davis, Andrew J. Daley, Steven S. Gubser, and Monika Schleier-Smith. Treelike interactions and fast scrambling with cold atoms. *Phys. Rev. Lett.*, 123:130601, Sep 2019.

[28] Gregory Bentsen, Ionut-Dragos Potirniche, Vir B. Bulchandani, Thomas Scaffidi, Xiangyu Cao, Xiao-Liang Qi, Monika Schleier-Smith, and Ehud Altman. Integrable and chaotic dynamics of spins coupled to an optical cavity. *Phys. Rev. X*, 9:041011, Oct 2019.

[29] Hannes Bernien, Sylvain Schwartz, Alexander Keesling, Harry Levine, Ahmed Omran, Hannes Pichler, Soonwon Choi, Alexander S. Zibrov, Manuel Endres, Markus Greiner, Vladan Vuletić, and Mikhail D. Lukin. Probing many-body dynamics on a 51-atom quantum simulator. *Nature*, 551(7682):579–584, 2017.

[30] Jean-Sébastien Bernier, Ryan Tan, Lars Bonnes, Chu Guo, Dario Poletti, and Corinna Kollath. Light-cone and diffusive propagation of correlations in a many-body dissipative system. *Phys. Rev. Lett.*, 120:020401, Jan 2018.

[31] Juliette Billy, Vincent Josse, Zhanchun Zuo, Alain Bernard, Ben Hambrecht, Pierre Lugan, David Clément, Laurent Sanchez-Palencia, Philippe Bouyer, and Alain Aspect. Direct observation of anderson localization of matter waves in a controlled disorder. *Nature*, 453(7197):891–894, 2008.

[32] E. S. (Merijn) Blaakmeer, Giuseppe Antinucci, Vincenzo Busico, Ernst R. H. van Eck, and Arno P. M. Kentgens. Solid-state nmr investigations of mgcl2 catalyst support. *The Journal of Physical Chemistry C*, 120(11):6063–6074, 2016.

[33] E. S. (Merijn) Blaakmeer, Frank J. Wensink, Ernst R. H. van Eck, Gilles A. de Wijs, and Arno P. M. Kentgens. Preactive site in ziegler–natta catalysts. *The Journal of Physical Chemistry C*, 123(23):14490–14500, 2019.

[34] E.S. (Merijn) Blaakmeer, Wouter M.J. Franssen, and Arno P.M. Kentgens. Quadrupolar nutation nmr to discriminate central and satellite transitions: Spectral assignments for a ziegler-natta catalyst. *Journal of Magnetic Resonance*, 281:199–208, 2017.

[35] Adam T Black, Hilton W Chan, and Vladan Vuletić. Observation of collective friction forces due to spatial self-organization of atoms: from rayleigh to bragg scattering. *Physical review letters*, 91(20):203001, 2003.

[36] Rainer Blatt and Christian F Roos. Quantum simulations with trapped ions. *Nature Physics*, 8(4):277–284, 2012.

[37] I. Bloch, T. W. Hänsch, and T. Esslinger. Measurement of the spatial coherence of a trapped bose gas at the phase transition. *Nature*, 403(6766):166–170, 2000.

[38] Immanuel Bloch, Jean Dalibard, and Sylvain Nascimbène. Quantum simulations with ultracold quantum gases. *Nature Physics*, 8(4):267–276, 2012.

[39] Immanuel Bloch, Jean Dalibard, and Wilhelm Zwerger. Many-body physics with ultracold gases. *Rev. Mod. Phys.*, 80:885–964, Jul 2008.

[40] Boris M Bolotovskii. Vavilov – cherenkov radiation: its discovery and application. *Physics-Uspekhi*, 52(11):1099–1110, nov 2009.

[41] Ricardo M. Borges, Sean M. Colby, Susanta Das, Arthur S. Edison, Oliver Fiehn, Tobias Kind, Jesi Lee, Amy T. Merrill, Kenneth M. Merz, Thomas O. Metz, Jamie R. Nunez, Dean J. Tantillo, Lee-Ping Wang, Shunyang Wang, and Ryan S. Renslow. Quantum chemistry calculations for metabolomics. *Chemical Reviews*, 121(10):5633–5670, 2021. PMID: 33979149.

[42] Mark Bostock and Daniel Nietlispach. Compressed sensing: Reconstruction of non-uniformly sampled multidimensional nmr data. *Concepts in Magnetic Resonance Part A*, 46A, 03 2017.

[43] Daniel Boyanovsky, David Jasnow, Xiao-Lun Wu, and Rob C. Coalson. Dynamics of relaxation and dressing of a quenched bose polaron. *Phys. Rev. A*, 100:043617, Oct 2019.

[44] Ferdinand Brennecke, Rafael Mottl, Kristian Baumann, Renate Landig, Tobias Donner, and Tilman Esslinger. Real-time observation of fluctuations at the driven-dissipative dicke phase transition. *Proceedings of the National Academy of Sciences*, 110(29):11763–11767, 2013.

[45] Vincent Bretin, Sabine Stock, Yannick Seurin, and Jean Dalibard. Fast rotation of a bose-einstein condensate. *Phys. Rev. Lett.*, 92:050403, Feb 2004.

[46] Kenneth R Brown, Jungsang Kim, and Christopher Monroe. Co-designing a scalable quantum computer with trapped atomic ions. *npj Quantum Information*, 2(1):16034, 2016.

[47] M. Brownnutt, M. Kumph, P. Rabl, and R. Blatt. Ion-trap measurements of electric-field noise near surfaces. *Rev. Mod. Phys.*, 87:1419–1482, Dec 2015.

[48] M. Bruderer, A. Klein, S. R. Clarks, and D. Jaksch. Transport of strong-coupling polarons in optical lattices. *New Journal of Physics*, 10, 2008.

[49] David L. Bryce. NMR crystallography: structure and properties of materials from solid-state nuclear magnetic resonance observables. *IUCrJ*, 4(4):350–359, Jul 2017.

[50] Berislav Buca, Cameron Booker, and Dieter Jaksch. Algebraic theory of quantum synchronization and limit cycles under dissipation. *arXiv preprint arXiv:2103.01808*, 2021.

[51] Berislav Buča and Dieter Jaksch. Dissipation induced nonstationarity in a quantum gas. *Physical review letters*, 123(26):260401, 2019.

[52] Berislav Buča, Joseph Tindall, and Dieter Jaksch. Non-stationary coherent quantum many-body dynamics through dissipation. *Nat. Comm.*, 10(1):1–6, 2019.

[53] Michael Buchhold and Sebastian Diehl. Nonequilibrium universality in the heating dynamics of interacting luttinger liquids. *Phys. Rev. A*, 92:013603, Jul 2015.

[54] Dmitry Budker, Thomas Cecil, Timothy E. Chupp, Andrew A. Geraci, Derek F. Jackson Kimball, Shimon Kolkowitz, Surjeet Rajendran, Jaideep T. Singh, and Alexander O. Sushkov. Quantum sensors for high precision measurements of spin-dependent interactions, 2022.

[55] Anton S. Buyskikh, Maurizio Fagotti, Johannes Schachenmayer, Fabian Essler, and Andrew J. Daley. Entanglement growth and correlation spreading with variable-range interactions in spin and fermionic tunneling models. *Phys. Rev. A*, 93:053620, May 2016.

[56] Pasquale Calabrese and John Cardy. Time dependence of correlation functions following a quantum quench. *Phys. Rev. Lett.*, 96(13):136801, 2006.

[57] Pasquale Calabrese, Fabian HL Essler, and Maurizio Fagotti. Quantum quench in the transverse-field ising chain. *Physical review letters*, 106(22):227203, 2011.

[58] A. Campa, T. Dauxois, and S. Ruffo. *Physics Reports 480, pp. 57-159*, 2009.

[59] I. Carusotto, S. X. Hu, L. A. Collins, and A. Smerzi. Bogoliubov-Čerenkov radiation in a bose-einstein condensate flowing against an obstacle. *Phys. Rev. Lett.*, 97:260403, Dec 2006.

[60] W. Casteels, J. Tempere, and J. T. Devreese. Polaronic properties of an impurity in a Bose-Einstein condensate in reduced dimensions. *Physical Review A - Atomic, Molecular, and Optical Physics*, 86(4), 2012.

[61] J. Catani, G. Lamporesi, D. Naik, M. Gring, M. Inguscio, F. Minardi, A. Kantian, and T. Giamarchi. Quantum dynamics of impurities in a one-dimensional bose gas. *Phys. Rev. A*, 85:023623, Feb 2012.

[62] M. Cetina, L. N. Egan, C. A. Noel, M. L. Goldman, A. R. Risinger, D. Zhu, D. Biswas, and C. Monroe. Quantum gates on individually-addressed atomic qubits subject to noisy transverse motion, 2020.

[63] Marko Cetina, Michael Jag, Rianne S. Lous, Isabella Fritsche, Jook T. M. Walraven, Rudolf Grimm, Jesper Levinsen, Meera M. Parish, Richard Schmidt, Michael Knap, and Eugene Demler. Ultrafast many-body interferometry of impurities coupled to a fermi sea. *Science*, 354(6308):96–99, 2016.

[64] Titas Chanda, Jakub Zakrzewski, Maciej Lewenstein, and Luca Tagliacozzo. Confinement and lack of thermalization after quenches in the bosonic schwinger model. *Phys. Rev. Lett.*, 124:180602, May 2020.

[65] Christos Charalambous, Miguel Ángel García-March, Gorka Muñoz-Gil, Przemysław Ryszard Grzybowski, and Maciej Lewenstein. Control of anomalous diffusion of a Bose polaron. *Quantum*, 4:232, 2020.

[66] Kuizhi Chen. A practical review of nmr lineshapes for spin-1/2 and quadrupolar nuclei in disordered materials. *International journal of molecular sciences*, 21(16):5666, 08 2020.

[67] Marc Cheneau, Peter Barmettler, Dario Poletti, Manuel Endres, Peter Schauß, Takeshi Fukuhara, Christian Gross, Immanuel Bloch, Corinna Kollath, and Stefan Kuhr. Light-cone-like spreading of correlations in a quantum many-body system. *Nature*, 481(7382):484–487, 2012.

[68] Andrew M. Childs, Dmitri Maslov, Yunseong Nam, Neil J. Ross, and Yuan Su. Toward the first quantum simulation with quantum speedup. *Proceedings of the National Academy of Sciences*, 115(38):9456–9461, 2018.

[69] Andrew M. Childs, Yuan Su, Minh C. Tran, Nathan Wiebe, and Shuchen Zhu. Theory of trotter error with commutator scaling. *Phys. Rev. X*, 11:011020, Feb 2021.

[70] Joonhee Choi, Adam L. Shaw, Ivaylo S. Madjarov, Xin Xie, Jacob P. Covey, Jordan S. Cotler, Daniel K. Mark, Hsin-Yuan Huang, Anant Kale, Hannes Pichler, Fernando G. S. L. Brandão, Soonwon Choi, and Manuel Endres. Emergent randomness and benchmarking from many-body quantum chaos, 2021.

[71] Joonhee Choi, Hengyun Zhou, Helena S. Knowles, Renate Landig, Soonwon Choi, and Mikhail D. Lukin. Robust dynamic hamiltonian engineering of many-body spin systems. *Phys. Rev. X*, 10:031002, Jul 2020.

[72] Rasmus Søgaard Christensen, Jesper Levinsen, and Georg M. Bruun. Quasiparticle Properties of a Mobile Impurity in a Bose-Einstein Condensate. *Physical Review Letters*, 115(16):1–5, 2015.

[73] J. Ignacio Cirac, Paolo Maraner, and Jiannis K. Pachos. Cold atom simulation of interacting relativistic quantum field theories. *Phys. Rev. Lett.*, 105:190403, Nov 2010.

[74] G. Marius Clore and Angela M. Gronenborn. Structures of larger proteins in solution: Three- and four-dimensional heteronuclear nmr spectroscopy. *Science*, 252(5011):1390–1399, 1991.

[75] Sam R. Cohen and Jeff D. Thompson. Quantum computing with circular rydberg atoms. *PRX Quantum*, 2:030322, Aug 2021.

[76] Iris Cong, Harry Levine, Alexander Keesling, Dolev Bluvstein, Sheng-Tao Wang, and Mikhail D. Lukin. Hardware-efficient, fault-tolerant quantum computation with rydberg atoms. *Phys. Rev. X*, 12:021049, Jun 2022.

[77] Kevin C Cox, Graham P Greve, Joshua M Weiner, and James K Thompson. Deterministic squeezed states with collective measurements and feedback. *Physical Review Letters*, 116(9):093602, 2016.

[78] F. M. Cucchietti and E. Timmermans. Strong-coupling polarons in dilute gas Bose-Einstein condensates. *Physical Review Letters*, 96(21):4–7, 2006.

[79] Elbio Dagotto. Correlated electrons in high-temperature superconductors. *Rev. Mod. Phys.*, 66:763–840, Jul 1994.

[80] Andrew J. Daley, Immanuel Bloch, Christian Kokail, Stuart Flannigan, Natalie Pearson, Matthias Troyer, and Peter Zoller. Practical quantum advantage in quantum simulation. *Nature*, 607(7920):667–676, 2022.

[81] Emanuele Dalla Torre, Sebastian Diehl, Mikhail Lukin, Subir Sachdev, and Philipp Strack. Keldysh approach for nonequilibrium phase transitions in quantum optics: Beyond the Dicke model in optical cavities. *Physical Review A*, 87(2):023831, February 2013.

[82] Emanuele G. Dalla Torre, Johannes Otterbach, Eugene Demler, Vladan Vuletic, and Mikhail D. Lukin. Dissipative preparation of spin squeezed atomic ensembles in a steady state. *Phys. Rev. Lett.*, 110:120402, Mar 2013.

[83] David Dasenbrook and Andreas Komnik. Semiclassical polaron dynamics of impurities in ultracold gases. *Phys. Rev. B*, 87:094301, Mar 2013.

[84] Emily J. Davis, Gregory Bentsen, Lukas Homeier, Tracy Li, and Monika H. Schleier-Smith. Photon-mediated spin-exchange dynamics of spin-1 atoms. *Phys. Rev. Lett.*, 122:010405, Jan 2019.

[85] Emily J. Davis, Avikar Periwal, Eric S. Cooper, Gregory Bentsen, Simon J. Evered, Katherine Van Kirk, and Monika H. Schleier-Smith. Protecting spin coherence in a tunable heisenberg model. *Phys. Rev. Lett.*, 125:060402, Aug 2020.

[86] Zohreh Davoudi, Mohammad Hafezi, Christopher Monroe, Guido Pagano, Alireza Seif, and Andrew Shaw. Towards analog quantum simulations of lattice gauge theories with trapped ions. *Physical Review Research*, 2(2), apr 2020.

[87] Sylvain de Léséleuc, Vincent Lienhard, Pascal Scholl, Daniel Barredo, Sebastian Weber, Nicolai Lang, Hans Peter Büchler, Thierry Lahaye, and Antoine Browaeys. Observation of a symmetry-protected topological phase of interacting bosons with rydberg atoms. *Science*, 365(6455):775–780, 2019.

[88] Sylvain de Léséleuc, Vincent Lienhard, Pascal Scholl, Daniel Barredo, Sebastian Weber, Nicolai Lang, Hans Peter Büchler, Thierry Lahaye, and Antoine Browaeys. Observation of a symmetry-protected topological phase of interacting bosons with rydberg atoms. *Science*, 365(6455):775–780, 2019.

[89] W. De Roeck and F. Huveneers. Asymptotic quantum many-body localization from thermal disorder. *Commun. Math. Phys.*, 332:1017, 2014.

[90] Nicolò Defenu. Metastability and discrete spectrum of long-range systems. *Proceedings of the National Academy of Sciences*, 118(30), 2021.

[91] Jozef Devreese and Sasha Alexandrov. Froehlich Polaron and Bipolaron: Recent Developments. pages 1–131, 2009.

[92] Sebastian Diehl, A Micheli, A Kantian, B Kraus, HP Büchler, and P Zoller. Quantum states and phases in driven open quantum systems with cold atoms. *Nature Physics*, 4(11):878–883, 2008.

[93] Sebastian Diehl, Enrique Rico, Mikhail A Baranov, and Peter Zoller. Topology by dissipation in atomic quantum wires. *Nature Physics*, 7(12):971–977, 2011.

[94] Nishant Dogra, Manuele Landini, Katrin Kroeger, Lorenz Hruby, Tobias Donner, and Tilman Esslinger. Dissipation-induced structural instability and chiral dynamics in a quantum gas. *Science*, 366(6472):1496–1499, 2019.

[95] D.L. Donoho. Compressed sensing. *IEEE Transactions on Information Theory*, 52(4):1289–1306, 2006.

[96] Davide Dreon, Alexander Baumgärtner, Xiangliang Li, Simon Hertlein, Tilman Esslinger, and Tobias Donner. Self-oscillating geometric pump in a dissipative atom-cavity system, 2021.

[97] Moritz Drescher, Manfred Salmhofer, and Tilman Enss. Real-space dynamics of attractive and repulsive polarons in bose-einstein condensates. *Phys. Rev. A*, 99:023601, Feb 2019.

[98] Moritz Drescher, Manfred Salmhofer, and Tilman Enss. Theory of a resonantly interacting impurity in a bose-einstein condensate. *Phys. Rev. Research*, 2:032011, Jul 2020.

[99] P. D. Drummond. Observables and moments of cooperative resonance fluorescence. *Phys. Rev. A*, 22:1179–1184, Sep 1980.

[100] PD Drummond and HJ Carmichael. Volterra cycles and the cooperative fluorescence critical point. *Optics Communications*, 27:157–159, 1978.

[101] Zachary Dutton, Michael Budde, Christopher Slowe, and Lene Vestergaard Hau. Observation of quantum shock waves created with ultra- compressed slow light pulses in a bose-einstein condensate. *Science*, 293(5530):663–668, 2001.

[102] H. Jane Dyson and Peter E. Wright. Nmr illuminates intrinsic disorder. *Current Opinion in Structural Biology*, 70:44–52, 2021.

[103] David Dzsotjan, Richard Schmidt, and Michael Fleischhauer. Dynamical variational approach to Bose polarons at finite temperatures. pages 1–13, 2019.

[104] Luke J. Edwards, D.V. Savostyanov, Z.T. Welderufael, Donghan Lee, and Ilya Kuprov. Quantum mechanical nmr simulation algorithm for protein-size spin systems. *Journal of Magnetic Resonance*, 243:107–113, 2014.

[105] Laird Egan, Dripto M Debroy, Crystal Noel, Andrew Risinger, Daiwei Zhu, Debopriyo Biswas, Michael Newman, Muyuan Li, Kenneth R Brown, Marko Cetina, and Christopher Monroe. Fault-tolerant operation of a quantum error-correction code, 2020.

[106] Christopher Eichler, Jonas Mlynek, Jonas Butscher, Philipp Kurpiers, Klemens Hammerer, Tobias J Osborne, and Andreas Wallraff. Exploring interacting quantum many-body systems by experimentally creating continuous matrix product states in superconducting circuits. *Physical Review X*, 5(4):041044, 2015.

[107] J Eisert and T Prosen. Noise-driven quantum criticality. *arXiv preprint arXiv:1012.5013*, 2010.

[108] Jens Eisert, Mauritz van den Worm, Salvatore R. Manmana, and Michael Kastner. Breakdown of quasilocality in long-range quantum lattice models. *Phys. Rev. Lett.*, 111:260401, Dec 2013.

[109] G A El, Yu G Gladush, and A M Kamchatnov. Two-dimensional periodic waves in supersonic flow of a bose–einstein condensate. *Journal of Physics A: Mathematical and Theoretical*, 40(4):611–619, jan 2007.

[110] Zachary Eldredge, Michael Foss-Feig, Jonathan A. Gross, S. L. Rolston, and Alexey V. Gorshkov. Optimal and secure measurement protocols for quantum sensor networks. *Phys. Rev. A*, 97:042337, Apr 2018.

[111] Zachary Eldredge, Zhe-Xuan Gong, Jeremy T. Young, Ali Hamed Moosavian, Michael Foss-Feig, and Alexey V. Gorshkov. Fast quantum state transfer and entanglement renormalization using long-range interactions. *Phys. Rev. Lett.*, 119:170503, Oct 2017.

[112] Dominic V. Else, Francisco Machado, Chetan Nayak, and Norman Y. Yao. An improved lieb-robinson bound for many-body hamiltonians with power-law interactions. *arXiv:1809.06369*, 2018.

[113] Francesco Ferri, Rodrigo Rosa-Medina, Fabian Finger, Nishant Dogra, Matteo Soriente, Oded Zilberberg, Tobias Donner, and Tilman Esslinger. Emerging dissipative phases in a superradiant quantum gas with tunable decay. *Phys. Rev. X*, 11:041046, Dec 2021.

[114] Bernard Field, Jesper Levinsen, and Meera M. Parish. Fate of the bose polaron at finite temperature. *Phys. Rev. A*, 101:013623, Jan 2020.

[115] Mattias Fitzpatrick, Neereja M. Sundaresan, Andy C. Y. Li, Jens Koch, and Andrew A. Houck. Observation of a dissipative phase transition in a one-dimensional circuit qed lattice. *Phys. Rev. X*, 7:011016, Feb 2017.

[116] S. Flannigan, N. Pearson, G. H. Low, A. Buyskikh, I. Bloch, P. Zoller, M. Troyer, and A. J. Daley. Propagation of errors and quantitative quantum simulation with quantum advantage, 2022.

[117] Michael Foss-Feig, Zhe-Xuan Gong, Charles W. Clark, and Alexey V. Gorshkov. Nearly linear light cones in long-range interacting quantum systems. *Phys. Rev. Lett.*, 114:157201, Apr 2015.

[118] Michael Foss-Feig, Jeremy T. Young, Victor V. Albert, Alexey V. Gorshkov, and Mohammad F. Maghrebi. Solvable family of driven-dissipative many-body systems. *Phys. Rev. Lett.*, 119:190402, Nov 2017.

[119] H. Fröhlich. Electrons in lattice fields. *Advances in Physics*, 3(11):325–361, 1954.

[120] Takeshi Fukuhara, Adrian Kantian, Manuel Endres, Marc Cheneau, Peter Schauß, Sebastian Hild, David Bellem, Ulrich Schollwöck, Thierry Giamarchi, Christian Gross, Immanuel Bloch, and Stefan Kuhr. Quantum dynamics of a mobile spin impurity. *Nature Physics*, 9(4):235–241, 2013.

[121] John Gaebler, Ting, Yong Wan, Yiheng Lin, Ryan Bowler, Adam Keith, Scott Glancy, Kevin Coakley, Emanuel Knill, Dietrich Leibfried, and David Wineland. High fidelity universal gate set for 9be+ ion qubits. 2016-08-04 2016.

[122] Oleksandr Gamayun, Oleg Lychkovskiy, Evgeni Burovski, Matthew Malcomson, Vadim V. Cheianov, and Mikhail B. Zvonarev. Impact of the injection protocol on an impurity's stationary state. *Phys. Rev. Lett.*, 120:220605, Jun 2018.

[123] Crispin Gardiner, Peter Zoller, and Peter Zoller. *Quantum noise: a handbook of Markovian and non-Markovian quantum stochastic methods with applications to quantum optics*. Springer Science & Business Media, 2004.

[124] I. M. Georgescu, S. Ashhab, and Franco Nori. Quantum simulation. *Rev. Mod. Phys.*, 86:153–185, Mar 2014.

[125] Annarita Giani and Zachary Eldredge. Quantum computing opportunities in renewable energy. *SN Computer Science*, 2, 09 2021.

[126] Yu. G. Gladush, G. A. El, A. Gammal, and A. M. Kamchatnov. Radiation of linear waves in the stationary flow of a bose-einstein condensate past an obstacle. *Phys. Rev. A*, 75:033619, Mar 2007.

[127] Yu G Gladush, L A Smirnov, and A M Kamchatnov. Generation of cherenkov waves in the flow of a bose–einstein condensate past an obstacle. *Journal of Physics B: Atomic, Molecular and Optical Physics*, 41(16):165301, aug 2008.

[128] A Goban, C-L Hung, JD Hood, S-P Yu, JA Muniz, O Painter, and HJ Kimble. Superradiance for atoms trapped along a photonic crystal waveguide. *Physical review letters*, 115(6):063601, 2015.

[129] A Goban, C-L Hung, S-P Yu, JD Hood, JA Muniz, JH Lee, MJ Martin, AC McClung, KS Choi, Darrick E Chang, et al. Atom–light interactions in photonic crystals. *Nature communications*, 5:3808, 2014.

[130] Zhe-Xuan Gong, Michael Foss-Feig, Spyridon Michalakis, and Alexey V. Gorshkov. Persistence of locality in systems with power-law interactions. *Phys. Rev. Lett.*, 113:030602, Jul 2014.

[131] Jérôme F. Gonthier, Maxwell D. Radin, Corneliu Buda, Eric J. Doskocil, Clena M. Abuan, and Jhonathan Romero. Identifying challenges towards practical quantum advantage through resource estimation: the measurement roadblock in the variational quantum eigensolver, 2020.

[132] Alejandro González-Tudela, C-L Hung, Darrick E Chang, J Ignacio Cirac, and HJ Kimble. Subwavelength vacuum lattices and atom–atom interactions in two-dimensional photonic crystals. *Nature Photonics*, 9(5):320, 2015.

[133] Christoph Gorgulla, Andras Boeszoermenyi, Zi-Fu Wang, Patrick D. Fischer, Paul W. Coote, Krishna M. Padmanabha Das, Yehor S. Malets, Dmytro S. Radchenko, Yurii S. Moroz, David A. Scott, Konstantin Fackeldey, Moritz Hoffmann, Iryna Iavniuk, Gerhard Wagner, and Haribabu Arthanari. An open-source drug discovery platform enables ultra-large virtual screens. *Nature*, 580(7805):663–668, 2020.

[134] Markus Greiner, Olaf Mandel, Tilman Esslinger, Theodor W. Hänsch, and Immanuel Bloch. Quantum phase transition from a superfluid to a mott insulator in a gas of ultracold atoms. *Nature*, 415(6867):39–44, 2002.

[135] Christian Gross and Immanuel Bloch. Quantum simulations with ultracold atoms in optical lattices. *Science*, 357(6355):995–1001, 2017.

[136] F. Grusdt. All-coupling theory for the Fröhlich polaron. *Physical Review B*, 93(14):1–8, 2016.

[137] F. Grusdt, R. Schmidt, Y. E. Shchadilova, and E. Demler. Strong-coupling bose polarons in a bose-einstein condensate. *Phys. Rev. A*, 96:013607, Jul 2017.

[138] F Grusdt, A Shashi, D Abanin, and E Demler. Bloch oscillations of bosonic lattice polarons. *Phys. Rev. A*, 90(063610):1–23, 2014.

[139] F. Grusdt, Y. E. Shchadilova, A. N. Rubtsov, and E. Demler. Renormalization group approach to the Fröhlich polaron model: Application to impurity-BEC problem. *Scientific Reports*, 5:12124, 2015.

[140] Fabian Grusdt, Gregory E Astrakharchik, and Eugene Demler. Bose polarons in ultracold atoms in one dimension: beyond the fröhlich paradigm. *New Journal of Physics*, 19(10):103035, oct 2017.

[141] Fabian Grusdt, Annabelle Bohrdt, and Eugene Demler. Microscopic spinon-chargon theory of magnetic polarons in the t-J model. *Physical Review B*, 99(22):1–14, 2019.

[142] Fabian Grusdt, Kushal Seetharam, Yulia Shchadilova, and Eugene Demler. Strong-coupling bose polarons out of equilibrium: Dynamical renormalization-group approach. *Phys. Rev. A*, 97:033612, Mar 2018.

[143] Nils-Eric Guenther, Pietro Massignan, Maciej Lewenstein, and Georg M. Bruun. Bose polarons at finite temperature and strong coupling. *Phys. Rev. Lett.*, 120:050405, Feb 2018.

[144] Nils-Eric Guenther, Richard Schmidt, Georg M. Bruun, Victor Gurarie, and Pietro Massignan. Mobile impurity in a Bose-Einstein condensate and the orthogonality catastrophe. 2020.

[145] Andrew Y. Guo, Minh C. Tran, Andrew M. Childs, Alexey V. Gorshkov, and Zhe-Xuan Gong. Signaling and scrambling with strongly long-range interactions. *Phys. Rev. A*, 102:010401, Jul 2020.

[146] Julia Hannukainen and Jonas Larson. Dissipation-driven quantum phase transitions and symmetry breaking. *Physical Review A*, 98(4):042113, 2018.

[147] Matthew B Hastings and Tohru Koma. Spectral gap and exponential decay of correlations. *Communications in mathematical physics*, 265(3):781–804, 2006.

[148] P. Hauke, D. Marcos, M. Dalmonte, and P. Zoller. Quantum simulation of a lattice schwinger model in a chain of trapped ions. *Phys. Rev. X*, 3:041018, Nov 2013.

[149] P. Hauke and L. Tagliacozzo. Spread of correlations in long-range interacting quantum systems. *Phys. Rev. Lett.*, 111:207202, Nov 2013.

[150] Loïc Henriet, James S Douglas, Darrick E Chang, and Andreas Albrecht. Critical open-system dynamics in a one-dimensional optical-lattice clock. *Physical Review A*, 99(2):023802, 2019.

[151] U. Las Heras, A. Mezzacapo, L. Lamata, S. Filipp, A. Wallraff, and E. Solano. Digital quantum simulation of spin systems in superconducting circuits. *Phys. Rev. Lett.*, 112:200501, May 2014.

[152] M. A. Hoefer, M. J. Ablowitz, I. Coddington, E. A. Cornell, P. Engels, and V. Schweikhard. Dispersive and classical shock waves in bose-einstein condensates and gas dynamics. *Phys. Rev. A*, 74:023623, Aug 2006.

[153] Michael Hoening, Matthias Moos, and Michael Fleischhauer. Critical exponents of steady-state phase transitions in fermionic lattice models. *Physical Review A*, 86(1):013606, 2012.

[154] H.J. Hogben, M. Krzystyniak, G.T.P. Charnock, P.J. Hore, and Ilya Kuprov. Spinach – a software library for simulation of spin dynamics in large spin systems. *Journal of Magnetic Resonance*, 208(2):179–194, 2011.

[155] M. Höning, M. Moos, and M. Fleischhauer. Critical exponents of steady-state phase transitions in fermionic lattice models. *Phys. Rev. A*, 86:013606, Jul 2012.

[156] Onur Hosten, Radha Krishnakumar, Nils J Engelsen, and Mark A Kasevich. Quantum phase magnification. *Science*, 352(6293):1552–1555, 2016.

[157] Andrew A. Houck, Hakan E. Tureci, and Jens Koch. On-chip quantum simulation with superconducting circuits. *Nature Physics*, 8:292 – 299, 2012.

[158] Ming-Guang Hu, Michael J. Van de Graaff, Dhruv Kedar, John P. Corson, Eric A. Cornell, and Deborah S. Jin. Bose polarons in the strongly interacting regime. *Phys. Rev. Lett.*, 117:055301, Jul 2016.

[159] Yunfei Hu, Kai Cheng, Lichun He, Xu Zhang, Bin Jiang, Ling Jiang, Conggang Li, Guan Wang, Yunhuang Yang, and Maili Liu. Nmr-based methods for protein analysis. *Analytical Chemistry*, 93(4):1866–1879, 2021. PMID: 33439619.

[160] Hsin-Yuan Huang, Richard Kueng, and John Preskill. Predicting many properties of a quantum system from very few measurements. *Nature Physics*, 16(10):1050–1057, 2020.

[161] I. N. Hulea, S. Fratini, H. Xie, C. L. Mulder, N. N. Iossad, G. Rastelli, S. Ciuchi, and A. F. Morpurgo. Tunable Fröhlich polarons in organic single-crystal transistors. *Nature Materials*, 5(12):982–986, 2006.

[162] C-L Hung, Alejandro González-Tudela, J Ignacio Cirac, and HJ Kimble. Quantum spin dynamics with pairwise-tunable, long-range interactions. *Proceedings of the National Academy of Sciences*, 113(34):E4946–E4955, 2016.

[163] Sven G. Hyberts, Koh Takeuchi, and Gerhard Wagner. Poisson-gap sampling and forward maximum entropy reconstruction for enhancing the resolution and sensitivity of protein nmr data. *Journal of the American Chemical Society*, 132(7):2145–2147, 2010. PMID: 20121194.

[164] F. Iemini, A. Russomanno, J. Keeling, M. Schirò, M. Dalmonte, and R. Fazio. Boundary time crystals. *Phys. Rev. Lett.*, 121:035301, Jul 2018.

[165] Fernando Iemini, Leonardo Mazza, Davide Rossini, Rosario Fazio, and Sebastian Diehl. Localized majorana-like modes in a number-conserving setting: An exactly solvable model. *Physical review letters*, 115(15):156402, 2015.

[166] Rajibul Islam, Ruichao Ma, Philipp M Preiss, M Eric Tai, Alexander Lukin, Matthew Rispoli, and Markus Greiner. Measuring entanglement entropy in a quantum many-body system. *Nature*, 528(7580):77–83, 2015.

[167] R. Jackiw and A. Kerman. Time-dependent variational principle and the effective action. *Physics Letters A*, 71(2-3):158–162, 1979.

[168] Paul Niklas Jepsen, Jesse Amato-Grill, Ivana Dimitrova, Wen Wei Ho, Eugene Demler, and Wolfgang Ketterle. Spin transport in a tunable heisenberg model realized with ultracold atoms. *Nature*, 588(7838):403–407, 2020.

[169] Jiasen Jin, Alberto Biella, Oscar Viyuela, Leonardo Mazza, Jonathan Keeling, Rosario Fazio, and Davide Rossini. Cluster mean-field approach to the steady-state phase diagram of dissipative spin systems. *Physical Review X*, 6(3):031011, 2016.

[170] Gyu-Boong Jo, Ye-Ryoung Lee, Jae-Hoon Choi, Caleb A. Christensen, Tony H. Kim, Joseph H. Thywissen, David E. Pritchard, and Wolfgang Ketterle. Itinerant ferromagnetism in a fermi gas of ultracold atoms. *Science*, 325(5947):1521–1524, 2009.

[171] Caroline H. Johnson, Julijana Ivanisevic, and Gary Siuzdak. Metabolomics: beyond biomarkers and towards mechanisms. *Nature Reviews Molecular Cell Biology*, 17(7):451–459, 2016.

[172] Nils B. Jørgensen, Lars Wacker, Kristoffer T. Skalmstang, Meera M. Parish, Jesper Levinsen, Rasmus S. Christensen, Georg M. Bruun, and Jan J. Arlt. Observation of attractive and repulsive polarons in a bose-einstein condensate. *Phys. Rev. Lett.*, 117:055302, Jul 2016.

[173] M. Kac and C. J. Thompson. Entanglement growth and correlation spreading with variable-range interactions in spin and fermionic tunneling models. *J. Math. Phys. 10, 1373- 1386*, 1969.

[174] Ben Kain and Hong Y. Ling. Generalized Hartree-Fock-Bogoliubov description of the Fröhlich polaron. *Physical Review A*, 94(1), 2016.

[175] Ivan Kassal, Stephen P. Jordan, Peter J. Love, Masoud Mohseni, and Alán Aspuru-Guzik. Polynomial-time quantum algorithm for the simulation of chemical dynamics. *Proceedings of the National Academy of Sciences*, 105(48):18681–18686, 2008.

[176] Michael Kastner. Diverging equilibration times in long-range quantum spin models. *Phys. Rev. Lett.*, 106:130601, Mar 2011.

[177] M. J. Kastoryano, F. Reiter, and A. S. Sørensen. Dissipative preparation of entanglement in optical cavities. *Phys. Rev. Lett.*, 106:090502, Feb 2011.

[178] Shane P Kelly, Ana Maria Rey, and Jamir Marino. Effect of active photons on dynamical frustration in cavity qed. *Physical Review Letters*, 126(13):133603, 2021.

[179] Eric M Kessler, Geza Giedke, Atac Imamoglu, Susanne F Yelin, Mikhail D Lukin, and J Ignacio Cirac. Dissipative phase transition in a central spin system. *Physical Review A*, 86(1):012116, 2012.

[180] Toshiya Kinoshita, Trevor Wenger, and David S. Weiss. Observation of a one-dimensional tonks-girardeau gas. *Science*, 305(5687):1125–1128, 2004.

[181] Michael Knap, Charles J. M. Mathy, Martin Ganahl, Mikhail B. Zvonarev, and Eugene Demler. Quantum Flutter: Signatures and Robustness. *Phys. Rev. Lett.*, 112:015302, 2014.

[182] Michael Knap, Charles J.M. Mathy, Martin Ganahl, Mikhail B. Zvonarev, and Eugene Demler. Quantum flutter: Signatures and robustness. *Physical Review Letters*, 112(1):1–5, 2014.

[183] Michael Knap, Aditya Shashi, Yusuke Nishida, Adilet Imambekov, Dmitry A. Abanin, and Eugene Demler. Time-dependent impurity in ultracold fermions: Orthogonality catastrophe and beyond. *Phys. Rev. X*, 2:041020, Dec 2012.

[184] Joannis Koepsell, Jayadev Vijayan, Pimonpan Sompet, Fabian Grusdt, Timon A. Hilker, Eugene Demler, Guillaume Salomon, Immanuel Bloch, and Christian Gross. Imaging magnetic polarons in the doped Fermi–Hubbard model. *Nature*, 572(7769):358–362, 2019.

[185] Alicia J Kollár, Alexander T Papageorge, Varun D Vaidya, Yudan Guo, Jonathan Keeling, and Benjamin L Lev. Supermode-density-wave-polariton condensation with a bose–einstein condensate in a multimode cavity. *Nature communications*, 8(1):1–10, 2017.

[186] M. Kormos, M. Collura, G. Takács, and P. Calabrese. Real time confinement following a quantum quench to a non-integrable model. *Nat. Phys.*, 13:246–249, 2017.

[187] Marton Kormos, Mario Collura, Gabor Takács, and Pasquale Calabrese. Real-time confinement following a quantum quench to a non-integrable model. *Nature Physics*, 13(3):246–249, 2017.

[188] P. Krantz, M. Kjaergaard, F. Yan, T. P. Orlando, S. Gustavsson, and W. D. Oliver. A quantum engineer's guide to superconducting qubits. *Applied Physics Reviews*, 6(2):021318, 2019.

[189] Hanna Krauter, Christine A. Muschik, Kasper Jensen, Wojciech Wasilewski, Jonas M. Petersen, J. Ignacio Cirac, and Eugene S. Polzik. Entanglement generated by dissipation and steady state entanglement of two macroscopic objects. *Phys. Rev. Lett.*, 107:080503, Aug 2011.

[190] S. Krinner, S. Lazar, A. Remm, C.K. Andersen, N. Lacroix, G.J. Norris, C. Hellings, M. Gabureac, C. Eichler, and A. Wallraff. Benchmarking coherent errors in controlled-phase gates due to spectator qubits. *Phys. Rev. Applied*, 14:024042, Aug 2020.

[191] Katrin Kroeger, Nishant Dogra, Rodrigo Rosa-Medina, Marcin Paluch, Francesco Ferri, Tobias Donner, and Tilman Esslinger. Continuous feedback on a quantum gas coupled to an optical cavity. *New Journal of Physics*, 22(3):033020, 2020.

[192] Ronen M Kroeze, Yudan Guo, Varun D Vaidya, Jonathan Keeling, and Benjamin L Lev. Spinor self-ordering of a quantum gas in a cavity. *Physical review letters*, 121(16):163601, 2018.

[193] Dominik J. Kubicki, Samuel D. Stranks, Clare P. Grey, and Lyndon Emsley. Nmr spectroscopy probes microstructure, dynamics and doping of metal halide perovskites. *Nature Reviews Chemistry*, 5(9):624–645, Sep 2021.

[194] Georg Kucsko, Soonwon Choi, Joonhee Choi, Peter C Maurer, Hengyun Zhou, Renate Landig, Hitoshi Sumiya, Shinobu Onoda, Junich Isoya, Fedor Jelezko, et al. Critical thermalization of a disordered dipolar spin system in diamond. *Physical review letters*, 121(2):023601, 2018.

[195] Michael Kühn, Sebastian Zanker, Peter Deglmann, Michael Marthaler, and Horst Weib. Accuracy and resource estimations for quantum chemistry on a near-term quantum computer. *Journal of Chemical Theory and Computation*, 15(9):4764–4780, 2019.

[196] Ilya Kuprov. Large-scale nmr simulations in liquid state: A tutorial. *Magnetic Resonance in Chemistry*, 56(6):415–437, 2018.

[197] T. D. Ladd, F. Jelezko, R. Laflamme, Y. Nakamura, C. Monroe, and J. L. O'Brien. Quantum computers. *Nature*, 464(7285):45–53, 2010.

[198] L D Landau and S I Pekar. Effective Mass of a Polaron. *Zhurnal Eksperimentalnoi i Teoreticheskoi Fiziki*, 18(5):419–423, 1948.

[199] Lev Davidovich Landau. Electron motion in crystal lattices. *Phys. Z. Sowjet.*, page 664, 1933.

[200] Renate Landig, Lorenz Hruby, Nishant Dogra, Manuele Landini, Rafael Mottl, Tobias Donner, and Tilman Esslinger. *Nature, 532, 476-479*, 2016.

[201] Manuele Landini, Nishant Dogra, Katrin Kröger, Lorenz Hruby, T Donner, and Tilman Esslinger. Formation of a spin texture in a quantum gas coupled to a cavity. *Physical review letters*, 120(22):223602, 2018.

[202] Florian Lange, Zala Lenarčič, and Achim Rosch. Time-dependent generalized gibbs ensembles in open quantum systems. *Physical Review B*, 97(16):165138, 2018.

[203] B. P. Lanyon, C. Hempel, D. Nigg, M. Müller, R. Gerritsma, F. Zähringer, P. Schindler, J. T. Barreiro, M. Rambach, G. Kirchmair, M. Hennrich, P. Zoller, R. Blatt, and C. F. Roos. Universal digital quantum simulation with trapped ions. *Science*, 334(6052):57–61, 2011.

[204] Tobias Lausch, Artur Widera, and Michael Fleischhauer. Prethermalization in the cooling dynamics of an impurity in a bose-einstein condensate. *Phys. Rev. A*, 97:023621, Feb 2018.

[205] David Layden and Paola Cappellaro. Spatial noise filtering through error correction for quantum sensing. *npj Quantum Information*, 4(1):30, 2018.

[206] M. P. Ledbetter, T. Theis, J. W. Blanchard, H. Ring, P. Ganssle, S. Appelt, B. Blümich, A. Pines, and D. Budker. Near-zero-field nuclear magnetic resonance. *Phys. Rev. Lett.*, 107:107601, Sep 2011.

[207] T. D. Lee, F. E. Low, and D. Pines. The motion of slow electrons in a polar crystal. *Phys. Rev.*, 90:297–302, Apr 1953.

[208] Julian Léonard, Andrea Morales, Philip Zupancic, Tilman Esslinger, and Tobias Donner. Supersolid formation in a quantum gas breaking a continuous translational symmetry. *Nature*, 543(7643):87, 2017.

[209] Alessio Lerose, Jamir Marino, Andrea Gambassi, and Alessandro Silva. Prethermal quantum many-body kapitza phases of periodically driven spin systems. *Phys. Rev. B*, 100:104306, Sep 2019.

[210] Alessio Lerose, Jamir Marino, Bojan Zunkovic, Andrea Gambassi, and Alessandro Silva. Chaotic dynamical ferromagnetic phase induced by nonequilibrium quantum fluctuations. *Phys. Rev. Lett.*, 120:130603, Mar 2018.

[211] Alessio Lerose and Silvia Pappalardi. Bridging entanglement dynamics and chaos in semiclassical systems. *Phys. Rev. A*, 102:032404, Sep 2020.

[212] Alessio Lerose and Silvia Pappalardi. Origin of the slow growth of entanglement entropy in long-range interacting spin systems. *Physical Review Research*, 2(1):012041, 2020.

[213] Alessio Lerose, Federica M. Surace, Paolo P. Mazza, Gabriele Perfetto, Mario Collura, and Andrea Gambassi. Quasilocalized dynamics from confinement of quantum excitations. *Phys. Rev. B*, 102:041118, Jul 2020.

[214] Alessio Lerose, Bojan Zunkovic, Jamir Marino, Andrea Gambassi, and Alessandro Silva. Impact of nonequilibrium fluctuations on prethermal dynamical phase transitions in long-range interacting spin chains. *Phys. Rev. B*, 99:045128, Jan 2019.

[215] Ian D Leroux, Monika H Schleier-Smith, and Vladan Vuletić. Implementation of cavity squeezing of a collective atomic spin. *Physical Review Letters*, 104(7):073602, 2010.

[216] Ian D. Leroux, Monika H. Schleier-Smith, and Vladan Vuletić. Implementation of cavity squeezing of a collective atomic spin. *Phys. Rev. Lett.*, 104:073602, Feb 2010.

[217] Jesper Levinsen, Meera M. Parish, Rasmus S. Christensen, Jan J. Arlt, and Georg M. Bruun. Finite-temperature behavior of the bose polaron. *Phys. Rev. A*, 96:063622, Dec 2017.

[218] Malcolm H. Levitt. *Spin Dynamics: Basics of Nuclear Magnetic Resonance*. John Wiley & Sons Ltd, 2008.

[219] Elliott H Lieb and Derek W Robinson. The finite group velocity of quantum spin systems. In *Statistical mechanics*, pages 425–431. Springer, 1972.

[220] Yiheng Lin, JP Gaebler, Florentin Reiter, Ting R Tan, Ryan Bowler, AS Sørensen, Dietrich Leibfried, and David J Wineland. Dissipative production of a maximally entangled steady state of two quantum bits. *Nature*, 504(7480):415–418, 2013.

[221] Fangli Liu, Rex Lundgren, Paraj Titum, Guido Pagano, Jiehang Zhang, Christopher Monroe, and Alexey V. Gorshkov. Confined quasiparticle dynamics in long-range interacting quantum spin chains. *Phys. Rev. Lett.*, 122:150601, Apr 2019.

[222] Yanbing Liu and Andrew A Houck. Quantum electrodynamics near a photonic bandgap. *Nature Physics*, 13(1):48–52, 2017.

[223] S. Lorenzo, T. Apollaro, G. M. Palma, R. Nandkishore, A. Silva, and J. Marino. Remnants of anderson localization in prethermalization induced by white noise. *Phys. Rev. B*, 98:054302, Aug 2018.

[224] I. Lovchinsky, A. O. Sushkov, E. Urbach, N. P. de Leon, S. Choi, K. De Greve, R. Evans, R. Gertner, E. Bersin, C. Müller, L. McGuinness, F. Jelezko, R. L. Walsworth, H. Park, and M. D. Lukin. Nuclear magnetic resonance detection and spectroscopy of single proteins using quantum logic. *Science*, 351(6275):836–841, 2016.

[225] David J. Luitz, Nicolas Laflorencie, and Fabien Alet. Many-body localization edge in the random-field heisenberg chain. *Physical Review B*, 91(8), Feb 2015.

[226] Jiaji Ma, Ruihan Yang, and Hanghui Chen. A large modulation of electron-phonon coupling and an emergent superconducting dome in doped strong ferroelectrics. *Nature Communications*, 12(1):2314, 2021.

[227] Jian Ma, Xiaoguang Wang, Chang-Pu Sun, and Franco Nori. Quantum spin squeezing. *Physics Reports*, 509(2-3):89–165, 2011.

[228] Ruichao Ma, Brendan Saxberg, Clai Owens, Nelson Leung, Yao Lu, Jonathan Simon, and David I Schuster. A dissipatively stabilized mott insulator of photons. *Nature*, 566(7742):51–57, 2019.

[229] Francisco Machado, Dominic V. Else, Gregory D. Kahanamoku-Meyer, Chetan Nayak, and Norman Y. Yao. Long-range prethermal phases of nonequilibrium matter. *Phys. Rev. X*, 10:011043, Feb 2020.

[230] Mohammad F Maghrebi and Alexey V Gorshkov. Nonequilibrium many-body steady states via keldysh formalism. *Physical Review B*, 93(1):014307, 2016.

[231] J Majer, JM Chow, JM Gambetta, Jens Koch, BR Johnson, JA Schreier, L Frunzio, DI Schuster, Andrew Addison Houck, Andreas Wallraff, et al. Coupling superconducting qubits via a cavity bus. *Nature*, 449(7161):443–447, 2007.

[232] H. J. Mamin, M. Kim, M. H. Sherwood, C. T. Rettner, K. Ohno, D. D. Awschalom, and D. Rugar. Nanoscale nuclear magnetic resonance with a nitrogen-vacancy spin sensor. *Science*, 339(6119):557–560, 2013.

[233] Tom Manovitz, Yotam Shapira, Nitzan Akerman, Ady Stern, and Roee Ozeri. Quantum simulations with complex geometries and synthetic gauge fields in a trapped ion chain. *PRX Quantum*, 1(2), oct 2020.

[234] Nurit Manukovsky, Akiva Feintuch, Ilya Kuprov, and Daniella Goldfarb. Time domain simulation of gd3+–gd3+ distance measurements by epr. *The Journal of Chemical Physics*, 147(4), 07 2017.

[235] D. Marcos, P. Rabl, E. Rico, and P. Zoller. Superconducting circuits for quantum simulation of dynamical gauge fields. *Phys. Rev. Lett.*, 111:110504, Sep 2013.

[236] D Marcos, Andrea Tomadin, Sebastian Diehl, and P Rabl. Photon condensation in circuit quantum electrodynamics by engineered dissipation. *New Journal of Physics*, 14(5):055005, 2012.

[237] M Marcuzzi, E Levi, W Li, J P Garrahan, B Olmos, and I Lesanovsky. Nonequilibrium universality in the dynamics of dissipative cold atomic gases. *New Journal of Physics*, 17(7):072003, jul 2015.

[238] J Marino and AM Rey. Cavity-qed simulator of slow and fast scrambling. *Physical Review A*, 99(5):051803, 2019.

[239] J Marino, YE Shchadilova, M Schleier-Smith, and EA Demler. Spectrum, landau–zener theory and driven-dissipative dynamics of a staircase of photons. *New Journal of Physics*, 21(1):013009, 2019.

[240] Jamir Marino and Sebastian Diehl. Driven markovian quantum criticality. *Physical review letters*, 116(7):070407, 2016.

[241] Jamir Marino and Alessandro Silva. Relaxation, prethermalization, and diffusion in a noisy quantum ising chain. *Phys. Rev. B*, 86:060408, Aug 2012.

[242] Jamir Marino and Alessandro Silva. Nonequilibrium dynamics of a noisy quantum ising chain: Statistics of work and prethermalization after a sudden quench of the transverse field. *Phys. Rev. B*, 89:024303, Jan 2014.

[243] Esteban A. Martinez, Christine A. Muschik, Philipp Schindler, Daniel Nigg, Alexander Erhard, Markus Heyl, Philipp Hauke, Marcello Dalmonte, Thomas Monz, Peter Zoller, and Rainer Blatt. Real-time dynamics of lattice gauge theories with a few-qubit quantum computer. *Nature*, 534(7608):516–519, 2016.

[244] Stuart J Masson, Igor Ferrier-Barbut, Luis A Orozco, Antoine Browaeys, and Ana Asenjo-Garcia. Many-body signatures of collective decay in atomic chains. *Physical review letters*, 125(26):263601, 2020.

[245] Eberhard Matern, Michael Engelhardt, and Gerhard Hägele. Solving the 31p{1H} nmr spectrum of (me3si)3p7 as b[ac]3 case. *Phosphorus, Sulfur, and Silicon and the Related Elements*, 192(6):727–731, 2017.

[246] L. Mathey, D.-W. Wang, W. Hofstetter, M. D. Lukin, and Eugene Demler. Luttinger liquid of polarons in one-dimensional boson-fermion mixtures. *Phys. Rev. Lett.*, 93:120404, Sep 2004.

[247] Ludwig Mathey and Anatoli Polkovnikov. Light cone dynamics and reverse kibble-zurek mechanism in two-dimensional superfluids following a quantum quench. *Physical Review A*, 81(3):033605, 2010.

[248] Charles J.M. Mathy, Mikhail B. Zvonarev, and Eugene Demler. Quantum flutter of supersonic particles in one-dimensional quantum liquids. *Nature Physics*, 8(12):881–886, 2012.

[249] Takuro Matsuta, Tohru Koma, and Shu Nakamura. Improving the lieb–robinson bound for long-range interactions. *Annales Henri Poincaré*, 18(2):519–528, Feb 2017.

[250] Jarrod R. McClean, Nicholas C. Rubin, Joonho Lee, Matthew P. Harrigan, Thomas E. O'Brien, Ryan Babbush, William J. Huggins, and Hsin-Yuan Huang. What the foundations of quantum computer science teach us about chemistry, 2021.

[251] F. Meinert, M. Knap, E. Kirilov, K. Jag-Lauber, M. B. Zvonarev, E. Demler, and H.-C. Nägerl. Bloch oscillations in the absence of a lattice. *Science*, 356(6341):945–948, 2017.

[252] Nicolas Merle, Guillaume Girard, Nicolas Popoff, Aimery De Mallmann, Yassine Bouhoute, Julien Trebosc, Elise Berrier, Jean-Francois Paul, Christopher P. Nicholas, Iker Del Rosal, Laurent Maron, Regis M. Gauvin, Laurent Delevoye, and Mostafa Taoufik. On the track to silica-supported tungsten oxo metathesis catalysts: Input from 17o solid-state nmr. *Inorganic Chemistry*, 52(17):10119–10130, 2013. PMID: 23944270.

[253] S I Mistakidis, F Grusdt, G M Koutentakis, and P Schmelcher. Dissipative correlated dynamics of a moving impurity immersed in a bose–einstein condensate. *New Journal of Physics*, 21(10):103026, oct 2019.

[254] S. I. Mistakidis, G. C. Katsimiga, G. M. Koutentakis, Th. Busch, and P. Schmelcher. Quench dynamics and orthogonality catastrophe of bose polarons. *Phys. Rev. Lett.*, 122:183001, May 2019.

[255] S I Mistakidis, G M Koutentakis, G C Katsimiga, and P Schmelcher. Many-body quantum dynamics and induced correlations of Bose polarons. pages 1–25, 2020.

[256] S. I. Mistakidis, A. G. Volosniev, N. T. Zinner, and P. Schmelcher. Effective approach to impurity dynamics in one-dimensional trapped Bose gases. *Physical Review A*, 100(1):1–12, 2019.

[257] Aditi Mitra. Correlation functions in the prethermalized regime after a quantum quench of a spin chain. *Physical Review B*, 87(20):205109, 2013.

[258] Farokh Mivehvar, Francesco Piazza, Tobias Donner, and Helmut Ritsch. Cavity qed with quantum gases: New paradigms in many-body physics. *arXiv preprint arXiv:2102.04473*, 2021.

[259] Farokh Mivehvar, Francesco Piazza, Tobias Donner, and Helmut Ritsch. Cavity QED with quantum gases: new paradigms in many-body physics. *Advances in Physics*, 70(1):1–153, jan 2021.

[260] C. Monroe, W. C. Campbell, L.-M. Duan, Z.-X. Gong, A. V. Gorshkov, P. W. Hess, R. Islam, K. Kim, N. M. Linke, G. Pagano, P. Richerme, C. Senko, and N. Y. Yao. Programmable quantum simulations of spin systems with trapped ions. *Rev. Mod. Phys.*, 93:025001, Apr 2021.

[261] S Morrison and AS Parkins. Dynamical quantum phase transitions in the dissipative lipkin-meshkov-glick model with proposed realization in optical cavity qed. *Physical review letters*, 100(4):040403, 2008.

[262] Steven A Moses, Jacob P Covey, Matthew T Miecnikowski, Deborah S Jin, and Jun Ye. New frontiers for quantum gases of polar molecules. *Nature Physics*, 13(1):13–20, 2017.

[263] K. Mukherjee, S. I. Mistakidis, S. Majumder, and P. Schmelcher. Pulse and continuously driven many-body quantum dynamics of bosonic impurities in a Bose-Einstein condensate. *Phys. Rev. A*, 023615:1–20, 2019.

[264] Rahul Nandkishore and David A. Huse. Many-body localization and thermalization in quantum statistical mechanics. *Annual Review of Condensed Matter Physics*, 6(1):15–38, Mar 2015.

[265] N. Navon, S. Nascimbène, F. Chevy, and C. Salomon. The equation of state of a low-temperature fermi gas with tunable interactions. *Science*, 328(5979):729–732, 2010.

[266] Hui Khoon Ng and John Preskill. Fault-tolerant quantum computation versus gaussian noise. *Phys. Rev. A*, 79:032318, Mar 2009.

[267] K Knakkergaard Nielsen, L A Peña Ardila, G M Bruun, and T Pohl. Critical slowdown of non-equilibrium polaron dynamics. *New Journal of Physics*, 21(4):043014, apr 2019.

[268] Michael A Nielsen. A simple formula for the average gate fidelity of a quantum dynamical operation. *Physics Letters A*, 303(4):249 – 252, 2002.

[269] Michael A. Nielsen and Isaac L. Chuang. *Quantum Computation and Quantum Information*. Cambridge University Press, 2000.

[270] Changsuk Noh and Dimitris G Angelakis. Quantum simulations and many-body physics with light. *Reports on Progress in Physics*, 80(1):016401, nov 2016.

[271] Matthew A Norcia, Robert J Lewis-Swan, Julia RK Cline, Bihui Zhu, Ana M Rey, and James K Thompson. Cavity-mediated collective spin-exchange interactions in a strontium superradiant laser. *Science*, 361(6399):259–262, 2018.

[272] Thomas E. O'Brien, Lev B. Ioffe, Yuan Su, David Fushman, Hartmut Neven, Ryan Babbush, and Vadim Smelyanskiy. Quantum computation of molecular structure using data from challenging-to-classically-simulate nuclear magnetic resonance experiments, 2021.

[273] B. Olmos, D. Yu, and I. Lesanovsky. Steady-state properties of a driven atomic ensemble with nonlocal dissipation. *Phys. Rev. A*, 89:023616, Feb 2014.

[274] P. J. J. O'Malley, R. Babbush, I. D. Kivlichan, J. Romero, J. R. McClean, R. Barends, J. Kelly, P. Roushan, A. Tranter, N. Ding, B. Campbell, Y. Chen, Z. Chen, B. Chiaro, A. Dunsworth, A. G. Fowler, E. Jeffrey, E. Lucero, A. Megrant, J. Y. Mutus, M. Neeley, C. Neill, C. Quintana, D. Sank, A. Vainsencher, J. Wenner, T. C. White, P. V. Coveney, P. J. Love, H. Neven, A. Aspuru-Guzik, and J. M. Martinis. Scalable quantum simulation of molecular energies. *Phys. Rev. X*, 6:031007, Jul 2016.

[275] Arijeet Pal and David A. Huse. Many-body localization phase transition. *Physical Review B*, 82(17), Nov 2010.

[276] CD Parmee and NR Cooper. Phases of driven two-level systems with nonlocal dissipation. *Physical Review A*, 97(5):053616, 2018.

[277] Daniel A Paz and Mohammad F Maghrebi. Critical dynamics of weakly-dissipative driven systems. *arXiv preprint arXiv:1906.08278*, 2019.

[278] Daniel A Paz and Mohammad F Maghrebi. Time-reversal symmetry breaking and resurrection in driven-dissipative ising models. *arXiv preprint arXiv:2105.12747*, 2021.

[279] Gerardo A Paz-Silva, Seung-Woo Lee, Todd J Green, and Lorenza Viola. Dynamical decoupling sequences for multi-qubit dephasing suppression and long-time quantum memory. *New Journal of Physics*, 18(7):073020, jul 2016.

[280] L. A. Peña Ardila and S. Giorgini. Impurity in a bose-einstein condensate: Study of the attractive and repulsive branch using quantum monte carlo methods. *Phys. Rev. A*, 92:033612, Sep 2015.

[281] L. A. Peña Ardila, N. B. Jørgensen, T. Pohl, S. Giorgini, G. M. Bruun, and J. J. Arlt. Analyzing a bose polaron across resonant interactions. *Phys. Rev. A*, 99:063607, Jun 2019.

[282] Solomon Pekar. Autolocalization of the electron in a dielectric inertially polarizing medium. *Zhurnal Eksperimentalnoi i Teoreticheskoi Fiziki*, 16(4):335–340, 1946.

[283] Avikar Periwal, Eric S. Cooper, Philipp Kunkel, Julian F. Wienand, Emily J. Davis, and Monika Schleier-Smith. Programmable interactions and emergent geometry in an atomic array, 2021.

[284] Luca Pezzè, Augusto Smerzi, Markus K. Oberthaler, Roman Schmied, and Philipp Treutlein. Quantum metrology with nonclassical states of atomic ensembles. *Rev. Mod. Phys.*, 90:035005, Sep 2018.

[285] L. Pitaevskii and S. Stringari. *Bose-Einstein Condensation*. Oxford University Press, Oxford, 2003.

[286] Andrea Pizzi, Johannes Knolle, and Andreas Nunnenkamp. Higher-order and fractional discrete time crystals in clean long-range interacting systems. *Nature Communications*, 12(1):1–7, 2021.

[287] Marcin Płodzień, Tomasz Sowiński, and Servaas Kokkelmans. Simulating polaron biophysics with Rydberg atoms. *Scientific Reports*, 8:9247, 2018.

[288] Luis Fernando dos Prazeres, Leonardo da Silva Souza, and Fernando Iemini. Boundary time crystals in collective d-level systems. *arXiv preprint arXiv:2102.03374*, 2021.

[289] John Preskill. Sufficient condition on noise correlations for scalable quantum computing, 2012.

[290] John Preskill. Quantum Computing in the NISQ era and beyond. *Quantum*, 2:79, August 2018.

[291] Kevin Qian, Zachary Eldredge, Wenchao Ge, Guido Pagano, Christopher Monroe, J. V. Porto, and Alexey V. Gorshkov. Heisenberg-scaling measurement protocol for analytic functions with quantum sensor networks. *Phys. Rev. A*, 100:042304, Oct 2019.

[292] Timothy Qian, Jacob Bringewatt, Igor Boettcher, Przemyslaw Bienias, and Alexey V. Gorshkov. Optimal measurement of field properties with quantum sensor networks. *Phys. Rev. A*, 103:L030601, Mar 2021.

[293] Steffen Patrick Rath and Richard Schmidt. Field-theoretical study of the bose polaron. *Phys. Rev. A*, 88:053632, Nov 2013.

[294] Bernd Reif, Sharon E. Ashbrook, Lyndon Emsley, and Mei Hong. Solid-state nmr spectroscopy. *Nature Reviews Methods Primers*, 1(1):2, Jan 2021.

[295] Markus Reiher, Nathan Wiebe, Krysta M. Svore, Dave Wecker, and Matthias Troyer. Elucidating reaction mechanisms on quantum computers. *Proceedings of the National Academy of Sciences*, 114(29):7555–7560, 2017.

[296] Florentin Reiter, Florian Lange, and Zala Lenarčič. Engineering generalized gibbs ensembles with trapped ions. *arXiv preprint arXiv:1910.01593*, 2019.

[297] Florentin Reiter, David Reeb, and Anders S Sørensen. Scalable dissipative preparation of many-body entanglement. *Physical review letters*, 117(4):040501, 2016.

[298] Philip Richerme, Zhe-Xuan Gong, Aaron Lee, Crystal Senko, Jacob Smith, Michael Foss-Feig, Spyridon Michalakis, Alexey V Gorshkov, and Christopher Monroe. Non-local propagation of correlations in long-range interacting quantum systems. *arXiv preprint arXiv:1401.5088*, 2014.

[299] Sabine Richert, Jonathan Cremers, Ilya Kuprov, Martin D. Peeks, Harry L. Anderson, and Christiane R. Timmel. Constructive quantum interference in a bis-copper six-porphyrin nanoring. *Nature Communications*, 8(1):14842, 2017.

[300] Rich Rines, Kevin Obenland, and Isaac Chuang. Empirical determination of the simulation capacity of a near-term quantum computer, 2019.

[301] Giacomo Roati, Chiara D'Errico, Leonardo Fallani, Marco Fattori, Chiara Fort, Matteo Zaccanti, Giovanni Modugno, Michele Modugno, and Massimo Inguscio. Anderson localization of a non-interacting bose–einstein condensate. *Nature*, 453(7197):895–898, 2008.

[302] Simone Rochfort. Metabolomics reviewed: A new "omics"platform technology for systems biology and implications for natural products research. *Journal of Natural Products*, 68(12):1813–1820, 12 2005.

[303] Maxie M. Roessler and Enrico Salvadori. Principles and applications of epr spectroscopy in the chemical sciences. *Chem. Soc. Rev.*, 47:2534–2553, 2018.

[304] Rodrigo Rosa-Medina, Francesco Ferri, Fabian Finger, Nishant Dogra, Katrin Kroeger, Rui Lin, R. Chitra, Tobias Donner, and Tilman Esslinger. Observing dynamical currents in a non-hermitian momentum lattice. *Phys. Rev. Lett.*, 128:143602, Apr 2022.

[305] P. Roushan, C. Neill, J. Tangpanitanon, V. M. Bastidas, A. Megrant, R. Barends, Y. Chen, Z. Chen, B. Chiaro, A. Dunsworth, A. Fowler, B. Foxen, M. Giustina, E. Jeffrey, J. Kelly, E. Lucero, J. Mutus, M. Neeley, C. Quintana,

D. Sank, A. Vainsencher, J. Wenner, T. White, H. Neven, D. G. Angelakis, and J. Martinis. Spectroscopic signatures of localization with interacting photons in superconducting qubits. *Science*, 358(6367):1175–1179, 2017.

[306] Andreas Rückriegel, Andreas Kreisel, and Peter Kopietz. Time-dependent spin-wave theory. *Physical Review B*, 85(5):054422, 2012.

[307] Angelo Russomanno, Fernando Iemini, Marcello Dalmonte, and Rosario Fazio. Floquet time crystal in the lipkin-meshkov-glick model. *Phys. Rev. B*, 95:214307, Jun 2017.

[308] Pablo Sala, Tibor Rakovszky, Ruben Verresen, Michael Knap, and Frank Pollmann. Ergodicity breaking arising from hilbert space fragmentation in dipole-conserving hamiltonians. *Phys. Rev. X*, 10:011047, Feb 2020.

[309] Y. Salathé, M. Mondal, M. Oppliger, J. Heinsoo, P. Kurpiers, A. Potočnik, A. Mezzacapo, U. Las Heras, L. Lamata, E. Solano, S. Filipp, and A. Wallraff. Digital quantum simulation of spin models with circuit quantum electrodynamics. *Phys. Rev. X*, 5:021027, Jun 2015.

[310] R. Scelle, T. Rentrop, A. Trautmann, T. Schuster, and M. K. Oberthaler. Motional coherence of fermions immersed in a bose gas. *Physical Review Letters*, 111(7):1–5, 2013.

[311] Florian Schäfer, Takeshi Fukuhara, Seiji Sugawa, Yosuke Takasu, and Yoshiro Takahashi. Tools for quantum simulation with ultracold atoms in optical lattices. *Nature Reviews Physics*, 2(8):411–425, 2020.

[312] M. Schecter, A. Kamenev, D. M. Gangardt, and A. Lamacraft. Critical velocity of a mobile impurity in one-dimensional quantum liquids. *Physical Review Letters*, 108(20):1–5, 2012.

[313] Olav Schiemann and Thomas F. Prisner. Long-range distance determinations in biomacromolecules by epr spectroscopy. *Quarterly Reviews of Biophysics*, 40(1):1–53, 2007.

[314] Mauro Schiulaz, Alessandro Silva, and Markus Müller. Dynamics in many-body localized quantum systems without disorder. *Phys. Rev. B*, 91:184202, May 2015.

[315] Monika H. Schleier-Smith, Ian D. Leroux, and Vladan Vuletić. Squeezing the collective spin of a dilute atomic ensemble by cavity feedback. *Phys. Rev. A*, 81:021804, Feb 2010.

[316] Stefan Schmid, Arne Härter, and Johannes Hecker Denschlag. Dynamics of a cold trapped ion in a Bose-Einstein condensate. *Physical Review Letters*, 105(13):1–4, 2010.

[317] Richard Schmidt and Mikhail Lemeshko. Deformation of a quantum many-particle system by a rotating impurity. *Phys. Rev. X*, 6:011012, Feb 2016.

[318] M. Schulz, C. A. Hooley, R. Moessner, and F. Pollmann. Stark many-body localization. *Phys. Rev. Lett.*, 122:040606, Jan 2019.

[319] K. Seetharam, A. Lerose, R. Fazio, and J. Marino. Correlation engineering via nonlocal dissipation. *Phys. Rev. Research*, 4:013089, Feb 2022.

[320] K. Seetharam, A. Lerose, R. Fazio, and J. Marino. Dynamical scaling of correlations generated by short- and long-range dissipation. *Phys. Rev. B*, 105:184305, May 2022.

[321] Kushal Seetharam, Debopriyo Biswas, Crystal Noel, Andrew Risinger, Daiwei Zhu, Or Katz, Sambuddha Chattopadhyay, Marko Cetina, Christopher Monroe, Eugene Demler, and Dries Sels. Digital quantum simulation of nmr experiments, 2021.

[322] Kushal Seetharam, Eleanor Crane, Alexander Schuckert, Michael DeMarco, and Eugene Demler. Parallel averaging advantage in simulations of nmr experiments using hybrid quantum simulators, (In preparation).

[323] Kushal Seetharam, Fabian Grusdt, Mikhail Zvonarev, and Eugene Demler. Probing the effective mass and quantum cherenkov behavior of bose polarons, (In preparation).

[324] Kushal Seetharam, Dries Sels, and Eugene Demler. Platform tailored co-design of gate-based quantum simulation, 2021.

[325] Kushal Seetharam, Yulia Shchadilova, Fabian Grusdt, Mikhail Zvonarev, and Eugene Demler. Quantum cherenkov transition of finite momentum bose polarons, 2021.

[326] Kushal Seetharam, Yulia Shchadilova, Fabian Grusdt, Mikhail B. Zvonarev, and Eugene Demler. Dynamical quantum cherenkov transition of fast impurities in quantum liquids. *Phys. Rev. Lett.*, 127:185302, Oct 2021.

[327] P. Sekatski, S. Wölk, and W. Dür. Optimal distributed sensing in noisy environments. *Phys. Rev. Research*, 2:023052, Apr 2020.

[328] Dries Sels, Hesam Dashti, Samia Mora, Olga Demler, and Eugene Demler. Quantum approximate bayesian computation for nmr model inference. *Nature Machine Intelligence*, 2(7):396–402, Jul 2020.

[329] Dries Sels, Hesam Dashti, Samia Mora, Olga Demler, and Eugene Demler. Quantum approximate bayesian computation for nmr model inference. *Nature Machine Intelligence*, 2(7):396–402, 2020.

[330] Dries Sels and Eugene Demler. Quantum generative model for sampling many-body spectral functions. *Phys. Rev. B*, 103:014301, Jan 2021.

[331] Athreya Shankar, Emil A. Yuzbashyan, Victor Gurarie, Peter Zoller, John J. Bollinger, and Ana Maria Rey. Simulating dynamical phases of chiral $p + ip$ superconductors with a trapped ion magnet, 2022.

[332] Aditya Shashi, Fabian Grusdt, Dmitry A. Abanin, and Eugene Demler. Radio-frequency spectroscopy of polarons in ultracold bose gases. *Phys. Rev. A*, 89:053617, May 2014.

[333] Yulia E. Shchadilova, Fabian Grusdt, Alexey N. Rubtsov, and Eugene Demler. Polaronic mass renormalization of impurities in bose-einstein condensates: Correlated gaussian-wave-function approach. *Phys. Rev. A*, 93:043606, Apr 2016.

[334] Yulia E. Shchadilova, Richard Schmidt, Fabian Grusdt, and Eugene Demler. Quantum dynamics of ultracold bose polarons. *Phys. Rev. Lett.*, 117:113002, Sep 2016.

[335] Yangchao Shen, Yao Lu, Kuan Zhang, Junhua Zhang, Shuaining Zhang, Joonsuk Huh, and Kihwan Kim. Quantum optical emulation of molecular vibronic spectroscopy using a trapped-ion device. *Chemical Science*, 9(4):836–840, 2018.

[336] Tao Shi, Eugene Demler, and J Ignacio Cirac. Variational study of fermionic and bosonic systems with non-gaussian states: Theory and applications. *Annals of Physics*, 390:245–302, 2018.

[337] Tao Shi, Eugene Demler, and J. Ignacio Cirac. Variational study of fermionic and bosonic systems with non-Gaussian states: Theory and applications. *Annals of Physics*, 390:245–302, 2018.

[338] Eric Sierra, Stuart J Masson, and Ana Asenjo-Garcia. Dicke superradiance in ordered lattices: role of geometry and dimensionality. *arXiv preprint arXiv:2110.08380*, 2021.

[339] Magnus G. Skou, Thomas G. Skov, Nils B. Jørgensen, Kristian K. Nielsen, Arturo Camacho-Guardian, Thomas Pohl, Georg M. Bruun, and Jan J. Arlt. Non-equilibrium quantum dynamics and formation of the bose polaron. *Nature Physics*, 2021.

[340] A. Smith, J. Knolle, D. L. Kovrizhin, and R. Moessner. Disorder-free localization. *Phys. Rev. Lett.*, 118:266601, Jun 2017.

[341] Collin Smith, Alfred K. Hill, and Laura Torrente-Murciano. Current and future role of haber–bosch ammonia in a carbon-free energy landscape. *Energy Environ. Sci.*, 13:331–344, 2020.

[342] Anders Sørensen and K Molmer. *Phys. Rev. A*, 66(022314), 2002.

[343] Anders Søndberg Sørensen and Klaus Mølmer. Entangling atoms in bad cavities. *Phys. Rev. A*, 66:022314, Aug 2002.

[344] Nicolas Spethmann, Farina Kindermann, Shincy John, Claudia Weber, Dieter Meschede, and Artur Widera. Dynamics of single neutral impurity atoms immersed in an ultracold gas. *Physical Review Letters*, 109(23):1–5, 2012.

[345] K. Stannigel, P. Hauke, D. Marcos, M. Hafezi, S. Diehl, M. Dalmonte, and P. Zoller. Constrained dynamics via the zeno effect in quantum simulation: Implementing non-abelian lattice gauge theories with cold atoms. *Phys. Rev. Lett.*, 112:120406, Mar 2014.

[346] T. Staudacher, F. Shi, S. Pezzagna, J. Meijer, J. Du, C. A. Meriles, F. Reinhard, and J. Wrachtrup. Nuclear magnetic resonance spectroscopy on a (5-nanometer)3 sample volume. *Science*, 339(6119):561–563, 2013.

[347] T. Stavenger*, E. Crane*, K. Smith, Christopher Kang, Nathan Wiebe, and Steven Girvin. *In prep.*, 2022.

[348] WL Tan, P Becker, F Liu, G Pagano, KS Collins, A De, L Feng, HB Kaplan, A Kyprianidis, R Lundgren, et al. Observation of domain wall confinement and dynamics in a quantum simulator. *arXiv preprint arXiv:1912.11117*, 2019.

[349] Kristan Temme, Sergey Bravyi, and Jay M. Gambetta. Error mitigation for short-depth quantum circuits. *Phys. Rev. Lett.*, 119:180509, Nov 2017.

[350] J. Tempere, W. Casteels, M. K. Oberthaler, S. Knoop, E. Timmermans, and J. T. Devreese. Feynman path-integral treatment of the BEC-impurity polaron. *Physical Review B - Condensed Matter and Materials Physics*, 80(18):1–8, 2009.

[351] T. Theis, P. Ganssle, G. Kervern, S. Knappe, J. Kitching, M. P. Ledbetter, D. Budker, and A. Pines. Parahydrogen-enhanced zero-field nuclear magnetic resonance. *Nature Physics*, 7(7):571–575, 2011.

[352] Jeffrey Douglas Thompson, TG Tiecke, Nathalie P de Leon, J Feist, AV Akimov, M Gullans, Alexander S Zibrov, V Vuletić, and Mikhail D Lukin. Coupling a single trapped atom to a nanoscale optical cavity. *Science*, 340(6137):1202–1205, 2013.

[353] Federico Tonielli, Jan Carl Budich, Alexander Altland, and Sebastian Diehl. Topological field theory far from equilibrium. *Physical Review Letters*, 124(24):240404, 2020.

[354] Minh C. Tran, Chi-Fang Chen, Adam Ehrenberg, Andrew Y. Guo, Abhinav Deshpande, Yifan Hong, Zhe-Xuan Gong, Alexey V. Gorshkov, and Andrew Lucas. Hierarchy of linear light cones with long-range interactions. *Phys. Rev. X*, 10:031009, Jul 2020.

[355] Minh C. Tran, Andrew Y. Guo, Christopher L. Baldwin, Adam Ehrenberg, Alexey V. Gorshkov, and Andrew Lucas. The lieb-robinson light cone for power-law interactions. *arXiv:2103.15828*, 2021.

[356] Kristopher Tucker, Bihui Zhu, Robert J. Lewis-Swan, Jamir Marino, Felix Jimenez, Juan G. Restrepo, and Ana Maria Rey. *New Journal of Physics*, 20, 2018.

[357] Varun D Vaidya, Yudan Guo, Ronen M Kroeze, Kyle E Ballantine, Alicia J Kollár, Jonathan Keeling, and Benjamin L Lev. Tunable-range, photon-mediated atomic interactions in multimode cavity qed. *Physical Review X*, 8(1):011002, 2018.

[358] Varun D. Vaidya, Yudan Guo, Ronen M. Kroeze, Kyle E. Ballantine, Alicia J. Kollár, Jonathan Keeling, and Benjamin L. Lev. Tunable-range, photon-mediated atomic interactions in multimode cavity qed. *Phys. Rev. X*, 8:011002, Jan 2018.

[359] Arjan F Van Loo, Arkady Fedorov, Kevin Lalumiere, Barry C Sanders, Alexandre Blais, and Andreas Wallraff. Photon-mediated interactions between distant artificial atoms. *Science*, 342(6165):1494–1496, 2013.

[360] Senne Van Loon, Wim Casteels, and Jacques Tempere. Ground-state properties of interacting bose polarons. *Phys. Rev. A*, 98:063631, Dec 2018.

[361] Evert van Nieuwenburg, Yuval Baum, and Gil Refael. From bloch oscillations to many-body localization in clean interacting systems. *Proc. Natl. Acad. Sci.*, 116(19):9269–9274, 2019.

[362] Frank Verstraete, Michael M Wolf, and J Ignacio Cirac. Quantum computation and quantum-state engineering driven by dissipation. *Nature physics*, 5(9):633–636, 2009.

[363] Jonas Vlietinck, Wim Casteels, Kris Van Houcke, Jacques Tempere, Jan Ryckebusch, and Jozef T. Devreese. Diagrammatic Monte Carlo study of the acoustic and the Bose-Einstein condensate polaron. *New Journal of Physics*, 17, 2015.

[364] Davide Vodola, Luca Lepori, Elisa Ercolessi, Alexey V Gorshkov, and Guido Pupillo. Kitaev chains with long-range pairing. *Physical review letters*, 113(15):156402, 2014.

[365] Davide Vodola, Luca Lepori, Elisa Ercolessi, and Guido Pupillo. Long-range ising and kitaev models: phases, correlations and edge modes. *New Journal of Physics*, 18(1):015001, 2015.

[366] Christian Vorwerk, Nan Sheng, Marco Govoni, Benchen Huang, and Giulia Galli. Quantum embedding theories to simulate condensed systems on quantum computers. *Nature Computational Science*, 2(7):424–432, 2022.

[367] DF Walls, PD Drummond, SS Hassan, and HJ Carmichael. Non-equilibrium phase transitions in cooperative atomic systems. *Progress of Theoretical Physics Supplement*, 64:307–320, 1978.

[368] Wenjie Wan, Shu Jia, and Jason W. Fleischer. Dispersive superfluid-like shock waves in nonlinear optics. *Nature Physics*, 3(1):46–51, Dec 2006.

[369] A. Wilzewski, S. Afach, J.W. Blanchard, and D. Budker. A method for measurement of spin-spin couplings with sub-mhz precision using zero- to ultralow-field nuclear magnetic resonance. *Journal of Magnetic Resonance*, 284:66–72, 2017.

[370] D. J. Wineland, J. J. Bollinger, W. M. Itano, F. L. Moore, and D. J. Heinzen. Spin squeezing and reduced quantum noise in spectroscopy. *Phys. Rev. A*, 46:R6797–R6800, Dec 1992.

[371] Stefan Wolff, Jean-Sébastien Bernier, Dario Poletti, Ameneh Sheikhan, and Corinna Kollath. Evolution of two-time correlations in dissipative quantum spin systems: Aging and hierarchical dynamics. *Phys. Rev. B*, 100:165144, Oct 2019.

[372] S Wölk, P Sekatski, and W Dür. Noisy distributed sensing in the bayesian regime. *Quantum Science and Technology*, 5(4):045003, Jun 2020.

[373] Steven G. Worswick, James A. Spencer, Gunnar Jeschke, and Ilya Kuprov. Deep neural network processing of deer data. *Science Advances*, 4(8):eaat5218, 2018.

[374] Kurt Wüthrich. The way to nmr structures of proteins. *Nature Structural Biology*, 8(11):923–925, 2001.

[375] Bo Yan, Steven A Moses, Bryce Gadway, Jacob P Covey, Kaden RA Hazzard, Ana Maria Rey, Deborah S Jin, and Jun Ye. Realizing a lattice spin model with polar molecules. *arXiv preprint arXiv:1305.5598*, 2013.

[376] Fei Yan, Philip Krantz, Youngkyu Sung, Morten Kjaergaard, Daniel L. Campbell, Terry P. Orlando, Simon Gustavsson, and William D. Oliver. Tunable coupling scheme for implementing high-fidelity two-qubit gates. *Phys. Rev. Applied*, 10:054062, Nov 2018.

[377] Zoe Z. Yan, Yiqi Ni, Carsten Robens, and Martin W. Zwierlein. Bose polarons near quantum criticality. *Science*, 368(6487):190–194, 2020.

[378] Yariv Yanay, Jochen Braumüller, Simon Gustavsson, William D. Oliver, and Charles Tahan. Two-dimensional hard-core bose–hubbard model with superconducting qubits. *npj Quantum Information*, 6(1):58, 2020.

[379] N. Y. Yao, C. R. Laumann, J. I. Cirac, M. D. Lukin, and J. E. Moore. Quasi-many-body localization in translation-invariant systems. *Phys. Rev. Lett.*, 117:240601, Dec 2016.

[380] Ed Younis, Koushik Sen, Katherine Yelick, and Costin Iancu. Qfast: Conflating search and numerical optimization for scalable quantum circuit synthesis, 2021.

[381] Johannes Zeiher, Jae-yoon Choi, Antonio Rubio-Abadal, Thomas Pohl, Rick van Bijnen, Immanuel Bloch, and Christian Gross. Coherent many-body spin dynamics in a long-range interacting ising chain. *Physical Review X*, 7(4):041063, 2017.

[382] Zhao Zhang, Davide Dreon, Tilman Esslinger, Dieter Jaksch, Berislav Buca, and Tobias Donner. Tunable non-equilibrium phase transitions between spatial and temporal order through dissipation, 2022.

[383] Hengyun Zhou, Joonhee Choi, Soonwon Choi, Renate Landig, Alexander M. Douglas, Junichi Isoya, Fedor Jelezko, Shinobu Onoda, Hitoshi Sumiya, Paola Cappellaro, Helena S. Knowles, Hongkun Park, and Mikhail D. Lukin. Quantum metrology with strongly interacting spin systems. *Phys. Rev. X*, 10:031003, Jul 2020.

[384] Bihui Zhu, Jamir Marino, Norman Y Yao, Mikhail D Lukin, and Eugene A Demler. Dicke time crystals in driven-dissipative quantum many-body systems. *New Journal of Physics*, 21(7):073028, jul 2019.

[385] M. W. Zwierlein, C. A. Stan, C. H. Schunck, S. M. F. Raupach, S. Gupta, Z. Hadzibabic, and W. Ketterle. Observation of bose-einstein condensation of molecules. *Phys. Rev. Lett.*, 91:250401, Dec 2003.